

**SELF-ASSEMBLED PEPTIDE BASED BIOMATERIALS FOR
DRUG DELIVERY AND REGENERATIVE MEDICINE**

A DISSERTATION SUBMITTED TO
THE GRADUATE SCHOOL OF ENGINEERING AND SCIENCE
OF BILKENT UNIVERSITY
IN PARTIAL FULFILLMENT OF THE REQUIREMENTS FOR
THE DEGREE OF
DOCTOR OF PHILOSOPHY
IN
MATERIALS SCIENCE AND NANOTECHNOLOGY

By

Göksu Çinar

June 2016

SELF-ASSEMBLED PEPTIDE BASED BIOMATERIALS FOR DRUG
DELIVERY AND REGENERATIVE MEDICINE

By Gökse Çınar

June 2016

We certify that we have read this dissertation and that in our opinion it is fully adequate, in scope and in quality, as a dissertation for the degree of Doctor of Philosophy.

Mustafa Özgür Güler (Advisor)

Ayşe Begüm Tekinay

Semra İde

Aykutlu Dana

İrem Erel Göktepe

Approved for the Graduate School of Engineering and Science:

Levent Onural
Director of the Graduate School

ABSTRACT

SELF-ASSEMBLED PEPTIDE BASED BIOMATERIALS FOR DRUG DELIVERY AND REGENERATIVE MEDICINE

Göksu Çinar

Ph.D. in Materials Science and Nanotechnology

Advisor: Mustafa Özgür Güler

June, 2016

Self-assembly is a nature inspired novel engineering tool to build functional new generation of adaptable and complex biomaterials with variety of chemical and physical properties based on recent discoveries at the interface of chemistry, biology and materials science. Within self-assembling building blocks, peptides consisting natural amino acids and possibilities to integrate other molecules via synthetic approaches are intriguing biomacromolecules to obtain dynamic architectures at both nano and bulk scales for biomedical applications. In this thesis, the development of novel biomaterials through molecular self-assembly of the biomimetic peptides, bioactive peptide amphiphiles and their composite architectures with polymeric system for biomedical applications were presented. In the first chapter, the concept of self-assembly, design principles of the self-assembling peptide based building blocks and advanced characterization techniques for these materials were discussed to provide general perspective on the field. The applications of peptide based biomaterials with an emphasis on the drug delivery and regenerative medicine purposes were also highlighted in this part. In the second chapter, amyloid inspired self-assembling

peptides and their supramolecular assemblies were presented in the context of developing nature-inspired biocompatible and mechanically stable supramolecular peptide based biomaterials. In the third chapter, supramolecular PA nanofiber gels which can form supramolecular nanofibrous networks at physiological conditions and encapsulate chemotherapeutics with high efficacy were examined as controlled local drug delivery system at both *in vitro* and *in vivo* conditions. In the fourth chapter, the facile fabrication strategy to create a novel self-assembled peptide amphiphile (PA) nanofibers and PEG composite hydrogel system as synthetic ECM analogues was discussed. It was showed that the synergistic combination of different classes of materials provide us new opportunities to develop biomaterials with independently tunable biochemical, mechanical and physical properties.

Keywords: Self-assembly, biomaterials, amyloid inspired peptides, peptide amphiphiles, nanofibers, supramolecular nanofiber gels, drug delivery, controlled drug release and regenerative medicine

ÖZET

MOLEKÜLER KONTROLLÜ BİR ARAYA GELME YÖNTEMİYLE OLUŞTURULAN PEPTİT BAZLI BİYOMALZEMELERİN İLAÇ TAŞINIMI VE REJENERATİF TIP ALANLARINDA UYGULAMALARI

Göksu Çınar

Malzeme Bilimi ve Nanoteknoloji, Doktora

Tez Danışmanı: Mustafa Özgür Güler

Haziran, 2016

Moleküler kontrollü kendiliğinden bir araya gelme, farklı fiziksel ve kimyasal özelliklere sahip yeni nesil malzemelerin üretilmesinde kullanılan doğadan esinlenerek geliştirilmiş bir yöntemdir. Günümüzde bu malzemeleri oluşturan moleküler düzeyde kontrol edilebilir yapı taşları; kimya, biyoloji ve malzeme bilimi gibi farklı bilimsel disiplinlerin ortak yaklaşımlarıyla geliştirilmektedir. Doğada bulunan yapı taşları içerisinde, peptit molekülleri kendilerini oluşturan amino asitler arasındaki kovalent olmayan etkileşimler yardımıyla programlanarak; dinamik ve çevresel etkilere duyarlı çeşitli biyomalzemelerin nano veya makro düzeydeki inşasında kullanılmaktadır. Bu tez çalışmasında, doğadaki akıllı tasarımlardan esinlenerek geliştirilmiş kendiliğinden bir araya gelerek elde edilen peptit tabanlı farklı biyomalzemelerin üretilmesi, malzeme özelliklerinin belirlenmesi ve farklı biyomedikal alanlardaki uygulamaları sunulmuştur. İlk kısımda, moleküler kontrollü bir araya gelme prensipleri, bu özelliğe sahip peptit tabanlı yapı tasarım stratejileri ve bu yapıların oluşturdukları malzemeler için kullanılan yeni nesil karakterizasyon

yöntemleri literatürdeki örnekler ışığında tartışılmıştır. İkinci kısımda, nörodejeneratif hastalıklara sebep olan amiloid peptit yapılarından esinlenerek tasarlanan peptit moleküllerinin kendiliğinden bir araya gelme davranışları, fizyolojik koşullarda oluşturdukları nanofiber ve supramoleküler jellerin malzeme özellikleri ve biyouyumlulukları incelenmiştir. Üçüncü bölümde, kemoterapötik ilaçların lokal bölgelere taşınımı hedefleyen supramoleküler peptit amfifil nanofiber jellerin geliştirilmesi, kontrollü ilaç salım davranışları ve ilaç taşıma sistemi olarak uygulanabilirliği *in vitro* ve *in vivo* koşullarda incelenmiştir. Dördüncü kısımda, peptit amfifil ağısı nanofiberleri ve kimyasal çapraz bağlanmış PEG ikili yapı iskelesi içeren biyoaktif doğal ekstraselüler matriks benzeri biyomalzemelerin, kompozit malzeme stratejisi kullanılarak geliştirilmesi incelenmiştir. Hücre-biyomalzeme etkileşimleri ve rejeneratif tıp alanında uygulaması, 2 ve 3 boyutlu *in vitro* hücre kültür ortamında test edilmiştir.

Anahtar kelimeler: Kendiliğinden bir araya gelme, biyomalzemeler, amiloid benzeri peptitler, peptit amfifiller, nanofiberler, supramoleküler nanofiber jeller, ilaç taşınımı, kontrollü ilaç salımı ve rejeneratif tıp

Acknowledgement

I would like to express my deepest appreciation to my PhD advisor Prof. Mustafa Özgür Güler for his scientific knowledge and support throughout my graduate studies. He always encouraged me to put my thoughts into the practice within the scientific research perspective. I am also sincerely grateful to Prof. Ayşe Begüm Tekinay, Prof. Dr. Semra İde and Prof. Aykutlu Dana and for their knowledge, guidance and support during my PhD studies. I would like to thank my jury members for their contribution to my thesis.

I would like to express my special thanks to Prof. E. Deniz Tekin, Dr. Ayşe Özdemir, İlghar Orijalipoor, Dr. Ruslan Garifullin, Dr. Rashad Mammadov, Dr. Hakan Ceylan, Dr. Aslı Çelebioğlu, Mustafa Ürel, Turan Selman Erkal and Melis Göktaş for their scientific knowledge and fruitful collaboration.

Being a member of BML is a privilege for me and I would like to acknowledge my previous and present lab and office members. I have special thanks to Dr. Handan Acar, Dr. Adem Yıldırım, Dr. Gözde Uzunallı, Dr. Seher Üstün Yaylacı, Dr. Gülcihan Gülseren, Dr. Özlem Erol, M. Aref Khalily, Gökhan Günay, Egemen Deniz Eren, Gülistan Tansık, Melike Sever, Alper Devrim Özkan, Berna Şentürk, Zeynep Aytaç, Yelda Ertaş, Samet Kocabey, Elif Arslan, Yasin Tümtaş, Didem Mumcuoğlu, Özüm Şehnaz Günel, Ahmet Emin Topal, Hepi Susapto, Begüm Dikeçoğlu, Oya İlke Şentürk, Hatice Kübra Kara, Aygül Zengin and Meryem Hatip for their friendship during my PhD in UNAM. I also thank to Mrs. Zeynep Erdoğan and Mr. Mustafa Güler for their technical contribution to my thesis.

I would like to acknowledge The Scientific and Technological Research Council of Turkey (TÜBİTAK BİDEB-2211C, 112T452 and 213M406) for funding my PhD research and financially supporting me in one international conference (2224-A).

I am so lucky and grateful to have my dearest friends Melis Şardan Ekiz, Oya Ustahüseyin, Okan Öner Ekiz, Bihter Dağlar, Seren Hamsici, Neşe Çakmak, Can Görür, Arda Yıldırım, Zeynep Erge Akbaş, Büşra Aşık, Cansu Ultav, Gözde Ultav and Nagihan Yalçınkaya. I appreciate their endless support and friendship throughout my life.

I would like to give my special thanks to Ali Çiftçi, Bilgin Çiftçi, Belgin Özdemir Fikri Özdemir and Bilge Özdemir for their love and support.

I would like to express my most sincere gratitude to my family, my mother Ayla Çınar, my father Güngör Çınar, my little sister Gökçe Çınar, my grandfather Mustafa Çınar and my super-grandmother Mevlüde Çınar for their endless love, encouragement and unquestionable belief in me. Without their support, I would not be able to finish this thesis.

Finally, I would like to express most heartfelt thankfulness to my partner, Barış Çiftçi, for his support, patience and encouragement throughout my life. My greatest accomplishment in life is to deserve his endless love. I dedicate this thesis to him.

Contents

ABSTRACT	iii
ÖZET.....	v
Acknowledgement.....	vii
List of Figures	xiv
List of Tables.....	xxv
Abbreviations	xxvi
Chapter 1	1
1. Introduction	1
1.1 Self-Assembly	1
1.2 Peptide Self-Assembly	4
1.3 Design of Self-Assembling Peptide Based Building Blocks	6
1.3.1 Peptides Composed of Only Amino Acids	6
1.3.2 Peptide Amphiphiles	10
1.3.3 Peptide Containing Other Hybrid Systems	14
1.4 Characterizations of Self-Assembled Peptide Based Materials	17
1.4.1 Spectroscopic Techniques	18
1.4.3 Imaging Techniques	24
1.4.4 Mechanical Characterization Techniques	26
1.5 Applications of Self-Assembled Peptide Based Biomaterials	30
1.5.1 Drug Delivery.....	30
1.5.2 Regenerative Medicine	34
Chapter 2	37

2. Amyloid Inspired Self-assembling Peptides (AIPs) and Their Supramolecular Assemblies	37
2.1 Introduction	37
2.2 Experimental Section	41
2.2.1 Materials.....	41
2.2.2 Synthesis and Characterizations of AIPs	41
2.2.3 Zeta Potential Measurements of AIPs.....	42
2.2.4 Scanning Electron Microscopy	42
2.2.5 Transmission Electron Microscopy.....	43
2.2.6 Molecular Dynamics Simulations	43
2.2.7 CD Analysis	44
2.2.8 FTIR Analysis	45
2.2.9 Congo-red Staining	45
2.2.10 ThT Binding Assay and Confocal Fluorescence Imaging	45
2.2.11 Turbidity Assay	47
2.2.12 SAXS Measurements and Data Fitting	47
2.2.13 Oscillatory Rheology	52
2.2.14 Atomic Force Microscopy	53
2.2.15 <i>In Vitro</i> Studies	54
2.3. Results and Discussion.....	55
2.3.1 Synthesis and Characterization of AIPs.....	55
2.3.2 Coassembly of AIPs into Nanofibers and Supramolecular Gels	57
2.3.2.1 Molecular Dynamics Simulation of AIP Coassembly	60
2.3.2.2 Secondary Structure Analysis of AIP Assemblies.....	64

2.3.2.3 Coassembly Kinetics of AIPs.....	67
2.3.2.4 SAXS Analysis of AIP Nanofibers	75
2.3.3 Viscoelastic Properties of AIP Supramolecular Gels.....	82
2.3.4 Nanomechanical Properties of AIP Nanofibers	87
2.3.5 Biocompatibility of AIP Nanofibers and Supramolecular Gels.....	94
2.4 Conclusion	99
Chapter 3	102
3. Controlled Local Chemotherapeutic Drug Delivery through Supramolecular Peptide Amphiphile (PA) Nanofiber Gels.....	102
3.1 Introduction	102
3.2 Experimental Section	103
3.2.1 Materials.....	103
3.2.2 Synthesis and Characterization of PA Molecules	103
3.2.3 Preparation of the PA Nanofiber Gels	104
3.2.4 Imaging of the PA Nanofibers and Gels	104
3.2.5 Zeta Potential Measurements	105
3.2.6 Secondary Structure Analysis using CD and FTIR.....	105
3.2.7 Oscillatory Rheology	106
3.2.8 Controlled Drug Release Experiments.....	106
3.2.9 FRAP measurements.....	107
3.2.10 <i>In Vitro</i> Studies	107
3.2.11 4T1 Tumor Model and <i>In Vivo</i> Studies.....	108
3.2.12 Statistical Analysis.....	109
3.3 Results and Discussion.....	110

3.3.1 Design, Synthesis and Characterizations of the PA Assemblies and Nanofiber Gels	110
3.3.2 Biodegradability of the PA Nanofiber Gels	115
3.3.3 Drug Encapsulation and Controlled Drug Release through the PA Nanofiber Gels	117
3.3.4 <i>In Vitro</i> Biocompatibility of the PA Nanofiber Gels	122
3.3.5 <i>In Vivo</i> Applicability of the PA Nanofiber Gels	125
3.4 Conclusion	128
Chapter 4	130
4. Self-Assembled Peptide Amphiphile Nanofibers and PEG Composite Hydrogels As Tunable ECM Mimetic Biomaterials	130
4.1 Introduction	130
4.2 Experimental Section	133
4.2.1 Materials.....	133
4.2.2 Synthesis and Characterizations of the Bioactive PA Molecules	134
4.2.3 PA/PEG Composite Hydrogels Preparation	135
4.2.4 Transmission Electron Microscopy Imaging	136
4.2.5 Scanning Electron Microscopy Imaging.....	136
4.2.6 Attenuated Total Reflectance-Fourier Transform Infrared Spectroscopy (ATR-FTIR)	137
4.2.8 SAXS Analysis of the PA/PEG Composite Hydrogels	138
4.2.9 Oscillatory Rheology	138
4.2.10 <i>In Vitro</i> Studies	139
4.2.11 Controlled Protein Release Experiments	143

4.3 Results and discussion	144
4.3.1 Design, Synthesis and Characterizations of the Bioactive PA Molecules	144
4.3.2 Chemical and Physical Characterizations of the PA/PEG Composite Hydrogels	148
4.3.3 <i>In Vitro</i> Studies	161
4.3.4 Protein Encapsulation and Controlled Protein Release through the PA/PEG Composite Hydrogels	172
4.4 Conclusion	176
Chapter 5	177
5. Conclusion and Future Prospects	177
Bibliography.....	181

List of Figures

Figure 1.1 Strength and properties of chemical interactions.....	1
Figure 1.2 Programmable self-assembly of simple or informed components. A variety of simple supramolecular architectures including peptide amphiphile nanofibers, nanoparticle polymers, vortex crystals and nanoparticle assemblies; and complex hierarchical architectures such as the ribosome or DNA bricks. (Adapted from Ref. 7 with permission from Nature Publishing Group).....	3
Figure 1.3 Schematic representation of the different class of amino acids and non-covalent interactions involved in the peptide self-assembly. (Reproduced from Ref. 11 with permission from Royal Society of Chemistry)	5
Figure 1.4 Self-assembling peptide building blocks consisting only natural amino acids and their supramolecular assemblies. (Adapted from Ref. 1 with permission from Wiley Periodicals, Inc.).....	7
Figure 1.5 Schematic representation, CD spectra and AFM images of the design of the self-assembled K-PA nanofibers and P-PA nanospheres developed as the oligonucleotide (ODN) carriers to modulate immune response. (Adapted from Ref. 54 with permission from Nature Publishing Group).....	13
Figure 1.6 Common characterization techniques for variety of self-assembled peptide nanostructures	17
Figure 1.7 The detailed structural model of a self-assembled peptide-based nanocarrier developed in the light of the solid-state NMR (ssNMR) experiments. (Reproduced from Ref. 105 with permission from American Chemical Society)	19
Figure 1.8 The scattering (a) and electron density (b) profiles of the self-assembled arginine-capped peptide bolaamphiphile assemblies prepared at different	

concentrations and the fitting lines of the model according to a bilayer form factor. (Reproduced from Ref. 18 with permission from American Chemical Society)..... 23

Figure 1.9 Label-free super-resolution imaging of the self-assembled amyloid inspired peptide structures by applying stochastic reconstruction to temporal fluctuations of the Surface Enhanced Raman Scattering (SERS) signal. (Reproduced from Ref. 123 with permission from Nature Publishing Group)..... 26

Figure 1.10 The nanomechanical characterizations of the D, L cyclic peptide assemblies. (Reproduced from Ref. 144 with permission from Nature Publishing Group) 29

Figure 1.11 Controlled drug delivery through self-assembled peptide assemblies via non-covalent encapsulation or covalent conjugation of the drug molecules (Adapted from Ref. 211 with permission from Royal Society of Chemistry)..... 32

Figure 1.12 Self-assembled RADA16-I peptide scaffolds examined for different regenerative medicine applications (Adapted from Ref. 236 with permission from Elsevier) 35

Figure 1.13 Self-assembled glycopeptide nanofibers and their supramolecular nanofiber gels promoted chondrogenesis and cartilage regeneration (Reproduced from Ref. 101 with permission from American Chemical Society) 36

Figure 2.1 The decoupling models which successfully describe the self-assembled AIPs nanostructures 51

Figure 2.2 Chemical representation of AIP-1 (a) and AIP-2 (b) peptides 56

Figure 2.3 a) AIP-1; $[M-H]^-$ (calculated): 752.33, $[M-H]^-$ (observed): 752.33. b) RP-HPLC chromatogram of the AIP-1, the change of response units with respect to time at 220 nm. c) AIP-2; $[M+H]^+$ (calculated): 752.44, $[M+H]^+$ (observed): 752.45,

[2M+H] ⁺ (calculated): 1503.88, [2M+H] ⁺ (observed): 1503.89, [M/2+H] ⁺ (calculated): 376.22, [M/2+H] ⁺ (observed): 376.74. d) RP-HPLC chromatogram of the AIP-2, the change of response units with respect to time at 220 nm.	57
Figure 2.4 Zeta potentials of the AIP-1, AIP-2 solutions; and AIPs assemblies at pH 7.4 in water.....	58
Figure 2.5 TEM images of the coassembled AIP nanofibers (scale bar 10 nm, 50 nm and 0.1 μm).....	59
Figure 2.6 Self-supporting 2% (w/v) coassembled AIP gel (AIP-1+2) formed after mixing AIP-1 and AIP-2 solutions at pH 7.4 in water.....	59
Figure 2.7 Selected snapshots of simulation of AIP-1 and AIP-2 peptides (five molecules per each peptide) obtained by 70 ns Molecular Dynamics Simulations...	60
Figure 2.8 a) Hydrophobic core interactions (number of contacts) of AIP-1 and AIP-2 based on the residues of FFAA-FFAA, b) aromatic group contacts (number of contacts) of AIP-1 and AIP-2 based on the residues of FF-FF, c) Solvent Accessible Surface Area (SASA), d) coulomb interactions between -Lys and -Glu residues of AIP-1 and AIP-2, and e) potential energy change of the system during simulation.	61
Figure 2.9 Residue based secondary structure change of peptides during simulation trajectory.	63
Figure 2.10 The secondary structure (a) and hydrogen bonding change (b) within the system during the simulation	64
Figure 2.11 a) Secondary structure analysis of AIP-1+2 nanofibers at various concentrations of dried AIP-1+2 gels with FTIR. b) Detailed analysis of Amide I region (1600-1700 cm ⁻¹)	65

Figure 2.12 FTIR spectra of the coassembled AIP network (a, b) (- - - Gaussian fittings), molar ellipticity of the coassembled AIP (AIP-1+2), AIP-1 and AIP-2 assemblies (c); and the absorbance spectra of congo red dye with and without AIP coassemblies.....	66
Figure 2.13 (a) A small fluorescent dye molecule; thioflavin T (ThT), is used as a probe for monitoring the coassembly of AIP-1 and AIP-2 molecules into nanostructures. (b) The normalized fluorescence intensity changes during the co-assembly process of the AIPs prepared at different peptide concentrations.	68
Figure 2.14 Time- and concentration-dependent co-assembly of oppositely charged AIPs at physiological conditions into supramolecular nanostructures. The aggregation kinetics of the AIPs were visualized using in situ confocal microscopy imaging during the coassembly process at different concentrations (all image scale bars are 200 μ m)	69
Figure 2.15 SEM images of the three dimensional nanofibrous 2%, 1.75% and 1.5% (w/v) AIPs networks coassembled for 1 h	70
Figure 2.16 Turbidity of AIP solutions at different concentrations was monitored as optical density at 313 nm under physiological conditions. Increase in the turbidity of the solutions correlate with nanostructure formation and sol-gel transition. AIP-1 and AIP-2 molecules rapidly self-assemble into the nanostructures a concentration over 1.25% (w/v) concentration within 1 h.....	72
Figure 2.17 Time dependent turbidity change of (a) AIP-1 and (b) AIP-2 at 313 nm, the peptide solutions were prepared at the different peptide concentrations.	73
Figure 2.18 Sonication enhances turbidity of 1% AIPs compared to the control groups; a) time dependent turbidity change and b) 1% AIPs solution images after the sonication	

was applied for different time periods (1, 2.5 and 5 min) (Control groups were also 1% AIPs which were incubated for 5, 2.5 and 1 min without sonication prior to the analysis.).....	75
Figure 2.19 (a) Small angle X-ray scattering (SAXS) profiles and 2D patterns (b) of coassembled 2%, 1.75% and 1% (w/v) AIP nanostructures after 1 h.....	76
Figure 2.20 The proposed structural model for co-assembled AIP nanostructures (a) and (b) the electron density distribution on the nanofiber, (c) AFM image of the coassembled AIP nanofibers and their bundles dried on a Si wafer.....	77
Figure 2.21 a) In situ SAXS measurements of 2% AIPs in water at neutral pH during coassembly, and (b) TEM images of the nanofibers prepared from the dilutions of coassembled 2% AIPs for 15 min (c) and (d) 60 min.....	80
Figure 2.22 a) SAXS profiles of 2% coassembled AIP nanostructures at different temperatures. (b) Increase in temperature did not disturb the organization of the AIP nanofibers and the density of the nanofibers slightly changed for elevated temperatures.....	81
Figure 2.23 Time sweep analysis (a) and (b) equilibrium storage (G') and loss moduli (G'') of the AIP coassemblies c) Linear dependence of storage moduli of the AIP gels to concentration change at pH 7 d) Damping factor (G''/G') change of the gels prepared at different concentrations of at pH 7 for 60 min.....	83
Figure 2.24 Frequency sweep (a, b) and thixotropic analysis (c, d) of the AIP coassemblies prepared at different peptide concentrations at pH 7 (Loss Modulus, w : angular frequency)	84

Figure 2.25 a) Time sweep analysis, and (b) equilibrium storage and loss moduli (G' , G'') of the 2% (w/v) coassembled AIP, AIP-1 and AIP-2 gels prepared at pH 7, 5 and 10, respectively	86
Figure 2.26 Effect of temperature on the mechanical stability of coassembled 2% (w/v) supramolecular AIP nanostructure network for 1 h (The co-assembled network preserved viscoelastic behavior at elevated temperatures)	87
Figure 2.27 AFM topography images of coassembled AIP nanofibers (a); and adhesion force (b) and (c) elastic modulus maps of the nanofibers determined from the slope of force-distance curves (Modulus, Pa) during retraction	88
Figure 2.28 Adhesion force (a, c, e) and elastic modulus maps (b, d, f) of individual AIP-1 and AIP-2 nanofibers and the coassembled AIP nanofibers during approach	89
Figure 2.29 The topography (a,b), adhesion force (c,d) and elastic modulus maps (e, f) of individual AIP-1 and AIP-2 nanofibers during retraction	89
Figure 2.30 Slope (a, b) and adhesion force histograms (c, d) of the coassembled AIPs at pH 7 and individually formed AIP-1 at pH 5 and AIP-2 nanofibers at pH 10 during approach and retraction of the AFM tip (— Gaussian fittings). Schematic representation of nanofiber and AFM tip interactions during nanomechanical characterizations (e)	91
Figure 2.31 Modulus (Pa) histograms of AIP-1+2 at pH 7, AIP-1 at pH 5, and AIP-2 at pH 10 nanofibers; a) approach and b) retraction of AFM tip (—: Gaussian fittings)	93
Figure 2.32 Maximum force histogram of the coassembled AIP nanofibers at pH 7, AIP-1 at pH 5, and AIP-2 at pH 10 nanofibers applied by AFM tip during the nanomechanical characterizations.....	94

Figure 2.33 a) Relative cell adhesion for 2 h, b) viability for 24 h; c) proliferation for 48 h; and d-f) the confocal images of the cells after 24 h cultured on the AIPs nanofibers, collagen I and bare glass.	95
Figure 2.34 Spreading of the cells on the AIPs nanofibers, collagen I and glass after 2 h based on a) cell diameter b) cell area (n.s.: Not significant).....	96
Figure 2.35 The confocal images of the cells after 2 and 48 h cultured on the AIPs nanofibers, collagen I and bare glass.	97
Figure 2.36 SEM images of the coassembled AIPs coated surfaces incubated with the cells under standard cell culture conditions for 24 h.....	98
Figure 2.37 SEM images of HUVECs cultured on the 3D coassembled AIPs gel surfaces after 24 h later	99
Figure 3.1 Liquid chromatograms and mass spectra of the synthesized PAs a) E ₃ PA; [M-H] ⁻ (calculated)= 912.50, [M-H] ⁻ (observed)= 912.48, (observed [M-2H] ⁻² m/z = 455.73) b) K ₃ PA; [M+H] ⁺ (calculated)= 910.67, [M+H] ⁺ (observed)= 910.68, (observed [M+2H] ⁺² m/z = 455.84)	110
Figure 3.2 a) Chemical representation of E ₃ PA and K ₃ PA molecules a) Zeta potential change of the E ₃ PA upon addition of the K ₃ PA at pH 7.4 in water c) Supramolecular PA network showed self-supporting gel property d) SEM and TEM image of the coassembled PA nanonetwork and nanofibers, respectively	111
Figure 3.3 SEM images of the self-assembled PA nanonetworks prepared using critical point dryer at different peptide concentrations	112
Figure 3.4 a) CD spectra of E ₃ PA, K ₃ PA and E ₃ /K ₃ PA and (b, c) the FTIR analysis of the E ₃ /K ₃ PA assemblies prepared at pH 7.4 in water.....	113

Figure 3.5 a) Time sweep analysis of the supramolecular PA nanofiber gels prepared at the different concentrations and b) Equilibrium storage (G') and loss moduli (G'') of the PA gels.	114
Figure 3.6 a) Time sweep analysis of the 1% (w/v) coassembled PA gels injected through a syringe or directly mixed on the rheometer stage b) Equilibrium storage (G') and loss moduli (G'') of the PA nanofiber gels.	115
Figure 3.7 Biodegradability of 1% (w/v) coassembled PA nanofiber gel via different proteases at pH 7.4 in Tris buffer.....	116
Figure 3.8 Schematic representation of the drug encapsulation and coassembly of the molecules into supramolecular PA nanofiber gel	117
Figure 3.9 a) Controlled release profile of Dox through the PA gels prepared at different concentrations at physiological conditions and b) The release ratios of the chemotherapeutic drug were modulated depending on the PA concentration within the gels.	119
Figure 3.10 Mathematical fitting results of FRAP experiments a) the estimated diffusion constants and b) immobile fractions of the drug molecules encapsulated within the PA gels prepared at the different concentrations	120
Figure 3.11 Hankel transform of the photobleaching profiles of Dox encapsulated self-assembled PA hydrogels prepared at different concentrations.	122
Figure 3.12 Cellular viability on (a) the control, (b) 1% (w/v) PA gel, (c) 1% (w/v) Dox/PA gel and (d) only Dox for 24 h and 48 h.....	123
Figure 3.13 Flow cytometry histograms of only Dox, Dox/PA, only PA and control groups at (a) 24 and (b) 48 h.....	124

Figure 3.14 a) Tumor growth of the only Dox, only PA, Dox/PA and control groups for 18 days and b) the final tumor volume (mm ³) at day 18.....	126
Figure 3.15 Caspase 3 immunohistochemistry staining of the tumor tissues of a) only Dox, b) only PA, c) Dox/PA and d) control groups at day 18.....	127
Figure 3.16 Histology staining of the different tissues obtained from the only Dox, only PA, Dox/PA and control groups at day 18.....	128
Figure 4.1 Chemical representations of the synthesized PA molecules.....	145
Figure 4.2 Liquid chromatography-mass spectrometry (LC-MS) results of the synthesized PAs	146
Figure 4.3 Transmission Electron Microscopy (TEM) images showing the nanofiber assembly of PA combinations. A), B) E ₃ -PA/K ₃ -PA; C), D) RGD-PA/ K ₃ -PA; E), F) DGEA-PA/ K ₃ -PA	147
Figure 4.4 Schematic representation of the fabrication approach for the PA/PEG composite hydrogels.....	149
Figure 4.5 a) The schematic of the crosslinking reaction; and b) FTIR spectra of PEG (w/o PNFs) and E ₃ /PEG samples after 15 min of UV crosslinking.....	150
Figure 4.6 SEM images of PEG (w/o PA nanofibers, PNFs) and PA/PEG composite hydrogels (scale bars are 4 μm)	151
Figure 4.7 Total pore volume and specific surface area of the hydrogels.	152
Figure 4.8 The pore size distributions and cumulative pore volumes of only PEG and PA/PEG composite hydrogels.....	153
Figure 4.9 a) The scattering data and fitting model of the PEG and PA/PEG composite hydrogels with (b, c) the PDD histograms of the samples.....	154

Figure 4.10 Illustration of the structural organization of E ₃ /PEG composite hydrogel using flexible cylinder-polydisperse length model	156
Figure 4.11 Equilibrium storage and loss moduli of the hydrogels	158
Figure 4.12 Equilibrium storage moduli (a) and limiting strain amplitude values (b) of the hydrogels prepared at different concentrations. Photographs of PA/PEG composite (c) and only PA hydrogel (d) with the same storage moduli.	159
Figure 4.13 Rheological characterizations of the hydrogels based on amplitude sweep analysis	160
Figure 4.14 Fluorescence images of Saos-2 cells cultured on PEG and PA/PEG composite hydrogels and stained with calcein-AM (green) and ethidium homodimer (red) (scale bars are 100 μm)	162
Figure 4.15 a) Fluorescence images of Saos-2 cells cultured on stiff PEG and PA/PEG (prepared with E ₃ -PA) composite hydrogels and stained with calcein-AM, b) the number of adhered cells on the all systems at 24 h in serum free culture conditions, c) the fluorescence images of the cells stained with phalloidin (green); and d) the spreading areas of the cells cultured on the substances at 72 h	163
Figure 4.16 Fluorescence images of Saos-2 cells cultured on stiff PEG and PA/PEG (prepared with E ₃ -PA) composite hydrogels and stained with calcein-AM (scale bars are 200 μm)	164
Figure 4.17 Representative fluorescence images of the cells with ICC staining at day 7 (scale bars are 50 μm). Green indicated RUNX2 and COL1 expressions at the top and bottom row images, respectively. In both rows, phalloidin staining was shown as red color	166

Figure 4.18 The gene expression levels of the cells cultured on PEG and PA/PEG composite hydrogels at day 3	167
Figure 4.19 The gene expression levels of the cells cultured on PEG and PA/PEG composite hydrogels at day 3 and 7	168
Figure 4.20 Fluorescence images of Saos-2 cells cultured within the 3D PEG and PA/PEG composite hydrogels and stained with calcein-AM (green) and ethidium homodimer (red) (scale bars are 100 μm)	171
Figure 4.21 The standard calibration curve for the determination of BSA concentration based on absorbance measurements	173
Figure 4.22 The controlled release profiles of the BSA molecules through the only PEG and PA/PEG composite hydrogels	174
Figure 4.23 The estimated apparent diffusion coefficients	175

List of Tables

Table 1.1 Recently reported self-assembling peptide hybrid systems	14
Table 2.1 Gaussian fitting parameters of FTIR data of AIP-1+2 self-assembled peptide nanofibers (see Figure 3c) obtained from MATLAB fitting program	65
Table 2.2 Fitting results of SAXS data of coassembled AIP nanostructures at different concentrations in water at neutral pH.....	78
Table 2.3 Recovery of 4, 3, 2, 1 and 0.5% (w/v) coassembled AIP gels after disruption of the networks with the increased strain.....	84
Table 4.1 Bioinspired self-assembling PA building blocks	144
Table 4.2 Nomenclature and composition of PEG (w/o PA nanofibers (PNFs)) and PA/PEG composite hydrogels.....	145
Table 4.3 Structural results obtained from the fitting process of E ₃ /PEG scattering data using flexible cylinder-polydisperse length model	155

Abbreviations

AIP	Amyloid-inspired peptide
AFM	Atomic force microscopy
ANOVA	Analysis of variance
ATR	Attenuated total reflectance
BET	Brunauer-Emmett-Teller
Boc	<i>Tert</i> -butoxycarbonyl
CD	Circular dichroism
Col-1	Collagen-1
CPP	Critical packing parameter
DCM	Dichloromethane
DIEA	<i>N,N</i> -diisopropylethylamine
DMEM	Dulbecco's modified Eagle's medium
DMF	<i>N,N</i> -Dimethylformamide
ECM	Extracellular matrix
EPR	Electron paramagnetic resonance
ESI	Electrospray ionization
FBS	Fetal bovine serum
Fmoc	9-Fluorenylmethoxycarbonyl
FTIR	Fourier transform infrared spectroscopy
GAG	Glycosaminoglycan
GAPDH	Glyceraldehyde 3-phosphate dehydrogenase
HBTU	<i>N,N,N',N'</i> -Tetramethyl- <i>O</i> -(1 <i>H</i> -benzotriazole-1-yl) uronium hexafluorophosphate
hMSC	Human mesenchymal stem cells
HPLC	High pressure liquid chromatography
HUVEC	Human umbilical vein endothelial cell
ICC	Immunocytochemistry
LC-MS	Liquid chromatography-mass spectroscopy
LSA	Limiting strain amplitude
LVR	Linear viscoelastic range

MD	Molecular dynamics
MDP	Multidomain peptide
NMR	Nuclear magnetic resonance
OD	Optical density
PA	Peptide amphiphile
PBS	Phosphate buffered saline
PDD	Pair distance distributions
PEG	Polyethylene glycol
PEGDMA	Polyethylene glycol dimethacrylate
PNAAs	Peptide nucleic acid amphiphile
PNFs	Peptide nanofibers
qRT-PCR	Quantitative real-time polymerase chain reaction
QTOF	Quadrupole time of flight
ROI	Region of interest
SAXS	Small angle X-ray scattering
SD	Standard deviation
SERS	Surface enhanced Raman scattering
SEM	Standard error of mean
SEM	Scanning electron microscopy
SLP	Surfactant like peptide
TCP	Tissue culture plate
TEM	Transmission electron microscopy
TFA	Trifluoroacetic acid
ThT	Thioflavin T
TIS	Triisopropyl silane
UV	Ultraviolet
VMD	Visual molecular dynamics
XRD	X-ray diffraction

Chapter 1

1. Introduction

1.1 Self-Assembly

Self-assembly is a ubiquitous process of nature, and it has numerous important roles for the construction of a wide variety of complex biological architectures.[1] It is defined as the spontaneous organization of the molecules into dynamic structures architectures joined through the noncovalent interactions.[2] The lipid bilayer cell membrane, actin filaments, capsid proteins of the viruses, collagen fibers are well-known hierarchical self-assembled architectures found in natural organisms.[3, 4]

Molecular self-assembly is an emerging powerful tool within bottom up approaches takes the advantages of noncovalent interactions including hydrogen bonding, van der Waals, electrostatic, π - π , hydrophilic and hydrophobic interactions etc.[5] Although individually, these types of non-covalent bonds are usually weak compare to the covalent systems (Figure 1.1), they drive the self-assembly process and guide the structural organization of the building blocks into thermodynamically stable, complex and adaptable architectures when used in combination at the desired conditions.[6]

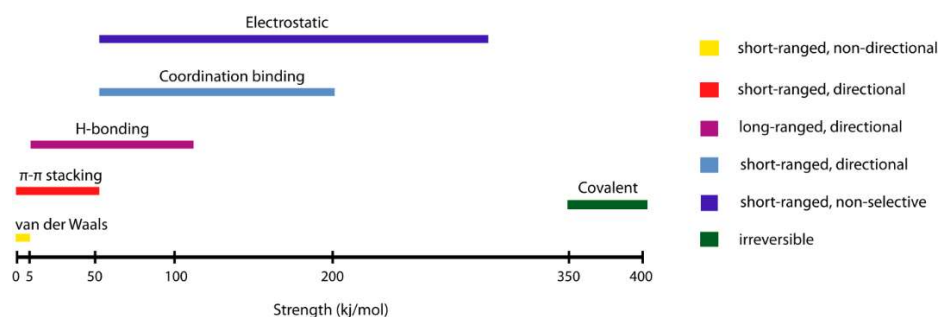


Figure 1.1 Strength and properties of chemical interactions

Over the past two decades, scientists and engineers have been inspired by nature's assembly principles to design simple or informed building blocks which can self-assemble into variety of functional nanoscale and bulk architectures (Figure 1.2).[7] The main advantage of this method is to anticipate size limitations of the top down approaches nanostructured materials via supramolecular chemistry without need of the equipments.[8] These self-assembled functional materials have been used in different applications including energy conversion and storage, electronics, photonics and biomedical purposes such as drug delivery, biosensing and tissue engineering.[9, 10]

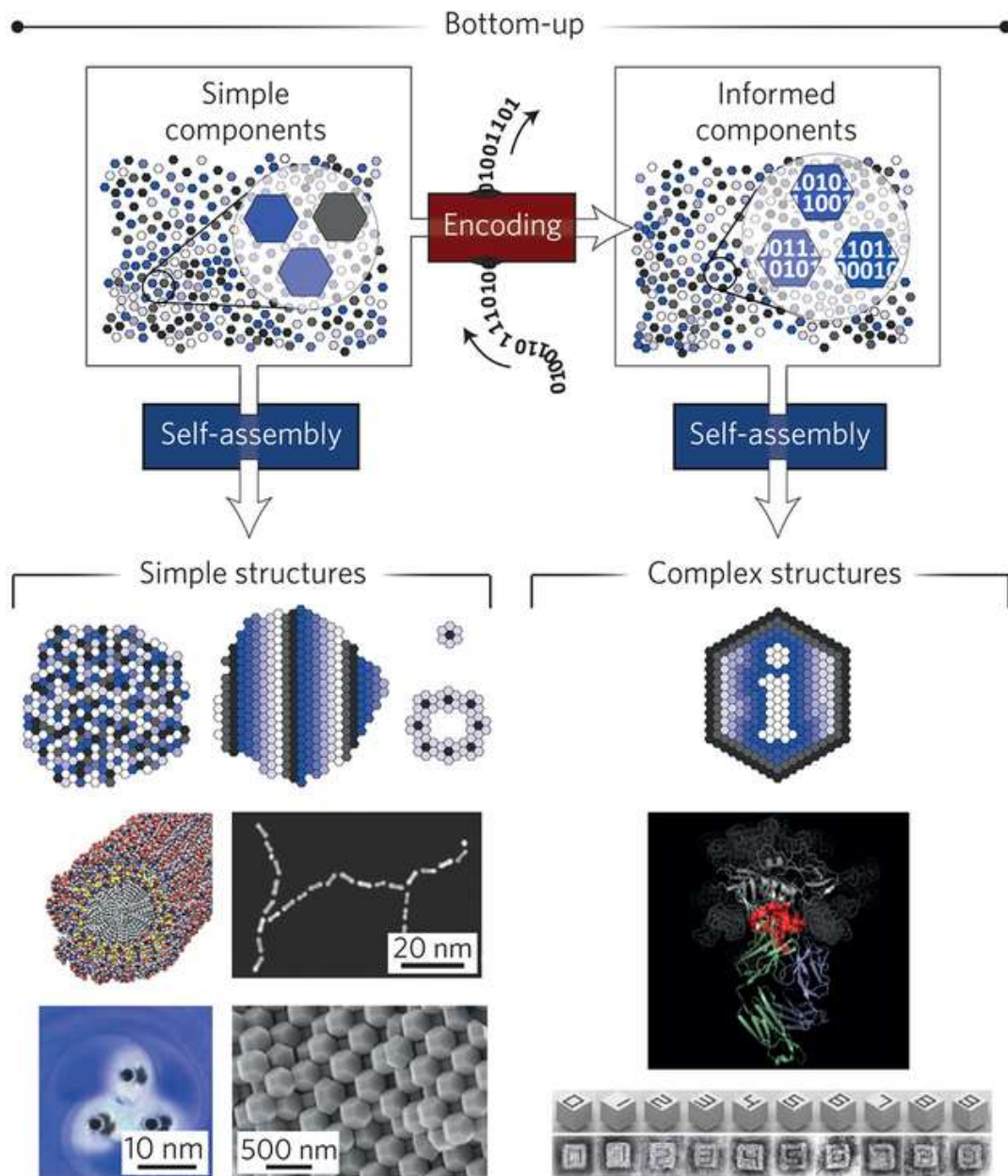


Figure 1.2 Programmable self-assembly of simple or informed components. A variety of simple supramolecular architectures including peptide amphiphile nanofibers, nanoparticle polymers, vortex crystals and nanoparticle assemblies; and complex hierarchical architectures such as the ribosome or DNA bricks. (Adapted from Ref. 7 with permission from Nature Publishing Group)

1.2 Peptide Self-Assembly

Peptides consisting only natural or synthetic amino acids are able to form self-assembled nanostructures and supramolecular architectures depending on the intrinsic properties of the building blocks. Amino acids which are the building blocks of the peptide molecules exhibit a variety of physicochemical properties due to different charge, hydrophobicity, size and polarity of their side chains. Non-polar amino acids, including aliphatic (alanine, leucine, valine) and aromatic (tyrosine, phenylalanine) amino acids, are mostly responsible for hydrophobic aggregation due to hydrophobic forces and π - π stacking, respectively. On the other hand, polar amino acids facilitate either hydrogen bonding or electrostatic interactions depending on their uncharged (serine, asparagine) or charged (lysine, histidine, glutamic acid) residues (Figure 1.3).[11] In addition to the side chain properties, the peptide backbone itself provides considerable stability through hydrogen bonds.

The stabilization of the multiple peptide backbone arrangements by hydrogen bonding interactions between the backbone amide and carbonyls results in the formation of β -sheets. The sheet is either parallel or anti-parallel depending on the direction of the strands. The α -helices are formed by individual peptide chains where backbone amide components are intramolecularly hydrogen bonded unlike the β -sheets. It leads to the presentation of the amino acid side chains on the surface of each helix and further enhances the accessibility of amino acid side chains to solvent. In some cases, these single α -helices can assemble by coiling together and form so called coiled coils.

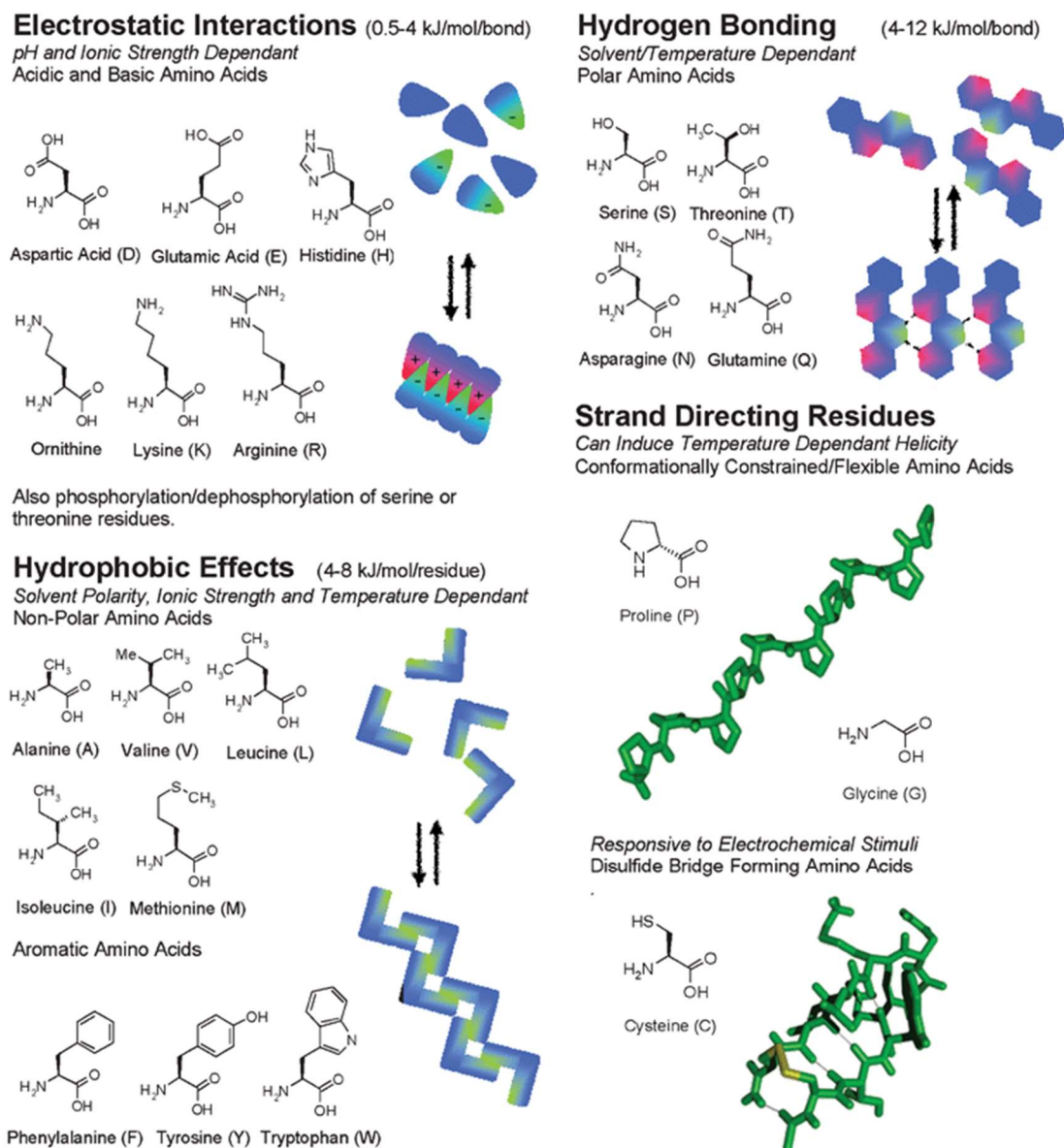


Figure 1.3 Schematic representation of the different class of amino acids and non-covalent interactions involved in the peptide self-assembly. (Reproduced from Ref. 11 with permission from Royal Society of Chemistry)

Peptide self-assembly is triggered via different external factors including pH, light, temperature, ultrasonication, ionic strength and solvent polarity due to the stimuli responsive dynamic nature of the noncovalent interactions between the peptide molecules.[12] In addition to the triggering the self-assembly process, these external

factors can be used to control and manipulate the structural properties such as size, shape or morphology of the self-assembled peptide architectures under different environmental conditions. This stimuli responsive nature of peptide self-assembly provide new opportunities to design materials which could satisfy the need of next generation devices and industries.

1.3 Design of Self-Assembling Peptide Based Building Blocks

1.3.1 Peptides Composed of Only Amino Acids

The distribution and the number of the hydrophobic and hydrophilic amino acids in the peptide sequence govern the final structural organization of the self-assembled peptides into nanofiber, nanotape, nanorod, nanovesicle, nanotube or micelle. Aggregation propensity and critical aggregation concentration (CAC) of the peptides can be modulated depending on the nature of the hydrophobic domain, which is very important for the stability of the assembly in aqueous environment.[13] The design of different self-assembling peptides consisting only natural amino acids and their supramolecular architectures formed via different triggering factors were given in Figure 1.4.[1]

Surfactant like peptides (SLPs) were designed as multiple 7-8 residue peptides consisting both consecutive hydrophobic residues (A_6 , V_6 , or L_6) and hydrophilic headgroup consisting one or two charged amino acid residues.[14] The type of nanostructure formed was mainly affected by the hydrophobicity of the tail but not by the number of integrated charged residues. The influence of the hydrophobic tail length on the formed SLP nanostructure was examined designing A_3K , A_6K , and A_9K peptides.[15] These peptides exhibited structural transition as their hydrophobic tail extended due to the change of packing within the nanostructure. While A_3K self-

assembled into unstable peptide sheet stacks, A₆K and A₉K formed long fibrillar-wormlike micelles and short nanorods, respectively.

Unlike the above-mentioned surfactant like peptides, the histidine attached hexaalanine sequence which had the ability to chelate to transition metal ions, particularly zinc cations, through its imidazole side chain were designed and synthesized.[16] In the study, the structural differences of the A₆H assemblies prepared in water and in ZnCl₂ containing solution at neutral and acidic pH were compared, respectively; and it was observed that while aqueous assemblies self-assembled into short sheets at pH 7, A₆H dissolved in ZnCl₂ solution formed pseudocrystalline particles containing plate/tape like sheets.

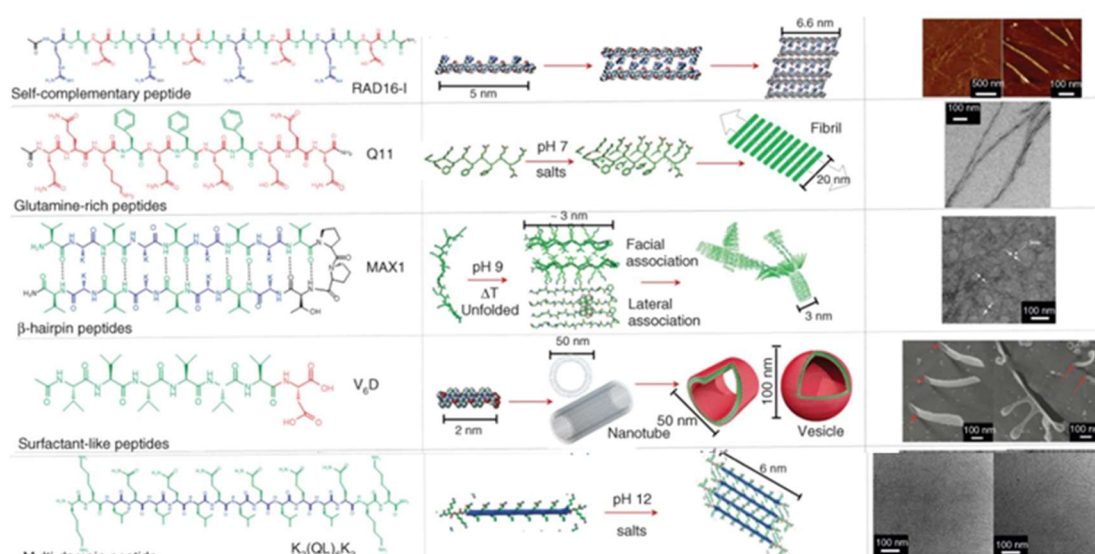


Figure 1.4 Self-assembling peptide building blocks consisting only natural amino acids and their supramolecular assemblies. (Adapted from Ref. 1 with permission from Wiley Periodicals, Inc.)

Alternative to the classical design of traditional amphiphilic or SLPs, double-headed architecture of bolaamphiphiles (composed of hydrophobic core and two hydrophilic moieties flanking the both ends of the core) received a growing interest for their ability to form different self-assembled nanostructures.[17-19] It was reported that the designed linear octapeptide (EFL₄FE) self-assembled into nanotubes at high concentrations whereas they tended to form sheet like structures at lower concentrations.[20] Very recently, the researchers devised several phenylalanine containing bolaamphiphiles, (EFFFFE, KFFFFK, and EFFFFK), whose terminal charges were modulated to investigate the effect of electrostatic interactions on the resulting polymorphic nanostructure.[21] That led to the twisting of the β -sheet tapes and accordingly the formation of fibrils, twisted ribbons and belts.

Self-assembly can also be induced by utilizing specific chemical functionalities found in the peptide backbone. For instance, amphiphilic gemini peptides, formed as a result of linking two cysteine containing single chain peptides with disulfide bond through oxidation, were designed. Its self-assembly behavior was compared with that of the corresponding single chain counterparts.[22] Furthermore, three different hydrophobic amino acids (alanine, valine, and isoleucine) were chosen to tune the molecular hydrophobicity of the peptides and to study its effect on the self-assembly together with the dimerization.

Amphiphatic peptides arranged in an alternating fashion were firstly developed by Zhang group.[23-25] This ionic self-complementary peptides formed stable β -strand and β -sheet structures which further self-assembled into well-ordered nanofibers due to the electrostatic interactions. Beta sheets are putatively arranged into bilayer structures leading to the concealment of hydrophobic side chain groups within the

bilayer interior that exposes hydrophilic side chains into the aqueous media. The effect of sequence pattern variation on the self-assembly of amphiphatic peptides was dissected by using frequently studied Ac-(FKFE)₂-Am peptide as a model.[26] It was figured out that the alteration in the amino acid groupings and the disruption of the alternating pattern not only reduced the self-assembly ability but also changed the morphology of the resulting materials.

Multidomain peptides (MDPs) are another design example of the self-assembling peptides in which the displayed domains were arranged in an ABA block motif where B block composed of alternating hydrophilic and hydrophobic amino acid residues and peripheral A blocks employed charged amino acids to control the self-assembly through electrostatic interactions.[27, 28] The extended β -sheet conformation of the peptides led to creating a facial amphiphile. Packing of two of the hydrophobic faces against each other formed a “hydrophobic sandwich” which further elongated through antiparallel beta sheet hydrogen bonding. The self-assembly of MDPs was further explored by introducing aromatic amino acid residues into the core and it was concluded that hydrogen bonding pattern changed depending on the type of substituted aromatic amino acid without affecting the basic nanofiber morphology.[29]

1.3.2 Peptide Amphiphiles

Peptide amphiphiles (PAs) which are naturally found in living organism as functional molecules for bioprocesses are composed of both hydrophobic alkyl tail and hydrophilic peptide sequences.[30, 31] PA molecules can form diverse nanostructures and supramolecular architectures via different factors such as pH change[32], oppositely charged molecules[33, 34], metal ions[35] or enzyme activation[36].

The design of the PAs is based on the balance between hydrophobic alkyl tail length and hydrophilic amino acid sequences since amphiphilicity is the main driving force for the self-assembly of PA building blocks into well-defined supramolecular nanostructures.[37] The stability and flexibility of the resulting assemblies can be further improved by enhancing the amphiphaticity of PAs. The balance between hydrophobic and electrostatic interactions is needed to be taken into account while determining the geometry of amphiphiles with minimum free energy.[37] Since an alteration in the hydrophilic segment can lead to a change in the critical packing parameter (CPP)[38], it can affect the morphology of the overall assembly.[39, 40]

The increase hydrophilicity towards the C-terminus of the designed PA molecule resulted the formation of the elongated self-assembled fibers due to pH triggering or salt induced charge neutralization of the acidic amino acid residues. Although both formulations exhibited similar morphologies, salt induced PA nanofibers formed stronger intra- and interfiber crosslinks through calcium mediated ionic bridges.[41] The same phenomena was also examined in another study using AFM nanoindentation technique, and the similar increase nanofiber stiffness due to Ca^{2+} crosslinking was shown.[42]

In addition, internal dynamics and fluctuations of supramolecular PA nanostructures have been studied in the help of quantitative electron paramagnetic resonance (EPR) spectroscopy in which local molecular motion within the assemblies can be tracked via site specific spin-label probes located at the PA molecules.[43] This technique also enable to reveal the relation between hydrogen bonding densities within β -sheet internal organization and the supramolecular cohesion of self-assembled PA nanostructures was effected by the design of the building blocks.[44]

In addition to the PA design examples given above, various self-assembling PA molecules which can self-assembly worm-like micelles due to their α -helix propensities were also shown.[45, 46] Individual helices in the micellar state was obtained due to the symmetrically distributed of the lysine residues on the PA backbone[45]; and the resulting supramolecular nanostructures revealed time dependent morphological transition from spherical to long nanofibrillar structures. In another study, the effects of hydrophobic amino acid residues on the self-assembly of PA by addition of four alanine residues between the palmitic acid and oligopeptide sequence.[46] Interposing of hydrophobic alanine residues led to the structural transition on the morphology of corresponding PA from nanoribbons to worm-like micelles, further being confirmed by a secondary structural change from α -helices to β -sheets.

The oppositely charged PA molecules was also designed to trigger their coassembly due to the electrostatic interactions and charge screening of the PA molecules by simply mixing them.[47, 48] Lauryl tail conjugated lysine and glutamic acid bearing PA molecules were coassembled into one dimensional nanofibers at physiological conditions without need of any external factor or environmental change.[49] In

addition, the integration of the short bioactive epitopes to these oppositely charged PA molecules did not change the structural properties of these assemblies; and coassembly approach enabled to dilute bioactive epitope densities on the nanofibers simply changing the mixing ratios of the PA molecule.[50-52] The coassembly properties of oppositely charged PA molecules were also studied by other groups by mixing them at different ratios; and it was shown that the coassembled PA fibers showed enhanced β -sheet formation compare to the self-assembled individual PA components due to the additional electrostatic interactions.[53]

Depending on the design of the PA molecules, it is also possible to obtain spherical nanostructures in addition to the one-dimensional architectures. The use of β -sheet breaking triproline residues instead of trileucine residues on the PA design change the direction of the hydrogen bonding and resulted the formation of spherical nanostructures.[13] In other study, proline residues incorporated PA molecules were also developed to obtain spherical nanostructures as an efficient delivery vehicle for the oligonucleotides (ODNs).[54] Recently, the importance of nanostructure morphology in tuning immune response was also examined designing two different PA molecules consisting beta-sheet forming or breaking amino acid residues which coassembled into nanofiber or nanospherical architectures delivering ODNs (Figure 1.5).[55]

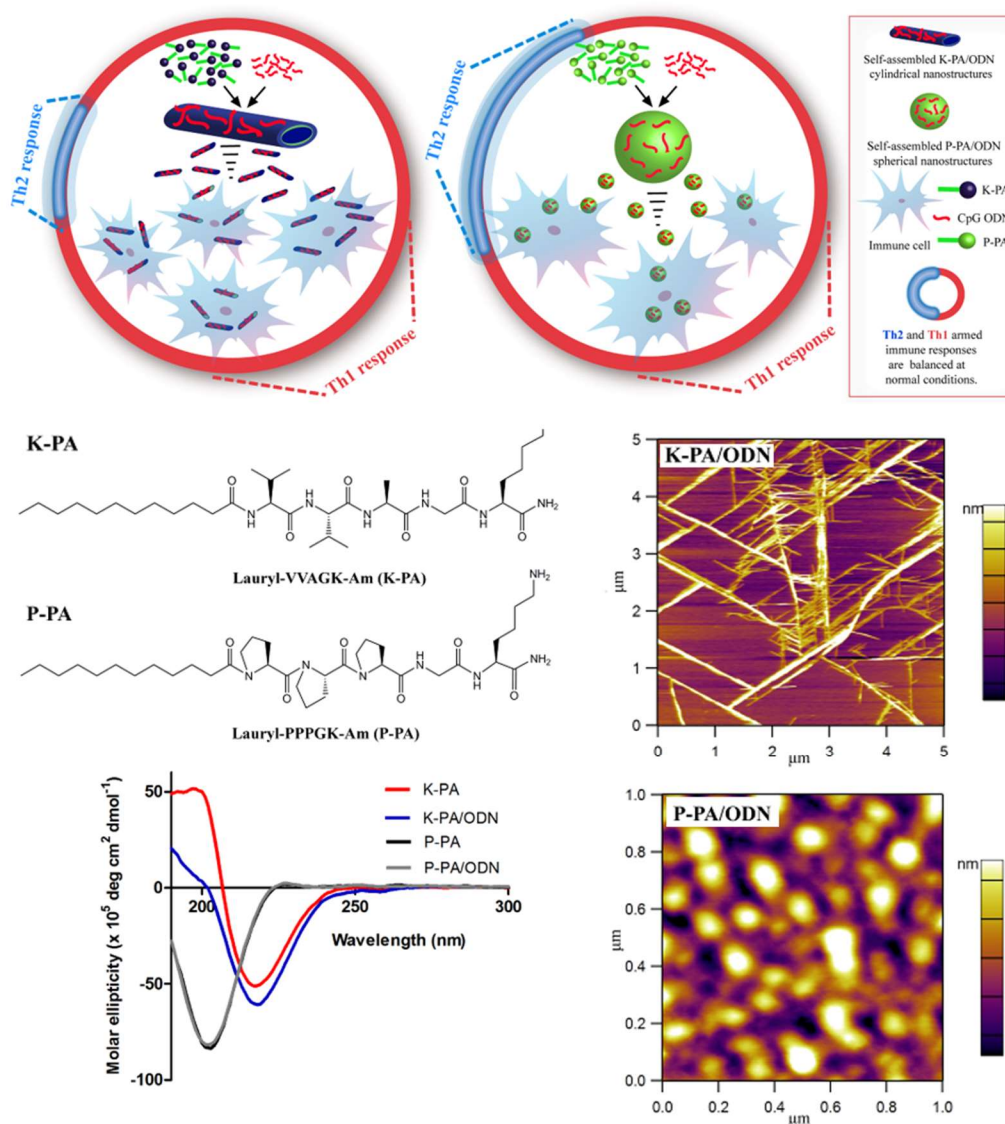


Figure 1.5 Schematic representation, CD spectra and AFM images of the design of the self-assembled K-PA nanofibers and P-PA nanospheres developed as the oligonucleotide (ODN) carriers to modulate immune response. (Adapted from Ref. 55 with permission from Nature Publishing Group)

1.3.3 Peptide Containing Other Hybrid Systems

Thanks to the organic chemistry, it is possible to obtain peptide hybrid systems composed of different chemical blocks besides peptides such as lipids, polymers, nucleobases, saccharides, aromatic groups, halogenic elements etc. Table 1.1 lists the self-assembled forms of recently reported hybrid peptide systems and gives additional information about regarding the structural properties. Peptides have been modified not only by changing the type of amino acid or order of its sequence, but also by using capping molecules at N- or C- terminus or by inserting a linker between peptide domains both to rationalize the self-assembly behavior and control the resultant structural features of formed assemblies.[56-58]

Table 1.1 Recently reported self-assembling peptide hybrid systems

Hybrid system	Structure	Ref.
Fmoc-FF, Fmoc-FG, Fmoc-GG, Fmoc-GF	Nanoribbon/fiber/sheet	[59]
Fmoc-n-X-Phe (n=2, 3 or 4 and X= F, Cl or Br)	Fibril	[60]
Fmoc-3-F-Phe-X and Fmoc-F ₅ -Phe-X (X=OH, NH ₂ or OMe)	Fibril	[61]
Naphthalene-FF-aurine	Nanotube	[62]
Phenothiazine-GFFY	Nanofiber	[63]
Pyrenebutyryl-ε-Ahx-VVAGH-Am	Nanofiber	[64]
Boc-FF	Nanosphere	[65]
E ₃ -X-G-perylene diimide-G-X-E ₃ (X= A ₃ or ^D A ₃)	Nanofiber/fiber bundle	[66]
Terthiophene-XE (X=G, V, I and L)	Nanosheet/nanotube	[67]
DXX-quaterthiophene-XXD (X=G, A, V, I, F)	Nanofiber	[68]
Trigonal WTW	Nanosphere/nanofiber	[69]
mPEO ₇ -F ₄ -OEt	Nanotube	[70]
PEG-Pep-fluorophore-Pep-PEG	Micelle	[71]
CREKA-PEG ₂₀₀₀ -DSPE	Micelle	[72]
KK(K-hepta thymine-K)G ₃ A ₃ K(-OC ₁₆ H ₃₁)-Am	Nanofiber	[73]
C ₁₈ H ₃₅ O-CTGACTGA-E ₄ -Am	Micelle	[74]
Nucleobase-F _n -glucoside (n=1 or 2)	Nanofiber/nanoparticle	[75]

Using aromatic moieties at the N-terminus of the peptide is another strategy to drive the self-assembly by providing amphiphilicity to the structure. Unlike the assembly mechanism of aliphatic peptide amphiphiles, aromatic group dominantly directs the self-assembly by its planar structure and resulting geometric restrictions due to the preferred stacking arrangements.[76] Various dipeptide combinations were exploited along with Fmoc (9-fluorenylmethoxycarbonyl) unit.[77-81] In a study, it was examined the self-assembly behavior of Fmoc-dipeptides composed of the combination of phenylalanine and glycine residues and revealed that the flexibility of the overall structure as well as the resultant conformation were affected from the amino acid type and sequence, leading to the formation of structurally different assemblies.[59]

Besides Fmoc-dipeptides, Fmoc-tripeptides together with tetra- and pentapeptide derivatives were also presented which exhibited nanofibrous or nanotubular structures.[82-85] In addition to the well-studied Fmoc group; naphthalene,[62, 86] phenothiazine,[63] pyrene,[64] carboxybenzyl,[87] azobenzene,[88, 89] naproxen[90] and benzimidazole[91] moieties were also utilized as aromatic capping at the N-terminus facilitating the self-assembly. The incorporation of non-proteinogenic amino acid, taurine, and naphthalene into the peptide backbone resulted in the formation of nanotubes, nanofibers or nanoribbons depending on the assembly conditions such as temperature, sonication and pH.[62]

Peptide π -electron systems are another well-studied class of hybrid peptide systems whose self-assembled architectures revealed different photo physical, electrical and mechanical properties. π -electron systems can be integrated into peptide backbone in many different ways such as a side chain[92], a linker between two peptide

sequences[93] or a capping molecule at the N-terminus.[94] While designing a peptide/ π -electron building block, amino acid sequence/ π -electron system pair should be selected carefully in terms of their energetic contributions to the self-assembly in order to form supramolecular structures with improved electron transport properties.[95, 96]

Amphiphilicity in the hybrid structure can alternatively be achieved by anchoring hydrophilic polymers to hydrophobic peptide segments, or vice versa, through the different chemistries to afford copolymer conjugates of different structures.[97] The nature of the polymer, the chemical heterogeneity of the peptide, the conjugation site, and the reaction medium can affect the structure, dynamics and function of corresponding hybrid system. A number of polymer-peptide conjugates have been reported until now in which polymers with different composition, number, length of the side chains were used to create different form of nanostructures.[98, 99]

Similar to lipids, nucleobases or saccharides can also be conjugated to the peptides.[80] Peptide nucleic acid/peptide amphiphile conjugate was constructed on a solid support and poly-thymine PNA heptamer was built on the peptide amphiphile whose self-assembly resulted in the formation of uniform nanofibers.[73] Similar approach was later used to synthesize a series of peptide nucleic acid amphiphiles (PNAA) containing different hydrophobic and hydrophilic moieties.[74] The self-assembly driven mainly by the base pair stacking of PNAA duplexes and intermolecular noncovalent interactions led to the formation of spherical micelles. Saccharide incorporated peptide conjugates were also developed in recent years, affording uniform self-assembled nanostructures. They can be synthesized through diverse synthetic approaches: by using glycosylated amino acid,[100] directly

conjugating to peptide backbone or amino acid side chain through amide bond formation,[101] or selecting proper linker for the anchorage.[102, 103]

1.4 Characterizations of Self-Assembled Peptide Based Materials

Characterizations of self-assembled nanoscale architectures require sophisticated techniques due to their complex and dynamic nanoscale nature of the materials. The integration of the knowledge on material characterization with the developments on nanotechnology enable us advance tools and approaches to examine chemical, physical, electrical and mechanical properties of the self-assembled peptide based nanostructures at nanometer and atomistic scales (Figure 1.6). Understanding of material and intrinsic characteristics of these architectures at nanoscale is quite important to determine applicability of the nanostructures for desired purposes and the limitations which can be improved via superior design and fabrication strategies.

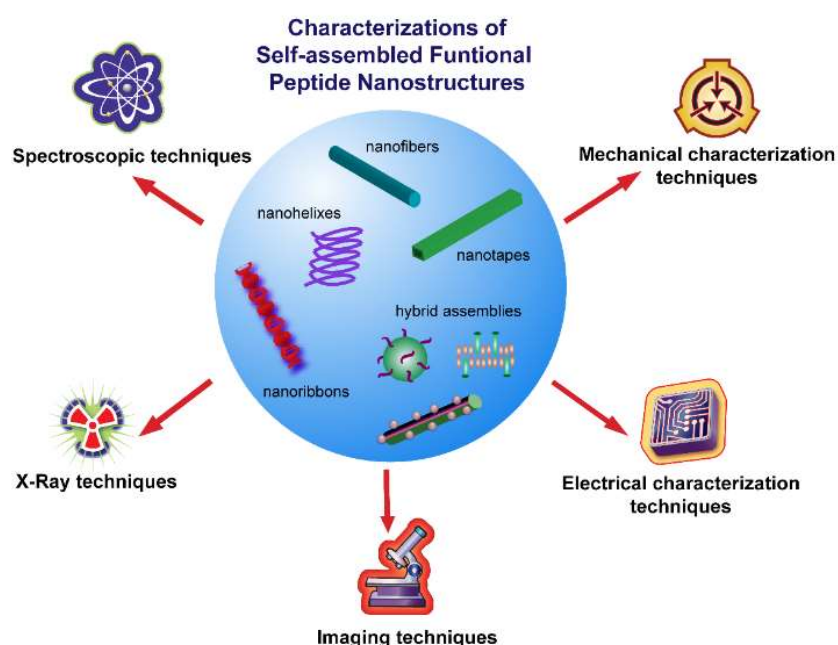


Figure 1.6 Common characterization techniques for variety of self-assembled peptide nanostructures

1.4.1 Spectroscopic Techniques

Spectroscopic methods are used to understand chemical and physical characteristics of the nanoscale peptide organizations focusing on the bond properties, vibrations, covalent and non-covalent interactions between the molecules. Although the basic principles of the spectroscopic techniques rely on the detection of the transitions on the molecules such as nuclear spin, molecular vibrations or electronic states; the detection methods for these transitions become different depending on the radiation source.

Within these spectroscopic approaches, Nuclear Magnetic Resonance (NMR) spectroscopy is a powerful technique enabling the analysis of the peptide based architectures at both liquid and solid conditions.[104] The self-assembly mechanism of fluorenylmethyloxycarbonyl (Fmoc) protected peptides which organize into three dimensional networks have been studied via 1D proton and 2D Nuclear Overhauser NMR spectroscopy in liquid and sol-gel transition states, and the results pointed the importance of hydrophobic and intermolecular interactions during the hydrogel formation.[105] On the other hand, solution state NMR methods limit the characterization of more complex peptide assemblies in liquid environment with high resolutions. Magic-angle spinning solid-state NMR (ssNMR) spectroscopy overcome the limits of solution based NMR techniques enabling through-space interatomic distance and torsion angle measurements on isotopically labelled peptide molecules.[106-108] Recently, ssNMR measurements revealed the high resolution structural organization of the supramolecular peptide based nanocarrier (Figure 1.7)[109] and self-assembled monomorphic MAX1 fibrils within hydrogel network.[110]

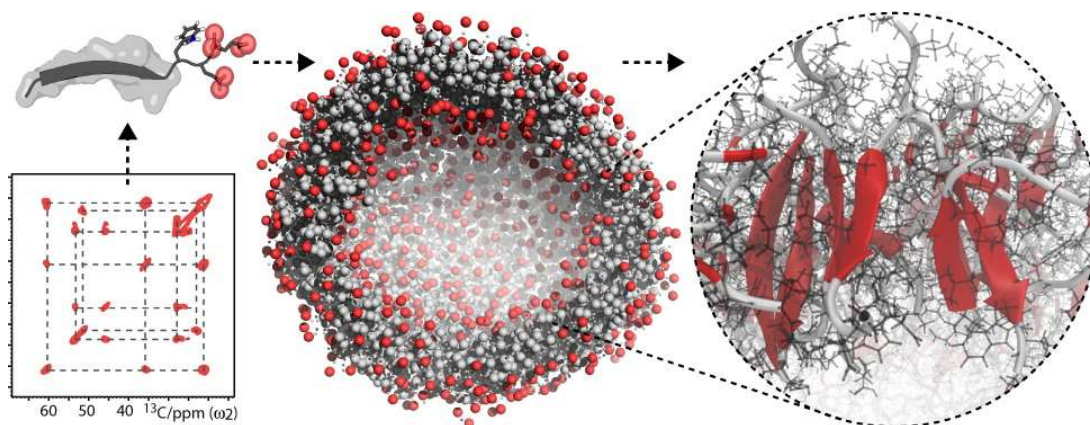


Figure 1.7 The detailed structural model of a self-assembled peptide-based nanocarrier developed in the light of the solid-state NMR (ssNMR) experiments. (Reproduced from Ref. 109 with permission from American Chemical Society)

Infrared (IR) spectroscopy deals with the electromagnetic spectrum change of peptides due to molecular vibrations and conformational changes within Amide A ($\sim 3200\text{--}3300\text{ cm}^{-1}$), Amide I ($\sim 1600\text{--}1700\text{ cm}^{-1}$), Amide II ($\sim 1480\text{--}1580\text{ cm}^{-1}$) and Amide III ($\sim 1200\text{--}1300\text{ cm}^{-1}$) bands in mid-infrared region.[111-113] The shifts in Amide I band were analyzed to monitor the structural changes as a result of the peptide self-assembly which can be triggered via different factors such as UV irradiation[114], ultrasonication[115, 116], pH, ion addition or electrostatically driven. Especially, the peaks in Amide I bands which are correlated with C=O stretching of the self-assembled peptide nanostructures contribute to the analysis of parallel or antiparallel β -sheet[117, 118], α -helix, β -turn or random-coil secondary structure organization of the peptide assemblies. Attenuated Total Reflectance (ATR) mode also enable to characterize the self-assembled peptide nanostructures at the surfaces or within the solutions[119] without any pellet preparation or sample manipulation.[120] The collected ATR-FTIR

spectrum of the pentapeptide assemblies was reported to show the vibrational peaks associated with β -sheet secondary structure organization within Amide I band.[121]

Similar to the vibrational IR techniques, the Raman scattering of the peptide assemblies assists the analysis of the structural properties in the help of the assigned modes of molecular bonds found in the peptide architectures.[122] However, conventional Raman spectroscopy lack the spatial resolution for the detailed characterizations of the peptide nanostructures due the low signal to noise ratios at dilute conditions; and different approaches have been developed to improve the scattering intensities for the analysis. The relatively low Raman signal of the peptide assemblies were also increased via Surface enhanced Raman scattering (SERS) using the localized surface plasmon resonances of the metallic clusters in liquid or solid environment.[123, 124] In addition to the surface enhancement, tip enhanced Raman scattering (TERS) enable the comprehensive characterization of the peptide nanostructures merging the scanning probe approach with vibrational spectroscopy.[125, 126]

The chiral biomolecules including DNA, proteins and peptides interact with right- and left-handed photons differently, and that difference generate non-zero Circular Dichroism (CD) signal depending on the conformation of the molecules.[127] CD spectroscopy provides the information about the secondary structure of the peptide assemblies[128], conformational changes due to pH change[129], chirality of the supramolecular peptide architectures[130] and also the interactions between toxic molecules[131] or metal ions[132] with self-assembling peptides at near and far UV region (180-320 nm). β -sheet organization of asymmetric self-neutralizing amphiphilic peptide wedges which enhances strong positive and negative peaks at 190

and 220 nm, respectively was reported as a result of CD analysis of the supramolecular assemblies.[133] Blue shifted CD spectra of the peptide assemblies with positive maximum at 195 nm and two negative maxima at around 205 and 218 nm showed the formation of the super-helical peptide assemblies.[134] The conformational differences such as twisting or disordered β -sheets in the assemblies can be detected via shift in the CD spectra due to the π - π^* transitions within the peptide backbone.[129, 135]

The simulation studies focus on the peptide self-assembly and molecular organization strengthen the initial design parameters and give useful insights for the experimental findings.[136-140] Incorporation of the experimental results and the simulation outputs developed using different molecular dynamics (MD) simulation programs improve the knowledge on the structural properties of the peptide assemblies.[109, 141-145] In the literature, the successful candidates determined within 8000 different peptide molecules using computational approaches were synthesized and their supramolecular assemblies were characterized using different spectroscopic techniques.[146] The assembly characteristics of synthetic amyloid peptide fragment at different conditions were characterized via detailed 2D NMR spectroscopy and the structural model was developed in the light of both the experimental outputs and the molecular dynamics simulations.[147] In addition, the spectral simulations of IR, vibrational CD and Raman techniques were conducted for the conformational study of the various peptide assemblies to highlight aggregation and fibril formation behaviors.[148, 149]

1.4.2 X-Ray Techniques

X-Rays are high energy electromagnetic waves and their interactions (reflection, diffraction or scattering) with the self-assembled peptide nanostructures provide the valuable information for the determination of size, shape and structural orientation. X-Ray diffraction (XRD) patterns of self-assembled peptide nanostructures were used to determine packing parameters and molecular organization focusing on the non-covalent interactions between the building blocks.[150-152] In the literature, the peaks associated with the hydrogen bonding, π - π stacking and β -sheet secondary structure organization were reported; and the spacing between peptide molecules were estimated using the Bragg's law.[153, 154] The crystalline organization and unit cell parameters of the self-assembled arginine-capped peptide bolaamphiphile nanosheets were revealed via XRD measurements in addition to the other characterization techniques.[18] On the other hand, the estimated structural parameters for the secondary structures could slightly change depending on the ordered and disordered degree of the peptide organization consisting different amino acids sequences to direct self-assembly. Besides the powder diffraction examples, the oriented nanofiber wide angle X-Ray scattering of isomeric tetrapeptide amphiphiles were performed on the peptide solutions loading into the quartz capillaries.[155] In another study, molecular organization of dipeptide assemblies and interatomic distances at gel state were determined using X-Ray fiber diffraction technique.[156]

Small angle X-Ray scattering (SAXS) eliminates the drawbacks of the powder diffraction and enables the analysis of disordered peptide assemblies without time consuming sample preparation steps in their native conditions based on the lower angle X-Ray scattering from 1° to 10° .[157, 158] In the literature, SAXS analysis of

arginine-capped peptide bolaamphiphile structures at liquid conditions revealed the nanosheet assembly with bilayer organization complementary to the other structural characterizations (Figure 1.8).[18] SAXS profiles of the oppositely charged PAs mixtures prepared at different ratios underlined the formation of bilayers after thermal treatment process.[159] In another study, self-assembly of the maspin-mimetic PA into a mixture of cylindrical and ribbon-like shapes were characterized based on the analysis of the scattering data in Guinier region.[160]

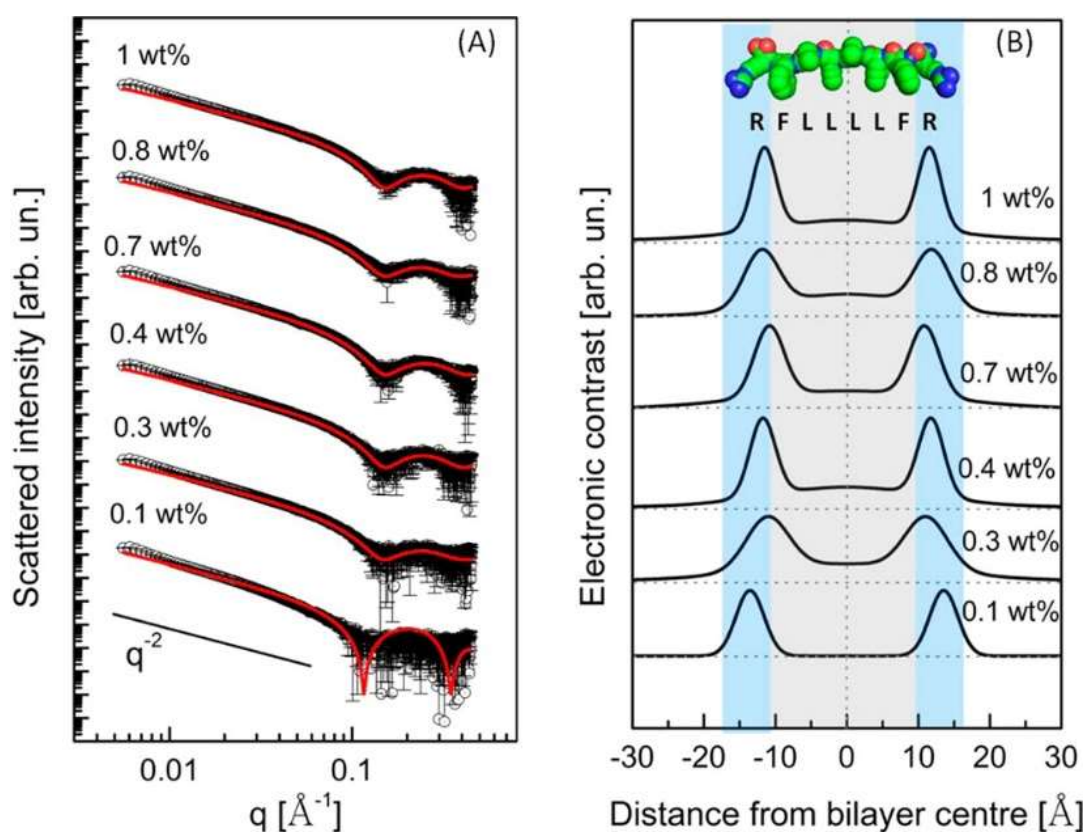


Figure 1.8 The scattering (a) and electron density (b) profiles of the self-assembled arginine-capped peptide bolaamphiphile assemblies prepared at different concentrations and the fitting lines of the model according to a bilayer form factor. (Reproduced from Ref. 18 with permission from American Chemical Society)

1.4.3 Imaging Techniques

Starting with the development of Transmission Light Microscopy (TEM) in 1930s, microscopic approaches became a fundamental way to understand the structural and material properties at nanoscale. Advances in microscopic tools enhanced the visualization of the peptide based materials using different imaging techniques including TEM, Atomic Force Microscopy (AFM), scanning electron microscopy (SEM), fluorescence and other microscopies at high resolutions.

Conventional TEM imaging of the peptide based nanostructures requires special sample preparation procedures including staining via heavy metal salt such as uranyl acetate and drying of the sample before the imaging.[161] In the literature, a variety of TEM images of the self-assembled peptide architectures including nanofibers, nanospheres, nanobundles, nanotubes, helices etc. were reported and the details of the sample preparation procedures were supported.[54, 55, 162, 163] Although TEM imaging is the crucial way to show the structural properties of the peptide nanostructures, the effects of drying and staining steps on the peptide organization cannot be disregarded. On the other hand, cryogenic TEM (cryo-TEM) in which the sample is vitrified using special tools overcomes the sample preparation limits and enable to image peptide nanostructures at their native conditions.[32, 164, 165] The direct structural analysis of the dimeric α -helical coiled coils within the de novo designed self-assembling fiber system was performed via incorporation of the cryo-TEM imaging with image processing.[166] In another study, the effect of salt concentration on the morphology of the self-assembled amyloid peptide assemblies has been showed via cryo-TEM, and the results pointed the formation of flat ribbons

and decrease of twisted fibrils due to the salt screening of electrostatic interactions between the peptide molecules.[167]

AFM facilitates *in situ* visualization of the self-assembly process of the variety of peptide building blocks into supramolecular nanostructures with nanoscale resolutions at liquid conditions.[168] The monitoring of the structural changes depending on the environmental factors including pH, ion effect, temperature, concentration etc. is also possible via time-lapse AFM procedures. In the literature, AFM imaging was performed to monitor time dependent changes of the resilin-elastin-collagen-like chimeric polypeptide assemblies incubated in water at 50 °C.[169] Right-twisted helical ribbon formation and their conversion to microcrystals of amyloid derived peptide fragment, ILQINS hexapeptide, which is normally found as left-handed helical ribbon and nanotube organization in lysozyme, has been showed via AFM imaging at different time periods at room temperature.[170]

Direct observation of the peptide self-assembly is also possible via covalent conjugation of the fluorescence probes to the peptides using fluorescence imaging techniques.[171] Stochastic imaging and deconvolution methods were also used to decrease resolution limits and monitor the supramolecular peptide organization at nano scales. Additionally, the intrinsic fluorescence properties of the peptide nanostructures were also used for the imaging of the assemblies via confocal microscopy without any probe conjugation.[172, 173]

Without any staining or probe conjugation, chemical and spatial information collected via Raman spectroscopy enhanced the stochastic imaging of the biological samples.[174, 175] The self-assembled amyloid inspired peptide assemblies were imaged using SERS blinking effect during the *in situ* Raman spectrum measurements

(Figure 1.9).[123] In addition, tip-enhanced Raman imaging technique which is the incorporation of the scanning probe microscopy with Raman spectroscopy[176] enabled the imaging of the self-assembled peptide nanotapes with additional chemical information.[125]

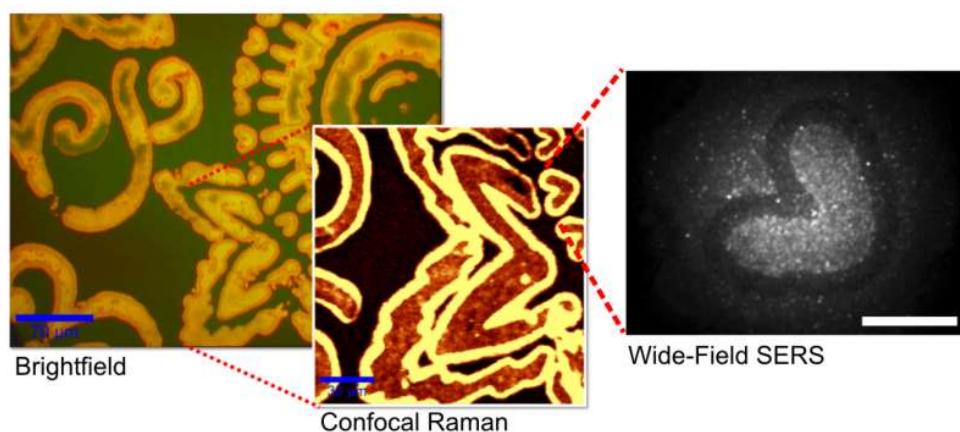


Figure 1.9 Label-free super-resolution imaging of the self-assembled amyloid inspired peptide structures by applying stochastic reconstruction to temporal fluctuations of the Surface Enhanced Raman Scattering (SERS) signal. (Reproduced from Ref. 123 with permission from Nature Publishing Group)

1.4.4 Mechanical Characterization Techniques

The development of nanomechanical characterization techniques for peptide nanostructures is a requirement since the traditional mechanical characterization methods incapable to operate at biologically relevant length and force scales with applicable time periods. The nanoscale AFM probes facilitates the implementation of traditional approaches including adhesion, tensile, compression or bending tests to analyze nanomechanics of self-assembled peptide nanostructures at miniaturized experimental conditions.

AFM based nanoindentation is widely used approach to determine the mechanical properties of the peptide nanostructures including hardness, stiffness and elasticity based on the load-distance curves collected during the analysis.[177, 178] The interactions between the tip and nanostructures were modeled based on different approaches to estimate nanomechanical characteristics processing the collected force-distance data of the nanostructures.[179-181] Elastic modulus values of the self-assembled PA nanofibers formed via Ca^{2+} crosslinking or pH change were estimated using the force-distance data obtained via AFM nanoindentation.[42] AFM nanoindentation experiments were conducted to show the nanomechanical differences of azide containing spherical peptide assemblies before and after UV irradiation.[182] In other study, the effects of the structural transition of chemically modified self-assembled diphenyl nanostructures on their mechanical properties were analyzed via AFM-based nanomechanical measurements.[89] Moreover, double pass-force-distance mapping assists the topography imaging and the mechanical characterization of the imaged area combining the tapping mode AFM operation with the acquisition of force–distance curves associated with the tip-oscillating sample interactions.[183] The technique increased the speed of nanomechanical characterization of the nanostructures and enhanced the high resolution force mapping of the amyloid inspired peptide assemblies using AFM.[184]

The unique mechanical behavior of the amyloid like peptide assemblies contribute to the design of functional materials including conductive fibers, energy harvesting systems or tissue scaffolds.[185-189] Cross- β sheet organization, excess hydrogen bonding and aromatic interactions between the amyloid based peptide are the inherent sources of the mechanical stability and rigidity of the amyloid derived peptide

assemblies.[190] Different studies were conducted to determine nanomechanical properties of the amyloid based assemblies using AFM nanoindentation technique. Recently, the nanomechanics of amyloid like fibrils assembled at different pH were revealed by peak force quantitative nanomechanical property mapping (PF-QNM).[191] In another study, the mechanical reinforcement of the electrospun polymer fibers incorporated with the peptide assemblies were revealed via AFM based nanoindentation experiments applied with a spherical colloidal tip.[192]

In addition to AFM based nanoindentation, different characterization approaches have been developed to determine mechanical characteristics of the self-assembled peptide nanostructures and their three-dimensional supramolecular networks.[193] Similar to amyloid based peptide assemblies, cyclic peptide architectures reveal intriguing hierarchical organizations with tunable mechanical properties and rigid geometries.[194] The nanomechanical properties of these architectures including elastic modulus, hardness, strength and Young's modulus were determined by using AFM nanoindentation; and self-assembled cyclic QL4 fibers exhibited the stiffest material characteristics within the known proteinaceous micro- and nanofibers (Figure 1.10).[144]

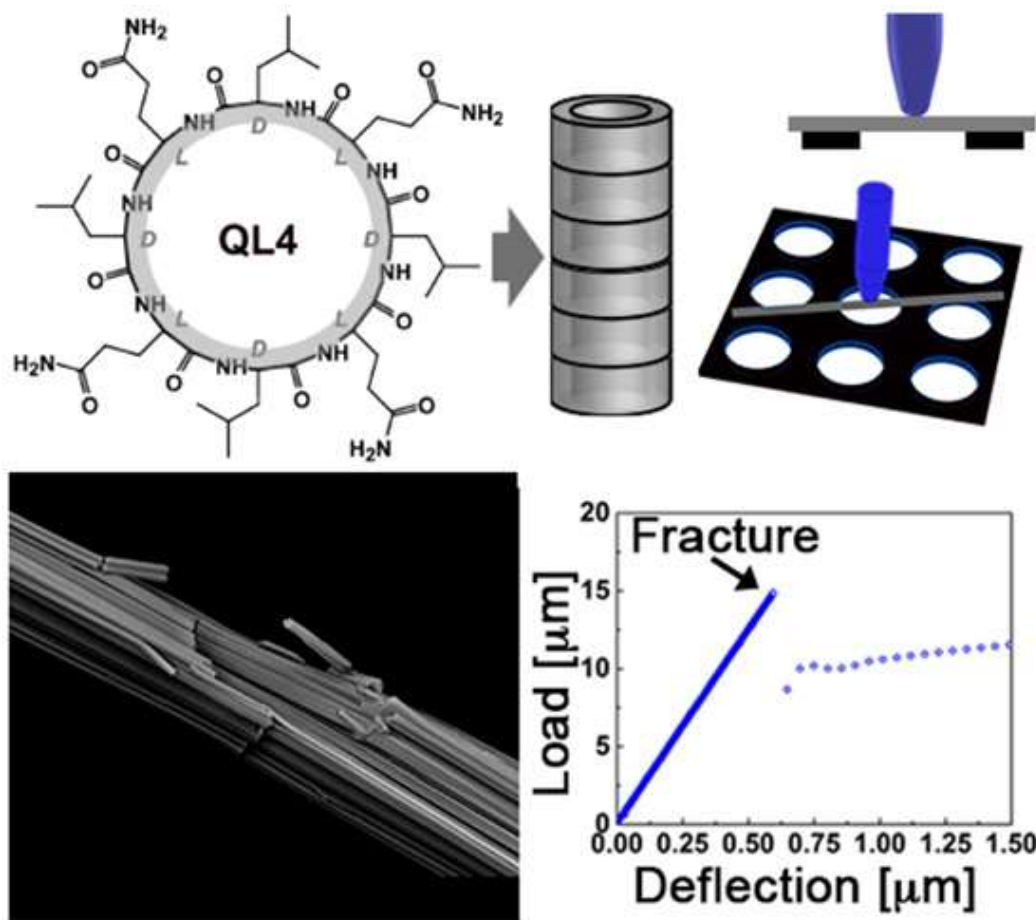


Figure 1.10 The nanomechanical characterizations of the D, L cyclic peptide assemblies. (Reproduced from Ref. 144 with permission from Nature Publishing Group)

Viscoelastic behavior of the different peptide assemblies were also determined using oscillatory rheology or microrheology techniques which highlight the sol-gel transition of the peptide architectures due to the external or internal stimulus.[195-199] Additionally, microfluidic based microcantilever system was developed to determine the forces produced by amyloid peptide polymerization monitoring the micro cantilever deflections which were correlated with the mechanical behavior of the process.[200]

1.5 Applications of Self-Assembled Peptide Based Biomaterials

1.5.1 Drug Delivery

Drug delivery systems have been developed to control drug release rate, maintain drug concentration within the desired levels, improve bioavailability and reduce side effects of the drugs lowering the therapeutic dosage for the treatment.[201] A variety of organic/inorganic materials, devices or complex formulations have been used as delivery vehicles to develop effective therapeutic modalities.[201, 202] Advances in material science and integration with nanotechnology provide us a new generation of biodegradable and biocompatible delivery systems with control over size, shape and multi-functionality.[202-205]

Self-assembly is a nature inspired an engineering tool to construct drug delivery systems with different chemical and physical properties.[206] Polymers, synthetic or natural biomacromolecules, lipids or hybrid systems are designed as building blocks by using multiple non-covalent interactions including hydrogen bonding, hydrophobic, aromatic, hydrophilic and also electrostatic interactions. Although these interactions are individually weak and fragile compare to the covalent systems, the overall non-covalent forces drive the self-assembly process and result the formation of complex, adaptable and highly tunable structures as drug delivery architectures.[207]

Self-assembling peptide based building blocks paid attention to build drug delivery architectures due to their bioactivity and capacity to direct cellular processes. In addition to their delivery capacity of variety of therapeutics via non-covalent interactions or covalent conjugation strategies at both nano and bulk scale conditions as given Figure 1.11[208], the targetability and cellular internalization ability of these self-assembled peptide based architectures make them novel drug delivery

systems.[209] Furthermore, the responsiveness of the self-assembled peptide based systems to the environmental conditions enable us to control smart delivery of the drugs to a desired area.[210]

Amphiphilic peptide assemblies provide both hydrophobic and hydrophilic structural organization for delivery of therapeutic moieties which can be modulated via the design building blocks.[211, 212] Moreover, PA structures are functionalized via bioactive epitopes, cell penetrating and internalization sequences for targeted delivery of the small therapeutics with high efficacy.[54] Biocompatibility and biodegradability of PA assemblies via different enzymes[213-215] also make them appropriate delivery architectures, especially for the chemotherapeutics which show high cytotoxicity when directly administrated to the blood stream. Previously, it was shown that bioresponsive anti-cancer drug delivery was sustained through the self-assembled PA nanofiber gels consisting matrix metalloproteinase-2 (MMP-2) cleavable amino acid sequence.[216] In another study non-covalent encapsulation of hydrophobic anti-tumor drug into the self-assembled PA nanofibers both enhanced the aqueous solubility and activity of the drug molecules which was examined developing an *in vivo* breast cancer model.[217] Recently, the self-assembled cell penetrating amphiphilic peptide nanostructures were developed for the targeted delivery of the hydrophobic cancer drug molecules towards the cell with enhanced antitumor activity.[218]

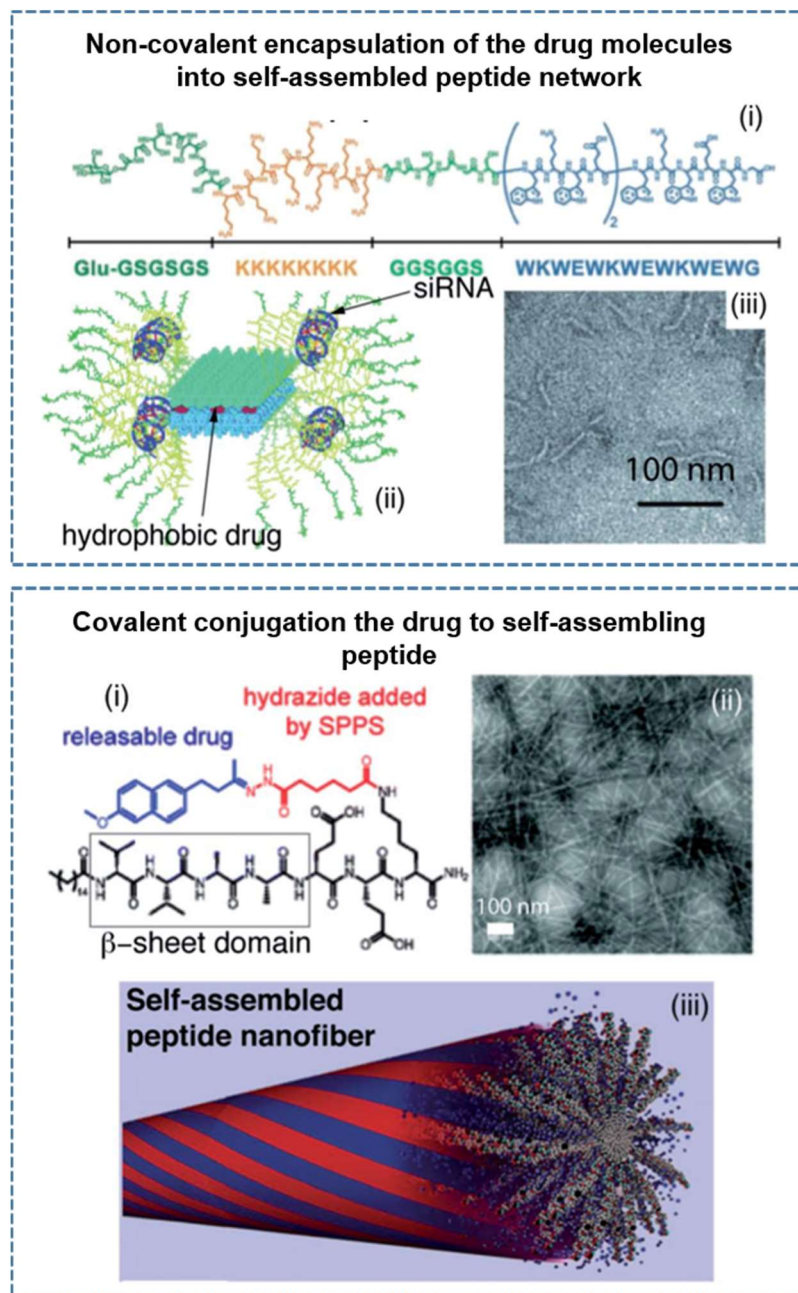


Figure 1.11 Controlled drug delivery through self-assembled peptide assemblies via non-covalent encapsulation or covalent conjugation of the drug molecules (Adapted from Ref. 208 with permission from Royal Society of Chemistry)

The chemical conjugation of the drug molecules to the self-assembling peptide backbone both prevent the degradation of the molecules in blood stream and improve the activity due to the delivery of them on the supramolecular architectures.[101, 219]

In the literature, the supramolecular nanotube formation of anticancer drug camptothecin conjugated to the Tau- β -sheet-forming peptide through a biodegradable linker was shown as a drug delivery system with enhanced *in vitro* efficacy.[220] In another study, the doxorubicin integrated amphiphilic peptide moiety consisting both cell penetrating Tat peptide and the enzymatically cleavable specific amino acid residues was examined as controlled drug delivery system.[221] The developed system showed enhanced anticancer activity compare to the free doxorubicin administration.[221]

In addition to the nano-scale peptide based delivery systems, these building blocks are able to form supramolecular self-assembled nanofiber gels which provide a mild environment to deliver variety of therapeutic molecules. The controlled drug release behavior through the peptide based gels was studied via different model small molecules.[222, 223] In addition, the long term sustained release of the therapeutics through injectable self-assembling peptide scaffold hydrogels was achieved preventing the bioactivity of the molecules for 3 months.[224]

Local delivery of the anticancer drugs using biocompatible scaffolds can be an alternative way to reduce overall invasiveness and systemic side effects on healthy tissues improving bioavailability of the chemotherapeutics at the target site.[225-228] Self-assembled peptide based nanofiber gels which were investigated for controlled delivery of small molecules including proteins[229], antibodies[224] and therapeutics[230-232] are suitable candidates for the local delivery of chemotherapeutics[216]. In the literature, the design of the injectable peptide based gel systems were presented in different studies.[151, 233, 234] Recently, β -hairpin

peptide hydrogel developed as injectable local drug delivery system was achieved the continuous release of the active chemotherapeutics over a month.[235]

1.5.2 Regenerative Medicine

Many biomaterials available in market have been specifically designed for promoting tissue growth and regeneration capacity. Biomimetic approach for tissue engineering focuses on the design of the biomaterials synthesized by polymers endowed with bioadhesive receptor-binding peptides or different sugar moieties. On the other hand, the integration of synthetic inert biomaterials into the living tissues whose physical properties are result of millions years of evolutionary optimization is still a difficult issue. To overcome the recent limitations in this field, peptide self-assembly provide new prospects to develop highly dynamic and responsive supramolecular architectures mimicking the chemical and physical properties of the native ECM microenvironment. In recent years, the self-assembled peptide based scaffolds which were incorporated with specific bioactive amino acid residues or soluble factors directing cellular differentiation and tissue regeneration capacities have been intensively studied. The scaffolds obtained via the self-assembly of RADA16-I peptide which was also commercialized and called as PuraMatrix™ were examined for the neural stem cell and osteoblast differentiation for *in vivo* spinal cord injury treatments and bone regeneration purposes, respectively (Figure 1.12).[236] In another self-assembling peptide design, collagen mimetic peptide building blocks[237, 238] formed 3D hierarchical architectures provided the similar features of native collagen matrix to promote tissue regeneration and repair.

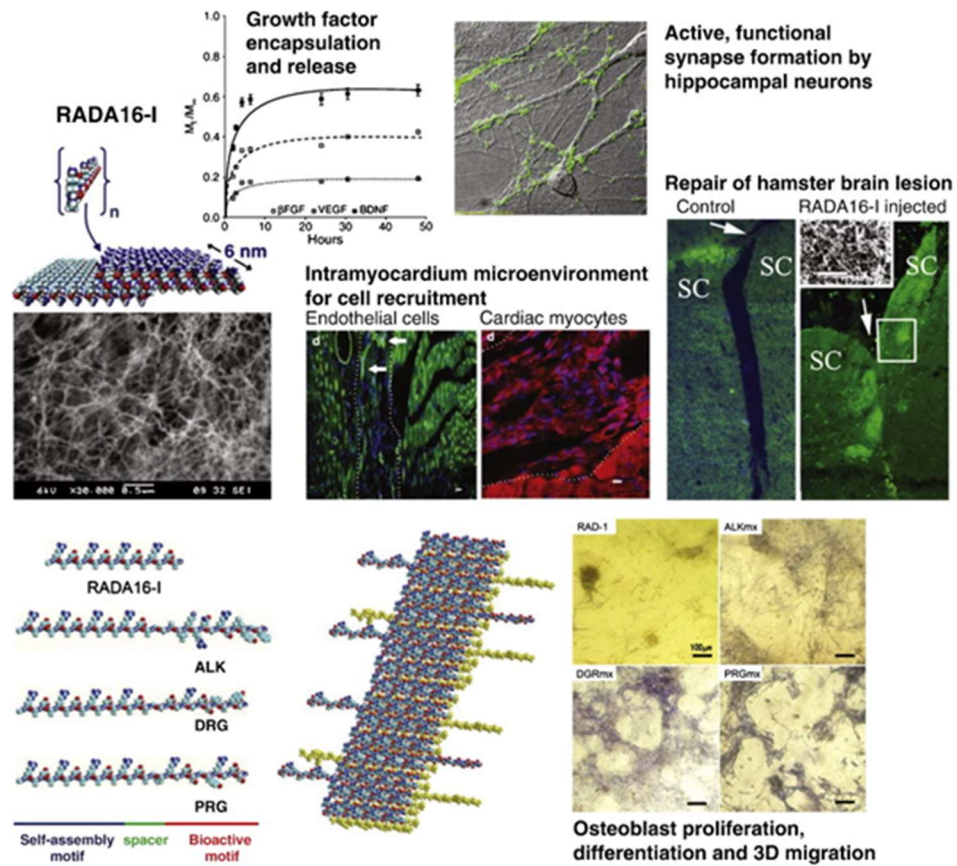


Figure 1.12 Self-assembled RADA16-I peptide scaffolds examined for different regenerative medicine applications (Adapted from Ref. 236 with permission from Elsevier)

In addition, the self-assembling PA designs mimicking the native components of the ECM showed high tissue regeneration capacity providing bioactive microenvironment for guided cellular differentiation. For example, the supramolecular assemblies of IKVAV-PA which consists of the neurite-promoting laminin epitopes eliminated scar tissue formation and enhanced axon elongation after the spinal cord injury model was developed under *in vivo* conditions.[239] The alignment of these bioactive nanostructures due to the shear force applied by pipetting also provided a physical guidance for the cells for aligned neurite growth.[240]

Growth factor binding PA assemblies enhanced the tissue repair and regeneration processes providing the interactions of the soluble factors and the cells within supramolecular highly dynamic microenvironment. In the literature, the enhanced bone formation and regeneration was obtained using a scaffold ensemble via BMP-2 binding PA molecules.[241] Heparin or GAG mimetic PA assemblies developed by our group with growth factor binding affinities[242] were also examined for their tissue regeneration capacities.[243, 244] In addition to the bioactive amino acid residues used in design of regenerative peptide based building blocks, sugar moieties have been also conjugated to self-assembling peptide molecules to mimic the structural and biochemical properties of glycopeptides which have specific roles and functions on the specific tissue regeneration processes. Self-assembled glycopeptide nanofibers which were designed and synthesized by our group (Figure 1.13)[100] promoted *in vitro* chondrogenic differentiation and *in vivo* cartilage tissue regeneration mimicking the biochemical and biophysical properties of natural hyaluronic acids which are the main components of native cartilage ECM.

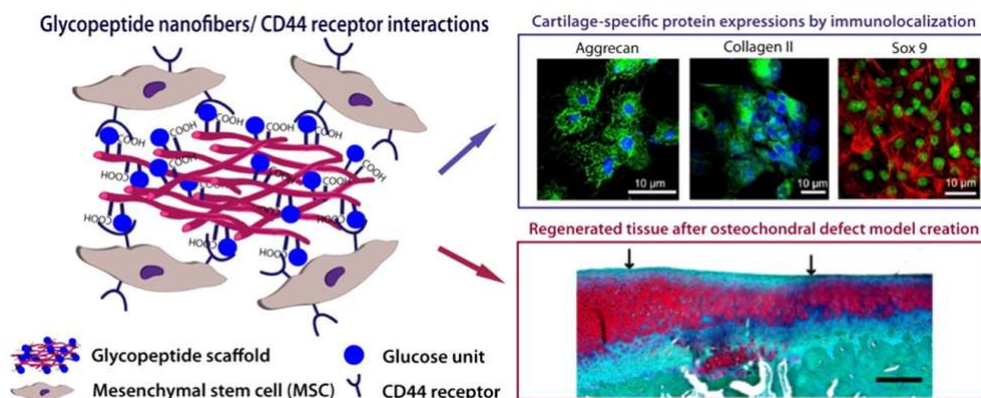


Figure 1.13 Self-assembled glycopeptide nanofibers and their supramolecular nanofiber gels promoted chondrogenesis and cartilage regeneration (Reproduced from Ref. 100 with permission from American Chemical Society)

Chapter 2

2. Amyloid Inspired Self-assembling Peptides (AIPs) and Their Supramolecular Assemblies

Part of this chapter of thesis is published in the following articles[184, 245]; Reprinted from “Amyloid inspired self-assembled peptide nanofibers”; Cinar, G.; Ceylan, H.; Urel, M.; Erkal, T. S.; Deniz Tekin, E.; Tekinay, A. B.; Dâna, A.; Guler, M. O., *Biomacromolecules*, 2012, 13, 3377-3387, with permission from American Chemical Society; and Reprinted from “Supramolecular nanostructure formation of coassembled amyloid inspired peptides”; Cinar, G.; Orujalipoor, I.; Su, C.-J.; Jeng, U. S.; Ide, S.; Guler, M. O., *Langmuir*, 2016, 32, 6506-6514, with permission from American Chemical Society.

2.1 Introduction

Amyloid proteins consisting of a broad variety of amino acids has provided inspiration for developing functional materials due to their stability against mechanical, thermal and chemical factors.[246, 247] These assemblies share the common structural property of a dense β -sheet organization, which enhances the stabilization of amyloid fibrils through multiple hydrogen bonding and noncovalent interactions.[248-251] In addition, π - π stacking between aromatic residues and electrostatic interactions between charged amino acids enhance to the stability of the amyloid fibers[252]. In addition to the structural organization of amyloid fibril, the studies conducted to determine mechanical properties of these structures is essential to understand the source of their rigid and stable existence.

Previously, nanomechanical properties of the different amyloid architectures including α -synuclein[253], A β (1-40) amyloid fibril[254], and insulin aggregates[255] were examined by using Atomic Force Microscopy (AFM). The results obtained via nanoindentation provided valuable information about fibril strength, adhesive properties and stiffness of the amyloid structures[256]. Furthermore, these studies showed that self-assembled amyloid architecture revealed high stiffness and rigidity compare to other natural proteinaceous materials such as silk, collagen and keratin. In addition, the Young's Modulus values of the amyloid assemblies can reach up to 10 GPa.[257]

In addition to their molecular organization, aggregation kinetics of these structures are interesting due to the aberrant deposition of their insoluble forms in natural organisms. This phenomenon is responsible for several classes of neurodegenerative disorders; and is caused by the nucleation-dependent formation of amyloid fibrils, which allows soluble monomers to assemble into existing filaments.[258, 259] Moreover, environmental conditions such as pH, temperature and ion concentrations have been demonstrated to alter the nucleation and growth kinetics of the amyloids in several studies.[260, 261] The hierarchical organization and thermal and mechanical stability exhibited by amyloid fibrils allow their use in the development of advanced functional materials.[188, 247, 262-264] In addition, the depth knowledge obtained from the material properties of amyloid structures guide the researchers to build amyloid-inspired hierarchical synthetic architectures for different applications including controlled drug delivery, catalysis, energy harvesting or tissue engineering.[257, 265]

Due to complex nature of the self-assembly process, it is quite difficult to monitor rapid assembly kinetics and to understand the parameters that play crucial roles in

peptide aggregation and nanostructure formation under different conditions. Thioflavin T (ThT) assay is the most commonly used method for studying amyloid assembly.[266] The binding of ThT to β -sheets results in red shift in excitation and emission spectra; and strong increase in fluorescence intensity during the fibrillization process.[267, 268] The self-assembly of amyloid fibrils may also be observed directly through the fluorescence enhancement facilitated by the binding of ThT, which can be visualized by fluorescence imaging techniques.[269, 270]

In addition to fluorescence-based approaches, SAXS is a highly powerful technique for the mechanistic studies of peptide nanostructures, as the method allows the analysis of molecules at native conditions without manipulation of the sample, and may be utilized to perform time-resolved experiments using a high flux source.[271] These techniques have been utilized for in-depth characterization of both functional and pathological amyloids[272, 273] and facilitated the design of rapidly self-assembling, nature-inspired synthetic peptide assemblies; however, greater insight into the organizational details and self-assembly characteristics of such synthetic peptide networks may further contribute to the development of functional designs for next-generation nanoscale materials.

In this chapter of the thesis, the design, synthesis and characterizations of amyloid-inspired peptides (AIPs) which can form biocompatible coassembled nanofibers and supramolecular gels with superior mechanical properties in the absence of external factors at physiological conditions[184] was presented. In addition to the smart design strategy of the peptides, we performed molecular dynamics simulations to understand the coassembly mechanism of oppositely charged peptides and noncovalent interactions taking place during the aggregation. We also investigated the coassembly

kinetics of oppositely charged AIPs by monitoring nanostructure formation and sol-gel transition at different peptide concentrations through various techniques, including ThT binding, real-time fluorescence imaging, turbidity assay and *in situ* SAXS analysis. Co-assembly kinetics were observed to depend strongly on initial peptide concentration, while peptide aggregation was found to be enhanced following fragmentation by sonication and exhibit amyloid-like sigmoidal assembly behavior. Structural properties of peptide assemblies were estimated by fitting the experimental scattering profiles of coassembled AIP nanostructures to theoretical models, and the mechanisms underlying their nanofibrous organization were analyzed with respect to the SAXS results. Mass fractal analysis of the AIP nanostructures and the conservation of their bulk material viscoelasticity at elevated temperatures also show the organizational stability of amyloid-inspired peptide architectures. Amyloid inspired design strategy also provided sol-gel conversion to obtain self-supporting peptide gels. The material properties of their supramolecular assemblies and formed by mixing AIP-1 and AIP-2 at pH 7 in water revealed remarkable mechanical properties without addition of any crosslinking reagents and inorganic materials[274]. In addition to bulk mechanical properties, nanomechanical characterizations of the coassembled AIP nanofibers and self assembles AIP-1 and AIP-2 molecules were conducted to understand the relationship between mechanical stability and the structural properties of the architectures. The potential of the amyloid inspired nanostructures as a synthetic extracellular scaffold system was also tested at *in vivo* conditions.

2.2 Experimental Section

2.2.1 Materials

All protected amino acids, Rink amide MBHA resin and 2-(1H-benzotriazol-1-yl)-1,1,3,3-tetramethyluronium hexafluorophosphate (HBTU) were purchased from NovaBiochem. Other chemicals used for peptide synthesis and material characterizations, including dichloromethane (DCM), dimethylformamide (DMF), acetonitrile, piperidine, acetic anhydride, *N,N*-Diisopropylethylamine (DIAE), trifluoroacetic acid (TFA), thioflavin T (ThT) and uranyl acetate, were purchased from Fisher, Merck, Alfa Aesar or Sigma-Aldrich. All chemicals and solvents used in this study were analytical grade. Cell culture chemicals were purchased from Gibco, Life Technologies.

2.2.2 Synthesis and Characterizations of AIPs

A solid phase peptide synthesis method was followed to obtain AIP-1 (Ac-EFFAAE-Am) and AIP-2 (Ac-KFFAAK-Am) molecules. Rink amide MBHA resins were used as solid support for the construction of the peptide molecules. Fmoc protecting groups of each amino acid were removed using 20% (v/v) piperidine/DMF solution for 20 min before the coupling reactions. Peptide synthesis was carried out on the resins by amino acid coupling with 2 mol equivalents of Fmoc-protected amino acid, 1.95 mole equivalents of HBTU and 3 mol equivalents of DIAE for 2 h. After each amino acid coupling, the resins were washed with DMF and DCM to remove unreacted components. Following the coupling reactions, resins were exposed to a 10% (v/v) acetic anhydride/DMF solution for 30 min to acetylate the unreacted amine groups and prevent the formation of impurities. Peptides were cleaved from the solid supports using a mixture of TFA:TIS:ddH₂O in a ratio of 95:2.5:2.5 for 2 h. Cleaved peptide

molecules were separated from the solid supports by washing with DCM, and excess TFA and DCM were removed by rotary evaporation. Peptides were then precipitated using diethyl ether at -20 °C overnight. The precipitate was collected by centrifugation at 7500 rpm for 20 min and dissolved in water, and the peptide solutions were then frozen at -80 °C and lyophilized for three days.

An Agilent 1200 series reverse-phase high performance liquid chromatograph (HPLC) equipped with an Agilent 6224 high resolution mass time-of-flight (TOF) mass spectrometer and an electrospray ionization (ESI) source was used for the characterization of the synthesized AIPs molecules. 1 mg/mL AIP-1 in water was analyzed at pH 7 using an Agilent Zorbax 300SB-C18, 3.5 μ m (100 x 4.6 mm) column in an optimized gradient of water (0.1% NH₄OH) and acetonitrile (0.1% NH₄OH) as the mobile phase, while an Agilent Zorbax Extend-C18, 3.5 μ m 80A (100 x 4.6 mm) column was used for the analysis of 1 mg/mL AIP-2 at pH 7 in water in an optimized gradient of water (0.1% formic acid) and acetonitrile (0.1% formic acid).

2.2.3 Zeta Potential Measurements of AIPs

Diluted AIP-1 and AIP-2 solutions at 0.04% (w/v) concentration was prepared in water at pH 7. AIP-1 and AIP-2 solutions were also mixed to obtain a coassembled nanofibrous architecture and incubated for 1 h; then diluted to a concentration of 0.04% (w/v). Malvern Nano-ZS Zetasizer was used for the measurements.

2.2.4 Scanning Electron Microscopy

AIP-1 and AIP-2 solutions were mixed at a 1:1 volume ratio at different concentrations in water and at neutral pH, and kept at room temperature for sol-gel transition on a Si wafer. Complete gelation was observed within 1 h for the AIPs mixtures prepared at

4, 3, 2, 1.75 and 1.5% (w/v) concentrations, and SEM imaging was performed on these samples. A series of ethanol solutions (40%, 60%, 80% and 100% (v/v)) were used to replace the water present in the samples, which were then dried using a critical point dryer to preserve their nanofibrous architecture and coated with 4 nm Au/Pd. A FEI Quanta 200 FEG Scanning Electron Microscope equipped with an ETD detector was used for SEM imaging. Although 1.25% and 1% (w/v) AIPs samples were also prepared, SEM imaging could not be performed on these samples as they did not exhibit self-supporting gelation within 1 h.

2.2.5 Transmission Electron Microscopy

2% (w/v) AIP-1 and AIP-2 solutions were mixed to obtain a co-assembled nanofibrous architecture and incubated for 15 min or 1 h. Samples were then diluted at a 1:10 ratio by the addition of water, drop cast onto a TEM grid and incubated for a further 5 min. Excess sample was then removed from the surface and the grid was stained using 2% (w/v) uranyl acetate. A FEI Tecnai G2 F30 TEM instrument was used for TEM imaging.

2.2.6 Molecular Dynamics Simulations

Argus Lab[275] with an ideal backbone geometry of a beta strand ($\phi = -120^\circ$, $\psi = 120^\circ$) were used to prepare peptide molecules. The peptide molecules were randomly distributed into a cubic box with size of size 690 nm[276]. The minimum distance between the solute and the box was set to 1.0 nm. For the solvation, the water molecules (22541) were also added into the box; neutralization of the system was done using counter-ions (Na^+ , Cl^-) within the box. The energy minimization of the system with all components were carried out steepest-descent method to get the appropriate structure. The energetically minimized system was equilibrated with 100 ps of NVT

and 100 ps of NPT using position restraints. Then, Molecular Dynamics (MD) production run to generate trajectory data for analysis. GROMACS code[276] with GROMOS96 53a6[277] united atom force field for the peptides and SPC (simple point charge)[278] force field for water was used for atomistic MD simulations. The integration of Newton's equation of motion was carried out using leap-frog algorithm[279]. 2 fs time interval was set for MD integrator and all bond lengths were restricted using linear constraint solver (LINCS) algorithm[280]. Simulations were performed at the periodic boundary conditions in all directions. The calculations of the long range electrostatic interaction with a grid spacing of 0.16 nm and a fourth order cubic interpolation were performed using particle mesh ewald algorithm[281, 282]. Short range electrostatic and van der Waals interactions were cut off at 1.0 nm radius. The pressure of the system was kept at constant at 1 bar with a coupling time constant of 2.0 ps and isothermal compressibility of $4.5 \times 10^{-4} \text{ bar}^{-1}$ using an isotropic Parrinello-Rahman barostat[283]. The simulation also ran at the constant temperature at 300 K. The system was coupled to a velocity rescaling thermostat[284] with a coupling time constant of 0.1 ps. Initial velocities were generated randomly from Maxwell distribution at 300 K. The snapshots were obtained via the visual molecular dynamics (VMD) software[285]. The simulations were continued for 70 ns.

2.2.7 CD Analysis

For the CD analysis, the coassembled PA assemblies were prepared by mixing 30 μL of 1% (w/v) (13.5 mM) AIP-1 and AIP-2 solutions with a 1:1 volumetric ratio. Then, the sample was diluted up to 0.34 mM for the CD measurements. As control groups, AIP-1 and AIP-2 solutions at 0.34 mM concentration were prepared at pH 7.4 in water. Jasco J-815 CD spectrophotometer was used for the analysis between 190 to 300 nm

with data pitch: 0.1 nm, sensitivity: standard, D.I.T: 4 sec, band width: 1 nm, scanning speed: 100 nm/min.

2.2.8 FTIR Analysis

For the FTIR measurement, the coassembled AIP gels at 4, 3, 2, 1% (w/v) concentrations were formed on petri dishes and instantly frozen in liquid nitrogen in order to preserve their architectural integrity. The frozen sample was kept at -80 °C overnight and then freeze-dried to remove water content. 1 mg dried gel powder was mixed with 100 mg KBr to prepare KBr pellets for the analysis. Bruker VERTEX 70 FTIR spectrometer was used for the measurement between 300 and 4000 cm^{-1} .

2.2.9 Congo-red Staining

The stock solution of congo red at 5 mM was prepared at neutral pH in water and then filtered with 0.2 μm filter. For the coassembly of AIP-1 and AIP-2 molecules, the mixture was prepared at 4% (w/v) concentration, and mixed with the stock solution of dye. AIPs mixture was also incubated for an hour after the addition of the dye solution. As a control group, the dye solution without the addition of the AIP assemblies was also prepared. The sample was diluted after the incubation; and the final peptide and dye concentration within the system were 0.008% (w/v) and 10 μM , respectively. Spectramax M5 Microplate Reader was used for UV measurements of the samples with three replicates.

2.2.10 ThT Binding Assay and Confocal Fluorescence Imaging

AIP-1 and AIP-2 solutions were prepared at 2, 1.75, 1.5, 1.25 and 1% (w/v) concentration dissolving the peptide powders in double distilled water, separately. The pH of each solution was adjusted to 7.4 using 1 M NaOH. Same procedure was

followed for all experiments. A Zeiss LSM 510 confocal microscope was used to monitor the co-assembly process of AIPs through fluorescent ThT binding. 1:1 (v/v) mixtures of AIPs were prepared at different concentrations (2, 1.75, 1.5, 1.25 and 1% (w/v)) in water and at neutral pH, and 100 μ L of each mixture was transferred to 96 well plates. Immediately following the mixing of AIPs, a ThT solution in water was added onto the mixture at a final concentration of 216 μ M. The samples were excited using a 458 nm Argon laser at 70% intensity and the emission was collected between 490 to 522 nm using appropriate filters to detect the binding of ThT to amyloid aggregates, which results in a shift in emission maxima from 440 nm to 490 nm.[286] Fluorescence images were captured using a Zeiss EC Plan-Neofluar10X objective at a resolution of 2048 x 2048 pixels. The dimensions of the scanned volume within the AIP mixtures were 1272.17 μ m x 1272.17 μ m x 25 μ m. The Z-depth separation between the planes was 5 μ m. The pixel dwell time, master gain, digital gain, digital offset and pinhole radius values were 0.80 μ s, 668, 1.09, -0.05 and 336 μ m, respectively. Fluorescence intensity changes were quantified with respect to time in the same defined region of the interest (ROIs) for 1 h at 25 $^{\circ}$ C for all groups. The time interval between each fluorescent measurement and image capture was 2 min. 3D image construction of each time interval was performed using Zeiss LSM 510 software, and the ImageJ program was used for the 3D video construction of the images at a rate of 1 frame per second. Results were reported as the average of three repeats and all experiments were conducted at the same sample positioning and microscope configurations.

2.2.11 Turbidity Assay

100 μ L of 1:1 (v/v) mixtures of AIPs were prepared as described above and transferred to 96 well plates. Turbidity of AIP mixtures were then monitored as optical density at 313 nm on a SpectraMax M5 Microplate Reader for 1 h at 25 °C. Measurements were reported as the average of three repeats. For the analysis of the effects of fragmentation on turbidity kinetics, AIP mixtures were sonicated for different time periods (1, 2.5 or 5 min) using an ultrasonic bath (VWR, USC100T, 230 V, 60 Hz) prior to turbidity measurements. Following sonication, samples were immediately transferred to 96 well plates and analyzed under identical conditions as the nonsonicated AIP mixtures.

2.2.12 SAXS Measurements and Data Fitting

SAXS measurements were performed using the SAXS/WAXS beamline 23A of the National Synchrotron Radiation Research Center (NSRRC), Hsinchu, Taiwan. The photon energy and sample-to-detector distance were set to be 15 keV and 3312.99 mm, respectively, in order to cover a scattering vector $q = (4\pi/\lambda) \sin(\theta/2)$ from 0.006 to 0.40 \AA^{-1} (where θ is the scattering angle and λ is the wavelength of the incident X-rays). Scattered X-rays were collected by means of a 2D CCD detector. The collected 2D data were circularly averaged to give a 1D scattering intensity distribution as a function of the scattering vector, treated with background subtraction and transmission correction and normalized to absolute scattering intensity. For concentration-dependent SAXS experiments, equal volumes of 2, 1.75 and 1% (w/v) AIP-1 were mixed with 2, 1.75 and 1% (w/v) AIP-2, respectively, and AIP mixtures were immediately loaded in 2.5 mm-thick cells with Kapton-walled windows at a constant temperature of 25 °C. Samples were incubated for 1 h before the measurements and subsequently had their scattering profiles collected. For the *in situ* SAXS analysis of

2% (w/v) AIPs, the time of the mixing was accepted as zero and SAXS measurements were conducted at defined time intervals (30 s to 300 s, $\Delta t=30$ s and at 1 h). In addition to time-dependent analysis, the effect of the temperature on 2% (w/v) AIPs was also analyzed through SAXS measurements at different temperatures (25 °C to 64 °C, $\Delta T=3$ °C) following 1 h of incubation. Scattering profiles of the AIP nanostructures were fitted into a combination of the polydisperse core-shell cylinder (Poly Core Shell Cylinder: PCSC)[287] and decoupling flexible cylinder (Flexible Cylinder Poly Radius: FCPR)[288, 289] models, which estimate the scattering properties of a polydisperse, right circular cylinder with a core-shell scattering length density profile and a cylinder in a flexible, ordered fractal aggregation form, respectively (Figure S6). The shell thickness on the flat ends of the cylinder is independent of the shell thickness on the radial surface. The polydispersity of the cylinder core radius was modeled using a log-normal distribution. The overall intensity was obtained by calculating the scattering from each particle size present and weighting it by the normalized distribution.

Data analysis was performed based on the fitting of the scattering curves to an appropriate model by a least-squares method using the software provided by NIST (NIST SANS analysis version 7.20 on IGOR Pro 6.37).[290] The scattering intensity of a monodisperse system of the particles with identical shape is described as;

$$I(q) = NP(q)S(q)$$

where N is the number of particles per unit volume, $P(q)$ is the form factor revealing the specific size and shape of the scatterers, and $S(q)$ is the structure factor that accounts for the interparticle interactions.[291]

In dilute solutions where the interactions between the objects is neglected, $S(q)$ equals to 1. In a polydisperse system of the particles with identical shape, the total intensity scattered from the sample is described by;

$$I(q) = N \int_0^{\infty} D_n(R) P(q, R) dR$$

where $D_n(R)$ is a distribution function and $D_n(R)dR$ is the number of particles, the size of which is between R and $R + dR$, per unit volume of the sample.

A form factor for a simple polydisperse core-shell cylinder, where the core and the shell have a uniform electron density, is given by;

$$P(q) = \int_0^{\pi/2} \sin \theta \cdot d\theta \left[V_l(\rho_l - \rho_{solv}) \frac{\sin\left(\frac{qH_l \cos\theta}{2}\right)}{\frac{qH_l \cos\theta}{2}} \frac{2J_1(qR_l \sin\theta)}{qR_l \sin\theta} + V_p(\rho_p - \rho_l) \frac{\sin\left(\frac{qH_p \cos\theta}{2}\right)}{\frac{qH_p \cos\theta}{2}} \frac{2J_1(qR_p \sin\theta)}{qR_p \sin\theta} \right]^2$$

$$V_x = \pi R_x^2 H_x$$

where $J_1(x)$ is the first order Bessel function. θ is defined as the angle between the cylinder axis and the scattering vector, q . R_p and R_l are the core and shell radii respectively. H_p and H_l are the core and shell lengths, and ρ is electron density.

The polydispersity of the core radius is modeled using a log-normal distribution as;

$$D_n(R_p) = \frac{\exp\left(-\frac{1}{2} \left[\frac{\ln\left(\frac{R_p}{R_0}\right)}{\sigma_p} \right]^2\right)}{\sqrt{(2\pi)} \sigma_p R_p}$$

where R_0 is the mean core radius and σ is equivalent to the standard deviation of the

log normal distribution (For 2% (w/v) AIPs, mean core radius is: 49.4 Å ; σ : 0.6).

Flexible cylinder poly radius: The model estimates the form factor for a flexible cylinder with a circular cross section and a uniform scattering length density. Polydispersity of the cross-section is included, using a Schulz distribution.[292] The non-negligible diameter of the cylinder is included by accounting for excluded volume interactions within the walk of a single cylinder. Inter-cylinder interactions are not included.

The form factor is normalized by the particle volume such that;

$$P(q) = \frac{scale \langle f^2 \rangle}{Vol} + bkg$$

where $\langle \rangle$ is an average over all possible orientations of the flexible cylinder (1D). The 2D scattering intensity is the same as 1D, regardless of the orientation of the q vector which is defined as;

$$q = \sqrt{q_x^2 + q_y^2}$$

The function is calculated using the reference in the part of “Method 3 With Excluded Volume”.[288] The model is a parametrization of simulations of a discrete representation of the worm-like chain model of Kratky and Porod[288, 293, 294] applied in the pseudo continuous limit.

Figure 2.1 describes the PCSC and FCPR models which were used together to calculate scattering intensities and to fit the data. The small χ^2 values (in the range of 1.3-2.4) were also obtained after the fitting process to show the well fitted models (the acceptable values: $\chi^2 < 7.0$)

The total scattering function can be obtained from the decoupling approximation of the above mentioned PCSC[287] and FCPR models[288, 289]. The approximations of the models have been used in least-squares fitting of the experimental small-angle x-ray scattering data. The FCPR model[290] uses the form factor calculations implemented in a c-library provided by the NIST Center for Neutron Research.

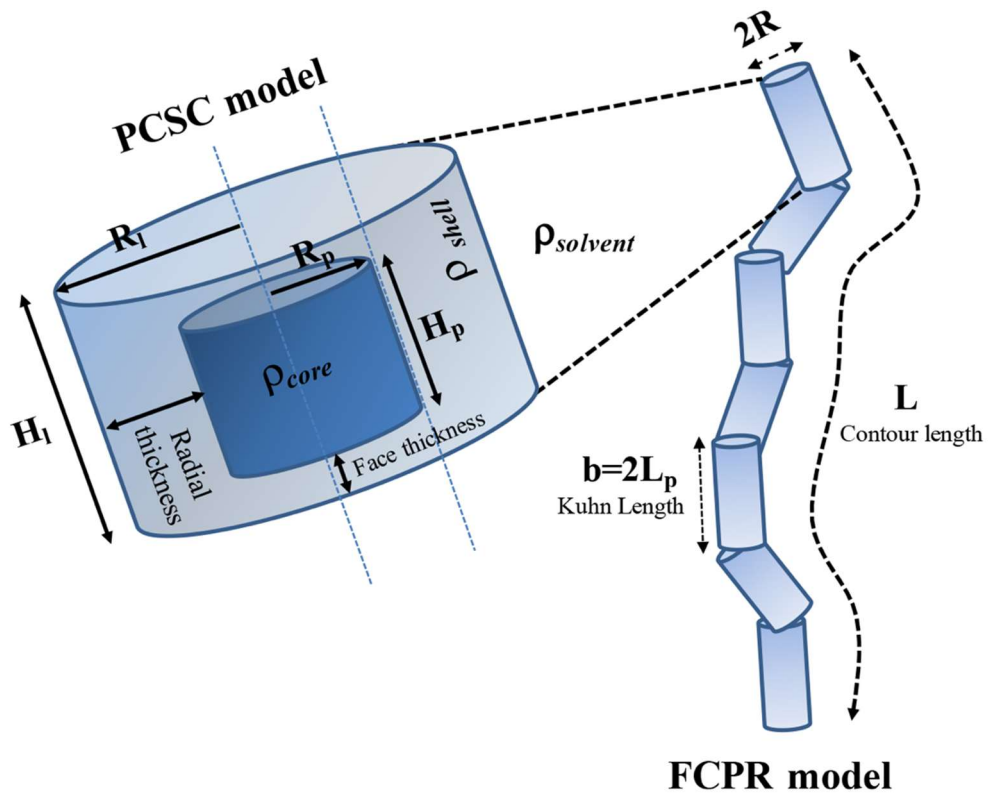


Figure 2.1 The decoupling models which successfully describe the self-assembled AIPs nanostructures

In the model, the chain of contour length (L) can be described as a chain of some number of locally stiffed segments. L_p can be defined as persistence length of the mentioned segments along the cylinder over which the flexible cylinder can be considered a rigid cylinder. The b parameter $b = 2L_p$ are defined as Kuhn length to describe the stiffness of a chain. SLD values represent the measure of electron densities

of the chain/cylinder and the solvent. The scattering functions of the semiflexible chains have been determined with a precision of 1–2% for $L/b = 6.93-7.11$.

2.2.13 Oscillatory Rheology

Time sweep analysis of the coassembled supramolecular AIP gels nanofiber gels of 4, 3, 2, 1, and 0.5% (w/v) concentrations at pH 7.4 was performed for 1 h at the constant angular frequency and strain; 10 rad/s and 0.1%, respectively. The sample volume was determined as 250 μL with 0.5 mm measuring distance from the stage. After the time sweep analysis, frequency and thixotropic tests were applied on the equilibrated gels. During the frequency analysis, the strain was kept constant at 0.1%, while angular frequency was logarithmically ramped from $\omega=0.1$ to 100 rad/s. During the thixotropic tests of the samples, the angular frequency and strain was kept constant at 10 rad/s and 0.1%, respectively for the first 5 min of the measurement, then the sample was exposed to logarithmically ramp the high shear between 0.1 to 1000% to break the gel integrity for a short time period. Finally, the recovery of the samples were analyzed keeping shear rate and angular frequency at constant values; 0.1% and 10 rad/min, respectively. Anton Paar MCR-301 Rheometer was used for the analysis. Measurements were reported as average of three repeats.

Temperature-dependent rheology measurements were performed in the range of 25-60 $^{\circ}\text{C}$ on 2% (w/v) AIP mixtures, which were prepared as described for TEM and AFM measurements and incubated for 1 h to complete sol-gel transition prior to analysis. The total volume of the sample was 250 μL , and a PP25-SN17979 measuring device with a diameter of 25 mm was used for rheology measurements. The measuring distance was determined as 0.5 mm. Time sweep analysis was carried out at elevated temperatures under 10 rad/s angular frequency and 0.1% strain magnitude. The heating

rate of the sample was $10\text{ }^{\circ}\text{C min}^{-1}$ with linear ramping. An Anton Paar MCR-301 Rheometer was used for the analysis. A solvent trap included with the instrument was used to maintain a humid environment and prevent the drying of the sample during measurement. Measurements are reported as average of the three repeats.

2.2.14 Atomic Force Microscopy

For the AFM sample preparation, the 4% (w/v) coassembled AIP gel at around 7, AIP-1 gel at pH 5 and AIP-2 gel at pH 10 were diluted up to 0.05% (w/v) concentration using distilled water. The diluted samples were dropped on the cleaned silicon wafer and air-dried at room conditions. The nanoindentation of the samples were carried out the optimized AFM system and the developed method in the light of the previous study.[295] Double pass force-distance method was applied for the measurements and initially the topography imaging was performed in non-contact AFM mode. During the second pass, the cantilever was lifted a few nanometers and the sample was oscillated using a piezoelectric material. The oscillation signal was obtained from a function generator (DS345, SRS) at 2 kHz with nominally 5 nm indentation. The cantilever was calibrated on a silicon wafer prior to the nanoindentation measuring the spring constant of cantilever, and transfer function for deflection to photodiode current response. The force-distance data was collected using an auxiliary digitizing oscilloscope during the measurements. Then, a custom program was used to interpretation of the force-distance data into the histograms of mechanical properties. Each force-distance curve was divided into approach and retraction parts. The adhesion forces, applied maximum forces and the contact slopes were also determined. AFM nanoindentation measurements were performed using a commercial microscope (MFP3D, Asylum Research) which was also integrated to an optical light microscope.

2.2.15 *In Vitro* Studies

Human umbilical vein endothelial cells (HUVEC) donated by Yeditepe University, Istanbul, Turkey were purified according to the protocol described previously[296]; and used for the *in vitro* cell culture studies. The immunostaining of the cells were carried out using specific markers for the characterization. The cells were cultured in 75 cm² polystyrene cell culture flasks with 10% fetal bovine serum (FBS), 2 mM L-glutamine and 1% penicillin/streptomycin containing Dulbecco's Modified Eagle medium (DMEM) during the maintenance.

Prior to the cell culture studies, the surfaces covered with the coassembled AIP nanofibers were prepared by mixing 50 μ L of 0.2% (w/v) AIP-1 and AIP-2 solutions prepared at neutral pH in water or collagen I as a positive control. The surfaces coated with the AIP nanofibers were air-dried at room conditions overnight; and then sterilized under UV light for 1 h. Before the cell culturing, the surfaces were washed with PBS to eliminate any unbound residue; and then the cells were cultured on the surfaces at the standard cell culture conditions for 24 h.

The cell adhesion test was conducted according to the similar protocol discussed previously[297] using serum-free DMEM supplemented with 0.05% (w/v) cyclohexamide and 4% (w/v) bovine serum albumin (BSA) with cellular density of 2×10^4 cells/cm². After 2 h culturing of the cells on the surfaces, PBS washing was applied to remove unbounded cells; and the adhered cells were stained with calcein-AM for the fluorescence imaging. The images taken from the at least four random frames on each replicate with 4 replicates for each group were used to quantify the adhered cell numbers on the surfaces.

Morphology and spreading of the cells at 2 h were also analyzed by fluorescently staining actin cytoskeleton with Phalloidin-TRITC and counterstaining cell nuclei with TO-PRO®-3 Iodide. For the cellular imaging a Zeiss LSM 510 confocal microscope was used. The images taken from the confocal microscope then used for the determination of cell diameter and area using Image J software from NIH.

The cellular viability on the surfaces covered with the coassembled AIP nanofibers or collagen I at a cellular density of 5×10^3 cells/cm² for 24 h, was determined via calcein staining of the viable cells for 24 h. The quantification of the viable cell number was performed similar to the adhesion test. The morphology of the viable cells on the surfaces at 24 h were also analyzed using the same staining procedure with the spreading assay.

The cellular proliferation on the coassembled fibers and bioactive coating was also quantified via Click-iT™ EdU with 2.5×10^3 cells/cm² cell density. After 12 h incubation of the cells on the surfaces; EdU (5-ethynyl-2'-deoxyuridine) was added into the cell culture media, and the incubation was continued for another 48 h. EdU incorporates into DNA during S phase of the cell cycle, and enable us to detect the proliferation cells due to the binding of Alexaflour-488 conjugated azide group containing substance.

2.3. Results and Discussion

2.3.1 Synthesis and Characterization of AIPs

Two oppositely charged short amyloid-inspired peptide sequences including Ac-EFFAAE-Am (AIP-1) and Ac-KFFAAK-Am (AIP-2) (Figures 2.2) coassemble into amyloid like nanofibers and supramolecular architectures upon mixing at around pH 7 in water. The design of these peptide molecules were inspired by the noncovalent

interactions between amyloid peptides and the structural motifs found in native amyloid protein aggregations assemblies[298]. To increase electrostatic interactions between the peptide molecules and control the coassembly, the charged –Glu and –Lys residues at the N and C terminals of the AIP-1 and AIP-2 peptides were used, respectively. In addition, hydrophobic domain of the AIP-1 and AIP-2 molecules supported the coassembly by hydrophobic[299] and π – π interactions[300], which are commonly found in amyloid structures[301].

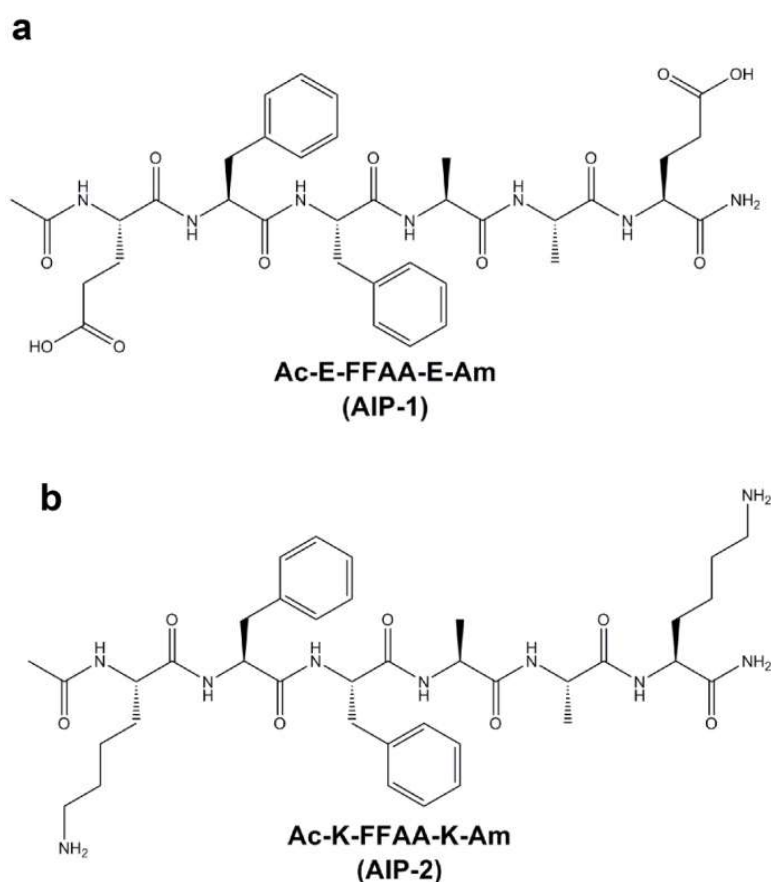


Figure 2.2 Chemical representation of AIP-1 (a) and AIP-2 (b) peptides

AIP-1 and AIP-2 peptide molecules were synthesized via Fmoc-solid phase method.[184] The products of the synthesis were characterized via Liquid Chromatography (LC)-Mass Spectroscopy (MS). LC histograms of the peptides

showed that the purity of the molecules were higher than 90%. MS spectra also showed the successful synthesis of the molecules using this technique (Figure 2.3).

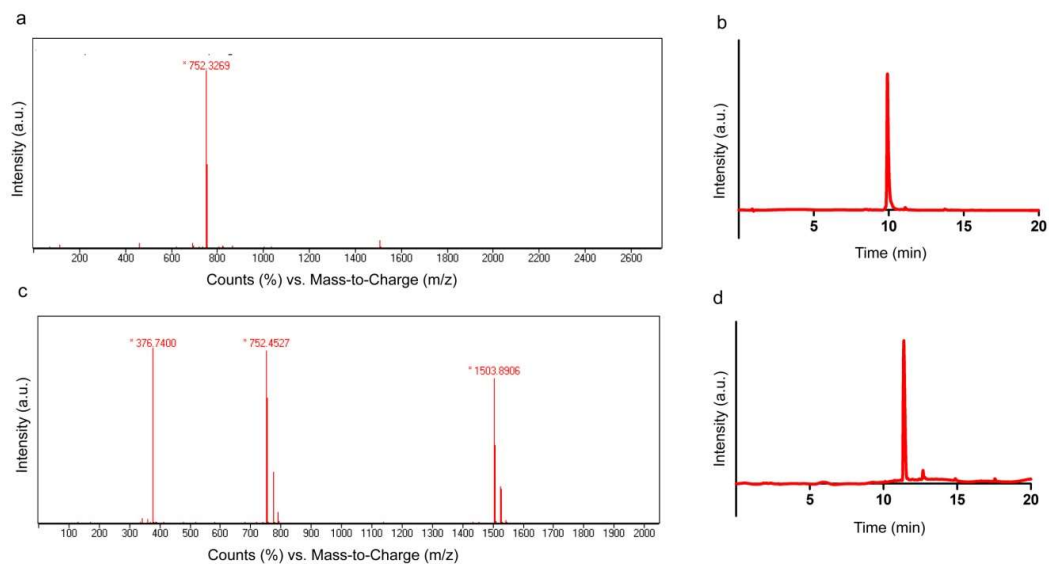


Figure 2.3 a) AIP-1; $[M-H]^-$ (calculated): 752.33, $[M-H]^-$ (observed): 752.33. b) RP-HPLC chromatogram of the AIP-1, the change of response units with respect to time at 220 nm. c) AIP-2; $[M+H]^+$ (calculated): 752.44, $[M+H]^+$ (observed): 752.45, $[2M+H]^+$ (calculated): 1503.88, $[2M+H]^+$ (observed): 1503.89, $[M/2+H]^+$ (calculated): 376.22, $[M/2+H]^+$ (observed): 376.74. d) RP-HPLC chromatogram of the AIP-2, the change of response units with respect to time at 220 nm.

2.3.2 Coassembly of AIPs into Nanofibers and Supramolecular Gels

Noncovalent interactions between short peptide molecules serve as a driving force for formation of co-assembled nanostructures under physiological conditions[302] and facilitate the growth of supramolecular fibrillar structures.[303, 304] In particular, positively-charged amino acids can interact with negatively-charged amino acids between peptide molecules, thereby playing an important role in mediating the peptide self-assembly process.[305, 306] AIP-1 and AIP-2 molecules consist of two Glu and

Lys residues, which carry -2 and +2 net charges at around pH 7 in water (Figure 2.2). The zeta potential measurements of the individual AIP-1 and AIP-2 solutions were also pointed their negative and positive charges in this condition (Figure 2.4).

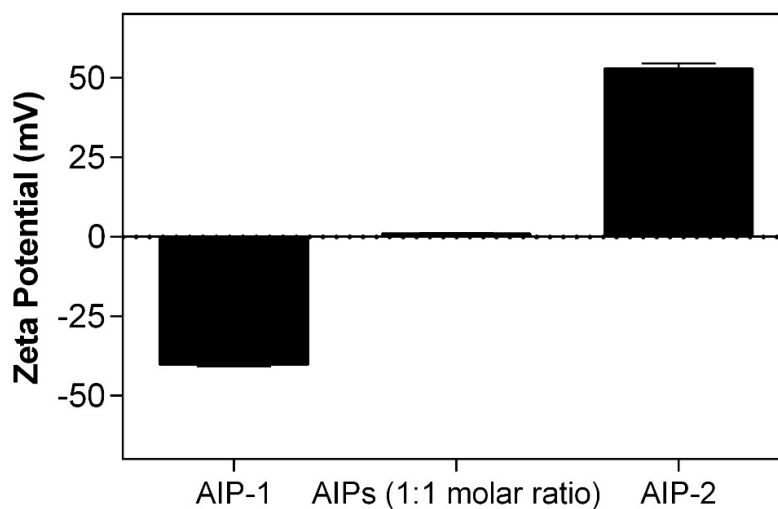


Figure 2.4 Zeta potentials of the AIP-1, AIP-2 solutions; and AIPs assemblies at pH 7.4 in water

Upon mixing peptide solutions with 1:1 molar ratio, the overall charge neutralization triggered coassembly of AIPs into supramolecular nanostructures (Figure 2.5). Above 2% (w/v) AIP concentration, these architectures can form self-supporting gels and three dimensional nanonetworks (Figure 2.6). Hydrophobic -FFAA- domain of AIPs also enhanced repetitive H-bonding, hydrophobic and aromatic interactions, which are commonly present in native amyloid aggregation.[301, 307, 308]

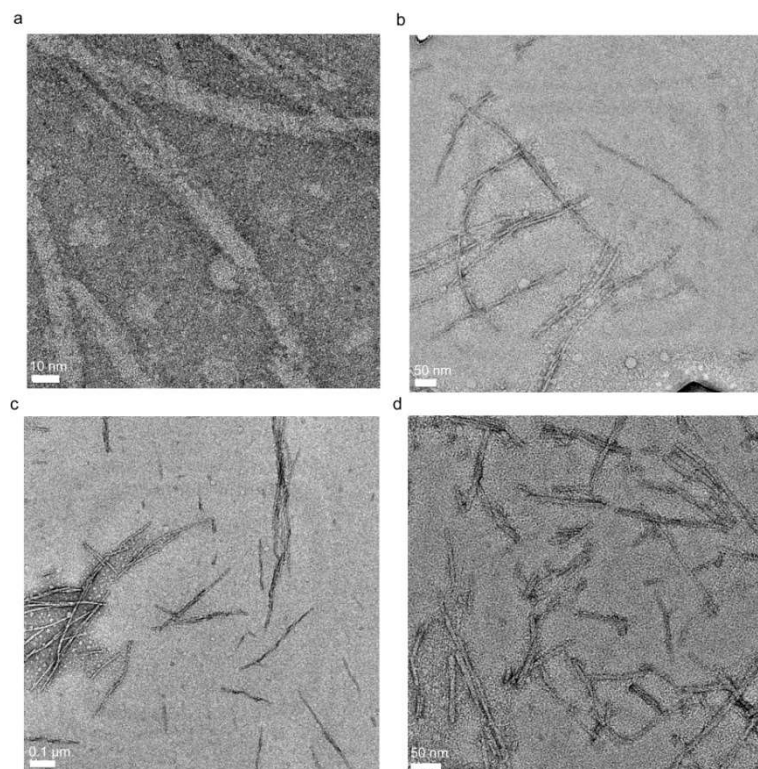


Figure 2.5 TEM images of the coassembled AIP nanofibers (scale bar 10 nm, 50 nm and 0.1 μm)

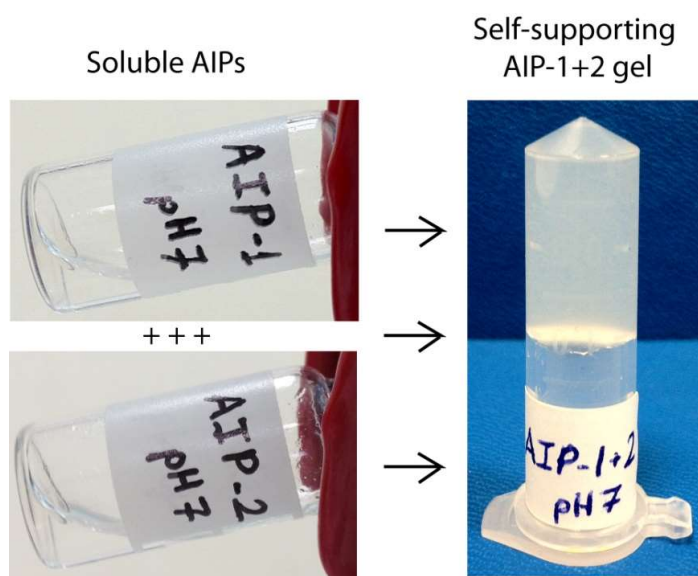


Figure 2.6 Self-supporting 2% (w/v) coassembled AIP gel (AIP-1+2) formed after mixing AIP-1 and AIP-2 solutions at pH 7.4 in water

2.3.2.1 Molecular Dynamics Simulation of AIP Coassembly

The coassembly behavior of AIP molecules due to the noncovalent interactions[252] was examined by molecular dynamics simulation. Visual Molecular Dynamics (VMD) was used to obtain the representative snapshots of the simulation carried for 70 ns given in Figure 2.7. Initially, AIP-1 and AIP-2 molecules at random coil structural organization were distributed within a defined volume. As simulation continued, AIP-1 had a tendency to form a dimer with AIP-2 changing their random coil configurations to β -sheet structures. When the same type of molecules were close to each other, the peptides couldn't form dimers and stayed at the random organization. At the end of the simulation, four dimers were formed out of five AIP-1 and five AIP-2 molecules; and only one AIP-1 and AIP-2 molecule stayed out of the β -sheet organization. Hence, it was revealed that the dimer formation of the oppositely charged AIP-1 and AIP-2 molecules could be the initial step of the peptide aggregation.

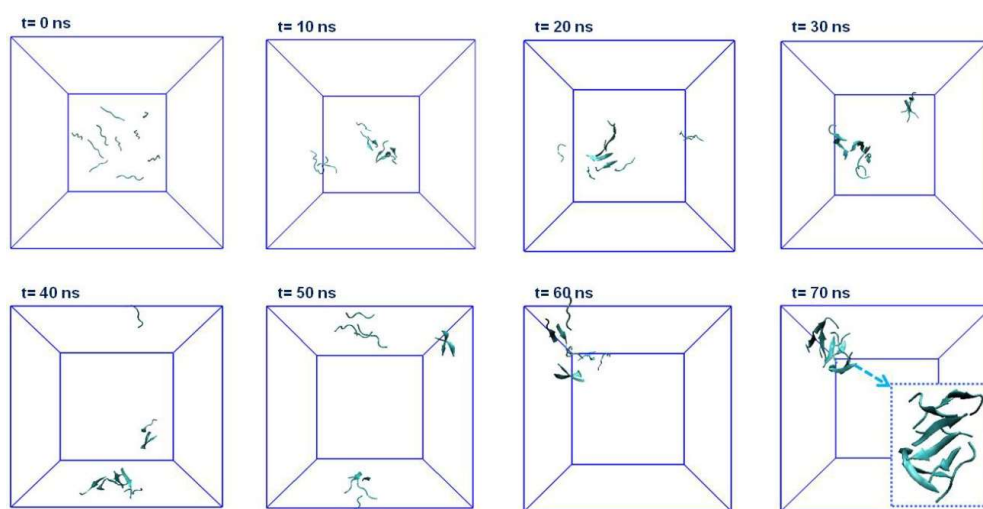


Figure 2.7 Selected snapshots of simulation of AIP-1 and AIP-2 peptides (five molecules per each peptide) obtained by 70 ns Molecular Dynamics Simulations

The total potential energy change within the system was also investigated during the simulation, it was seen that the final aggregated peptide structures obtained the lowest potential energy (Figure 2.8). The short range electrostatic interactions between positively and negatively charged amino acid residues were also determined via the simulation. The electrostatic potential energy between the amino acid residues decreased over time since the molecules aggregated into β -sheet structures.

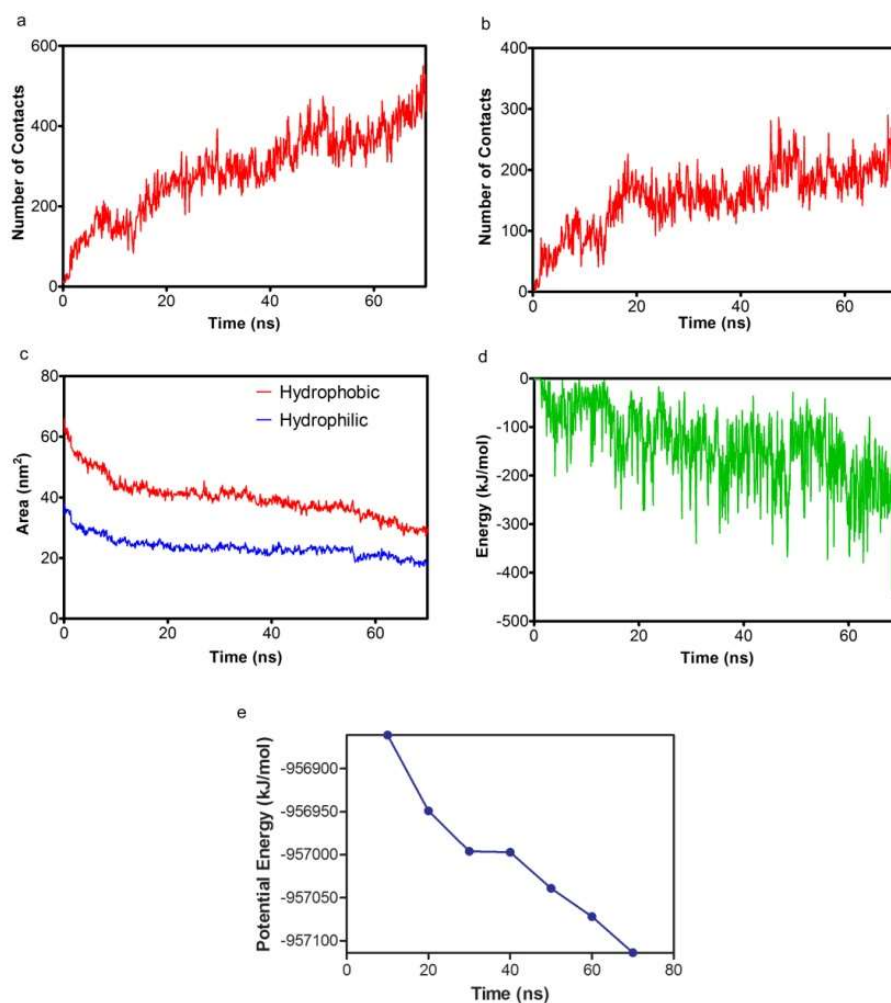


Figure 2.8 a) Hydrophobic core interactions (number of contacts) of AIP-1 and AIP-2 based on the residues of FFAA-FFAA, b) aromatic group contacts (number of contacts) of AIP-1 and AIP-2 based on the residues of FF-FF, c) Solvent Accessible

Surface Area (SASA), d) coulomb interactions between -Lys and -Glu residues of AIP-1 and AIP-2, and e) potential energy change of the system during simulation.

The secondary structure analysis of the simulation was carried out quantitatively using Dictionary of Secondary Structure of Proteins (DSSP) program[309] as a function of time. DSSP results indicated that the initial random coil configuration of the peptide molecules changed into β -sheet rich secondary structure containing different forms of β -sheets (Figures 2.9 and 2.10a) at the end of 70 ns. At the end of the simulation, the secondary structure distribution within the system was 60% of β -sheets, 30% of β -bridges and 10% of mixture of random coil and β -bends (Figure 2.9). Since the AIP dimer formation was the initial step of the aggregation as mentioned above, the structural organization of the aggregates analyzed in details and given in Figure 2.9.

Hydrogen bonds among the AIP-1 and AIP-2 molecules; and the interactions between the peptides and surrounding water molecules were also studied in complementary to the secondary structure analysis. During the aggregation of the peptides, the number of hydrogen bonds between peptides and water molecules continued to decrease while hydrogen bonding among the molecules resulting in formation of β -sheets increased (Figure 10b). Hydrophobic core interactions between AIP-1 and AIP-2 based on the residues of FFAA-FFAA; and aromatic group interactions between AIP-1 and AIP-2 based on the residues of FF-FF increased during the simulation and had an important effect on the aggregation behavior (Figures 2.8a and b).

Solvent accessible surface area (SASA) between the peptide and water molecules were also investigated to reveal interactions of the peptide molecules with the solvent during the aggregation process. It was determined that both hydrophilic and hydrophobic SASA decreased during the simulation from $\approx 38 \text{ nm}^2$ to $\approx 18 \text{ nm}^2$ and from $\approx 66 \text{ nm}^2$

to $\approx 29 \text{ nm}^2$, respectively (Figure 2.8c). This result was expected since the aggregation of the peptide molecules resulted in the increase of the number of contacts between the amino acid residues and decrease in the number of contacts with the water molecules.

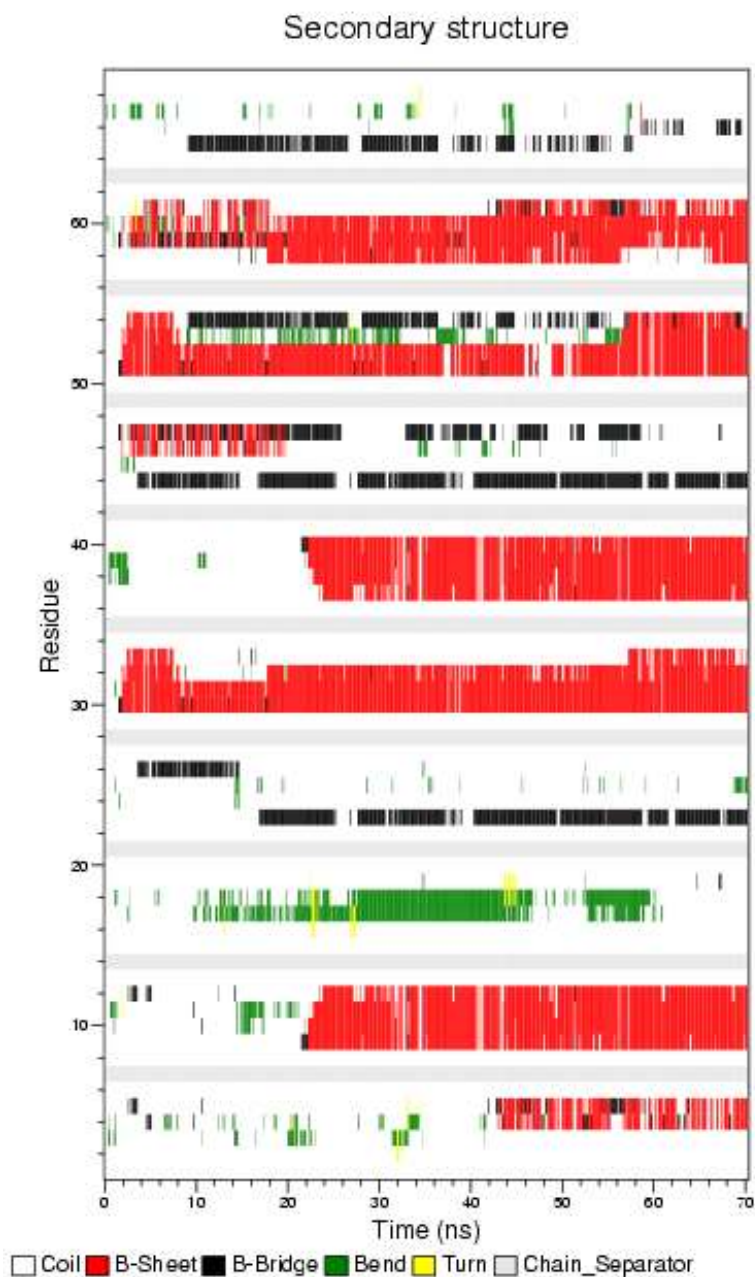


Figure 2.9 Residue based secondary structure change of peptides during simulation trajectory.

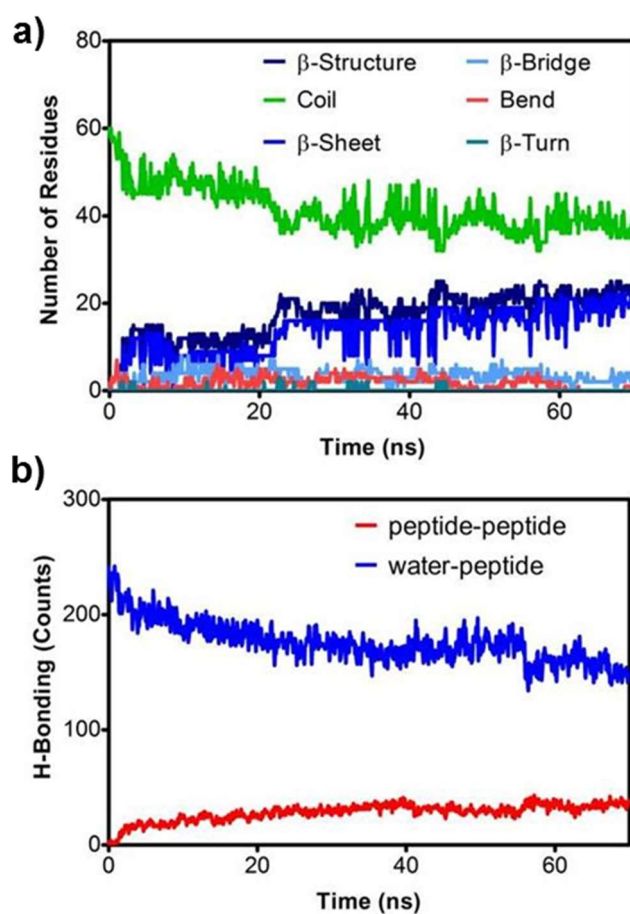


Figure 2.10 The secondary structure (a) and hydrogen bonding change (b) within the system during the simulation

2.3.2.2 Secondary Structure Analysis of AIP Assemblies

The secondary structure analysis of the AIP assemblies were also examined using the experimental techniques such as FTIR, circular dichroism (CD), and Congo red staining in complementary to the simulation results discussed above. The common secondary structure of the native amyloid aggregates is the cross β -sheet motif in which β -strands stay perpendicular to the fiber axis[310].

FTIR spectra of the coassembled AIP networks prepared at the different concentrations revealed a broad peak between $1600\text{-}1700\text{ cm}^{-1}$ in Amide I band region[311] as it was

seen in Figures 2.11 and 2.12. To determine the exact peak positions within the broad range, Gaussian fitting was applied to the data (Table 2.1); and the fitting procedure gave us the two significant peak positions at 1632 cm^{-1} and 1662 cm^{-1} . The peak position at 1632 cm^{-1} corresponded to the C=O stretching vibrations associated with the β -sheet secondary structure.[312, 313] On the other hand, the presence of a β -turn secondary structure was also observed at 1662 cm^{-1} .^[313] FTIR results showed us the β -sheet rich secondary structure of the coassembled AIP nanofibers which was also in parallel to the simulation and DSSP analysis.

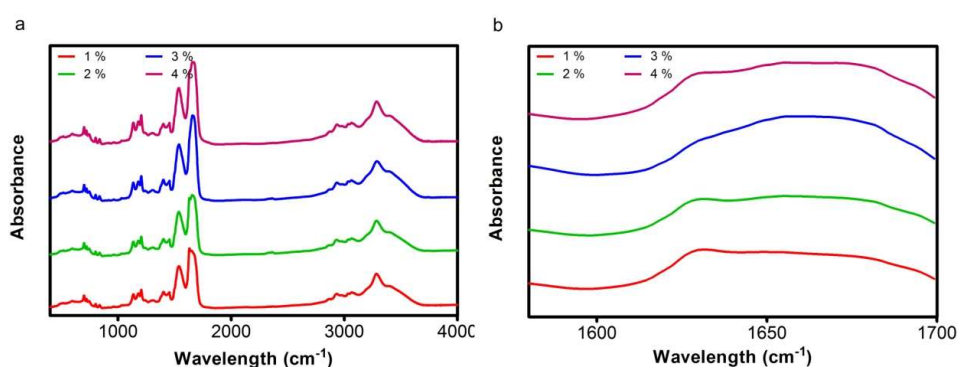


Figure 2.11 a) Secondary structure analysis of AIP-1+2 nanofibers at various concentrations of dried AIP-1+2 gels with FTIR. b) Detailed analysis of Amide I region ($1600\text{-}1700\text{ cm}^{-1}$)

Table 2.1 Gaussian fitting parameters of FTIR data of AIP-1+2 self-assembled peptide nanofibers (see Figure 3c) obtained from MATLAB fitting program

	A (height of the peak)	Mu (μ)	Sigma (σ)
Fit-1	1.1859	1632	13.9407
Fit-2	1.2557	1662	40.1168

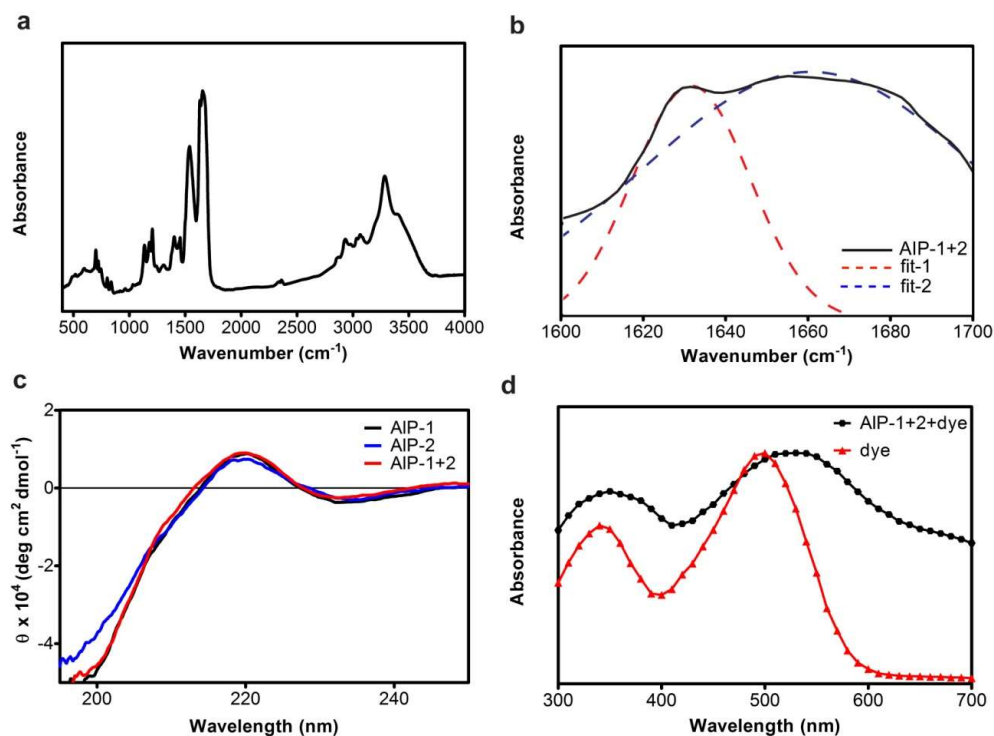


Figure 2.12 FTIR spectra of the coassembled AIP network (a, b) (--- Gaussian fittings), molar ellipticity of the coassembled AIP (AIP-1+2), AIP-1 and AIP-2 assemblies (c); and the absorbance spectra of congo red dye with and without AIP coassemblies.

In addition to the FTIR analysis of the AIP networks obtained from the dried samples, CD analysis of the AIP coassemblies was carried out in the solution phase to determine the secondary structure of the aggregates. As it was seen in Figure 2.12c, the CD spectrum of AIP coassemblies revealed a red-shift showed red-shift compare to the typical β -sheets spectrum with a maximum at 195 nm and a minimum at 216 nm[314]. Previously, it was shown that twisted β -sheet organization led to a red-shift in the peak positions of the common β -sheet signal[315, 316]; and the amount of such a red shift was correlated with the twisting degree of β -sheets[314]. Hence, the AIP coassemblies had a twisted β -sheet secondary structure organization with a maximum molar

ellipticity at around 220 nm and a minimum at 232 nm depending on twisting degree of β -sheets (Figure 2.12c). Similar to the CD spectrum of AIP assemblies, individual AIP-1 and AIP-2 assemblies which obtained via pH change of the solutions also revealed red shifted CD spectra with β -sheet signal (Figure 2.12c). In addition to FTIR and CD results, the AIP coassemblies bind to congo red; and that interaction resulted in the change of the maximum absorbance of the dye from 500 to 530 nm (Figure 2.12d). That also pointed us the β -sheet structural organization of the assemblies since congo red preferentially intercalated into β -sheet causing a shift in its absorbance maxima peak as shown previously.[317, 318]

2.3.2.3 Coassembly Kinetics of AIPs

To study the coassembly kinetics of AIP molecules at physiological conditions, AIP-1 and AIP-2 solutions were prepared at varying concentrations between 1% and 2% (w/v), and mixed at a molar ratio of 1:1 at the physiological conditions. Coassembly kinetics of the AIPs were monitored via addition of ThT, a small molecule[319, 320], which binds the β -sheets of the AIP aggregates and exhibits an increase in fluorescence emission intensity during coassembly (Figure 2.13). Time-dependent increase in fluorescence intensities were monitored using confocal fluorescent microscopy and normalized to maximum ThT intensity to analyze the peptide assembly process (Figure 2.14). This technique facilitates the analysis of turbid peptide solutions due to the formation of opaque supramolecular nanostructure networks. In addition, z-stacking within the AIP mixtures allowed tracking the changes in 3D fluorescence intensity and correlate this information to the formation of aggregates during the coassembly process.

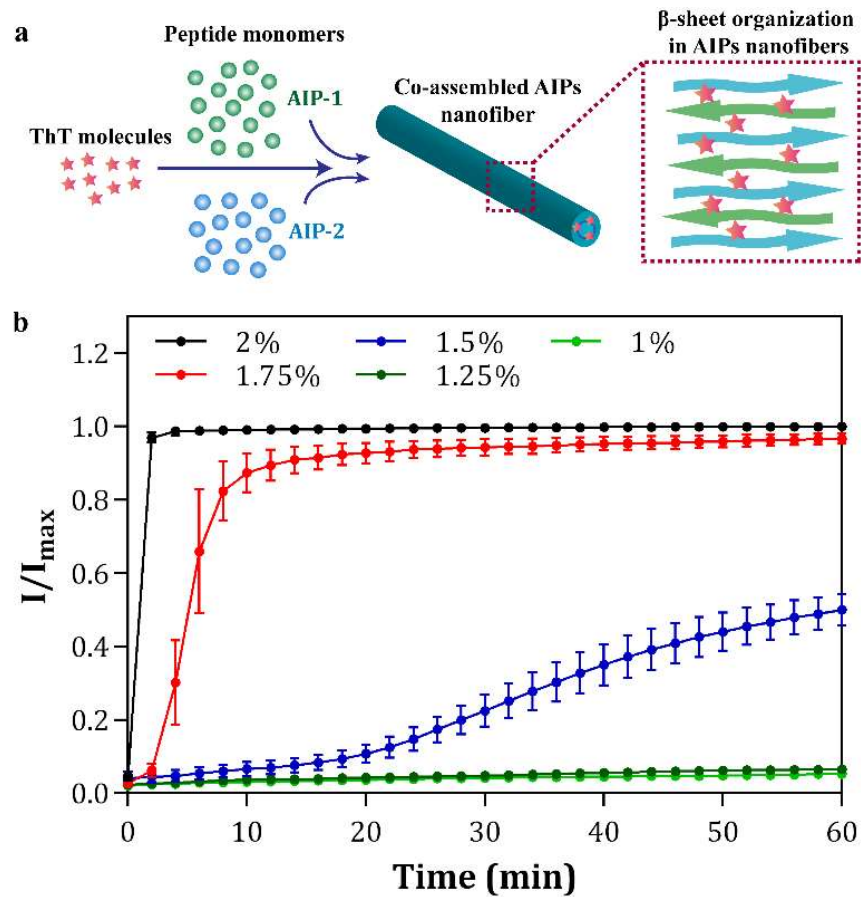


Figure 2.13 (a) A small fluorescent dye molecule; thioflavin T (ThT), is used as a probe for monitoring the coassembly of AIP-1 and AIP-2 molecules into nanostructures. (b) The normalized fluorescence intensity changes during the co-assembly process of the AIPs prepared at different peptide concentrations.

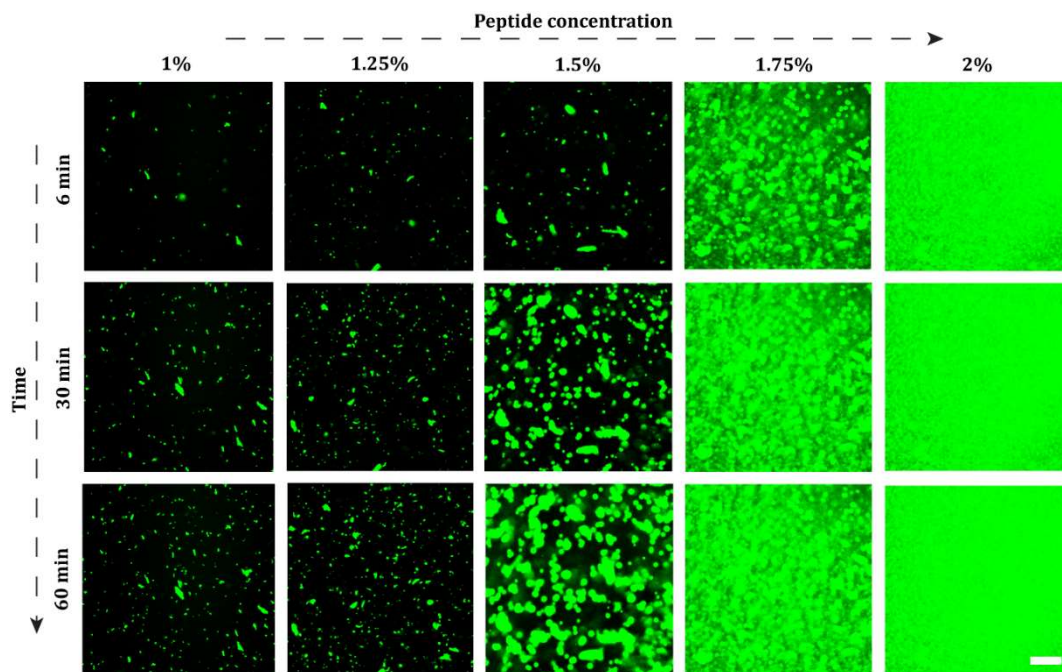


Figure 2.14 Time- and concentration-dependent co-assembly of oppositely charged AIPs at physiological conditions into supramolecular nanostructures. The aggregation kinetics of the AIPs were visualized using in situ confocal microscopy imaging during the coassembly process at different concentrations (all image scale bars are 200 μm)

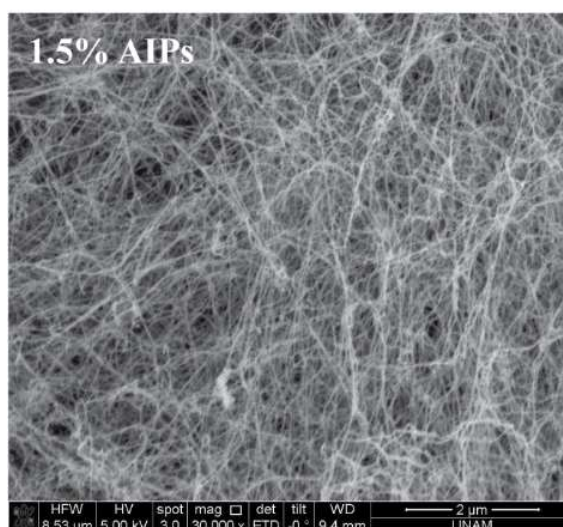
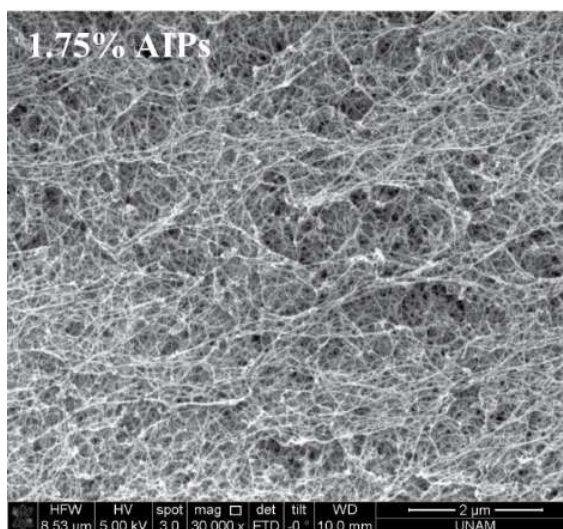
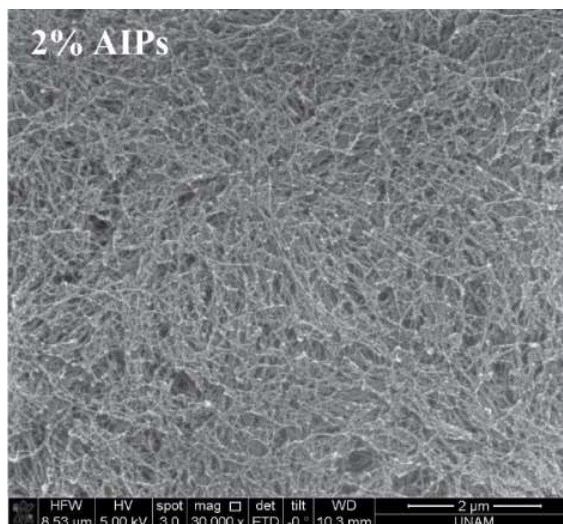


Figure 2.15 SEM images of the three dimensional nanofibrous 2%, 1.75% and 1.5% (w/v) AIPs networks coassembled for 1 h

AIPs showed different coassembly kinetics depending on the peptide concentration (Figure 2.13). Above 1.5% (w/v) concentration, the AIP mixtures rapidly self-assemble into supramolecular systems within 1 h. On the other hand, the coassembly process slowed down and did not reach to maximum fluorescence within 1 h for 1.25% and 1% (w/v) AIP samples. Although an initial delay of up to 20 min was observed in the aggregation of AIPs at the threshold concentration of 1.5% (w/v), this delay was followed by a rapid increase in self-assembly, which also failed to reach the rates observed in higher AIP concentrations after 1 h. In the literature, ThT binding assay has been used to determine the kinetics of the aggregation process and important parameters that effect the aggregation behavior of amyloids. It is known that higher initial concentrations increase the assembly kinetics and decrease the lag-time of the aggregation process in amyloid solutions.[321-323] In addition, growth curves associated with amyloid formation typically approximate a sigmoidal shape, in which the nucleation of the monomers is followed by their rapid aggregation into filamentous nanostructures.[324] AIP coassembly kinetics were overall similar to these displayed by native amyloid assemblies, as the peptide molecules were observed to form self-supporting three-dimensional networks (Figure 2.15) under sigmoidal-like formation kinetics over a concentration of 1.25%. Although initial nucleated aggregates have been detected via ThT binding for all concentrations of AIP mixtures (Figure 2.14), their coassembly kinetics reach to maxima within 1 h only for concentrations above 1.5% (w/v).

Turbidity assay was also used to follow the self-assembly process and analyze peptide aggregation kinetics[325, 326] in addition to the ThT binding assay. AIP mixtures were prepared as described for the ThT binding assay and their turbidities at 313 nm

were normalized to their maximum absorbance to determine the time-dependent assembly of the peptide networks (Figure 2.16). Turbidity kinetics of the AIPs showed a similar pattern with the ThT binding kinetics, exhibiting a time-dependent increase within 1 h at concentrations over 1.25% (w/v). A rapid increase was also observed in the turbidity of the 1.5% (w/v) sample after 20 min, supporting our ThT results. Although two different assays have been utilized for analyzing the behavior of AIP mixtures, both ThT binding and turbidity assays overall suggest that the AIPs exhibit amyloid-like aggregation and sigmoidal assembly kinetics above a concentration of 1.25% (w/v).

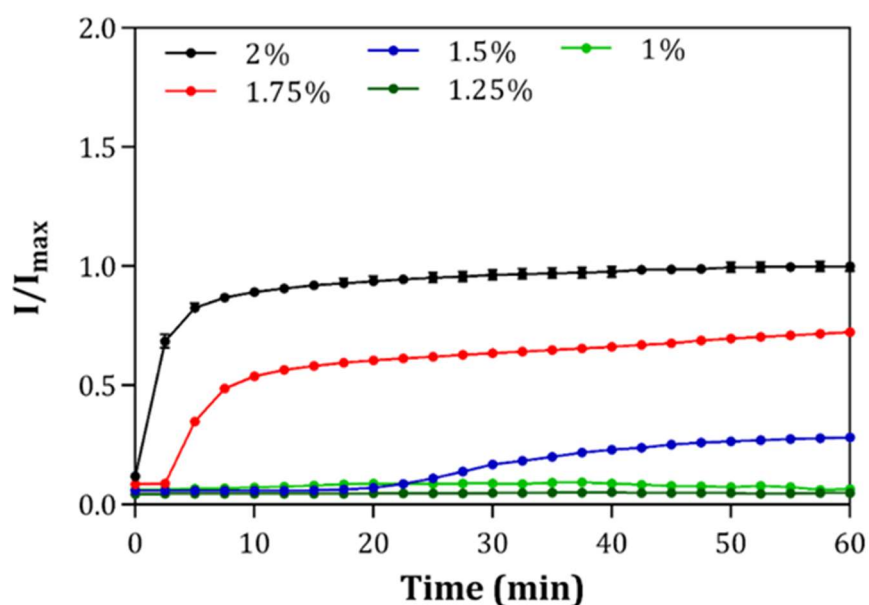


Figure 2.16 Turbidity of AIP solutions at different concentrations was monitored as optical density at 313 nm under physiological conditions. Increase in the turbidity of the solutions correlate with nanostructure formation and sol-gel transition. AIP-1 and AIP-2 molecules rapidly self-assemble into the nanostructures a concentration over 1.25% (w/v) concentration within 1 h.

As a control experiment, turbidities of AIP-1 and AIP-2 solutions were also measured separately at 313 nm and normalized to the maximum absorbance of the curves; however, no increase in solution turbidity could be detected when the peptide components were not mixed with one another (Figure 2.17).

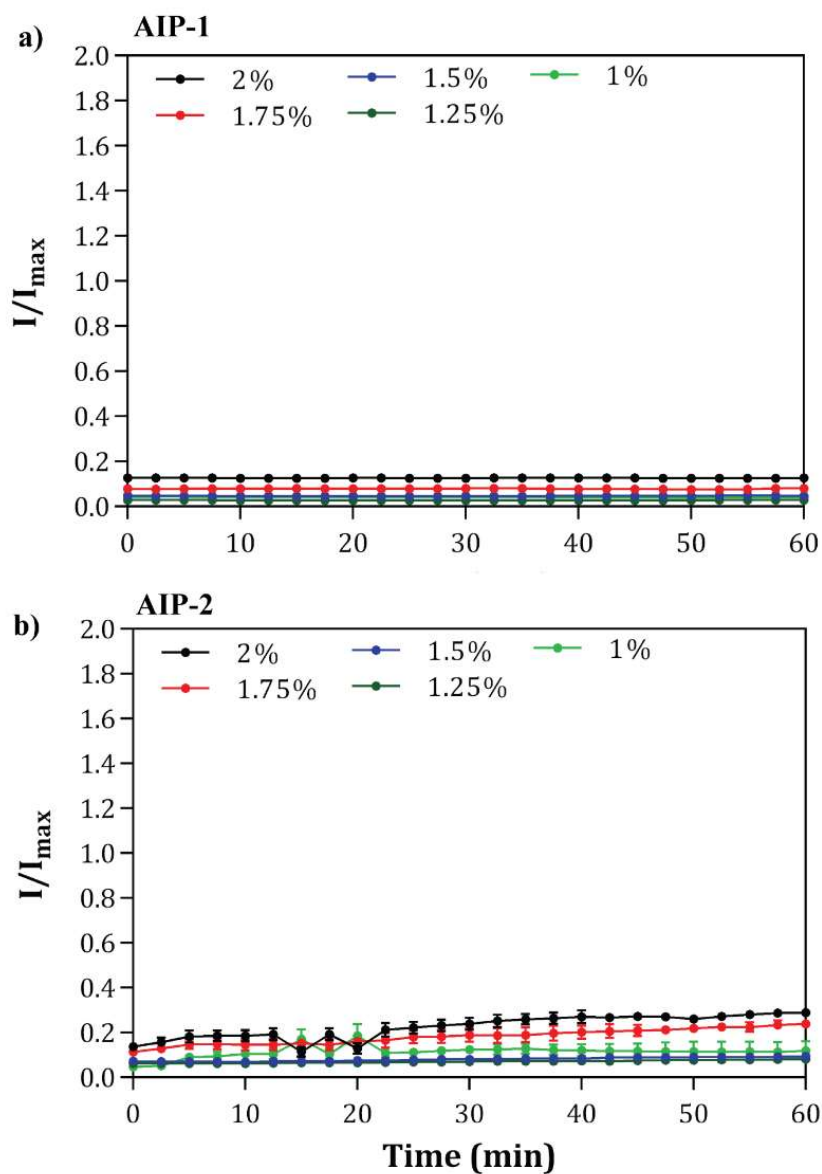


Figure 2.17 Time dependent turbidity change of (a) AIP-1 and (b) AIP-2 at 313 nm, the peptide solutions were prepared at the different peptide concentrations.

Fragmentation of amyloid aggregates may accelerate the assembly kinetics of fibril formation, since amyloid fibril ends behave as nucleation point for fiber elongation. The analogy between enzymatic reactions and amyloid aggregation has previously been underlined in the literature.[322] Sonication is a way to break the nucleated amyloid aggregates via sound waves, and the technique was used to enhance the spontaneous fibril formation of amyloid peptides.[327]

In this study, sonication was applied for different time periods after 1% (w/v) AIP-1 and AIP-2 solutions were mixed at around pH 7 in water, and the turbidity changes exhibited by AIP mixtures were then monitored at 313 nm for 1 h (Figure 2.18a). Although 1% (w/v) AIPs solution was not observed to form three-dimensional networks within 1 h in both ThT binding and turbidity assays; turbid AIP mixtures were obtained at this concentration when the samples were sonicated. In addition, short term sonication of 1% (w/v) AIPs before the turbidity study enhanced the coassembly process, and no change was observed on the turbidity of the solutions within 1 h (Figure 2.18b). In addition to the effects of monomer concentration on coassembly kinetics, fragmentation via sonication also enhanced the formation of supramolecular AIP nanostructures at physiological conditions, which is in agreement with the previous records on amyloid aggregation behavior.

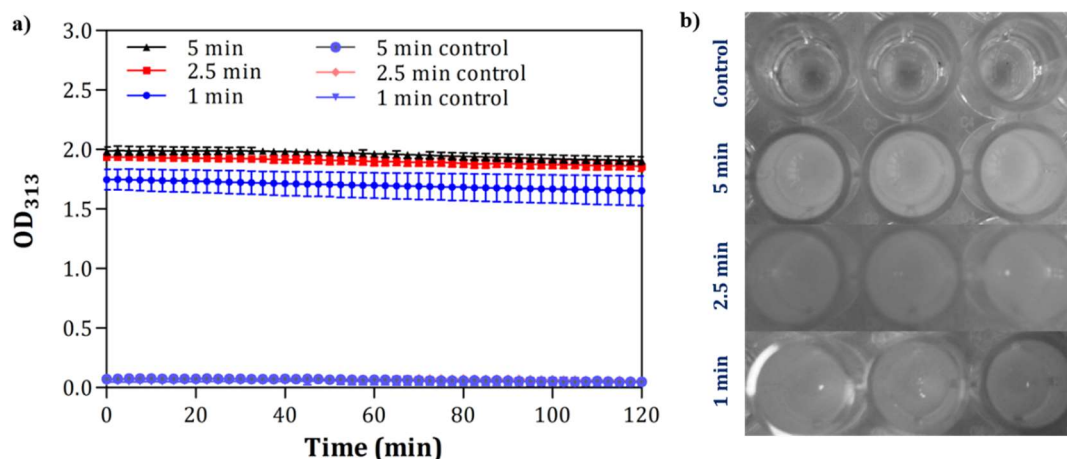


Figure 2.18 Sonication enhances turbidity of 1% AIPs compared to the control groups; a) time dependent turbidity change and b) 1% AIPs solution images after the sonication was applied for different time periods (1, 2.5 and 5 min) (Control groups were also 1% AIPs which were incubated for 5, 2.5 and 1 min without sonication prior to the analysis.)

2.3.2.4 SAXS Analysis of AIP Nanofibers

To characterize structural properties of the peptide nanostructures, AIP mixtures were incubated for 1 h under physiological conditions in a 2.5 mm-thick, Kapton-walled sample cell and analyzed by SAXS to determine their scattering profiles. Scattering intensity (I) was recorded as a function of the magnitudes of scattering vectors q (\AA^{-1}) of the co-assembled AIPs at different concentrations (Figure 2.19), and scattering data in the Guinier region was used to determine the radius of gyration for the co-assembled AIP nanostructures (Figure 2.19). Data fitting and processing were performed by using IGOR Pro 6.3[290], and the data were best-fitted to a combined model defined by the polydisperse core-shell cylinder (PCSC)[287] and decoupling flexible cylinder (FCPR)[288, 289] models (Figure 2.1 and 2.20).

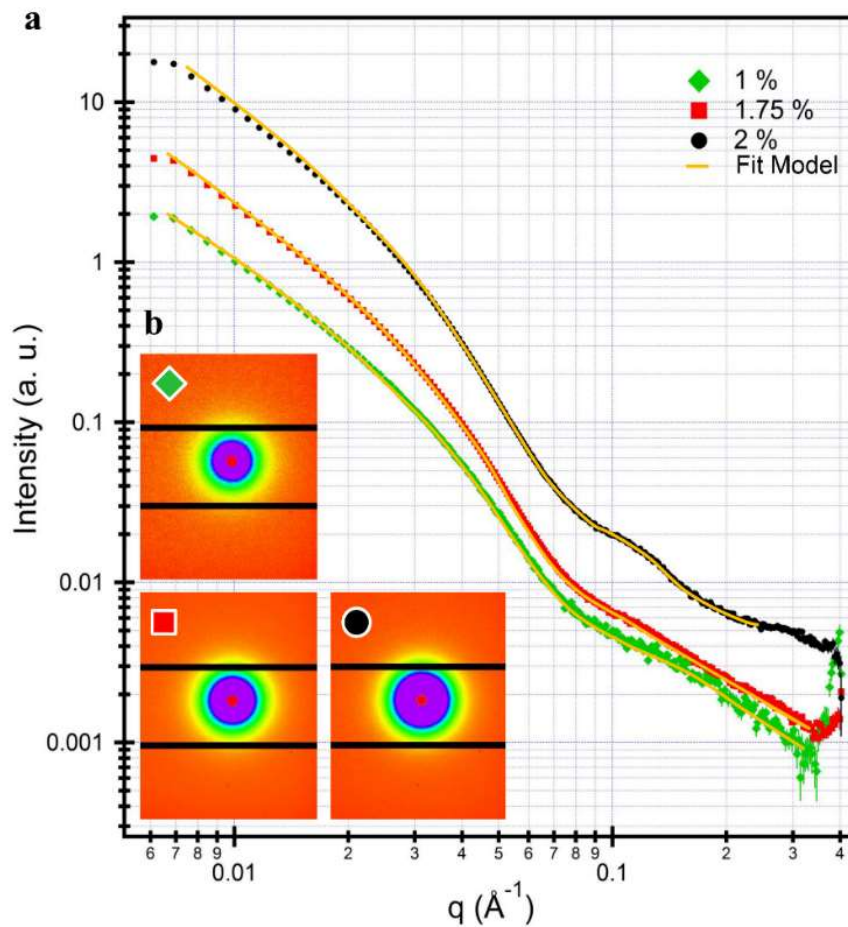


Figure 2.19 (a) Small angle X-ray scattering (SAXS) profiles and 2D patterns (b) of coassembled 2%, 1.75% and 1% (w/v) AIP nanostructures after 1 h.

The obtained structural parameters are shown in Table 1. The electron density of core section was higher than the shell, possibly due to the tendency of the hydrophobic domains of AIPs (-FFAA-) to stay in the inner region of coassembled AIP nanofibers (Figure 2.20b). In addition, the shell region, consisting of hydrophilic -Lys and -Glu residues, provided a contact area with water molecules. The electron densities were also found to change repetitively at a periodicity of 3.1 nm across the longitudinal axis of the fiber. π - π stacking of aromatic residues and twisted β -sheet organization of AIPs in the fibers may cause this periodicity exhibited by electron density. The nanofibrous

organization of the coassembled AIP supramolecular nanostructures were also observed using AFM imaging of peptide networks dried on Si wafers, (Figure 2.20c) and are consistent with the model developed in the light of the scattering data.

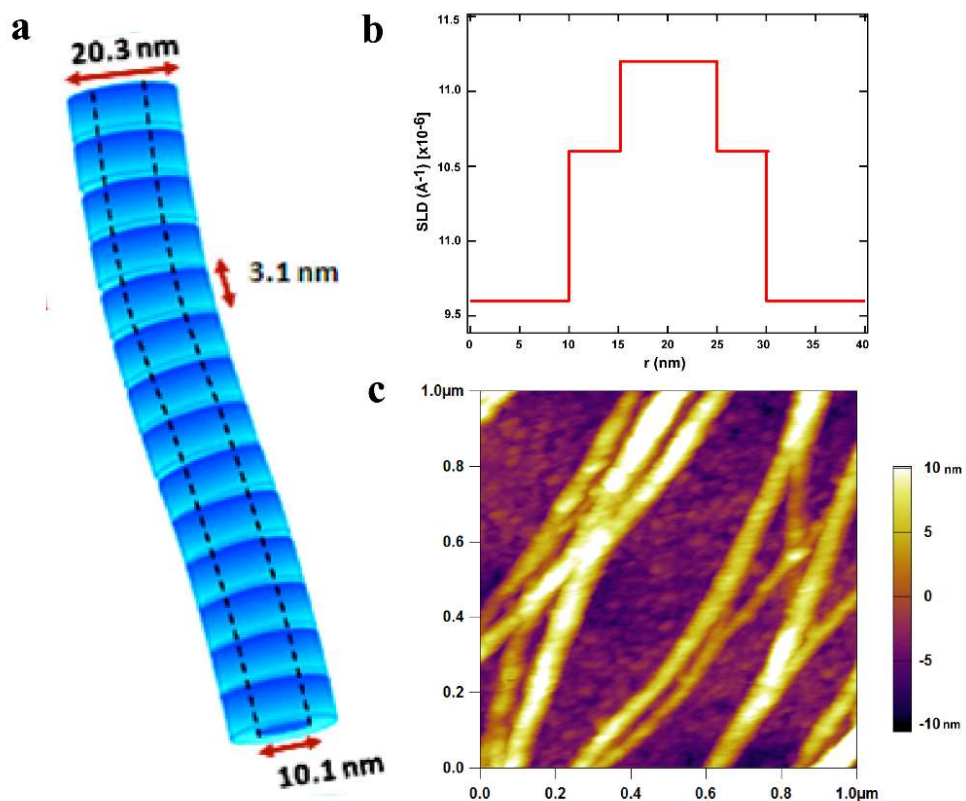


Figure 2.20 The proposed structural model for co-assembled AIP nanostructures (a) and (b) the electron density distribution on the nanofiber, (c) AFM image of the coassembled AIP nanofibers and their bundles dried on a Si wafer

Table 2.2 Fitting results of SAXS data of coassembled AIP nanostructures at different concentrations in water at neutral pH.

Model	Parameters	1%	1.75%	2%
PCSC	R_p , core radius (Å)	47.6 ± 0.60	51.6 ± 0.80	48.7 ± 0.70
	Radial shell thickness (Å)	55.7 ± 0.50	53.5 ± 0.90	52.3 ± 0.70
	Radial polydispersity, sigma	0.9	0.8	0.6
	H_p , core length (Å)	23.9 ± 0.10	24.0 ± 0.10	21.6 ± 0.10
	Face shell thickness (Å)	3.2 ± 0.10	3.1 ± 0.10	4.5 ± 0.10
	R_1 , shell radius (Å)	103.3 ± 0.80	105.1 ± 0.90	101.2 ± 0.50
	H_1 , shell length (Å)	30.3 ± 0.10	30.2 ± 0.10	30.6 ± 0.10
	SLD core (Å ⁻²)	10.8×10^{-6}	11.1×10^{-6}	11.3×10^{-6}
	SLD shell (Å ⁻²)	10.1×10^{-6}	10.2×10^{-6}	10.6×10^{-6}
	SLD solvent (Å ⁻²)	9.6×10^{-6}	9.7×10^{-6}	9.6×10^{-6}
FCPR	L, contour length (Å)	420.2 ± 0.90	430.1 ± 0.30	434.7 ± 0.40
	b, Kuhn length (Å)	60.6 ± 0.10	60.5 ± 0.10	61.3 ± 0.20
	R, radius (Å)	103.3 ± 0.80	105.1 ± 0.90	101.2 ± 0.70
	Polydispersity of radius	3.2	5.6	4.3
	SLD cylinder (Å ⁻²)	10.2×10^{-6}	11.6×10^{-6}	11.9×10^{-6}
	SLD solvent (Å ⁻²)	9.7×10^{-6}	9.5×10^{-6}	9.6×10^{-6}

* Core radius = R_p , core length = H_p (the mean core radius is R_o); the shell radius and shell length incorporate the dimensions of the bare particle ($H_1 = H_p + 2 \times$ face thickness and $R_1 = R_p +$ radial thickness). Sigma is equivalent to the standard deviation of the log-normal distribution.

In situ SAXS measurements were also performed on a 2% (w/v) AIP mixture to monitor its structural organization during the co-assembly process. Experiments were performed at this concentration due to the rapid co-assembly kinetics of the 2% (w/v) AIP mixture, which would allow the observation of both short- and long-term changes in the peptide network. The first scattering profile was collected immediately after ($t \sim 30$ s) the mixing and transfer of AIPs into capillary tubes, while following measurements were acquired every 30 s within the first 5 min. Scattering profiles were then analyzed to determine whether a structural or organizational transition had occurred during the coassembly process (Figure 2.21a, b). All scattering profiles collected within the first 5 min were best-fitted to the same structural model given in Figure 2.1, and the results showed that AIP-1 and AIP-2, when mixed above the critical sol-gel transition concentration at pH 7 in water, are able to coassemble into nanofibers without any transition from another structural organization within the collected time intervals. In addition, no structural or organizational changes were observed on the TEM images of the AIP nanostructures prepared from the dilutions of 2% co-assembled AIPs for 15 min and 1 h, further supporting our SAXS results (Figure 2.21c, d).

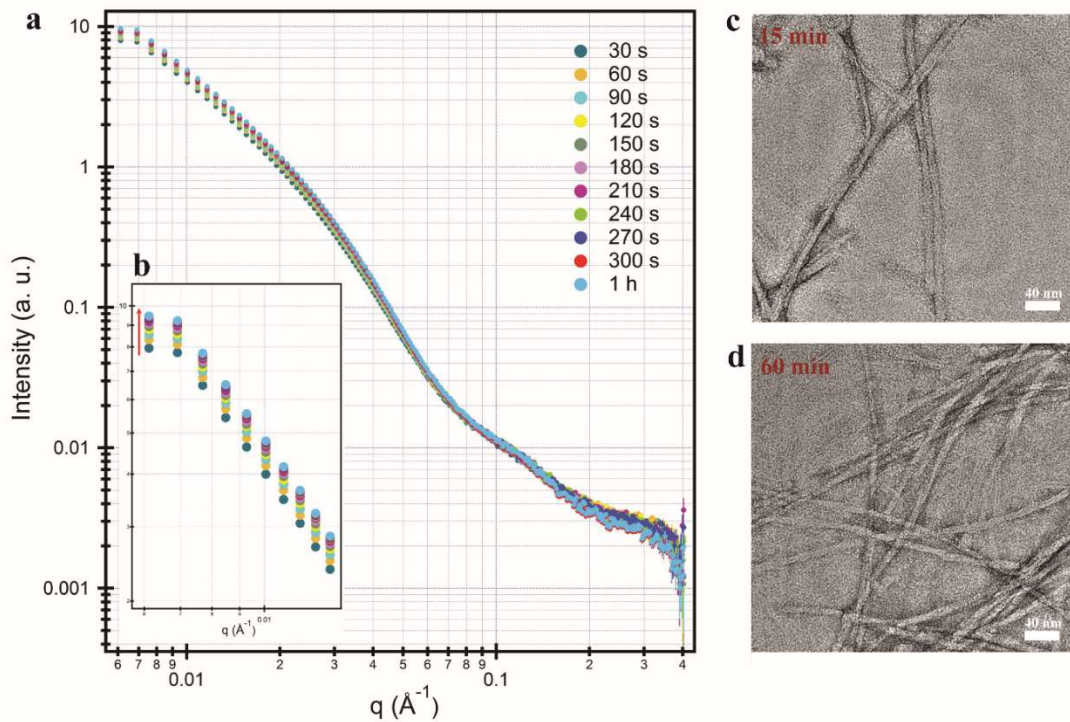


Figure 2.21 a) In situ SAXS measurements of 2% AIPs in water at neutral pH during coassembly, and (b) TEM images of the nanofibers prepared from the dilutions of coassembled 2% AIPs for 15 min (c) and (d) 60 min

Temperature-dependent structural stability of co-assembled 2% (w/v) AIP nanostructures for 1 h was also investigated by SAXS analysis performed at elevated temperatures between 25 to 64 °C (Figure 2.22). In addition to the scattering profiles analysis of peptide assemblies at different temperatures, which were best fitted to the flexible core-shell cylinder model described above, fractal mass analysis was performed to probe the AIP nanostructures in high q regimes (Figure 2.22b). The scattering exponent α can be estimated from the slope of a $\log I(q)$ vs. $\log q$ curve derived from scattering data.[328] In a high q regime; α is equal to the mass fractal dimension, D_m , revealing the degree of compactness of the scattering object.[271, 328] For semi-ordered structures, D_m has a value between 1 to 3[329], and higher D_m values

indicate the denser structural organization of the co-assembled peptide aggregates.[305] Hence, it was expected to obtain loose nanostructures and lower D_m values are expected to be observed at higher temperatures, which weaken noncovalent interactions between the AIP molecules. However, D_m values of 2% (w/v) co-assembled AIP nanostructures changed only slightly up to 61 °C, and a rapid decrease was observed above this temperature (Figure 2.22b).

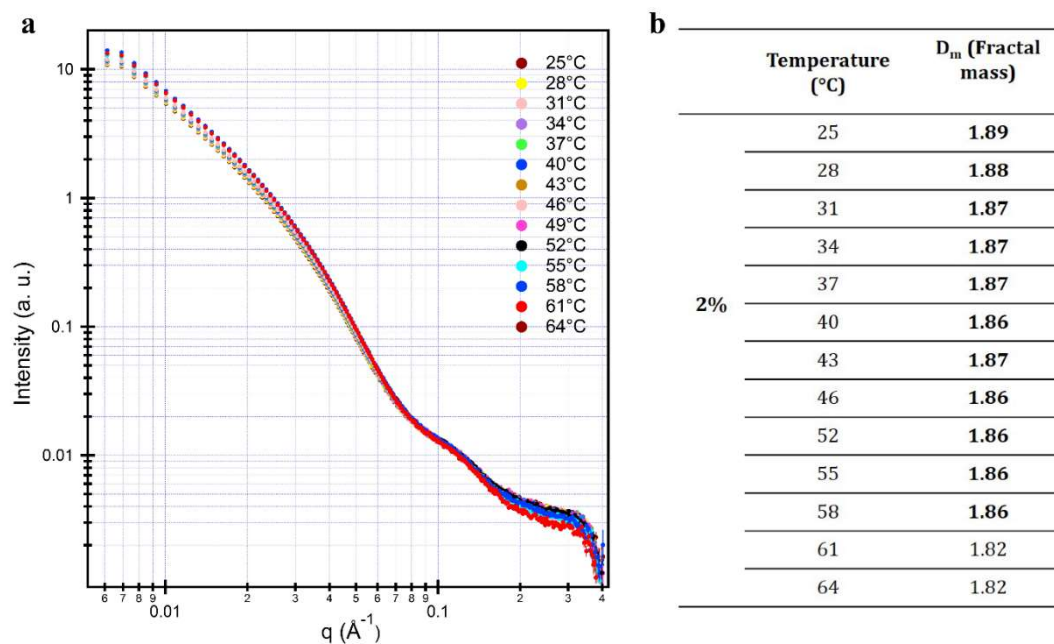


Figure 2.22 a) SAXS profiles of 2% coassembled AIP nanostructures at different temperatures. (b) Increase in temperature did not disturb the organization of the AIP nanofibers and the density of the nanofibers slightly changed for elevated temperatures

2.3.3 Viscoelastic Properties of AIP Supramolecular Gels

Amyloid peptide assemblies reveal high elasticity modulus and mechanical strength due to their intriguing hierarchical organization due to noncovalent interactions[257, 330]. The viscoelastic behavior and mechanical properties of AIP assemblies prepared at 4, 3, 2, 1 and 0.5% (w/v) AIPs concentration were also examined to understand the gel formation characteristics using oscillatory rheology in the linear viscoelastic regime (LVR). This technique enabled us to determine storage (G') and loss modulus (G'') which are the stored and lost energy during deformation of the sample under dynamic mechanical forces. As gelation occurs, new elastic chains within the samples are formed and led to decrease in the damping factor which is the ratio of loss to storage modulus.

In complementary to the coassembly kinetics studies results obtained via ThT and turbidity assays, the weak gelation was observed below 2% (w/v) AIPs concentration as seen in Figure 2.23. Above this concentration, the supramolecular AIP assemblies revealed weak mechanical properties and viscoelasticity (Figure 2.23b). In addition above this concentration, the gelation rapidly occurred within few seconds of mixing; and equilibrium elastic moduli of the samples reached up to 200 kPa. To the best of our knowledge, no other study reported a similar elastic modulus for peptide gels formed coassembly of synthetic short peptides due to the non-covalent interactions. In addition, the peptide concentration within the supramolecular gels linearly correlated with storage moduli of the samples above 2% (w/v) concentration (Figure 2.23c). The linear dependence on the peptide concentration could be related with the newly formed elastically active nanofibers participating in gel formation. This was further verified

by inverse relationship between damping factor and initial peptide concentration (Figure 2.23d).

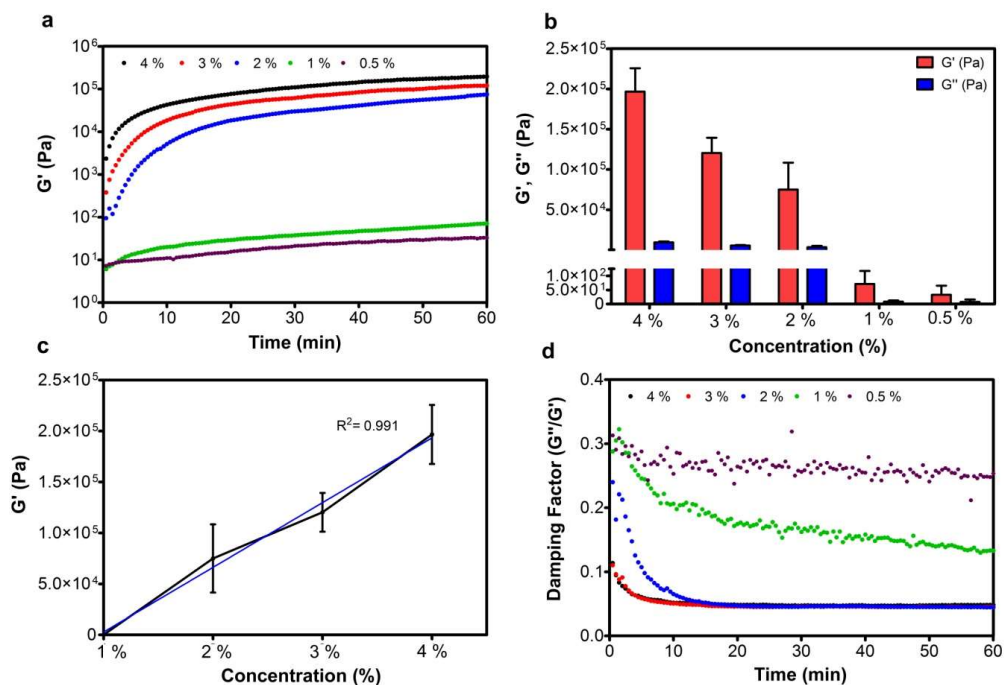


Figure 2.23 Time sweep analysis (a) and (b) equilibrium storage (G') and loss moduli (G'') of the AIP coassemblies c) Linear dependence of storage moduli of the AIP gels to concentration change at pH 7 d) Damping factor (G''/G') change of the gels prepared at different concentrations of at pH 7 for 60 min.

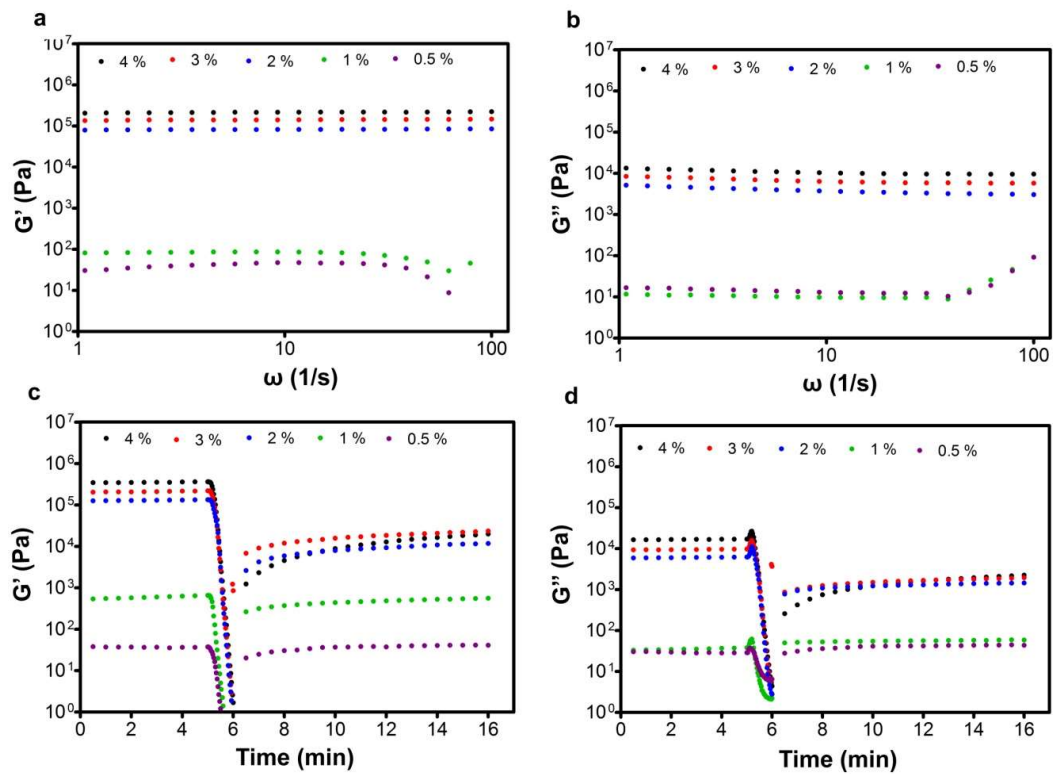


Figure 2.24 Frequency sweep (a, b) and thixotropic analysis (c, d) of the AIP coassemblies prepared at different peptide concentrations at pH 7 (Loss Modulus, ω : angular frequency)

Table 2.3 Recovery of 4, 3, 2, 1 and 0.5% (w/v) coassembled AIP gels after disruption of the networks with the increased strain

	G' (Storage Modulus) at t= 300 s	G' (Storage Modulus) at t= 960 s	Recovery (%)
0.5% (w/v)	38	41	107.9
1% (w/v)	658	563	85.6
2% (w/v)	134117	11836	8.8
3% (w/v)	219833	23647	10.8
4% (w/v)	363500	19987	5.5

In order to reveal superior mechanical properties of the coassembled AIP gels at pH 7, we also individually examined the viscoelastic behavior and gel formation capacity of its constituent peptides; AIP-1 and AIP-2. As it was discussed, AIP-1 and AIP-2 consists of negatively and positively charged amino acids at neural pH; hence pH change of the AIP-1 and AIP-2 solutions, separately resulted the charge screening and self-assembly of the molecules into supramolecular gels at pH 5 and 10, respectively.

The coassembled AIP system revealed rapid gelation kinetics compare to the individual AIP-1 and AIP-2 gels as seen in Figure 2.25a. This could be related with the presence of the additional electrostatic interaction between the molecules in complementary to the other non-covalent forces. On the other hand, the self-assembly of the AIP-1 and AIP-2 was triggered charge neutralization of the acidic or basic groups on the molecules hence the major non-covalent interaction between the building blocks were hydrogen bonding and π - π stacking. Hence, the coassembled AIP gels presented at least an order of magnitude higher equilibrium modulus than either of the AIP-1 and AIP-2 gels. Here, opposite charges within the network further contributed to the stability of elongating coassembled AIP nanofibers, which accounted for the strong mechanical properties (Figure 2.25b).

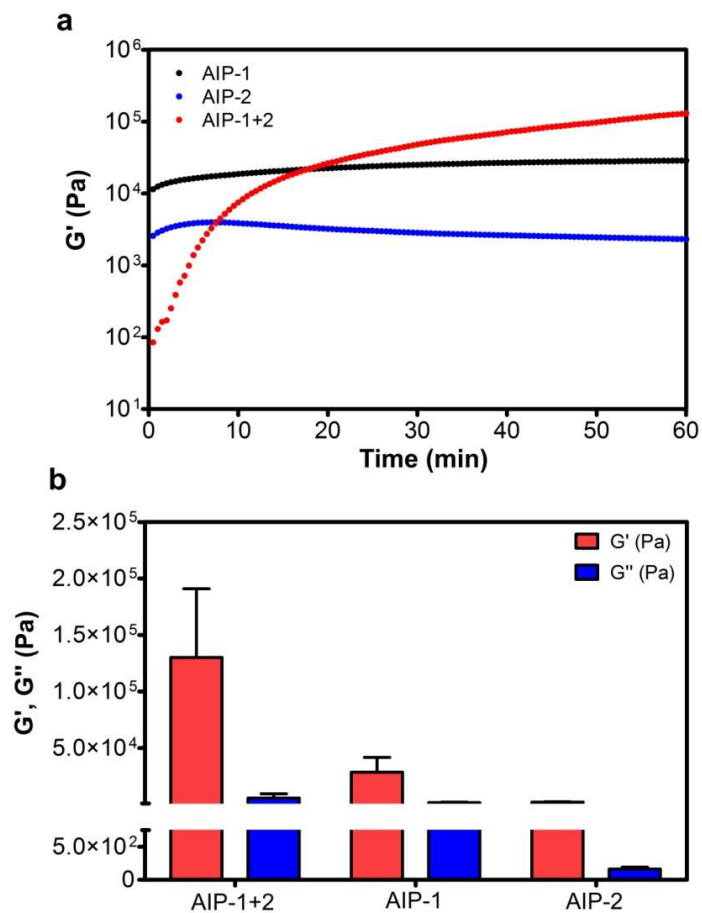


Figure 2.25 a) Time sweep analysis, and (b) equilibrium storage and loss moduli (G' , G'') of the 2% (w/v) coassembled AIP, AIP-1 and AIP-2 gels prepared at pH 7, 5 and 10, respectively

Bulk viscoelastic character of 2% (w/v) co-assembled AIP nanostructure network was also analyzed at elevated temperature range for 1 h to confirm out the temperature dependent SAXS experiments (Figure 2.26). The viscoelastic gel properties of the coassembled AIPs were found to be preserved in the 25-64 °C range, which agrees with the non-significant change in structural organization monitored via SAXS analysis in this temperature interval.

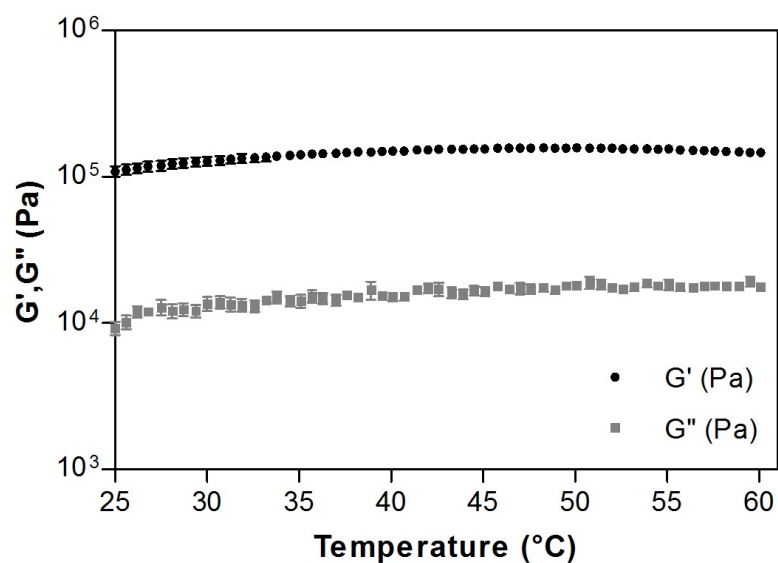


Figure 2.26 Effect of temperature on the mechanical stability of coassembled 2% (w/v) supramolecular AIP nanostructure network for 1 h (The co-assembled network preserved viscoelastic behavior at elevated temperatures)

2.3.4 Nanomechanical Properties of AIP Nanofibers

Since the supramolecular nanofiber gels were formed via the entanglement of the self-assembled AIP nanofibers, the resulting gels stability can be related with the mechanical properties of the individual AIP nanofibers and their bundles. Previously, in the literature it was shown that the mechanical strength of both interfiber and intrafiber adhesion was the important parameters to determine mechanical properties of the nanofibers and bundles[42]. Naturally, increased adhesion of the peptides within the self-assembled nanofibers improves strength and elastic modulus of an individual nanofiber; and increased adhesion between the nanofibers forming a bundle leads to formation of a more rigid supramolecular nanofiber gels due to the improved non-covalent interactions between the entangled bundles.[42]

We conducted nanomechanical characterizations of individual AIP-1 and AIP-2 nanofibers which were self-assembled due to the pH change and the coassembled AIP nanofibers using double-pass force-distance mapping technique allowing us to investigate the elastic properties of the materials at the nanoscale[295] in complementary to the oscillatory rheology analysis of the gels. Both approach and retraction of the AFM tip during force-distance measurements results the physical interactions of the tip with the self-assembled peptide nanostructures; and the effects such interactions pronounced on the force-distance curves. The physical interpretation of the force-distance data collected during the nanoindentation were used to determine adhesion and elastic modulus maps of the individual AIP-1 and AIP-2 nanofibers and the coassembled AIP nanofibers during approach (Figure 2.28) and retraction of the AFM tip (Figures 2.27b-c and 2.29c-f). In the maps, monolayer islands of peptides were also resolved on silicon, correlated with similar characteristics in the topography (Figures 6 and S11).

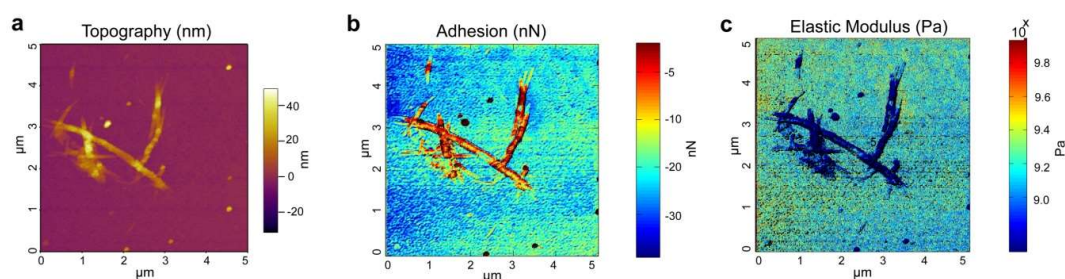


Figure 2.27 AFM topography images of coassembled AIP nanofibers (a); and adhesion force (b) and (c) elastic modulus maps of the nanofibers determined from the slope of force-distance curves (Modulus, Pa) during retraction

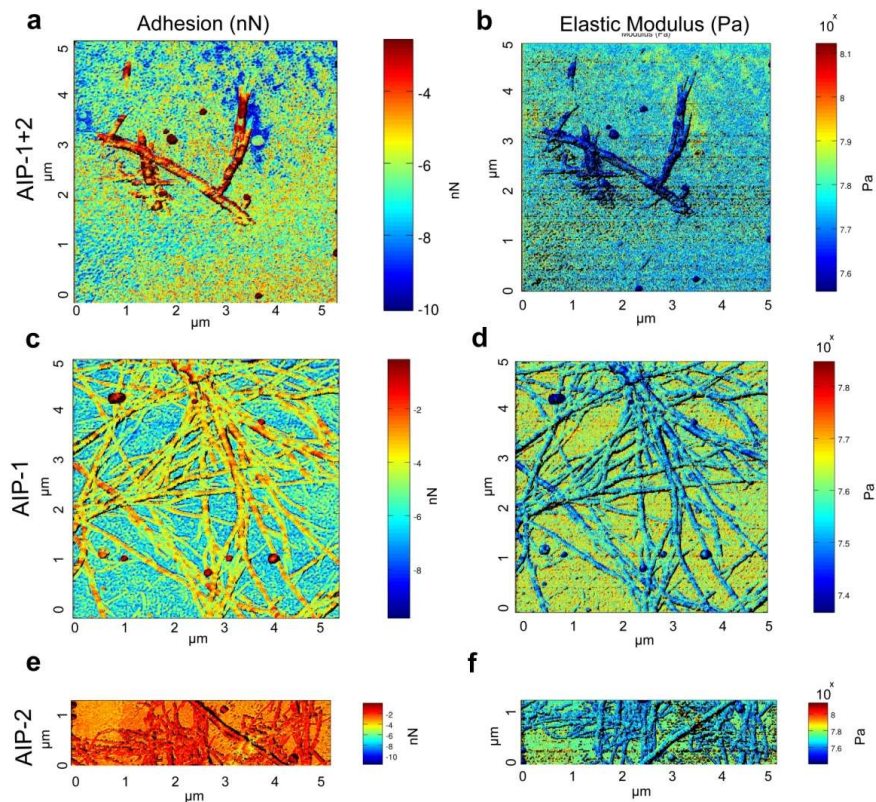


Figure 2.28 Adhesion force (a, c, e) and elastic modulus maps (b, d, f) of individual AIP-1 and AIP-2 nanofibers and the coassembled AIP nanofibers during approach

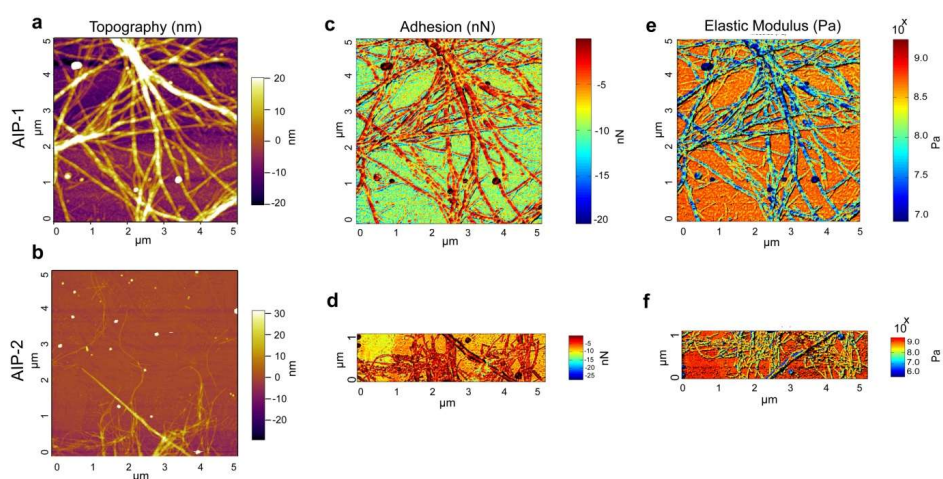


Figure 2.29 The topography (a,b), adhesion force (c,d) and elastic modulus maps (e, f) of individual AIP-1 and AIP-2 nanofibers during retraction

Since the only visual maps alone did not provide a good insight for the mechanical properties of the nanofibers, the slope and adhesion histograms of the nanofibers were also presented for a better comparison. Slope and adhesion histograms of individual AIP-1 and AIP-2 and the coassembled AIP nanofibers (Figures 2.30a-d) were obtained at the similar maximum pressing forces given in Figure 2.32. The slope of the force-distance curves was positively correlated with the elasticity of the nanofibers, hence it was strongly related with the strength of non-covalent interactions between the peptide molecules which were assembled into the nanofibers.

Surfaces containing the coassembled AIPs and individually formed AIP-1 and AIP-2 nanofibers showed single peak elasticity distributions given in Figure 2.30. The elasticity of undisturbed nanofibers was the coassembled AIPs and individually formed AIP-1 and AIP-2 nanofibers, respectively (Figure 2.30a). On the other hand AIP-1 and AIP-2 nanofibers showed wider elastic moduli distributions, while the coassembled AIP nanofibers continued to display a single peak in the histogram during retraction as given in Figure 2.30b.

The change in the elasticity histograms of AIP-1 and AIP-2 nanofibers was pointed us the organizational change of the supramolecular nanofibers, possibly related with the disruption of the non-covalent interactions within and in-between nanofibers during the nanoindentation. The appearance of a tail towards lower elasticity values in the histogram in Figure 2.30b might be related with the structural changes, where the individual nanofibers of nanofibers AIP-1 and AIP-2 triggered via pH stimuli might show a transition from a closed cylindrical shell to a partially or completely ripped shell. On the other hand, the coassembled AIP nanofibers continued to reveal a single peak elasticity distribution.

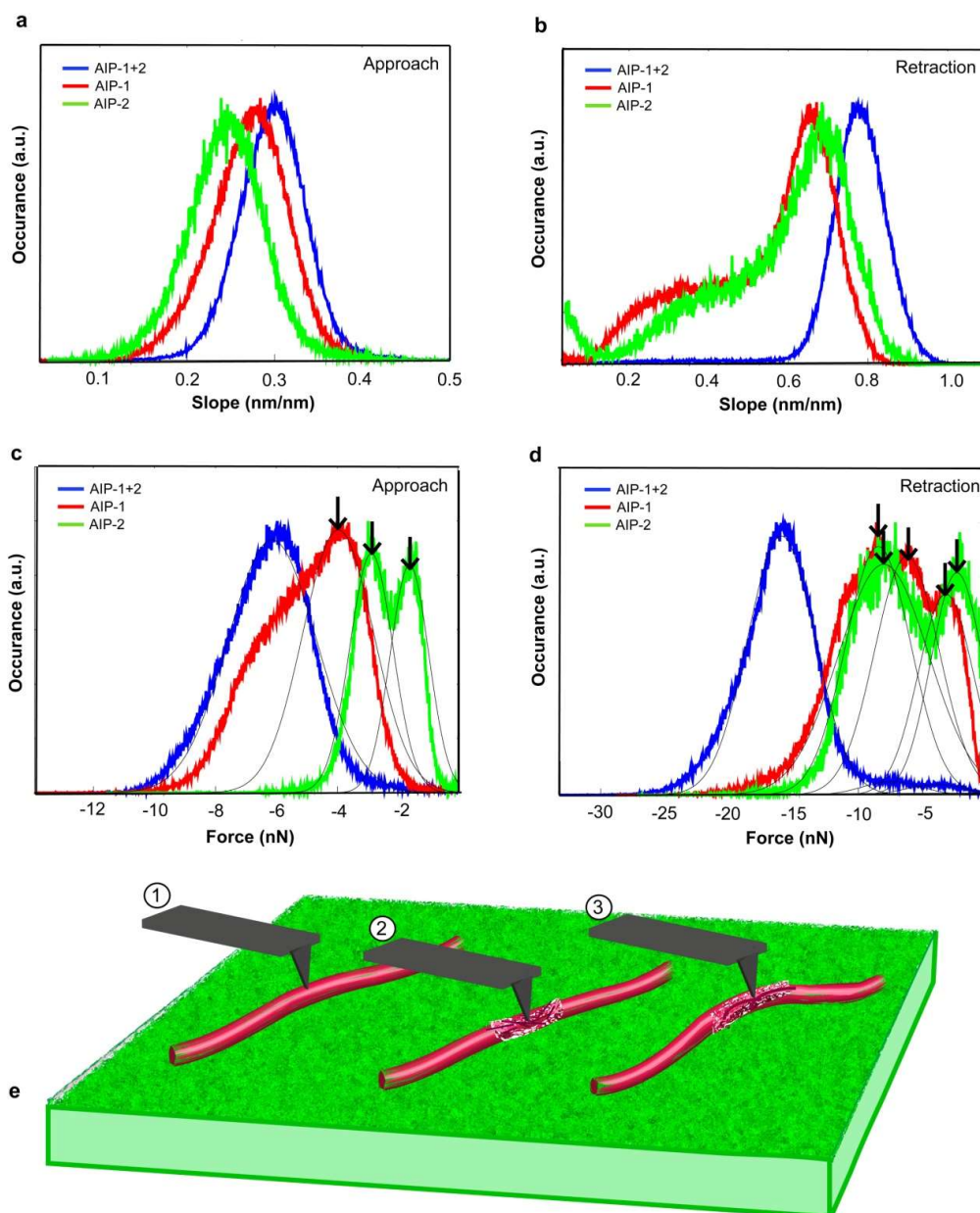


Figure 2.30 Slope (a, b) and adhesion force histograms (c, d) of the coassembled AIPs at pH 7 and individually formed AIP-1 at pH 5 and AIP-2 nanofibers at pH 10 during approach and retraction of the AFM tip (— Gaussian fittings). Schematic representation of nanofiber and AFM tip interactions during nanomechanical characterizations (e)

In complementary to the slope histograms of the nanofibers, similar results was obtained in the adhesion force histograms of the coassembled AIPs at pH 7 and individually formed AIP-1 at pH 5 and AIP-2 nanofibers at pH 10 (Figures 2.30c, d). While individual AIP-1 and AIP-2 nanofibers showed multiple peaks in the approach (Figure 2.30c), the coassembled AIP nanofibers exhibited a single peak with increased adhesion force. It was thought that the individual AIP-1 and AIP-2 nanofibers had a multiple nanoscale configurations or exposed sites during the tip-structure interactions.

The lower adhesion forces for AIP-1 and AIP-2 compared to the coassembled AIP nanofibers also indicated the stronger non-covalent interaction and bond formation within the coassembled nanofibers. Stronger adhesion in the coassembled nanofibers was expected to outcome in greater strength and storage modulus for the supramolecular AIPs gels complementary to the macroscopic rheology results. Furthermore, the adhesion histograms of the coassembled nanofibers during at both approach and retraction of the tip (Figure 2.30c, d) revealed a single peak in the adhesion distribution; on the other hand, the significant changes in the distributions for the individually formed nanofibers via pH effect. AIP-1 and AIP-2 nanofibers were observed. That was also supported the conclusion related with the greater strength, structural integrity and stability of the coassembled AIP nanofibers compare to the pH triggered individually formed supramolecular architectures.

In addition to comparison of the nanofibers and understanding nanomechanical behaviors of the AIP nanostructures, the adhesion and stiffness properties of the coassembled AIP nanofibers at pH 7 were used to categorize these supramolecular architectures compare to the other natural proteinaceous materials. Hence, the coassembled AIP nanofibers presented mechanical stiffness up to 10 GPa (Figure 2.31) similar to mechanical properties of natural amyloid fibrils and collagen[257] found in natural organism.

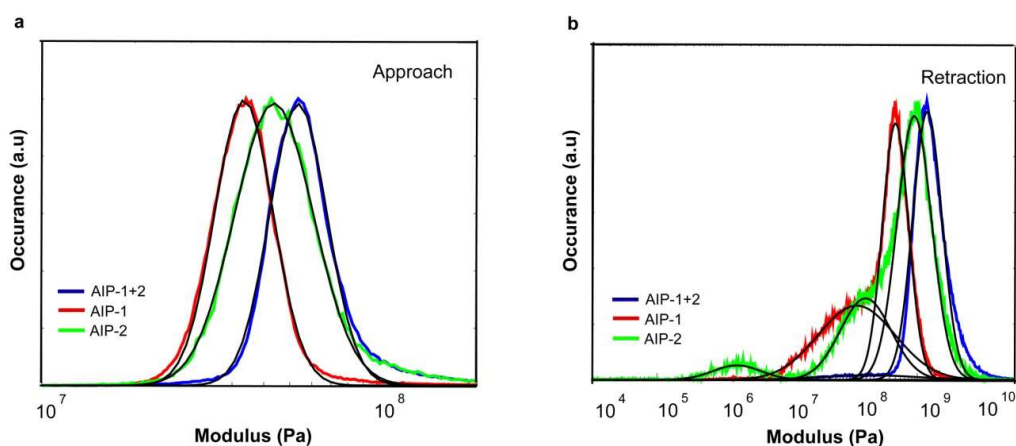


Figure 2.31 Modulus (Pa) histograms of AIP-1+2 at pH 7, AIP-1 at pH 5, and AIP-2 at pH 10 nanofibers; a) approach and b) retraction of AFM tip (—: Gaussian fittings)

In addition, nanoindentation studies were performed under relatively small peak forces such that on the order of 10 nN as given in Figure 2.32. The peak indentation depth was determined using the Hertzian contact theory, which gave us a value of 2 nm for a 25 nm radius tip, for 10 nN applied force. The thickness of the AIP nanofibers and bundles that can reach up to 40 nm as seen in Figures 2.27a and 2.29a, b. Hence the obtained results could not be affected by the indentation forces since the indentation depth was smaller than a typical fiber diameter.

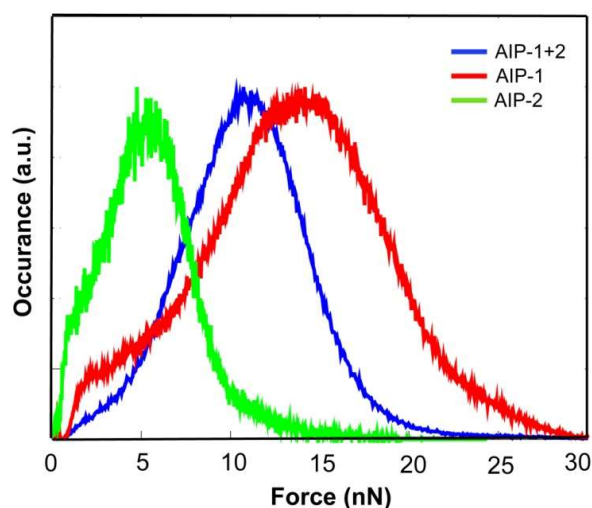


Figure 2.32 Maximum force histogram of the coassembled AIP nanofibers at pH 7, AIP-1 at pH 5, and AIP-2 at pH 10 nanofibers applied by AFM tip during the nanomechanical characterizations

2.3.5 Biocompatibility of AIP Nanofibers and Supramolecular Gels

The dynamic nature of ECM, soluble factors and cell-cell interactions control cellular behavior and determine the cell fate in natural organisms. Interfering cellular behavior towards the directed cellular responses has recently gained tremendous interest due to recent advances on the tissue/organ regeneration and other therapeutic applications. Within this perception, self-assembling peptides and their supramolecular architectures emerged as useful biomaterials due to their adaptability, bioactivity and biocompatibility. Hence, we aimed to investigate the potential of AIP nanofibers and gels as cell culture scaffold; and understand the cell-material interaction at *in vitro* conditions quantifying the critical cellular responses such as adhesion, spreading, viability, and proliferation.

For this purpose, Human umbilical vein endothelial cells (HUVECs) were selected as model cells since they had previously been used for similar studies[297]. To prevent

the interference of soluble ECM factors enhance cellular adhesion with our results, the experiments were conducted under serum-free medium which was prepared with the addition of cyclohexamide translation inhibitor eliminating the effect of endogenous proteins on cell adhesion. HUVEC adhesion and spreading was sustained on the AIP nanofibers for 2 h, and then the adhered cells which were stained via calcein were imaged and quantified using fluorescence microscopy as given Figure 2.33a. As it was seen, the adhered cell numbers were comparable with the control groups after 2h; and there was no significant difference.

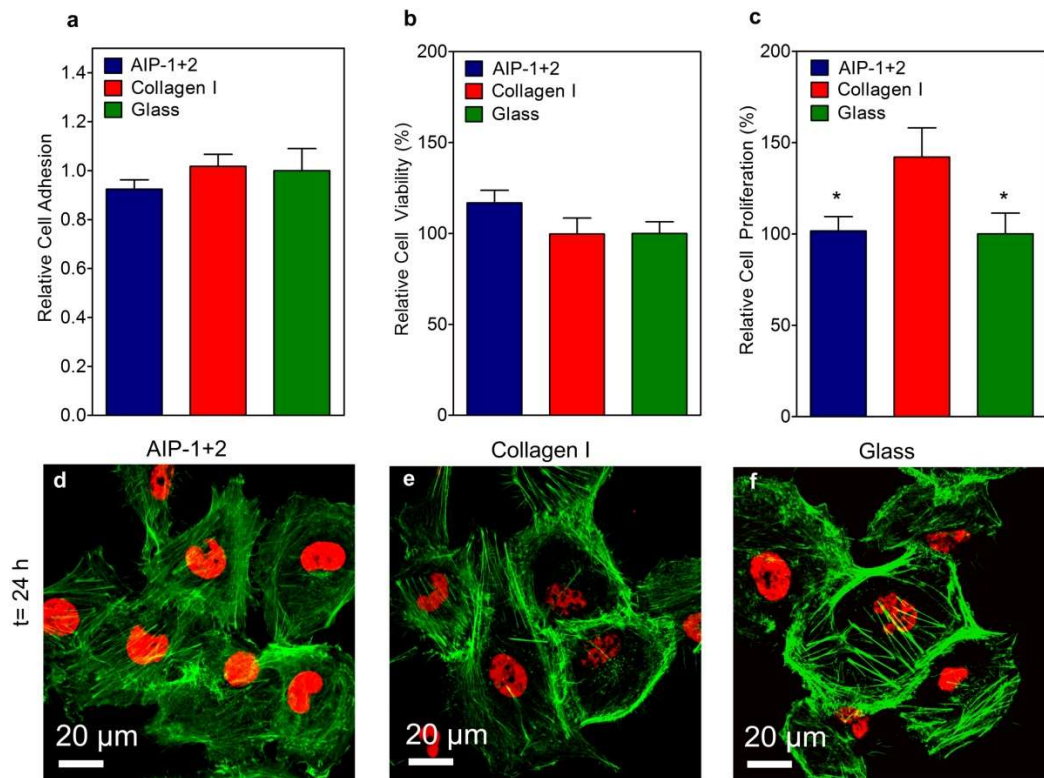


Figure 2.33 a) Relative cell adhesion for 2 h, b) viability for 24 h; c) proliferation for 48 h; and d-f) the confocal images of the cells after 24 h cultured on the AIPs nanofibers, collagen I and bare glass.

Although the significant difference on the adhered cell numbers between the AIPs nanofibers and collagen I control groups were not seen, the spreading of the cells on collagen I was higher compared to the AIPs nanofibers (Figures 2.34) due to bioactive peptide sequence of collagen I interacting with the integrin receptors of the cells. Although the coassembled AIPs nanofibers did not present any bioactive epitopes on the supramolecular nanostructures, the average cell diameter were longer on the AIPs nanofibers compare to the other groups (Figure 2.34a).

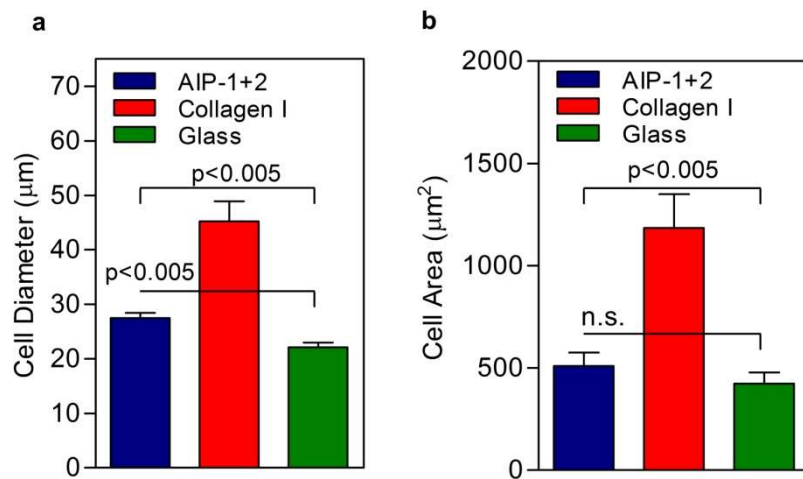


Figure 2.34 Spreading of the cells on the AIPs nanofibers, collagen I and glass after 2 h based on a) cell diameter b) cell area (n.s.: Not significant).

The viability of the cells were also determined at 24 h, and showed that there were no cytotoxic effect of the coassembled AIPs nanofibers on the cellular viability comparable to collagen I coated and bare glass surfaces (Figure 2.33b). On the other hand, the proliferation of the cells were faster rate on the surfaces coated with collagen I compare to the other groups which was quantified via the proliferation assay at 48 h (Figure 2.33c). The cells cultured on the AIPs nanofibers and the controls groups were also stained with Phalloidin-TRITC and TO-PRO®-3 Iodide for the confocal imaging

of their morphologies. As it was seen in Figures 2.33 and 2.35 for 24 h and 48 h, respectively, the native morphologies of the cells were preserved on all the surfaces. Hence, it was concluded that the biocompatibility of the coassembled AIPs nanofibers was comparable with bioactive collagen I network which is a natural ECM component. Furthermore, the integration of bioactive epitopes on AIP building blocks and presentation of the supramolecular nanofibers which had unique mechanical properties can make these architectures promising candidates for biomedical studies.

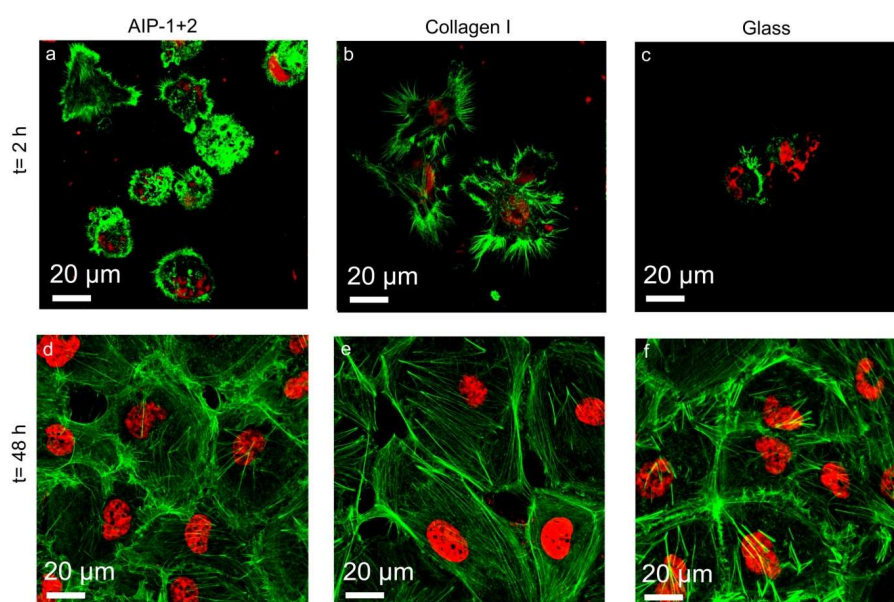


Figure 2.35 The confocal images of the cells after 2 and 48 h cultured on the AIPs nanofibers, collagen I and bare glass.

The stability of amyloid-inspired peptide coated surfaces incubated with cells under standard cell culture conditions (37 °C, 5 % CO₂) for 24 h were investigated using SEM imaging, also. Nanofibrous peptide layer was clearly identifiable in Figure 2.36, pointing the stability of the peptide coating during the *in vitro* experiments.

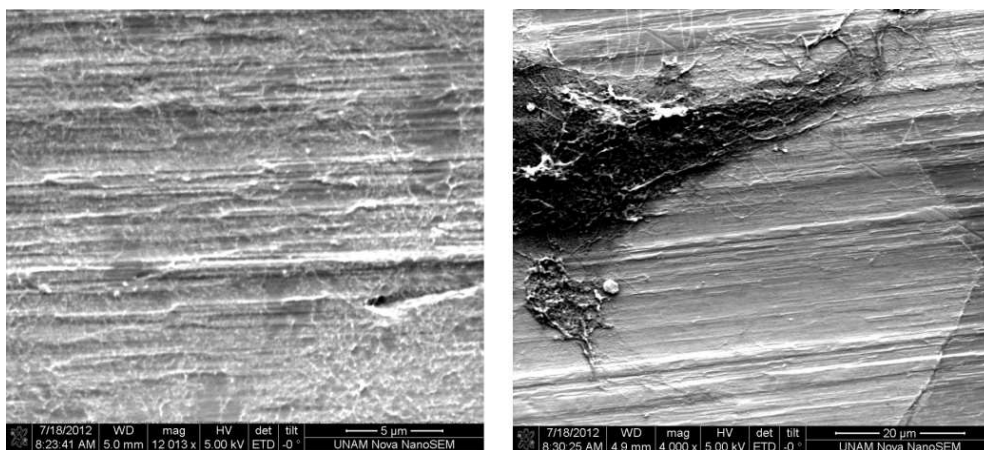


Figure 2.36 SEM images of the coassembled AIPs coated surfaces incubated with the cells under standard cell culture conditions for 24 h.

The 3D cell culturing studies were also performed to analyze the cell-material interactions on the coassembled AIPs gels at 4 and 3 % (w/v) concentrations. HUVECs cells were cultured on the gels for 24 h and then, SEM images of the gels with the cells were obtained (Figure 2.37). As it was seen in the images, the coassembled AIPs gels sustained the cell-material interactions. The enhanced the cellular spreading and cell-cell contacts on the surfaces also pointed the biocompatibility and the stability of the supramolecular assemblies of AIPs as functional biomaterials for biomedical applications.

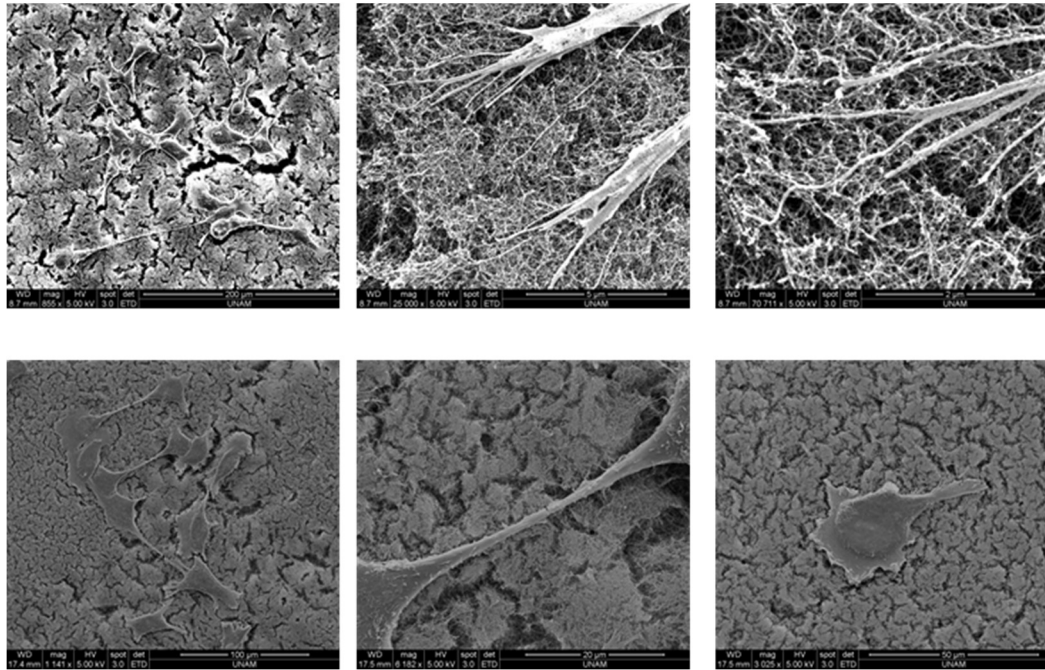


Figure 2.37 SEM images of HUVECs cultured on the 3D coassembled AIPs gel surfaces after 24 h later

2.4 Conclusion

The design of short self-assembling synthetic peptides, inspired by noncovalent interactions in native amyloid aggregations, allows the formation of co-assembled supramolecular nanostructures at neutral pH through hydrogen bonding, hydrophobic and electrostatic forces. The interactions between the oppositely-charged short amyloid-inspired AIP-1 and AIP-2 peptide molecules supported the formation of stable nanofibers at physiological conditions.

The aggregation behavior and secondary structure organization of these oppositely charged peptides was also studied via both molecular dynamic simulations of the self-assembly process and other experimental techniques. The coassembly kinetics of the peptides displayed nucleation-dependent, amyloid-like aggregation characteristics above a critical monomer concentration, which was monitored via both ThT binding

and turbidity assays. In addition, fragmentation of the AIP nanostructures by ultrasonication enhanced the aggregation of the 1% (w/v) AIP mixture, which normally could not reach maximum turbidity within 1 h.

Models developed by the detailed SAXS analysis of co-assembled AIP nanostructures also revealed the core-shell nanofibrous organization of the oppositely charged short AIP molecules, which is likely to stem from the hydrophobicity of aromatic residues and hydrophilicity of –Lys and –Glu residues on AIP-1 and AIP-2 molecules, respectively. In addition to the structural model and estimated organizational parameters, *in situ* SAXS analysis suggests that no transition in the structural organization of peptide molecules during the co-assembly process of 2% (w/v) AIP mixture.

The stability of the co-assembled AIP nanostructures in both nanoscale fiber organization and bulk viscoelastic properties was shown via temperature dependent SAXS analysis, nanoindentation using AFM and oscillatory rheology measurements. The nanomechanical characterization via AFM underlined the increased resilience and stability of AIP-1+2 nanofibers under applied pressure by the AFM tip as compared to AIP-1 and AIP-2 nanofibers.

Furthermore, *in vitro* biocompatibility of the non-bioactive AIP nanofibers and their supramolecular gels comparable to Collagen I showed their potential as ECM mimetic scaffold and nanosized delivery system. Although a variety of short peptide designs and self-assembled architectures were reported to display amyloid-like structural organizations in the literature, the facile self-assembly mechanism of the AIPs into mechanically stable nanofibers and supramolecular gels at physiological conditions provide an advantage particularly for possible biomedical applications. Furthermore,

the systematic information about the self-assembly process of short synthetic peptides presented in this study can facilitate the development of therapeutic strategies for protein-folding disorders and the design of improved materials derived from self-assembled amyloid inspired peptides.

Chapter 3

3. Controlled Local Chemotherapeutic Drug Delivery through Supramolecular Peptide Amphiphile (PA) Nanofiber Gels

3.1 Introduction

Peptide amphiphiles (PA) self-assemble into three dimensional supramolecular nanofiber gels providing a suitable environment for the encapsulation of both hydrophobic and hydrophilic drug molecules. PA gels have significant advantages for the controlled drug delivery applications due to their high capacity to retain water, biocompatibility, and biodegradability.

Doxorubicin hydrochloride (Dox) is FDA approved and clinically used chemotherapeutic molecule for the treatments of variety of cancer types.[331, 332] However, systemic administration of the drug to whole body via intravenous injection causes serial health problems.[333, 334] To overcome the limitations of the Dox treatments, we developed biocompatible, biodegradable and injectable PA nanofiber gels which provide both hydrophilic and hydrophobic nanofibrous environment for the local delivery of the Dox molecules at physiological conditions.

For this purpose, oppositely charge PA molecules were designed as the building blocks of the self-supporting gels which encapsulate the drug molecules with 100% efficiency during the sol-gel transition at pH 7.4 in water. The chemical and physical properties of the nanofibrous PA networks including secondary structure, viscoelastic behaviors depending on PA concentration and injectability were studied using several

characterization techniques. Biodegradability of the coassembled PA gels via different proteases was also tested at the physical conditions. After the bulk materials characterizations of the PA nanofiber gels, the controlled release characteristics were investigated via *in vitro* bulk release experiments and Fluorescence Recovery After Photobleaching (FRAP) technique. The transport parameters including diffusion coefficients and immobile fractions of the drug molecules within the PA gels were estimated using semi-empirical methods. In addition, biocompatibility of the PA gels and controlled drug release dependent cellular viability were studied *in vitro* conditions. Finally, we examined the potential of the PA nanofiber gel as local delivery system at *in vivo* conditions developing a breast cancer tumor model on Balb/c mice.

3.2 Experimental Section

3.2.1 Materials

All protected amino acids, rink amide MBHA resin and 2-(1H-benzotriazol-1-yl)-1,1,3,3-tetramethyluronium hexafluorophosphate (HBTU) were purchased from NovaBiochem. Other chemicals including dichloromethane (DCM), dimethylformamide (DMF), acetonitrile, piperidine, acetic anhydride, N,N-Diisopropylethylamine (DIAE), trifluoroacetic acid (TFA), uranyl acetate and doxorubicin hydrochloride were purchased from Fisher, Merck, Alfa Aesar or Sigma-Aldrich. The enzymes; proteinase K from tritirachium album and α -chymotrypsin from bovine pancreas were purchased from VWR chemicals and Sigma, respectively. All chemicals and solvents used in this study were analytical grade.

3.2.2 Synthesis and Characterization of PA Molecules

E₃PA (Lauryl-VVAGEEE) and K₃PA (Lauryl-VVAGKKK-Am) were synthesized according to the solid phase 9-fluorenylmethoxycarbonyl (Fmoc) peptide synthesis

method reported previously.[34] An Agilent 1200 series reverse-phase high performance liquid chromatograph (HPLC) equipped with an Agilent 6224 high resolution mass time-of-flight (TOF) mass spectrometer and an electrospray ionization (ESI) source was used for the characterization of the synthesized PAs (Figure S1). 1 mg/mL E₃PA in water was analyzed at pH 7 using an Agilent Zorbax 300SB-C18, 3.5 μm (100 x 4.6 mm) column in an optimized gradient of water (0.1% NH₄OH) and acetonitrile (0.1% NH₄OH) as the mobile phase, while an Agilent Zorbax Extend-C18, 3.5 μm 80A (100 x 4.6 mm) column was used for the analysis of 1 mg/mL K₃PA at pH 7 in water in an optimized gradient of water (0.1% formic acid) and acetonitrile (0.1% formic acid).

3.2.3 Preparation of the PA Nanofiber Gels

E₃PA and K₃PA were dissolved in water, separately and the pH of the individual solutions were adjusted to 7.4 using 1 M NaOH. Negatively charged E₃PA solution was mixed with the positively charged K₃PA solution with 3:4 volumetric ratio to trigger coassembly of PAs into supramolecular nanofiber gels via overall charge neutralization. The final PA concentrations within the coassembled gels were 3, 2, 1 and 0.5% (w/v), respectively.

3.2.4 Imaging of the PA Nanofibers and Gels

For the TEM imaging of the individual PA nanofibers, 1% (w/v) PA gel was diluted by addition of water, and the sample was casted onto TEM grid for the staining with 2% (w/v) uranyl acetate. After air-drying of the sample, a FEI Tecnai G2 F30 TEM instrument was used for the imaging. For the SEM imaging, the coassembled PA nanofiber gels at 3, 2, 1 and 0.5% (w/v) concentrations at pH 7.4 in water were prepared. The water content in the gels was replaced by series of ethanol (40%, 60%,

80% and 100%) to preserve their nanofibrous architecture during critical point drying (CPD). The samples were coated with 6 nm Au/Pd; and then imaged using a FEI Quanta 200 FEG Scanning Electron Microscope.

3.2.5 Zeta Potential Measurements

E₃PA and K₃PA solutions at 0.186 mM and 0.132 mM concentration were prepared, respectively; and the pH of the solutions were adjusted to 7.4 using 1 M NaOH. The mixtures of the PAs were prepared by adding 0.4 ml E₃PA solution onto the 10 ml K₃PA solution, continuously. After each addition of the E₃PA, the mixture was well mixed and then the zeta potential of the mixture was measured. The analysis was performed with Malvern Nano-ZS Zetasizer equipped with a titrator and pH meter.

3.2.6 Secondary Structure Analysis using CD and FTIR

For the CD analysis, the coassembled PA gel were prepared according to the protocol given in above. Then, the gel was diluted up to 0.272 mM for the analysis. As control groups, E₃PA and K₃PA solutions at the same concentration were prepared at pH 7.4 in water. Jasco J-815 CD spectrophotometer was used for the analysis between 190 to 300 nm. For the FTIR measurement, 1% (w/v) PA gel was formed on petri dishes and instantly frozen in liquid nitrogen in order to preserve their architectural integrity. The frozen sample was kept at -80 °C overnight and then freeze-dried to remove water content. 1 mg dried gel powder was mixed with 100 mg KBr to prepare KBr pellets for the analysis. Bruker VERTEX 70 FTIR spectrometer was used for the measurement between 300 and 4000 cm⁻¹.

3.2.7 Oscillatory Rheology

Time sweep analysis of the coassembled PA nanofiber gels at 3, 2, 1 and 0.5% (w/v) concentrations at pH 7.4 was performed for 1 h at the constant angular frequency and strain; 10 rad/s and 0.1%, respectively. The sample volume was determined as 250 μ L with 0.5 mm measuring distance from the stage. Anton Paar MCR-301 Rheometer with 25 mm PP25-SN17979 measuring device was used for the measurements. The viscoelastic properties of the 1% (w/v) PA gel mixed within the syringe and injected through a ½ inch 26 gauge needle to the rheometer stage were also determined via time sweep analysis and compared with the non-injected control PA gel at the same concentration. The same parameters given above were also used for the analysis.

3.2.8 Controlled Drug Release Experiments

For the drug encapsulation, E₃PA and K₃PA solutions at 3, 2, 1 and 0.5% (w/v) concentration were prepared at pH 7.4 in water. The stock solution of Dox (833.3 μ M) was also prepared in water. The stock drug solution initially was mixed with positively charged K₃PA and then co-assembly was triggered upon addition of the negatively charged E₃PA at physiological conditions with 3:4 volumetric ratio. The final Dox concentration within 100 μ l of PA gels prepared within small vials was 40 μ M. After 2 h incubation, 100 μ l of water was added onto the PA gels and at the determined time intervals, 1 μ l of the sample was removed for the fluorescence based concentration determination using ThermoScientific Nanodrop 3300. After the each measurement, the same amount of the water was put onto the gels. The measurements were replicated for 4 different groups for each gel concentration. For the measurements, $\lambda_{\text{excitation}}$ and $\lambda_{\text{emission}}$ were determined as 565 and 630 nm; and the maximum RFU value at 588 nm was recorded.

3.2.9 FRAP measurements

SNOM Confocal Raman microscopy was used for the FRAP experiments with a 20X magnification. The area was monitored by pre-bleach scanned images at low laser intensity, then bleached at 100% laser intensity (40 mW) for 15 sec, and followed by detection of the fluorescence recovery again at low intensity. The Dox encapsulated PA gels at 3, 2, 1 and 0.5% (w/v) concentration were prepared according to the protocol given above. Instead of small vials, the Dox encapsulated gels were prepared within the closed petri dishes to prevent drying. The final concentration within the PA gels was 40 μ M.

3.2.10 *In Vitro* Studies

The 4T1 breast cancer cell line was maintained in DMEM (Dulbecco's modified Eagle's medium) supplemented with 1% antibiotics and 10% fetal bovine serum at 37 °C with 5% CO₂ flow. The cellular viability and apoptotic behavior on the 1% (w/v) PA gel (with or without 40 μ M Dox) prepared according to the procedures given above were determined via flow cytometry technique.

Before seeding the cells, all groups were treated with cell medium for 1h, and 4T1 breast cancer cell lines (5×10^4 cells/well) were seeded onto 48-well culture plates. The cells were treated for 24h and 48h; and then trypsin/collagenase (1:1 (v/v)) were used in order to degrade the gels and remove the cells from the peptide extract. Then, the degraded samples was strained with falcon strainers (40 μ m pore size) and centrifuged at 4000 rpm for 6 mins. The supernatants were removed and the remained cells were washed with PBS in order to get rid of cell medium. After that, the cells were centrifuged at 4000 rpm for 6 mins, discarding supernatant and dissolved with 1X annexin binding buffer in 100 μ l. For the flow cytometry analysis, cells were labeled

with Annexin V and PI and incubated at room temperature for 15 mins. Before the analysis, 400 µl 1X annexin binding buffer added to all samples and immediately read out flow cytometry.

3.2.11 4T1 Tumor Model and *In Vivo* Studies

All protocols involving animals were approved by Institutional Animal Care and Use Committee of Diskapi Yildirim Beyazit Training and Research Hospital. A total of 40 female Balb/c mice (8-10 week old) from ADACELL Laboratories (Ankara, Turkey) were used for the drug delivery experiments and histological studies. Animals were housed under specific pathogen-free environment with 12 hour light–dark cycles and *ad libitum* access to food and water.

In order to develop orthotropic 4T1 mammary carcinoma model, 4T1 cells were purchased from American Type Culture Collection (ATCC, Manassas, VA, USA) and were cultured in RPMI 1640 supplemented with 10% fetal calf serum (Biowest, Nuaille, France), 100 U/ml penicillin and 100 µg/ml streptomycin (Gibco/Invitrogen, Carlsbad, CA, USA). Just before the inoculation, 2×10^6 viable 4T1 cells were suspended in 1 ml serum free RPMI 1640 medium. Cells in 50 µL medium were subcutaneously injected into the second mammary fat pad on the right of BALB/c mice using a ½ inch 26 gauge needle. Tumor formation was observed 8 days after implantation.

Tumor volume was calculated according to following formula; $V = \frac{1}{2} (D \times d^2)$ where the tumor volume, defined as V, D was the measurement of the greatest longitudinal diameter of the tumor and the d was the greatest transverse diameter of the tumor as measured with digital caliper. When the tumor volume reached 100 mm³, forty mice were randomly divided into four groups and treated with Dox encapsulated 1% (w/v)

PA gel or controls (n=8): Dox/PA, only Dox, only PA and PBS. Treatments were administered via subcutaneous injection near to the tumor at equivalent dose of 10 mg Dox/kg body weight. The body weight and tumor volume were monitored every 3 days. Animals were sacrificed by day 18.

On day 18 after injection, the rats were sacrificed and the tumors were individually dissected and removed from the subcutaneous abdomen. The tissues were immediately fixed with 10% (v/v) formalin and embedded in paraffin. The embedded specimens were sectioned (5 μ m) along the longitudinal axis of the tumor, and the sections were stained with hematoxylin and eosin (H&E). Caspase-3 mediated apoptosis in tumor tissue of different treatment groups were also evaluated with histology analysis. The tumor sections were stained using the antibodies; caspase-3 (Asp 175) 1:300 (9661 Cell Signalling Technology, Danvers, MA, USA) and HRP conjugated Goat-Anti Rabbit (GAR) secondary antibody. Bright-field microscopy was used to obtain the histology images.

3.2.12 Statistical Analysis

All statistical analyses were carried out by one-way, two-way ANOVA or unpaired student t-test whichever applicable. For the statistical significance, a *p*-value of less than 0.05 was determined.

3.3 Results and Discussion

3.3.1 Design, Synthesis and Characterizations of the PA Assemblies and Nanofiber Gels

Two different PA molecules (E₃PA and K₃PA) were designed as building blocks of the drug delivery system and synthesized via Fmoc-solid phase method[34] (Figure 3.1). The purity of the PA molecules were higher than 90%.

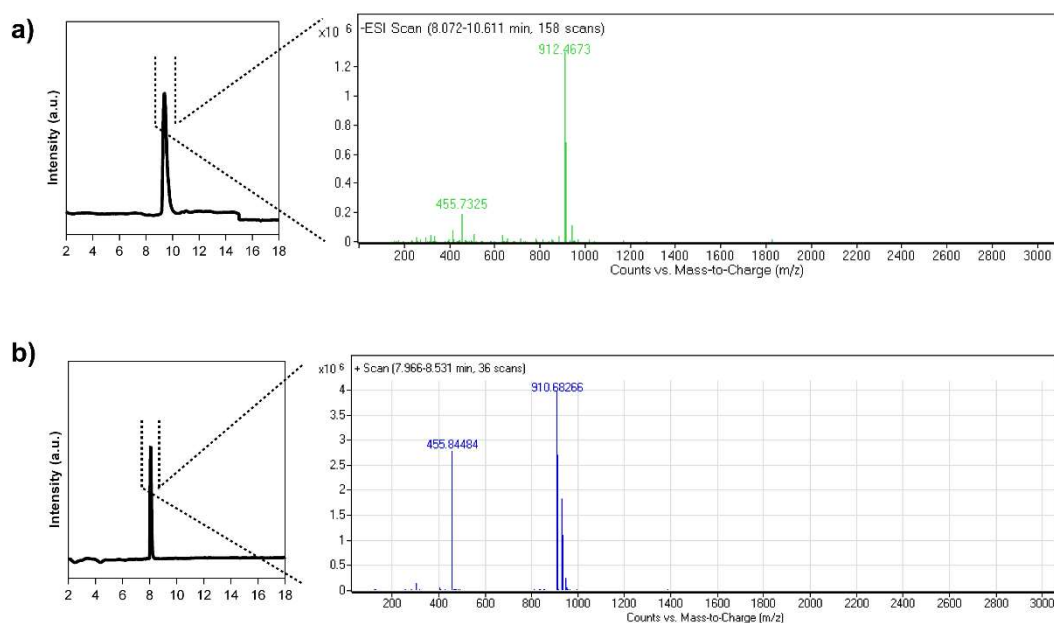


Figure 3.1 Liquid chromatograms and mass spectra of the synthesized PAs a) E₃PA; [M-H]⁻ (calculated)= 912.50, [M-H]⁻ (observed)= 912.48, (observed [M-2H]⁻² m/z = 455.73) b) K₃PA; [M+H]⁺ (calculated)= 910.67, [M+H]⁺ (observed)= 910.68, (observed [M+2H]⁺² m/z = 455.84)

The PA molecules consists of aliphatic tail, beta sheet forming motif (-VVAG-) and oppositely charged amino acids to trigger the co-assembly via hydrophobic interactions, hydrogen bonding and electrostatic interactions at physiological conditions. Especially, the overall charge neutralization within the system which was determined with the zeta potential measurements of the PA mixtures (E₃/K₃PA) enable

the formation of the self-supporting supramolecular PA gel upon mixing the E₃PA and K₃PA solutions with 3:4 molar ratio (Figure 3.2c, d) above 0.5% (w/v) PA concentration. The nanofibrous structural organization within the PA gels prepared at different concentration was analyzed via SEM imaging (Figure 3.3) and the individual co-assembled PA nanofibers were shown in the TEM image (Figure 3.2e).

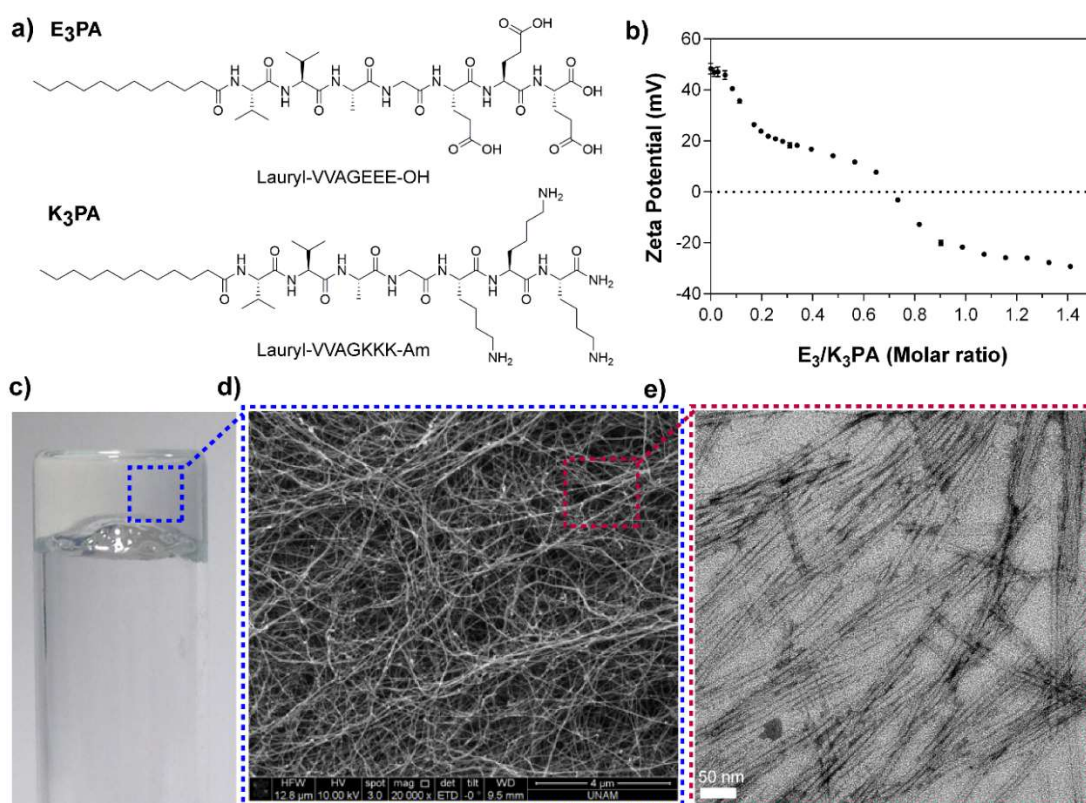


Figure 3.2 a) Chemical representation of E₃PA and K₃PA molecules a) Zeta potential change of the E₃PA upon addition of the K₃PA at pH 7.4 in water c) Supramolecular PA network showed self-supporting gel property d) SEM and TEM image of the coassembled PA nanonetwork and nanofibers, respectively

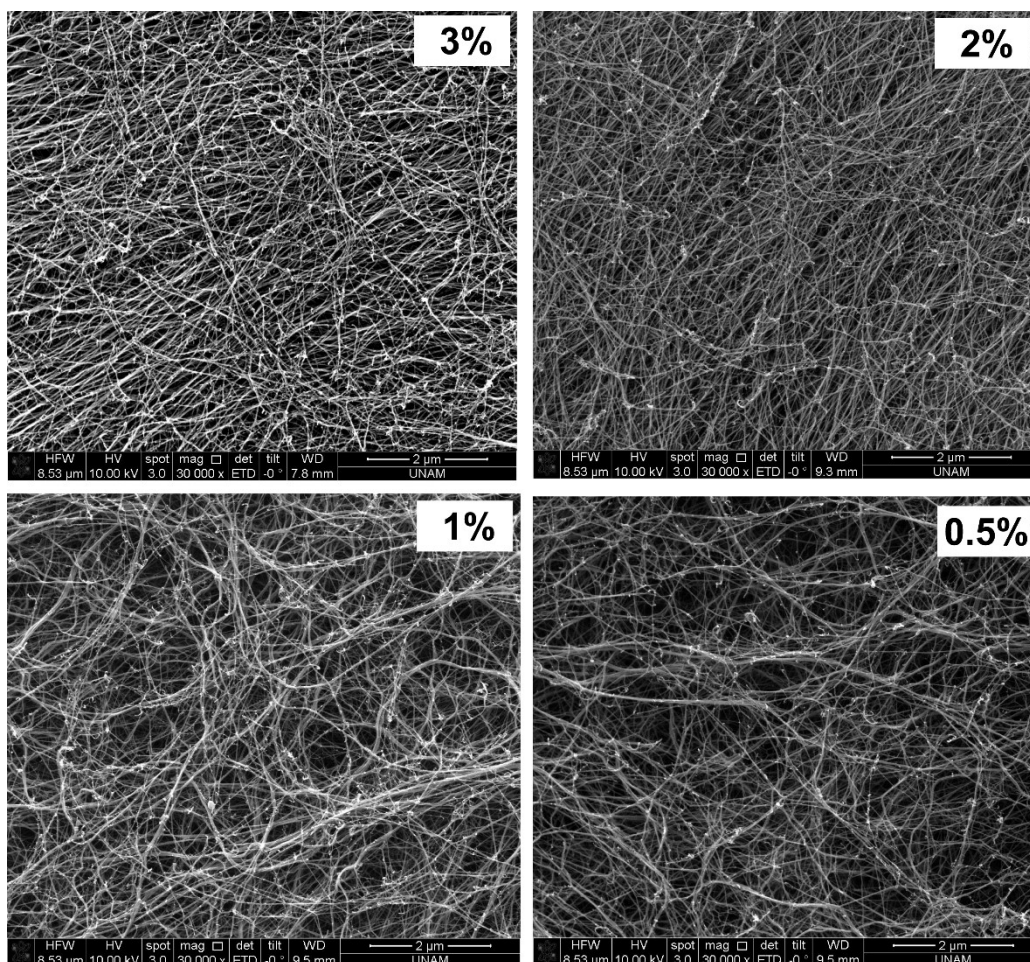


Figure 3.3 SEM images of the self-assembled PA nanonetworks prepared using critical point dryer at different peptide concentrations

The structural organization of the PA coassemblies was revealed via CD and FTIR techniques (Figure 3.4). CD spectra of the E₃/K₃PA assemblies with strong positive and negative peaks at around 190 and 220 nm, respectively showed the formation of twisted β-sheets within the PA nanofibers. On the other hand, E₃PA and K₃PA solutions as control groups did not show any aggregation and preserve their random coil organization at pH 7.4 in water, separately. FTIR analysis of the PA assemblies was also pointed the beta-sheet organization of the coassembled nanofibers with the

observed peaks at around 1632 cm^{-1} and 1672 cm^{-1} within Amide I[184] region in complementary to the CD spectra.

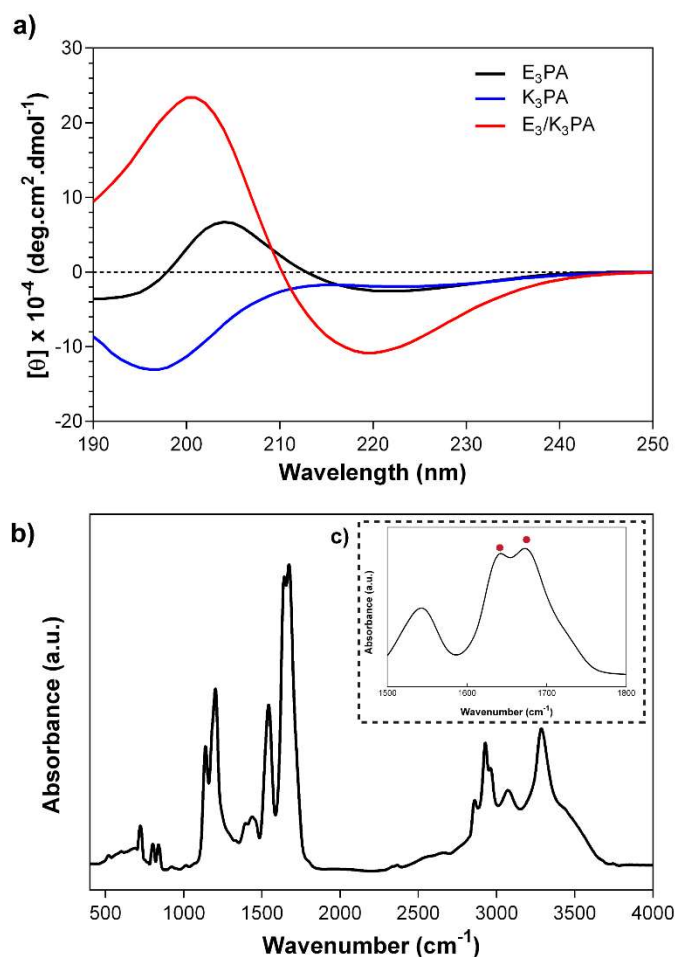


Figure 3.4 a) CD spectra of E₃PA, K₃PA and E₃/K₃PA and (b, c) the FTIR analysis of the E₃/K₃PA assemblies prepared at pH 7.4 in water

The viscoelastic behavior of E₃/K₃PA assemblies depending on the PA concentration were characterized using dynamic oscillatory rheology technique. Time sweep analysis of all groups revealed the gel-like behavior since the storage modulus (G') values of the samples were higher than the loss modulus (G'') (Figure 3.5a). In addition, the equilibrium storage and loss modulus values of the PA gels were modulated depending on the PA concentration within the co-assembled gels (Figure 3.5b).

Although these architectures formed via non-covalent interactions between the PA building blocks, the viscoelasticity of the gel systems were reached up to 10 kPa and provide the mechanical stability as drug delivery systems for the local soft tissue applications.

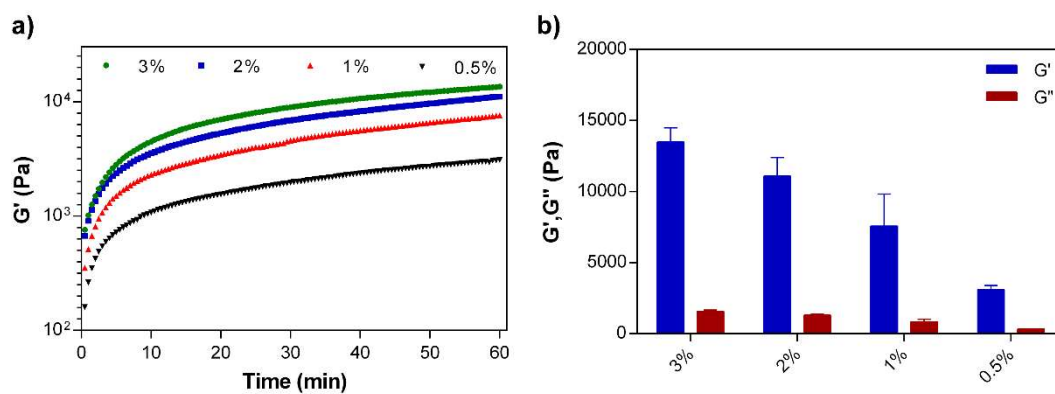


Figure 3.5 a) Time sweep analysis of the supramolecular PA nanofiber gels prepared at the different concentrations and b) Equilibrium storage (G') and loss moduli (G'') of the PA gels.

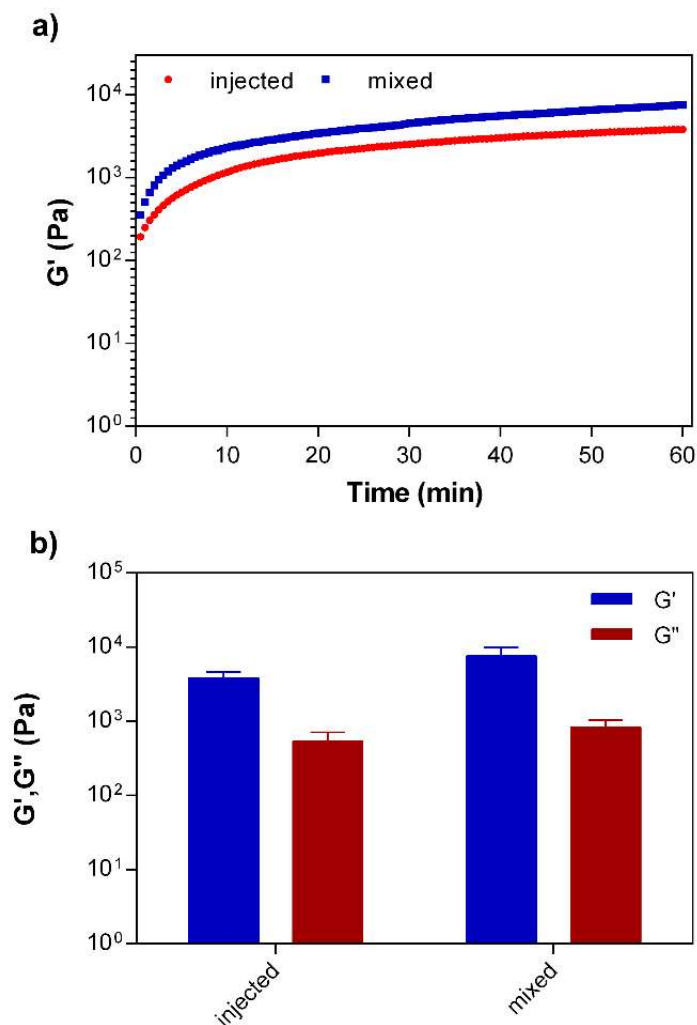


Figure 3.6 a) Time sweep analysis of the 1% (w/v) coassembled PA gels injected through a syringe or directly mixed on the rheometer stage b) Equilibrium storage (G') and loss moduli (G'') of the PA nanofiber gels.

3.3.2 Biodegradability of the PA Nanofiber Gels

The degradation profile of the 1% (w/v) coassembled PA gel via proteases were monitored based on the gel mass change over the time. Two different serine proteases, proteinase K and α -chymotrypsin were selected due to their broad specify for the cleavage of the peptide bonds primarily from the aromatic or hydrophobic residues.[335] The gels were incubated with the enzyme solutions prepared in Tris

buffer at pH 7.4 or only the buffer as control group. At the time intervals, the solutions were removed and the remaining gel mass was weighted (Figure 3.7). The PA gel via proteinase K were rapidly degraded via proteinase K and only 10% of the gel mass was remained at day 25. On the other hand, the degradation of the PA gel via α -chymotrypsin was slower compare to the proteinase K for 25 day; and approximately 50% the gel were remained without degradation at the same concentration.

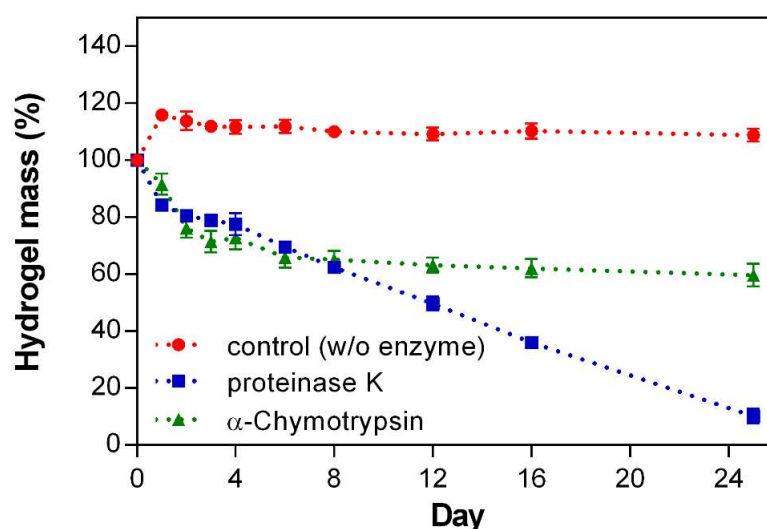


Figure 3.7 Biodegradability of 1% (w/v) coassembled PA nanofiber gel via different proteases at pH 7.4 in Tris buffer

In the literature, it was showed that α -chymotrypsin predominantly cleaves the peptide bonds from the aromatic residues.[336] On the other hand, proteinase K has also affinity to the aliphatic amino acids in addition to the hydrophobic and aromatic residues.[337] This difference on the degradation behavior could be related with easier cleavage of the aliphatic beta sheet forming motif (-VVAG-) that interspace the hydrophobic aliphatic tail and hydrophilic amino acids of the PA molecules via proteinase K compare to the α -chymotrypsin. Additionally, control group incubated

with the only buffer system without the enzymes remained its weight for 25 days and the stability of the co-assembled gel system was reported at this condition.

3.3.3 Drug Encapsulation and Controlled Drug Release through the PA Nanofiber Gels

To encapsulate the Dox molecules within the supramolecular PA nanofiber gels, the drug solution initially was mixed with positively charged K_3PA and then coassembly was triggered upon addition of the negatively charged E_3PA at physiological conditions. This approach enabled the 100% encapsulation and homogenous dispersion of the drug molecules within the PA gels. In addition, the nanofibrous architecture of the gels provided suitable nanoporous environment for the controlled release of the small molecules and sustain the therapeutic level for the local application of the delivery system through the soft tissues (Figure 3.8).

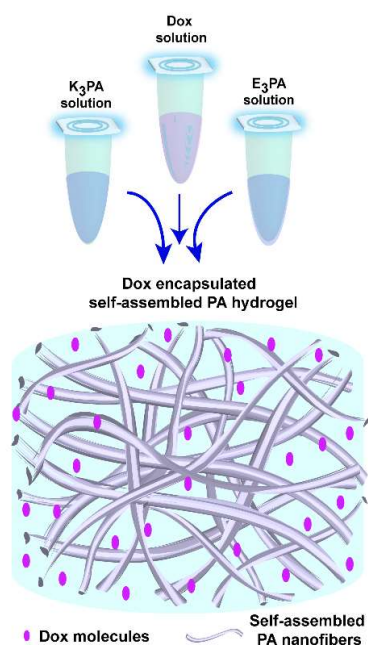


Figure 3.8 Schematic representation of the drug encapsulation and coassembly of the molecules into supramolecular PA nanofiber gel

Drug release profiles depending on the PA concentration within the coassembled PA gels were monitored and quantified based on the concentration dependent fluorescence intensity calibration of the molecules. The sustained release of the drug molecules through the PA gels were observed for 48 h, and then *in vitro* release kinetics were slowed down reaching an equilibrium for 156 h (Figure 3.9a).

Non-linear transport kinetics of the all PA groups indicated the non-Fickian release behavior of the co-assembled PA gel which consists three different interfaces: i) the hydrophobic alkyl domain, ii) the hydrophilic amino acids carrying both negative and positive charges and iii) the water molecules entrapped within the system. The possible non-covalent interactions between the Dox molecules and these interfaces could be the reason of this non-linearity on the transport properties and prevent the complete release of the encapsulated drug molecules through the gel system. In addition, the release kinetics and the amount of the released molecules at equilibrium conditions were modulated via PA concentration (Figure 3.9b) which has an effect on both porosity of the network and entanglement of the nanofibers[222] within the co-assembled PA gel system.

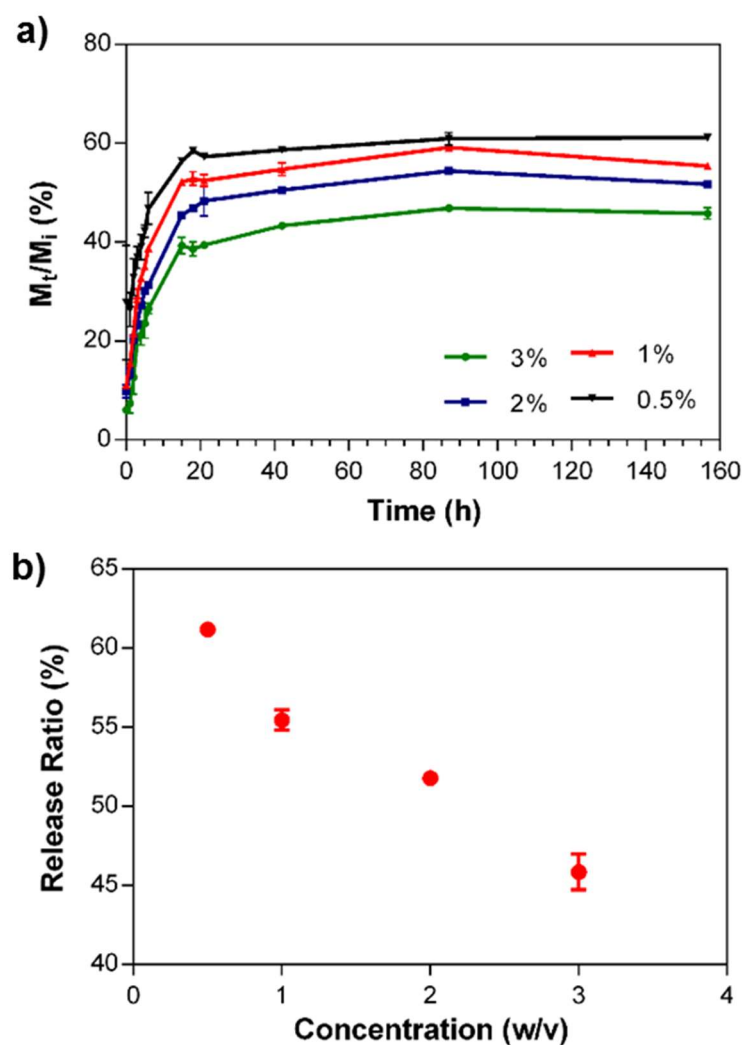


Figure 3.9 a) Controlled release profile of Dox through the PA gels prepared at different concentrations at physiological conditions and b) The release ratios of the chemotherapeutic drug were modulated depending on the PA concentration within the gels.

In addition to the *in vitro* bulk release studies; the mobility of the drug molecules within co-assembled PA gels were investigated via FRAP technique in which the fluorescence molecules are photobleached through a high power laser source and the recovery of the fluorescence intensity at the bleached area was followed to estimate

the transport parameters of the molecules. Dox encapsulated gels at different PA concentrations were prepared within closed system to prevent drying effect. The fluorescence intensity change after photobleaching of the drug molecules were monitored (Figure 3.10a); and the data analysis was performed using the program developed via Jönsson et al.[338]

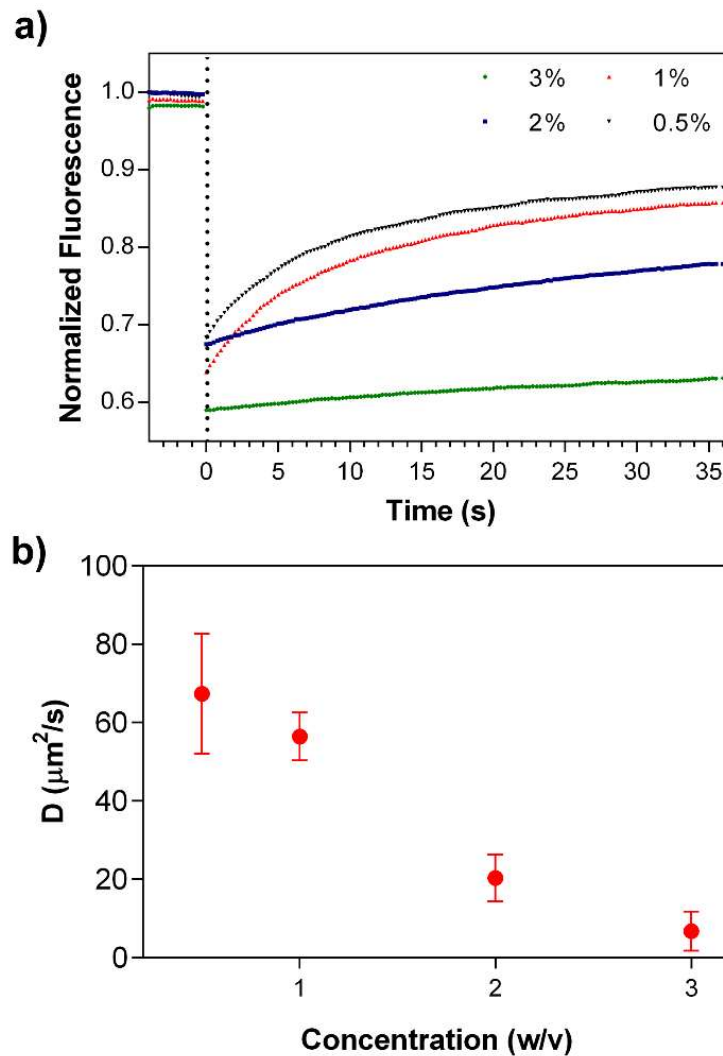


Figure 3.10 Mathematical fitting results of FRAP experiments a) the estimated diffusion constants and b) immobile fractions of the drug molecules encapsulated within the PA gels prepared at the different concentrations

The diffusion constants of the Dox molecules within the 3, 2, 1 and 0.5% (w/v) PA nanofiber gels were estimated via Hankel transform of the data, respectively (Figures 3.10b and 3.11). It was seen that the drug release and mobility of the molecules can be modulated and controlled depending on the PA concentration.

In addition, immobile fractions of the Dox molecules within the gels were also determined as 0.56 ± 0.17 , 0.26 ± 0.05 , 0.19 ± 0.05 and 0.17 ± 0.02 , respectively using the FRAP technique. The increase in immobile Dox molecule amount depending on the PA concentration within the gel systems also pointed us the affinity of the PA network towards the drug molecules in complementary to the non-Fickian transport characteristics of the gels. Although the non-covalent interaction between the PA nanofiber gels and the drug molecules led to entrapment of the some portion of the molecules within the system, the biodegradability of the nanofibrous PA system could improve the availability of the immobile drug molecules via enzymatic degradation of the PA delivery system.

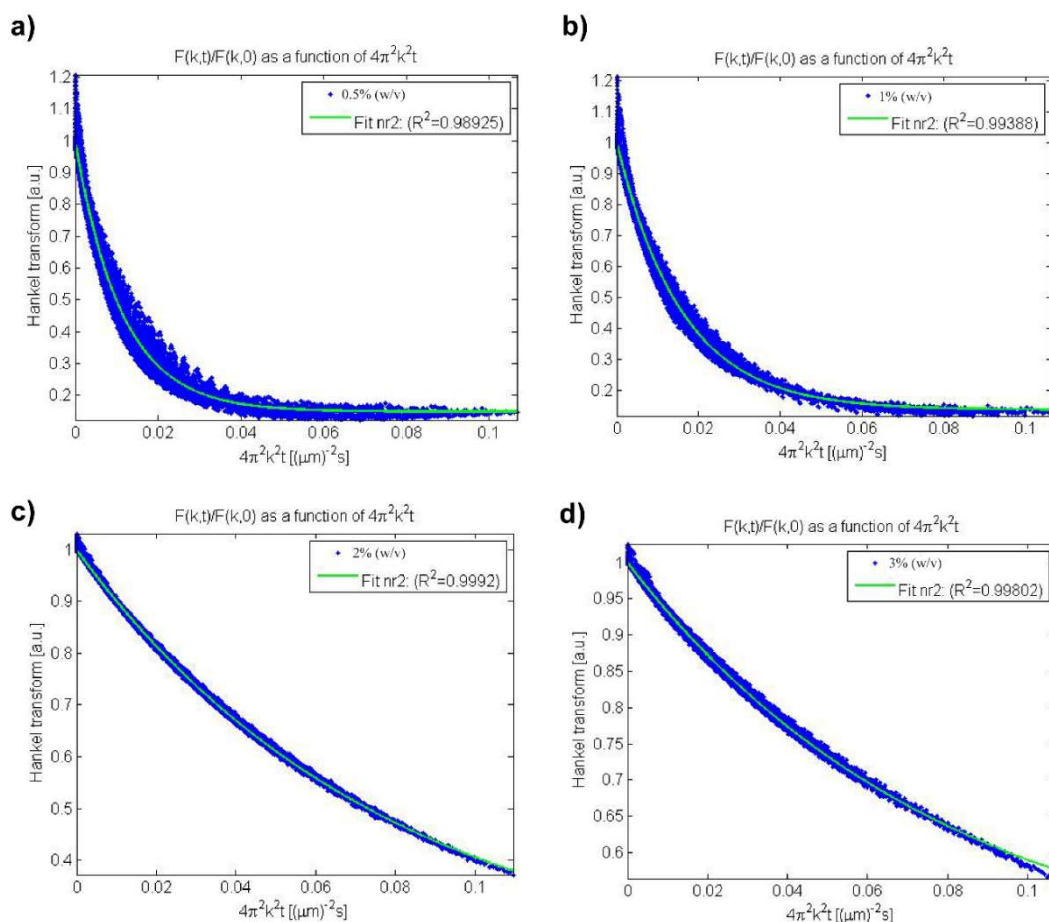


Figure 3.11 Hankel transform of the photobleaching profiles of Dox encapsulated self-assembled PA hydrogels prepared at different concentrations.

3.3.4 *In Vitro* Biocompatibility of the PA Nanofiber Gels

To determine biocompatibility and the controlled drug release dependent cellular viability using flow cytometry, the breast cancer cells were cultured on the only PA gel, Dox encapsulated PA gel (Dox/PA) or TCP. The same amount of Dox encapsulated within the gels was also directly administrated to the cell culture media as a positive control for 24 and 48 h. As it was seen in Figures 3.12 and 3.13, only PA gel was not showed any cytotoxicity compare to the TCP control. On the other hand, the cellular viability was decreased for 24 h and 48 h at both only Dox and Dox/PA groups. Although the significant difference was not obtained on the viability of the

cells cultured on the Dox/PA gel or directly treated with Dox for 24 h, this difference on the cellular viability became clear for 48 h due to the sustained release of the Dox molecules through the gel system. The PA nanofiber gel providing a suitable protection environment for the drug molecules enhanced both bioavailability and activity of the drug molecules at *in vitro* conditions.

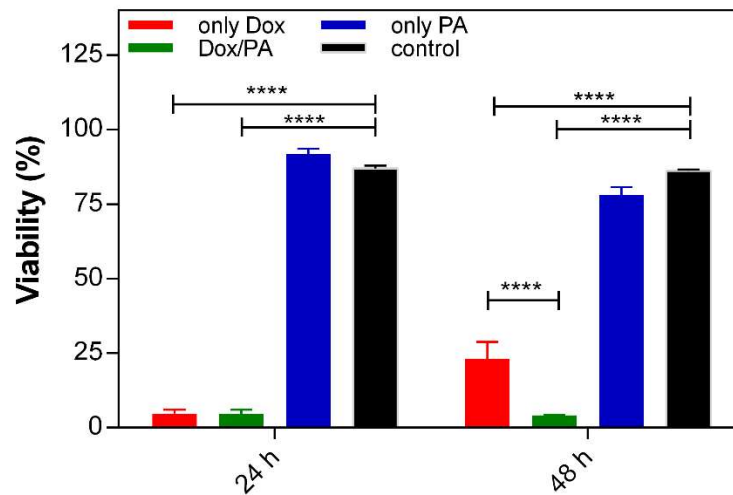
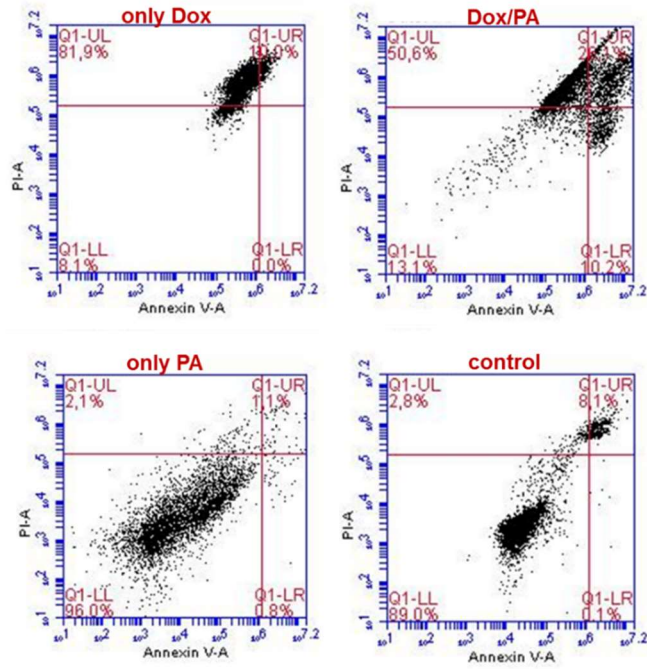


Figure 3.12 Cellular viability on (a) the control, (b) 1% (w/v) PA gel, (c) 1% (w/v) Dox/PA gel and (d) only Dox for 24 h and 48 h.

a) 24 h



b) 48 h

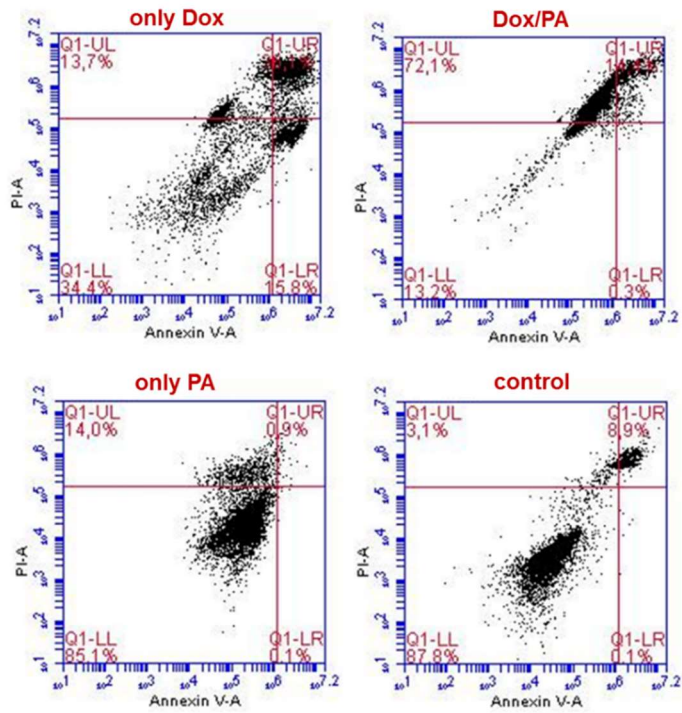


Figure 3.13 Flow cytometry histograms of only Dox, Dox/PA, only PA and control groups at (a) 24 and (b) 48 h

3.3.5 *In Vivo* Applicability of the PA Nanofiber Gels

After the examining of the biocompatibility of the PA gels and controlled drug release dependent cellular viability at *in vitro* conditions, the applicability of the Dox/PA gels as a local drug delivery systems was tested developing a solid tumor model on the animals at *in vivo* conditions. For this purpose, highly aggressive and metastatic 4T1 breast cancer cells were subcutaneously injected to the mammary fat pad of the Balb/c mice for the tumor growth. When the tumor volume reached to 100 mm³; same amount of 1% (w/v) Dox/PA gel, only PA gel, Dox solution or PBS as a control group were injected to the tumor site; and the tumor sizes were measured each three days using electronic caliper. Tumor growth rate was followed for 18 days at which the animals were sacrificed for the histological analysis of the tumors and organs (Figure 3.14a). As it was seen in Figure 3.14b, the local delivery of the Dox molecules via coassembled PA gels significantly limited the tumor growth compare to the direct injection of the drug solution. Furthermore, the PA gels without the drug encapsulation did not cause additional cytotoxicity compare to the PBS control that indicated the *in vivo* biocompatibility of the coassembled PA nanofiber gels as local delivery system.

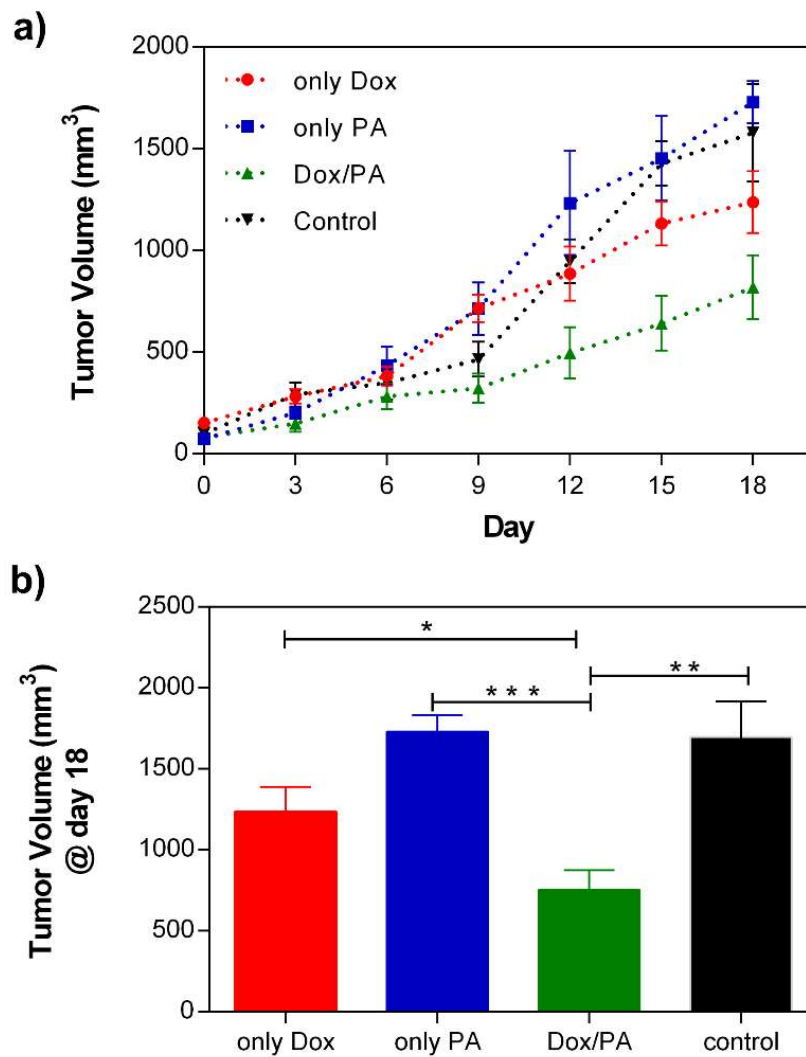


Figure 3.14 a) Tumor growth of the only Dox, only PA, Dox/PA and control groups for 18 days and b) the final tumor volume (mm³) at day 18

To reveal the effects of the administration of the Dox molecules via controlled delivery system on the tumor tissue, the caspase 3 immunostainings which is the apoptotic cell marker were performed on the tissues. Doxorubicin demonstrates its chemotherapeutic activity by inducing caspase-3 activation which mediates apoptosis and DNA fragmentation through the p53 pathway.[339] Therefore, the efficiency of the drug delivery system was evaluated by the caspase-3 immunostaining of tumor tissues. The

cleaved caspase-3 positive cells were clearly observed in tumor tissues treated with Dox/PA. Analysis of tissue sections stained with caspase-3 indicated that the sustained release of the drug molecules through the PA gels enhanced the apoptosis of the cells within the tumor tissue and facilitated the activity of the chemotherapeutic Dox molecules at the local site (Figure 3.15) compare to the local injection of the Dox molecules without controlled delivery system.

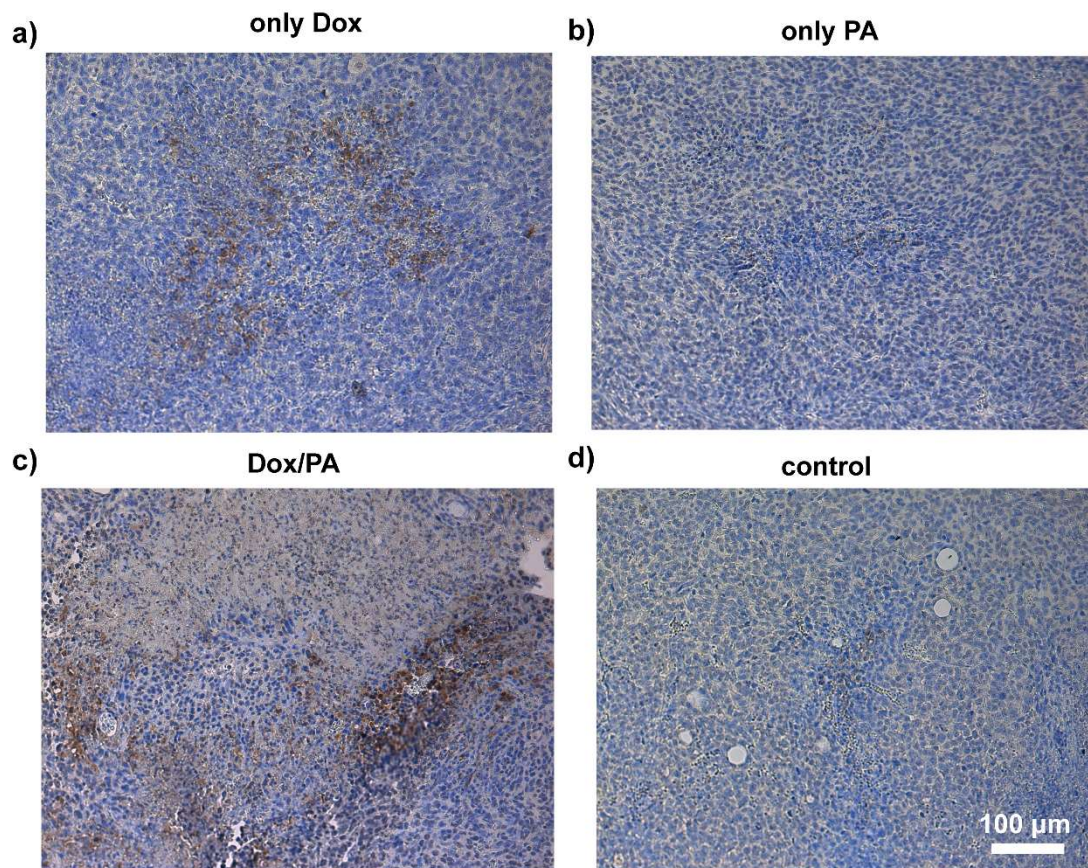


Figure 3.15 Caspase 3 immunohistochemistry staining of the tumor tissues of a) only Dox, b) only PA, c) Dox/PA and d) control groups at day 18

H&E staining of the tumor tissue and other tissues obtained from liver, kidney and spleen was also pointed the promoted activity and reduce side effects of the drug

molecules when introduced to the animals within the supramolecular PA nanofiber gels (Figure 3.16). Especially, the spleen tissue preserved its native morphology

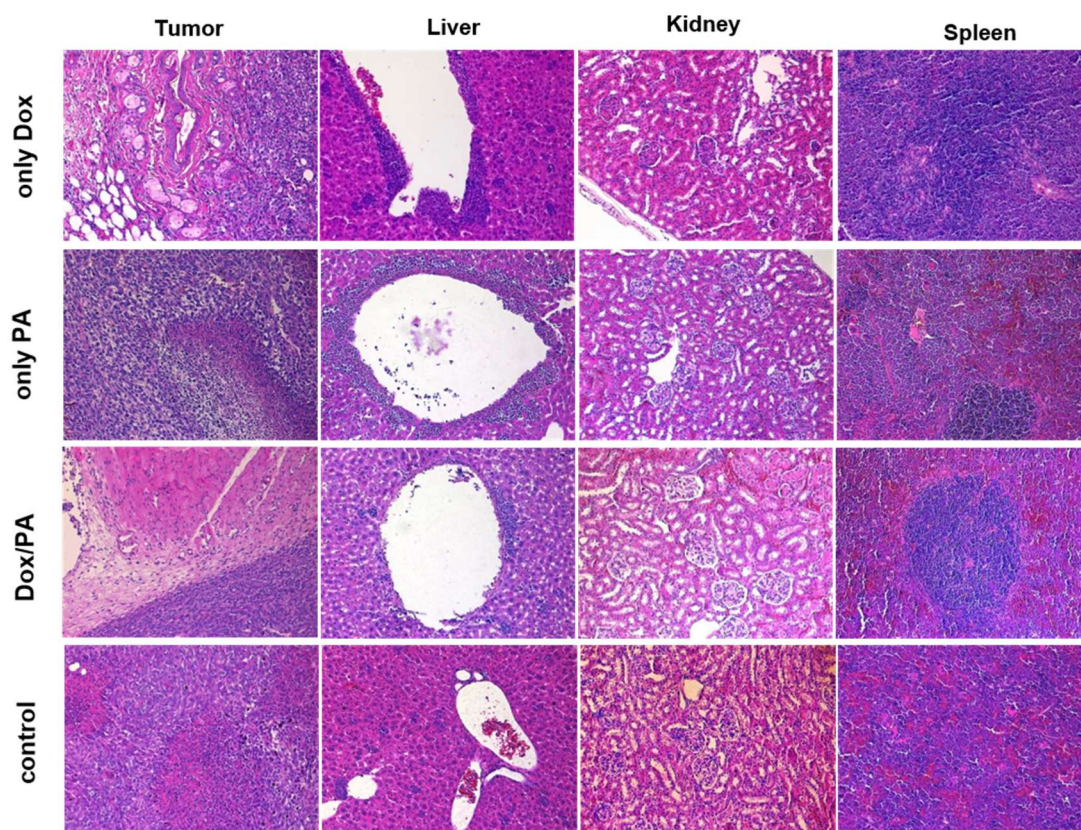


Figure 3.16 Histology staining of the different tissues obtained from the only Dox, only PA, Dox/PA and control groups at day 18

3.4 Conclusion

The advances on the biocompatible and injectable drug delivery systems can facilitate the local chemotherapeutic applications for the treatment of soft-tissue cancer types. Especially, supramolecular PA nanofiber gels are potential candidates for the prolonged local delivery of the chemotherapeutics at physiological conditions. In this study, we showed the PA gels consisting coassembled nanofibers with β -sheet secondary structure organization can form with facile assembly properties at pH 7.4 in

water due to the non-covalent interactions between the oppositely charged PA molecules. In addition, the controlled drug release characteristics of the PA nanofiber gels were modulated depending on the PA concentration; and the non-covalent interaction between the PA network and drug molecules enabled us to obtain affinity controlled release behavior in complementary to the concentration gradient triggered molecule release. Biocompatibility and biodegradability of the PA nanofiber gels also other advantages of these architectures for drug delivery. The significant decrease in tumor growth rate via injection of Dox/PA gels at *in vivo* conditions compare to the other groups also showed us the potential of the supramolecular PA nanofiber gels for the clinical applicability for the local chemotherapy applications.

Chapter 4

4. Self-Assembled Peptide Amphiphile Nanofibers and PEG Composite Hydrogels As Tunable ECM Mimetic Biomaterials

Part of this thesis is published in the following article; Reprinted from “Self-Assembled Peptide Amphiphile Nanofibers and PEG Composite Hydrogels as Tunable ECM Mimetic Microenvironment”; Goktas, M.; Cinar, G.; Orujalipoor, I.; Ide, S.; Tekinay, A. B.; Guler, M. O., *Biomacromolecules*, 2015, 16 (4), 1247-1258, with permission from American Chemical Society

4.1 Introduction

Extracellular Matrix (ECM) is highly complex and dynamic microenvironment and cells get necessary information through its heterogeneous composition such as proteins, proteoglycans and also signaling molecules found in the system.[340] It is not only physical support and protection environment for the cells but also the hierarchal architecture to orchestrate biochemical processes including cell survival, proliferation, migration and differentiation.[341] Hence, overall understanding of these properties and cell material interactions are quite important to design successful ECM mimicking biomaterials for cell culture and tissue engineering applications. There are different examples of natural and synthetic polymeric biomaterials which are designed as ECM analogs to direct cellular behavior and differentiation.[342] Within a variety of examples, hydrogels[343, 344] consisting high water content and

porous structural organization mimic native ECM properties and have been used in biomedical applications.[345-347]

Poly(ethylene glycol) (PEG) is one of the widely used synthetic polymeric building block of hydrogels which can be chemically functionalized with different crosslinkable chemical groups.[348] PEG hydrogels provide several advantages compare to the other synthetic approaches due to its good solubility, non-immunogenicity, biocompatibility and formation of the three dimensional mechanically controllable systems at mild conditions. On the other hand, the lack of bioactivity and its protein-repellent material property are the drawbacks of the PEG hydrogels for biomedical applications. Hence, the different approaches have been develop to obtain bioactivity in the PEG hydrogels to sustain cellular adhesion and viability and direct cellular activity. The chemically conjugation of ECM-derived functional epitopes such as RGD peptide was commonly used strategy via crosslinking reactions.^[349-352] This specific peptide sequence enhanced the adhesion of the cells on the PEG hydrogels and introduce the bioactivity.^[349, 353] However, the limited porosity of the PEG hydrogels results in the lack of accessibility of the biological signals through the cells and prevents the cell-material or cell-cell interactions. Although the porosity of the PEG hydrogels can be further enhanced via several approaches including freeze-drying[354], salt leaching[355] or enzymatic degradation of the hydrogel component[356]; these approaches still cannot support the homogenous and distributed pore interconnectivity and not present the physical properties of the native ECM microenvironment.

Self-assembling PA molecules can form supramolecular nanofiber gels with tunable bioactivity depending on the design of amino acids sequences. These biomaterials use

the advantages of molecular self-assembly and eliminates the drawbacks of current synthetic polymeric hydrogels without the requirement of covalent crosslinking or chemical reactions.[357] The dynamic and bioactive nature of the supramolecular PA networks also closely mimic the nanofibrous ECM organization and its biofunctionality through the incorporation of the specific amino acid residues to the PA molecules. The different bioactive moieties and ligands can be presented on the surface of one-dimensional self-assembled nanofibers within the PA gels with high density; and it can be tuned via epitope dilution using non-bioactive group bearing PA molecules for the coassembly.[358] For example, the self-assembled PA nanofibers presenting $\alpha_v\beta_3$ integrin binding RGD epitope increased the cellular adhesion the synthetic scaffolds.[359, 360] The cooperation of DGEA bioactive peptide sequence derived from collagen type-1 on the PA nanofibers promoted the osteogenic differentiation of human mesenchymal stem cells (hMSCs)[361, 362] via specifically binding $\alpha_2\beta_1$ integrin on the cell membrane[363]. Although the native biofunctionality of the self-assembled PA networks provides many opportunity to create ECM analogues architectures, their low mechanical stability due to the dynamic nature of molecular self-assembly and relatively poor control over their mechanical properties limits their usage especially for tissue engineering applications.

In the literature, hybrid hydrogel and dual-network approaches have been developed to enhance and control physical and biochemical material properties.[352] The cooperation of the covalently crosslinked polyacrylamide chains with ionically triggered alginate network resulted the formation of highly tough and stretchable hydrogels.[364] In another example, the combination of collagen network with chemically crosslinked poly(ethylene glycol)diacrylate (PEGDA) hydrogel promoted

the cellular adhesion and elongation as being biofunctional scaffolds for vascular tissue engineering.[365]

In this part of the thesis, the development of a double network composite hydrogel system to eliminate individual drawbacks of the chemically crosslinked and self-assembled synthetic polymeric biomaterials was presented. Synergistic combinations of different class of building blocks (chemically crosslinkable PEG monomers and self-assembling PA molecules) created new matrix opportunities with independently tunable biochemical, mechanical and physical properties.[34] The bioactivity was modulated via the incorporation of the self-assembling PA building blocks which formed nanofibrous functional cytoskeleton of the composite hydrogel due to the non-covalent interaction. In addition, the crosslinked PEG network sustained the mechanical stability and rigidity that was also tuned via the PEG concentration within the system.

4.2 Experimental Section

4.2.1 Materials

The chemical used for the peptide synthesis including Fmoc-Glu(OtBu)-Wang resin, Rink amide MBHA resin, Fmoc-Aps(OtBu)-Wang resin, Fmoc protected all protected amino acids, lauric acid, *N,N,N',N'*-Tetramethyl-O-(1*H*-benzotriazole-1-yl) uronium hexafluorophosphate (HBTU), diisopropylethylamine (DIEA), triisopropylsilane (TRIS) and trifluoroacetic acid (TFA) were obtained from Novabiochem, Merck, Alfa Aesar or Sigma-Aldrich. The other chemical, reagents and solvent used in materials characterizations and *in vitro* experiments were analytical grade and purchased from Invitrogen, Fisher, Merck, Alfa Aesar, and/or Sigma-Aldrich.

4.2.2 Synthesis and Characterizations of the Bioactive PA Molecules

Lauryl-Val-Val-Ala-Gly-Lys-Lys-Lys-Am (K_3 -PA), Lauryl-Val-Val-Ala-Gly-Glu-Glu-Glu (E_3 -PA), Lauryl-Val-Val-Ala-Gly-Glu-Arg-Asp (RGD-PA), Lauryl-Val-Val-Ala-Gly-Glu-Gly-Asp-Gly-Glu-Ala-Am (DGEA-PA) were synthesized via Fmoc-solid phase method. As a solid support, Rink amide MBHA resin was used for the synthesis of K_3 -PA and DGEA-PA while Fmoc-Glu(OtBu)-Wang resin (100-200 mesh) and Fmoc-Asp(OtBu)-Wang resin (100-200 mesh) were used for E_3 -PA and RGD-PA, respectively. The carboxylate group of 2 mole equivalents of amino acid was activated by 1.95 mole equivalents of HBTU, and 3 mole equivalents of DIEA on the 1 mole equivalent of the solid support. Prior to the amino acid couplings which was carried out for at least 2 h, Fmoc protecting groups were cleaved with 20% (v/v) piperidine/dimethylformamide (DMF) mixture for 20 min; and that step was repeated at each coupling. To the conjugation of the alkyl tail to the peptide domain, lauric acid was used and the reaction was performed similar to the amino acid coupling. For the protection from the side reactions, 10% (v/v) acetic anhydride/DMF mixture was used to acetylate the unreacted amine groups for 30 min. The cleavage solution prepared as the mixture of 95% TFA, 2.5% water, 2.5% TRIS was used to cleave the amino acid side chain protecting groups and remove the PA molecules from the solid support for 3 h. After the cleavage step, the resins were washed with dichloromethane (DCM) to obtain the synthesized PA molecules in the solution phase. The excess organic solvent and TFA was evaporated using the rotary evaporation system, and then cold diethyl ether was added onto the synthesized PAs for the precipitation and sedimentation for overnight. The PA precipitate was then centrifuged at 4 °C and collected. The

precipitate was dissolved in distilled water and freeze-dried at -80 °C. The water content was removed via lyophilization and the dried PA powders were obtained.

The purity of the synthesized PAs was determined using Agilent 6530 quadrupole time of flight (Q-TOF) mass spectrometry with electrospray ionization (ESI) source connected to reverse-phase analytical high performance liquid chromatography (HPLC) system. The further purification was carried out with Agilent 1200 series preparative HPLC system.

4.2.3 PA/PEG Composite Hydrogels Preparation

The stock solutions of Poly(ethylene glycol) dimethacrylate (PEGDMA) with $M_n=550$ and 1% (w/v) photoinitiator, 2,2'-Azobis (2-methyl-propionamide) dihydro-chloride were prepared in distilled water. 3% (w/v) stock solutions of PAs were also prepared at neutral pH in water. Firstly, E₃-PA, RGD-PA or DGEA-PA which carries negatively charged amino acids residues was mixed with the stock solutions of PEGDMA consisting the initiator for UV crosslinking reactions. Then, K₃-PA consisting positively charged lysine residues at neutral pH PA was added to the solution to sustain self-assembly of PAs via charge screening and form one-dimensional nanofibrous architecture within the composite system due to the non-covalent interactions. The mixtures containing both PEGDMA, the initiator and the self-assembled PA network were put into the wells of 48 or 96 well-plates to obtain chemically crosslinked composite system exposing to ultraviolet (UV) light at 365 nm wavelength for 15 min. The 8 Watt UVP™ UVLMS-38 EL series UV lamp was used for the chemical crosslinking, and it was placed to the top of the cell culture plates with an approximately 0.5 cm distance. 1:1 volumetric ratio of PEGDMA to mixture of PAs was obtained within the composite hydrogels to trigger self-assembly of the PA

building blocks. Hence, the final PA concentrations within the composite hydrogels were 1.5% (w/v) for all samples. Since the self-assembly of the PA molecules was dependent on the complete charge neutralization of the system due to the electrostatic interactions, the volumetric ratios of oppositely charged PA mixtures were decided as 3:4 for E₃-PA:K₃-PA, 3:2 for RGD-PA:K₃-PA, 1:1 for DGEA-PA/K₃-PA mixtures within the system. The final crosslinkable polymer concentrations were determined as 4%, 8% and 12% (w/v), and initiator concentration was 0.1% (w/v). For the preparation of control hydrogels (without self-assembled PA network), the stock solutions of PEGDMA were mixed with the distilled water at the same volume of PA solutions and the final polymer concentrations were kept as similar with the other groups.

4.2.4 Transmission Electron Microscopy Imaging

The self-assembled PA nanofibers were obtained via mixing the oppositely charged PA solutions (1.5% (w/v)) at the volumetric ratios as 3:4 for E₃-PA:K₃-PA, 3:2 for RGD-PA:K₃-PA, 1:1 for DGEA-PA/K₃-PA as given above. Then, the samples were diluted using the distilled water and dropped casted on the TEM grid for uranyl acetate staining with the 2% (w/v) dye solution. The excess dye was removed via washing of the grid with the distilled water. After the air-drying of the samples, the imaging was performed using A FEI Tecnai G2 F30 TEM instrument.

4.2.5 Scanning Electron Microscopy Imaging

The structural organization and physical properties of the composite hydrogels and the control groups were analyzed using scanning electron microscopy (SEM). The composite hydrogels and control groups were prepared according to the protocol given in the section 4.2.3 in details on the surfaces of the cleaned silicon wafers. After the

sample preparation, the water content within the hydrogels was replaced with the gradually increasing concentrations of ethanol prior to the drying of the samples with a Tourismis Autosamdri-815B critical-point-drier (CPD) to keep the nanofibrous architecture network structure. After the CPD procedure, the samples were covered with 4 nm electron conductive Au/Pd coating using a sputter; and then SEM imaging was carried out using an FEI Quanta 200 FEG scanning electron microscope equipped with an ETD detector.

4.2.6 Attenuated Total Reflectance-Fourier Transform Infrared Spectroscopy (ATR-FTIR)

The composite hydrogel system (E₃/PEG) and the control PEG group without nanofibrous architecture were prepared according to the procedure discussed above. Before the analysis, the hydrogels were dried in ambient air at 25 °C for two days. The crosslinking reaction, the newly formed covalently crosslinked bonds and the secondary structure organization of the self-assembled PA network within the composite hydrogels were analyzed obtaining FTIR spectra between 800 to 4000 cm⁻¹, with a 16 scan per sample cycle using a Thermo Scientific NICOLET 6700-FTIR system attached with a universal ATR accessory.

4.2.7 Brunauer-Emmett-Teller (BET) Analysis

BET analysis of the dried composite hydrogel system (E₃/PEG) and the control PEG network was conducted to estimate pore size distribution, total pore volume and specific surface of the samples. The nitrogen adsorption isotherms obtained via this technique was used for the determination of the critical physical parameters related with the porosity of the synthetic polymer hydrogels in the literature.[366, 367] The samples were prepared following the same drying procedure given at SEM imaging

part. For the analysis, the dried networks were degassed at 150 °C for 4 h; and then nitrogen adsorption isotherms were collected at 77 K. The data analysis was performed based on quenched solid density functional theory (QSDFT) and the structural parameters including total pore volume and specific surface area were estimated.

4.2.8 SAXS Analysis of the PA/PEG Composite Hydrogels

The samples (E₃/PEG composite hydrogel and 4% (w/v) PEG control group without containing PA network for the SAXS analysis were formulated according to the protocol given above. However, the crosslinked reactions using with a UV light source at 365 nm were carried out within in quartz capillaries instead of the cell culture plates for 15 min to obtain the hydrogels. The measurements were conducted under Nickel-filtered CuK α -radiation ($\lambda=1.54$ Å), originating from a Philips X-Ray generator with copper anode operating at a power of 2 kW (50 kV and 40 mA). A SWAXS system with Kratky optic HECUS (Hecus X-ray systems, M. Braun, Graz, Austria) and attached to a linear collimation system was used for the SAXS measurements. The scattering data in small angle q ranges ($0.004-0.55$ Å⁻¹) was collected via a linear-position sensitive detector OED 50-M (M. Braun, Garching, Germany) with 1024 channel resolution. Prior to the analysis, silver behenate was used for the calibration of the system. The distance between the channels were determined as 54 μ m; and the sample was placed to 28.1 cm far behind to the detector, respectively. The analysis was performed at the room conditions with 600 s exposure time. ASAV2.3 (HECUS M. Braun, Graz, Austria) program was used for the scattering data acquisition.

4.2.9 Oscillatory Rheology

The viscoelastic behavior of the composite hydrogels, the control PEG gels and self-assembled only PA gels were analyzed using an Anton Paar Physica RM301

Rheometer with a 25 mm parallel-plate measuring device attached to the equipment. The sample volume was determined as 300 μL ; and the composite hydrogels and only PEG control were prepared within 48-well cell culture plates; and then they were placed on the stage of the equipment. On the other hand, PA gels were prepared on the stage mixing the individual PA solutions at given volumetric ratios above. The distance between the measuring device and the samples was determined as 0.5 mm. Initially, time sweep analysis at constant angular frequency (10 rad s^{-1}) and shear strain (0.01%) was conducted on the gels to reveal gelation behavior at the room temperature. At the end of the time sweep, the gels were equilibrated; and amplitude sweep measurements were continued on the same sample to reveal the linear viscoelastic range (LVR) of the gels at constant angular frequency of 10 rad s^{-1} with logarithmically ramping the strain amplitude from 0.01 to 1000%.

4.2.10 *In Vitro* Studies

All *in vitro* experiments including cellular viability, adhesion, spreading, immunocytochemistry (ICC) staining and quantitative Reverse Transcription-Polymerase Chain Reaction (qRT-PCR) gene expression analysis were carried out using Saos-2 human osteosarcoma cells (ATCC®HTB-85™) cultured in 75 cm^2 cell culture flasks using Dulbecco's Modified Eagle Medium (DMEM) supplemented with 10% Fetal Bovine Serum (FBS), 1% penicillin/streptomycin and 2 mM L-glutamine. The cells were incubated within a humidified chamber supplied with 5% CO_2 at 37 °C. When 80 to 90% confluency was reached, the cells were passaged using trypsin and EDTA reagents. The cell culture medium was replaced with the freshly prepared DMEM for every 3–4 days. The osteogenic medium consisting DMEM additional with 10% FBS, 10 mM β -glycerophosphate, 50 $\mu\text{g mL}^{-1}$ ascorbic acid and 10 nM

dexamethasone was used for the osteogenic differentiation experiments including ICC stainings and qRT-PCR analysis.

All samples used in the in vitro experiments were prepared according to the sample preparation protocol given above. Differently, the hydrogels were incubated within the PBS overnight prior to the cell culturing. The viability of the cells cultured on the surfaces of the composite hydrogels or only PEG at a density of 1.5×10^4 cells/cm² was analyzed using Calcein-AM/Ethidium homodimer staining method in 48 well cell culture plates. As a positive control, the cells were also cultured on the surfaces of tissue culture plates (TCP). After the incubation of the cells on the surfaces of the samples placed within the media for 3 days, the incubation medium was removed from the top of the samples; and all samples were washed with PBS. Then, the PBS solution consisting 2 μ M Calcein-AM/Ethidium homodimer (Invitrogen) was transferred to the wells and incubated for 20–30 min at room conditions. Cellular imaging at 10X magnification was performed using a fluorescence microscope taking the random images from each well.

For the cellular viability within 3D conditions, the cells were encapsulated within into 200 μ L of 3D matrices prepared with DMEDM instead of water. Prior to the crosslinking reaction, the cell suspension was mixed with PEGDMA solution consisting the initiator; and then the PA solutions were added into the mixture at the determined volumetric ratios. After the preparation of pre-crosslinked samples, the system consisting PEGDMA monomers with the initiator, self-assembled PA architectures and the cells were placed into the small tubes and exposed to UV light at 365 nm for 15 min for the final crosslinking of the 3D gels. Then, synthecon RCCS-4H bioreactor was used to culture the PEG and RGD/PEG composite gels with Saos-

2 cells sustaining 3D microenvironment with rotating vessels. Calcein-AM/Ethidium homodimer staining was also performed to visualize live/death cells within the matrices after 7 days cultivation.

The adhesion behavior of the cells on the PEG and PA/PEG hydrogels were also determined by quantifying the attached cells on the hydrogel surfaces stained with Calcein-AM. For these experiments, the cell density on the hydrogels were determined as 5×10^3 cells/cm² in serum-free culture conditions with DMEM media supplemented with 1% penicillin/streptomycin and 2 mM L-glutamine incubating at the similar cell culture conditions given above. After the cell culturing for 24, 48 and 72 h, the non-adhered cells were removed by washing the gels with away with PBS. Then, the staining of the cells was performed using Calcein-AM. The fluorescence images of the adhered cell numbers on the gels were analyzed using Image J program to count the cell numbers.

For the spreading and morphological analysis of the cells cultured on the PEG and PA/PEG hydrogels for 72 h, the samples were prepared similar to the adhesion assay. On the other hand, the cells were treated with 3.7% formaldehyde for 15 min for the fixation and permeabilized with 0.1% Triton X-100 for 10 min before the staining. TRITC-conjugated phalloidin (Invitrogen) prepared within 1X PBS was placed onto the gels for the staining of the actin filaments for 20 min. For the fluorescence imaging of the actin filaments, Zeiss LSM 510 confocal microscope was used. The spreading areas of the cells were quantified using Image J program.

For the analysis of the osteogenic differentiation potentials of the cells cultured on the PEG and PA/PEG hydrogels, ICC stainings were performed. The cells cultured with differentiation medium were fixed using 4% formaldehyde for 15 min and the cell

membranes were permeabilized with 0.5% Triton-X for 10 min at room temperature. As a blocking solution, 3% (w/v) BSA prepared in PBS was placed onto the samples and incubated for 1 h. Rabbit-raised, anti-human, RUNX2 and COL1 primary antibodies and a goat-raised, antirabbit, IgG H&L DyLight 488 conjugated secondary antibody (Abcam) were used for ICC staining. The confocal imaging of the stained cells was performed using Zeiss LSM 510 confocal microscope.

qRT-PCR technique was used to determine RUNX2 and COL1 gene expression profiles of Saos-2 cells cultured on the PEG and PA/PA composite hydrogels for 3 and 7 days. The RNA isolation from the differentiated cells was carryout out using TRIzol reagent (Ambion). The amount and the purity of the isolated RNA was determined using Nanodrop 2000 (Thermo Scientific). Primer 3 software was used to design the primer sequences. The PCR reaction was continued with a temperature cycling as 55 °C for 5 min, 95 °C for 5 min, 40 cycles of 95 °C for 15 s, T_m (58.0 °C for RUNX2 and GAPDH, 60.0 °C for COL1) for 30 s, and 40 °C for 1 min. The expression of the GAPDH gene was quantified as control, and RUNX2 and COL1 expressions were normalized to the control gene.

The experiments were conducted at least twice, independently and at least three replicates for each group were prepared. The error between the replicates were presented as \pm standard error of means (s.e.m). One-way or two-way analysis of variance (ANOVA) methods were applied for statistical analyses of the results, whichever applicable. The significance between the groups were concluded when a *P*-value of less than 0.05.

4.2.11 Controlled Protein Release Experiments

For the preparation of the protein encapsulated PEG and E₃/PEG composite hydrogels consisting 4%, 8% or 12% (w/v) PEGDMA with a final concentration of 0.1% (w/v) initiator and 1.5% (w/v) self-assembled PA network, the same procedure given above was followed. Differently, the stock solution of bovine serum albumin (BSA) (10 mg/mL) was added into the mixture before the addition of PA solutions. The final BSA concentration in the composite hydrogels was determined as 2 mg/mL. The distilled water was added onto the samples to obtain concentration gradient and sustain release of the proteins through the samples. The release experiments were carried out at the room temperature. For the quantification of the released BSA amount, the Bradford assay was performed to obtain standard BSA concentration dependent UV absorbance graph as a calibration curve. 2 mg/mL stock solution of BSA was prepared; and it was diluted up to 31.3 µg/mL with serial dilutions to prepare the standard samples. The Bradford reagent (Bio-Rad) was diluted 5-fold in water. 5 µL of the standards were put into the wells of 96-well plate and then, 250 µL of the diluted Bradford reagent was added to the all wells. The samples with the reagent were incubated for 15 min. The UV absorbance at 595 nm was measured for each sample; and the calibration curve was obtained. The same procedure was followed to determine the released BSA amount at the determined time intervals converting the measured absorbance to the BSA concentration using the standard calibration curve.

4.3 Results and discussion

4.3.1 Design, Synthesis and Characterizations of the Bioactive PA Molecules

In this study, four different PA molecules including negatively charged E₃-PA, RGD-PA, DGEA-PA and positively charged K₃-PA (Figure 4.1) were designed and synthesized using Fmoc-solid phase synthesis method. The liquid chromatography-mass spectrometry (LC-MS) results of the synthesized PAs were given in Figure 4.2. As it was seen in LC histograms of the PA molecules, the purities of the all samples were higher than 90%.

All PA molecules consist of lauryl tail, beta-sheet forming region (-VVAG-) and the charged hydrophilic segments such as integrin binding bioactive -RGD- or -DGEA-, non-integrin binding bioactive -EEE- or non-bioactive -KKK- amino acid residues.

The self-assembly of the bioactive negatively charged PA molecules (E₃-PA, RGD-PA, DGEA-PA) into one-dimensional supramolecular fibers were triggered upon addition of the negatively charged K₃-PA at different volumetric ratios determined based on the overall charge neutralization of the each system. TEM images of the all PA combinations given in Figure 4.3 showed the similar nanofiber formation and structural properties. The details of the PA mixing ratios, net charges of PA molecules at physiological conditions were given in Table 4.1 and Table 4.2.

Table 4.1 Bioinspired self-assembling PA building blocks

PA sequence	Nomenclature	Net charge*
Lauryl-VVAGEEE	E ₃ -PA	-4
Lauryl-VVAGKKK-Am	K ₃ -PA	+3
Lauryl-VVAGERGD	RGD-PA	-2
Lauryl-VVAGEGDGEA-Am	DGEA-PA	-3

* Theoretical net charge at pH 7.4.

Table 4.2 Nomenclature and composition of PEG (w/o PA nanofibers (PNFs)) and PA/PEG composite hydrogels

Nomenclature	Nanofiber composition	Molar mixing ratio
PEG (w/o PNFs)	-----	-----
E ₃ /PEG	E ₃ -PA/K ₃ -PA	3:4
RGD/PEG	RGD-PA/K ₃ -PA	3:2
DGEA/PEG	DGEA-PA/K ₃ -PA	1:1

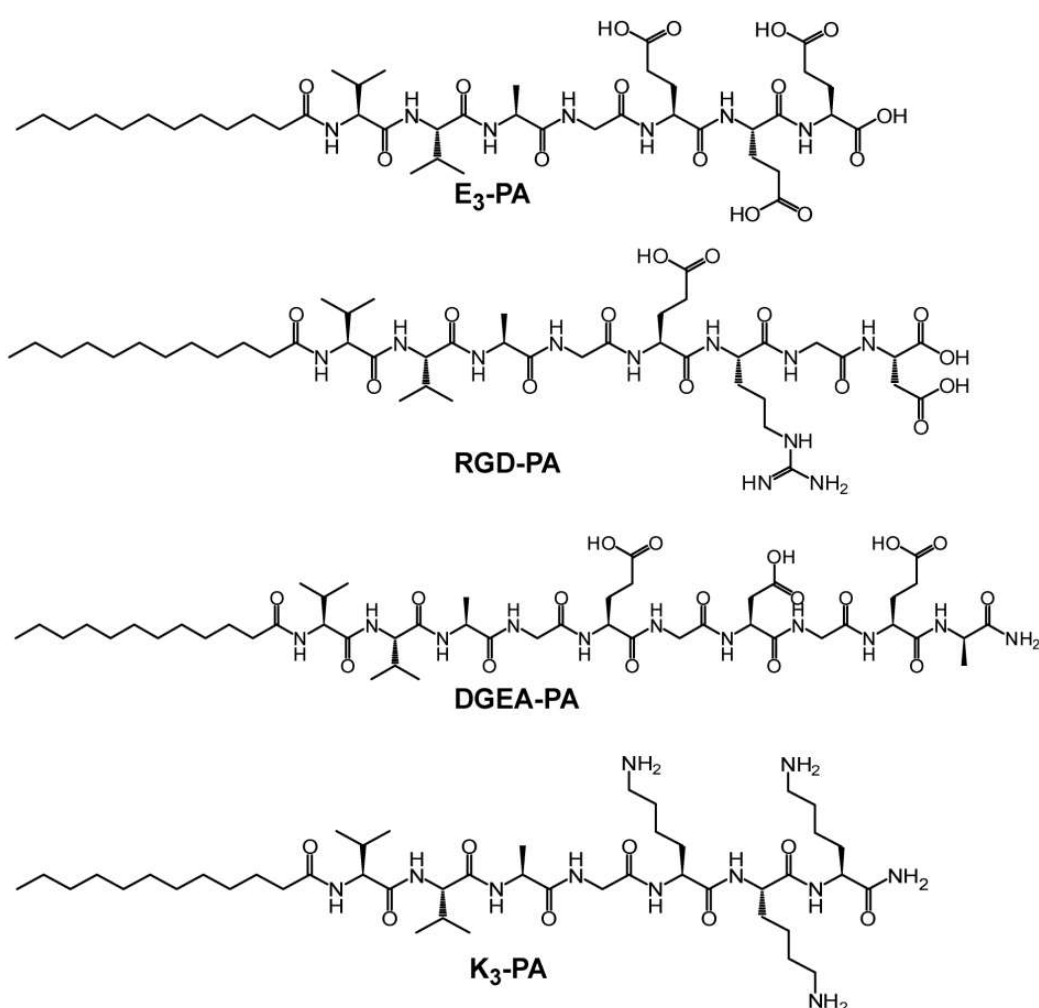


Figure 4.1 Chemical representations of the synthesized PA molecules

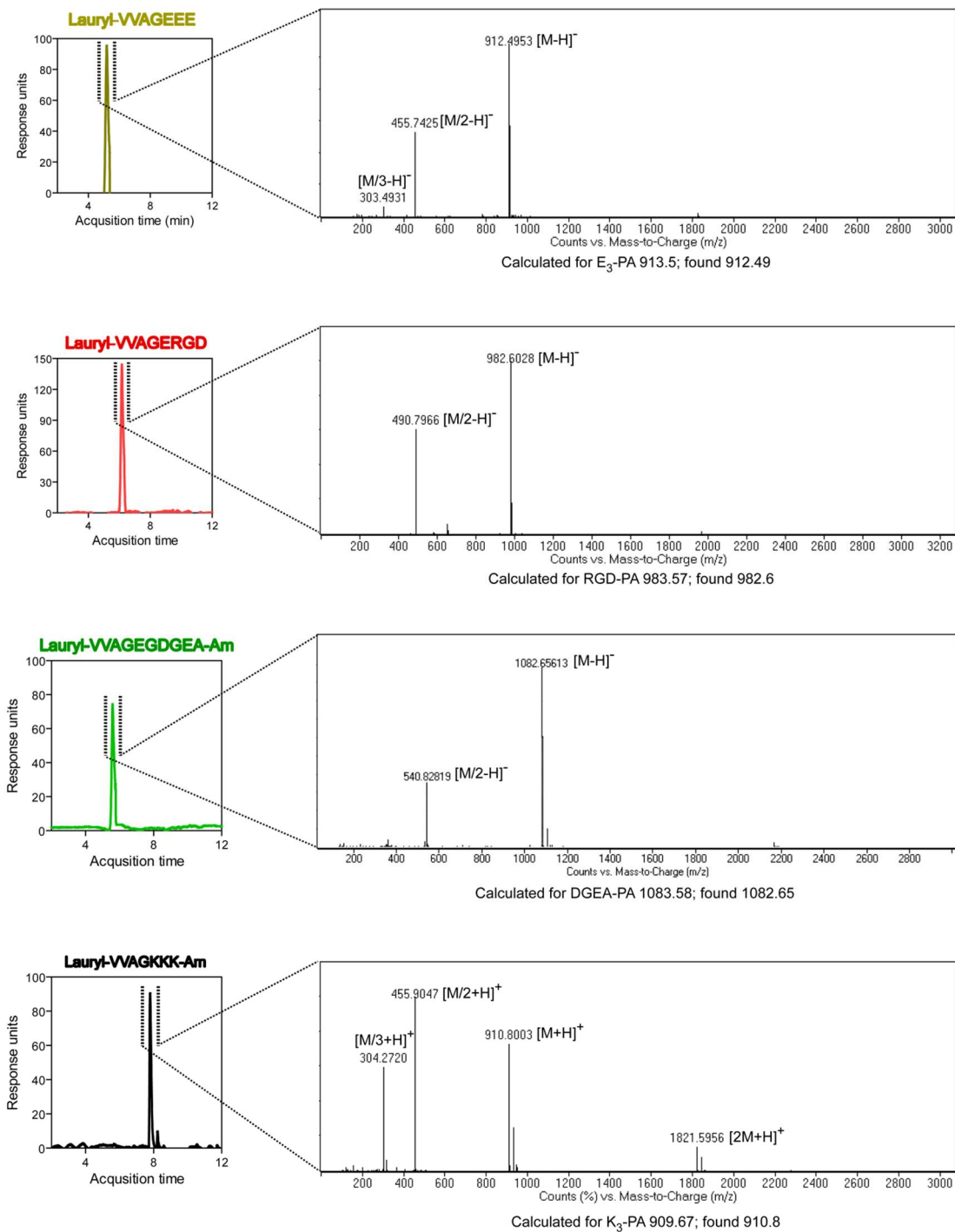


Figure 4.2 Liquid chromatography-mass spectrometry (LC-MS) results of the synthesized PAs

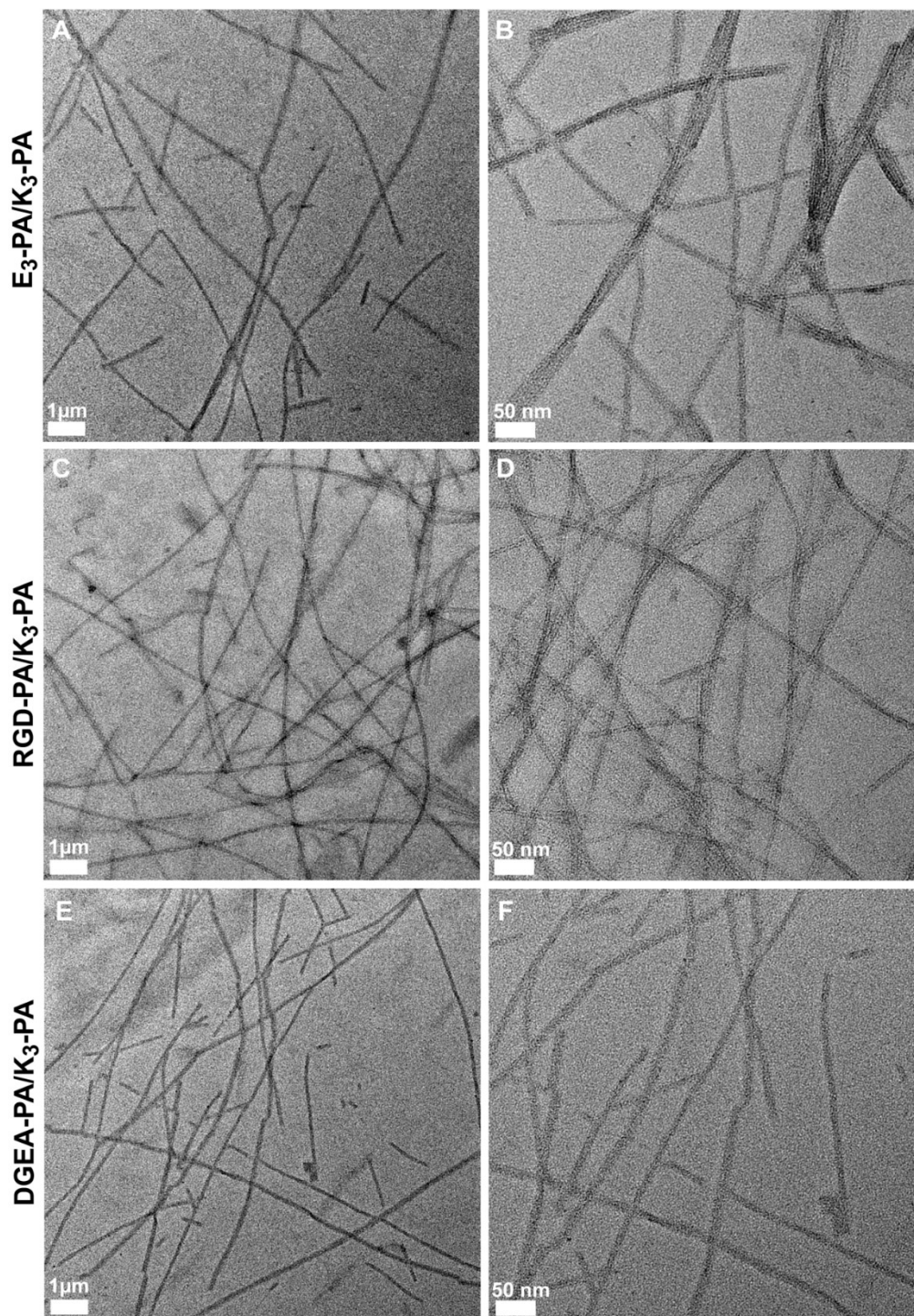


Figure 4.3 Transmission Electron Microscopy (TEM) images showing the nanofiber assembly of PA combinations. A), B) E₃-PA/K₃-PA; C), D) RGD-PA/ K₃-PA; E), F) DGEA-PA/ K₃-PA

4.3.2 Chemical and Physical Characterizations of the PA/PEG Composite Hydrogels

To obtain PA/PEG composite hydrogels, crosslinkable polyethylene glycol dimethacrylate (PEGDMA, $M_n=550$) was selected due to its biocompatibility and non-immunogenicity. Furthermore, the crosslinking reaction is quite rapid and can be carried out at physiological conditions that provide an advantage for cell encapsulation and the usage of the scaffolds for biomedical applications. The polymer concentration within the hydrogels were determined as 4%, 8%, and 12% (w/v) to obtain a stiffness range for the mechanical properties of the composite hydrogels.

To fabricate nanofibrous composite hydrogels with independently tunable mechanical and biochemical properties, a simple method was developed (Figure 4.4). Initially, the photoinitiator solution was mixed with the PEG solutions prepared at the different concentrations. Then, negatively charged PA solutions (3% (w/v)) was added into the system; and the self-assembly of the PA molecules was triggered via addition of the positively charged K_3PA solution, separately. The final PA concentration within the composite system was determined as 1.5% (w/v) for all combinations. The PA/PEG solutions were transferred to the cell culture plates immediately without any incubation step, and exposed to ultraviolet (UV) light at 365 nm wavelength for 15 min to induce photo-polymerization.

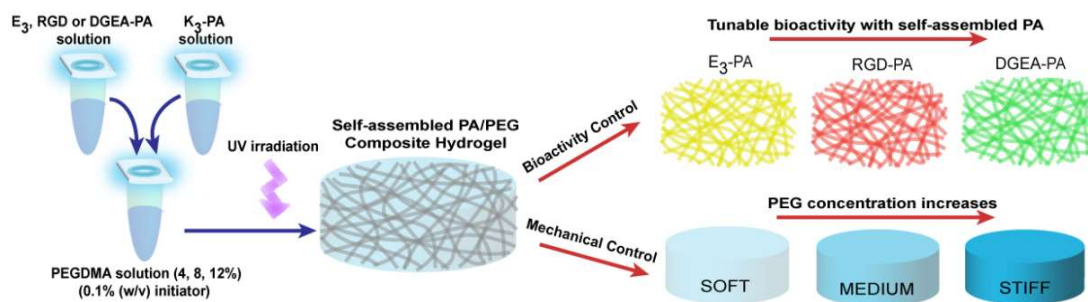


Figure 4.4 Schematic representation of the fabrication approach for the PA/PEG composite hydrogels

PEGDMA monomers within the hydrogels were crosslinked via radical polymerization reaction which continued with the additional crosslinking of the system into a branched polymeric architecture[368] (Figure 4.5a). Moreover, ATR-FTIR analysis on the samples also indicated the formation of the self-assembled PA network with β -sheet secondary structure organization[369] and the crosslinked methacrylate groups[368] within the hydrogels (Figure 4.5b). The peaks on the FTIR spectra corresponded to Amide II band ($\sim 1545\text{ cm}^{-1}$) and Amide I band ($\sim 1630\text{ cm}^{-1}$) due to presence of self-assembled PA network[369] and C=O stretching ($\sim 1738\text{ cm}^{-1}$)[368] due to stretch of a saturated aliphatic ester (crosslinked methacrylate chains).

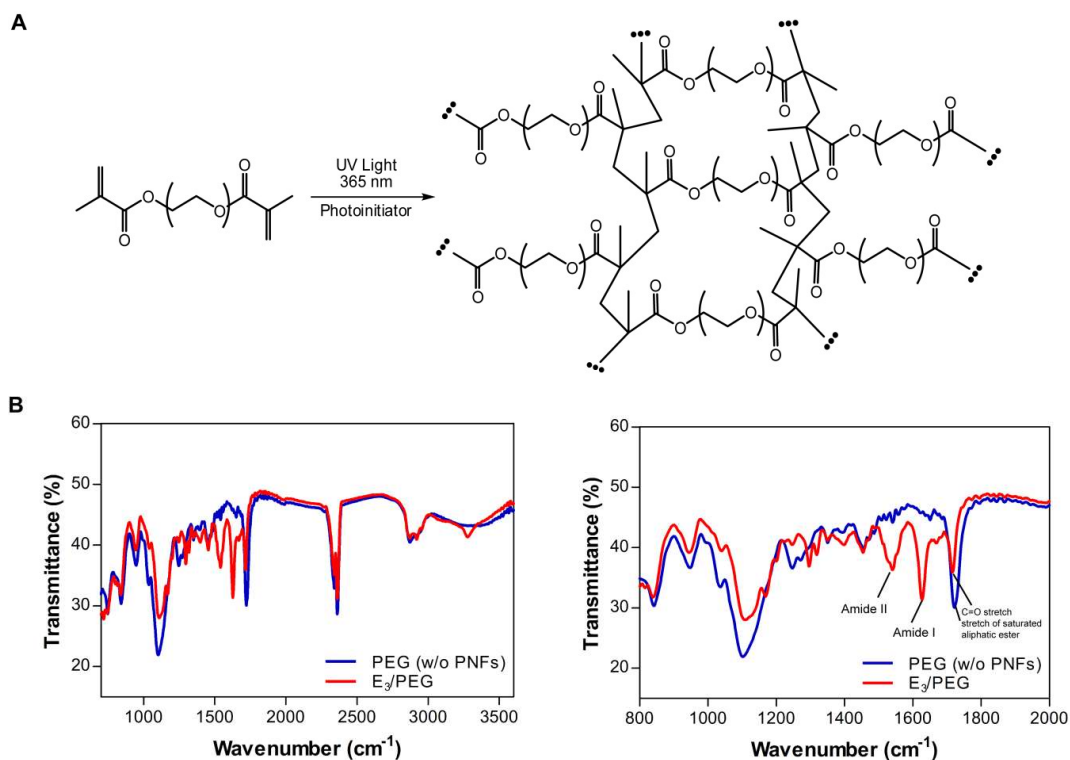


Figure 4.5 a) The schematic of the crosslinking reaction; and b) FTIR spectra of PEG (w/o PNFs) and E₃/PEG samples after 15 min of UV crosslinking

SEM imaging of the hydrogels clearly indicated that the self-assembly of the oppositely charged PA molecules into the bioactive nanofibrous structures within the composite hydrogels increased the porosity of the scaffolds compare to the PEG network (w/o PA nanofibers (Figure 4.6). Although the bioactivity of the resulting composite hydrogels were different due to the integration of different bioactive epitope to the PA molecules, the structural organization and nanofibrous morphology were similar for the all composite hydrogel groups (Figure 4.6).

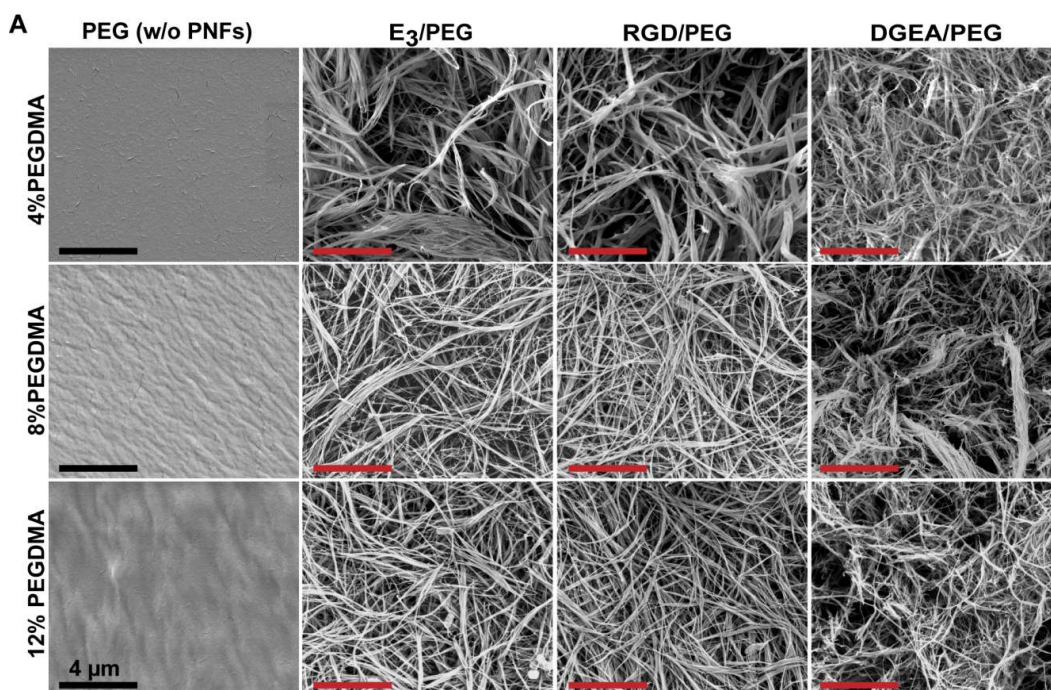


Figure 4.6 SEM images of PEG (w/o PA nanofibers, PNFs) and PA/PEG composite hydrogels (scale bars are 4 μm)

The porous nature of the hydrogels were quantitatively determined using Brunauer-Emmett-Teller (BET) method[366, 367]. The technique enable us to analyze the samples reporting pore size distribution, cumulative pore volume and specific surface area within the hydrogels which were dried using CPD device to prevent the nanofibrous architecture. The hydrogels prepared at 4% (w/v) polymer concentration were not be examined due to the high water content and disregarded for the analysis. The addition of the self-assembled nanofibrous PA network within the hydrogel with a composite approach led to significant increase in both total pore volume and specific surface areas of the samples at both polymer concentrations (Figure 4.7). Furthermore, the PA/PEG composite scaffold had a wide range of pore size distribution between 5 to 35 nm (Figure 4.8). That mesoporous pore distribution can enhance the cell-material

interactions and provide suitable environment for the encapsulation of protein therapeutics.^[370, 371]

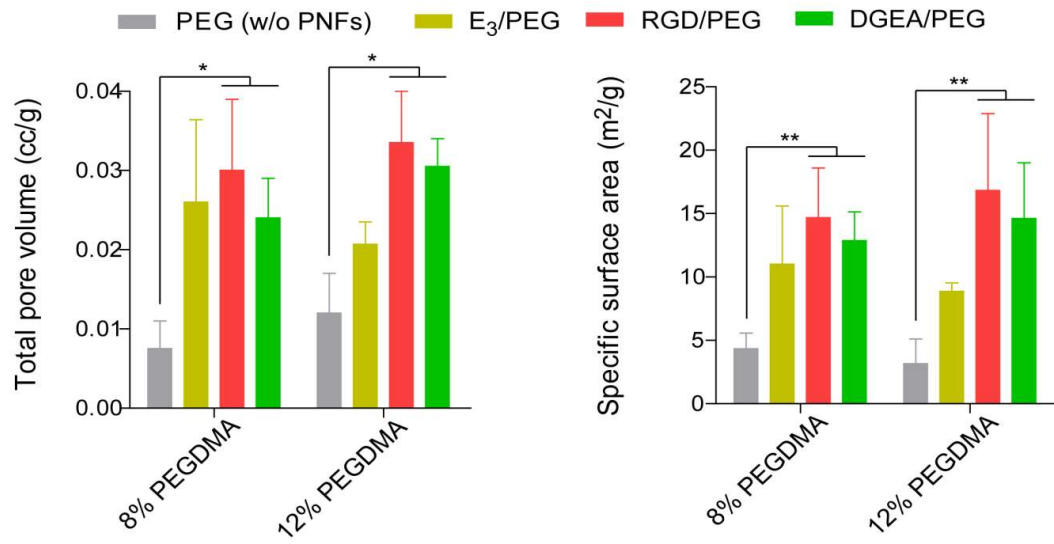


Figure 4.7 Total pore volume and specific surface area of the hydrogels.

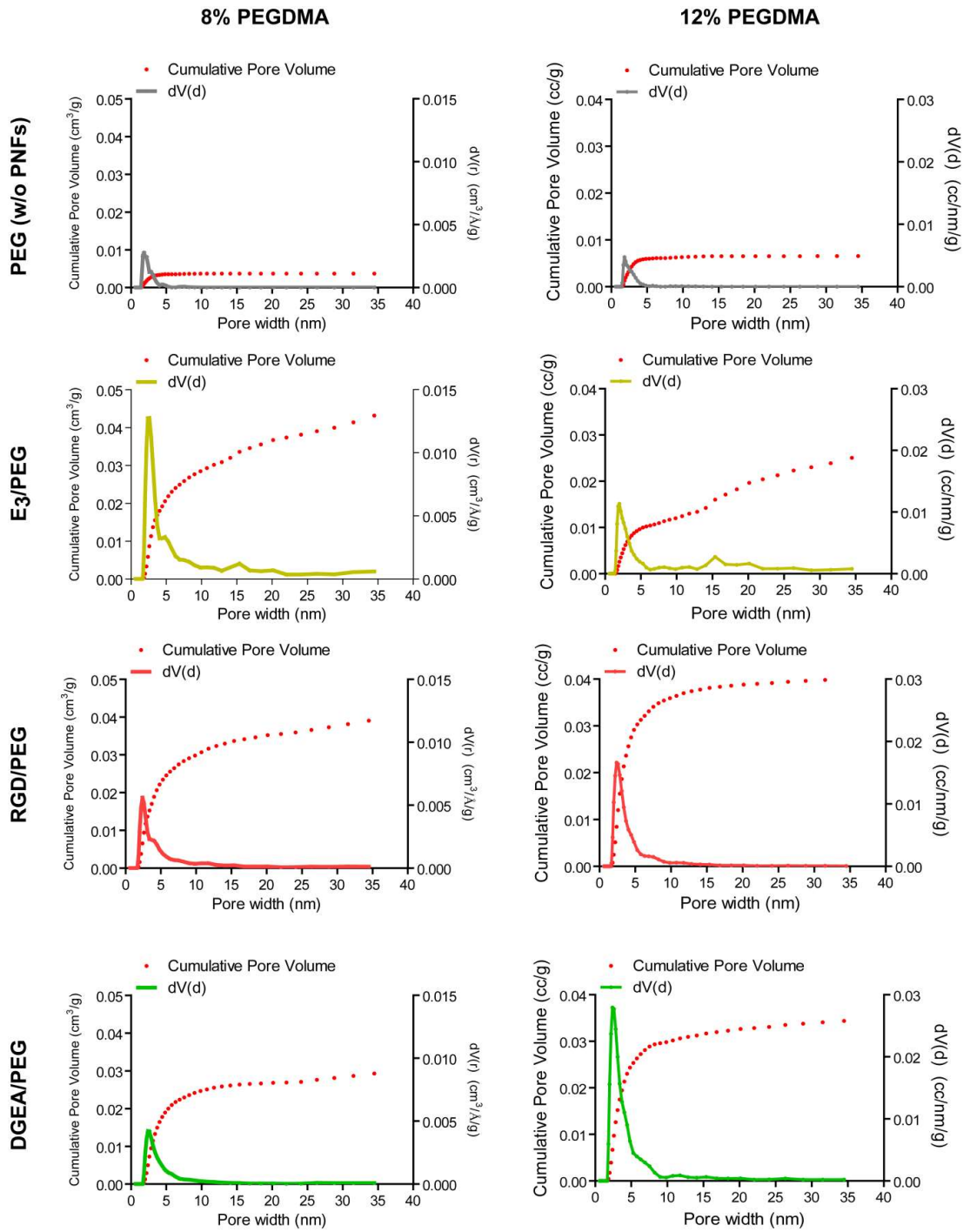


Figure 4.8 The pore size distributions and cumulative pore volumes of only PEG and PA/PEG composite hydrogels

SAXS experiment was performed since the technique allows the analysis of the samples at native conditions without any manipulation. 4% (w/v) PEG (w/o PA nanofibers) and E₃/PEG composite hydrogels were prepared in quartz capillaries with a similar approach to preparation of 2D hydrogels. After loading of 4% (w/v) PEG (w/o peptide nanofibers) and E₃/PEG composite systems into the quartz capillaries, the samples were exposed to ultraviolet (UV) light at 365 nm wavelength for 15 min for the formation of crosslinked hydrogels, and then SAXS analysis was performed using these samples without any dehydration step. Complementary to SEM and BET analysis, SAXS results also showed us nanofibrous organization within the composite hydrogel and the scattering data of the composite hydrogel was best fitted to a flexible cylinder-polydisperse length model for the cylindrical nanostructures (Figure 4.9 and Table 4.3).[288, 289] On the other hand, the ordered structural organization or aggregation was not obtained for the only PEG hydrogel as a control. The details of the structural model that the scattering data was fitted and the fitting procedure were discussed below in details.

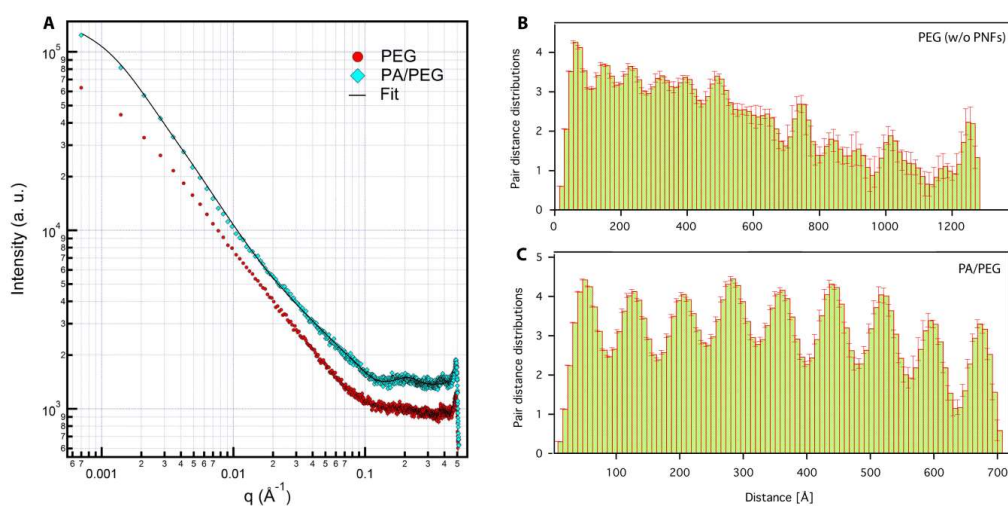


Figure 4.9 a) The scattering data and fitting model of the PEG and PA/PEG composite hydrogels with (b, c) the PDD histograms of the samples

Table 4.3 Structural results obtained from the fitting process of E₃/PEG scattering data using flexible cylinder-polydisperse length model

Fitting Results (Flexible cylinder-polydisperse length model)	E₃/PEG
Scale	1.2
Contour Length, L (nm)	276.71±1.62
Polydispersity of Contour Length	0.09
Kuhn Length, b (nm)	83.60 ± 0.75
Length of cylinder, L _p (nm)	41.83 ± 1.99
Radius, R (nm)	5.53 ± 0.12
SLD cylinder (Å ⁻²)	2.3×10 ⁻⁵
SLD solvent (Å ⁻²)	9.3×10 ⁻⁶

Moore's indirect Fourier transform method was used in the fitting process of 4% (w/v) PEG (w/o PA nanofibers) scattering data to reach real space structural information since the sample did not have structural organization and defined morphology.[372] In addition, flexible cylinder-polydisperse length model which was convenient to the nano-scale organization of E₃/PEG composite hydrogel was used to determine nano-structural information.[288, 289] The acceptable χ^2 values of 2.9 (for Moore.) and 1.4 (for Flex.Cyl.) indicate high-quality fitting and successful refinements of the scattering data.

In the model given in Figure 4.10 below, the form factor for a flexible cylinder with a circular cross section and a scattering length density were calculated. Polydispersity of the length was determined using a Schulz distribution. The non-negligible diameter of the cylinder was included accounting for excluded volume interactions within the walk of a single cylinder. Inter-cylinder interactions were neglected. The form factor is normalized by the particle volume such as;

$$P(q) = \frac{\text{scale} \langle f^2 \rangle}{\text{Vol}} + Bkg$$

where $\langle \rangle$ is an average over all possible orientations of the flexible cylinder. An instrument resolution smeared version was also provided. The chain of contour length, L , (the total length) can be described a chain of some number of locally stiff segments of length L_p . The persistence length, L_p , is the length along the cylinder over which the flexible cylinder can be considered a rigid rod. The Kuhn length (b) used in the model is also used to describe the stiffness of a chain, and is simply $b=2L_p$. Polydispersity was included integrating the form factor over a Schulz distribution of cylinder length. The integration has been normalized by the second moment of the length distribution. This ensures that the invariant is constant when the polydispersity is varied and all other structural parameters are held fixed. The returned value is in units of $[\text{cm}^{-1}]$, on absolute scale.

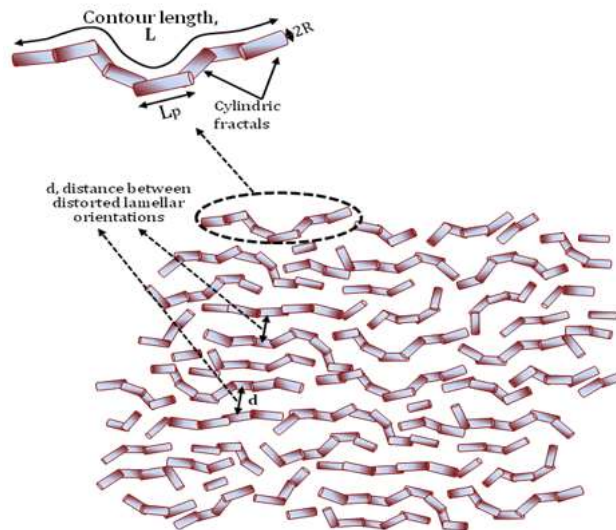


Figure 4.10 Illustration of the structural organization of E₃/PEG composite hydrogel using flexible cylinder-polydisperse length model

SLD (Scattering Length Density) is a measure of electron density and electron density contrast related scatters and Scattering contrast ($\Delta\rho$) = SLD (cylinder or chain) - SLD (solvent). The scale and contrast are both multiplicative factors in the model and are perfectly correlated. If the scale factor is set equal to the particle volume fraction, f , the returned value is the scattered intensity per unit volume;

$$I(q) = f P(q)$$

However, inter-particle interference effects were not included in the calculation. The structural results of the fitting process of E₃/PEG scattering data were given in Table S3.

One-dimensional pair distance distributions (PDDs) were also derived from the scattering data using IGOR Pro6 program to obtain structural information related with the origin of micro scale globular distribution.[373] PDDs are used to observe the orientation, clustering of the aggregations and the homogeneity of the sample. Symmetrical humps and well-ordered histogram bars are also evidences of nanosized crystalline structures. The distance and thickness of the layers can be determined using PDDs.[374]

PDDs histogram of E₃/PEG composite hydrogel presented quasi-lamellar structural properties with 8.27 ± 1.14 nm distance between the lamellar aggregations (Figure 4.9b, c). The homogenous structural organization within the composite hydrogel resulted the uniform electron density the structures ($2.3 \times 10^{-5} \text{ \AA}^{-2}$) within the composite hydrogel (Table 4.3). Although only E₃/PEG composite hydrogel sample was analyzed using this technique, structural differences between other composite hydrogel groups consisting self-assembled RGD-PA and DGEA-PA nanofibers were

not expected since change of the bioactivity did not affected the self-assembly mechanism and nanostructure organization as it was also seen in SEM images of the all samples.

The mechanical properties of the only PEG, only PA and PA/PEG composite hydrogels prepared at different polymer concentration were examined using the technique called as oscillatory rheology. The viscoelasticity and gel formation capacities of the resulting hydrogels were examined. Time sweep tests were applied to the all groups to determine equilibrium moduli of the hydrogels at the constant angular frequency and shear strain. As it was seen in Figure 4.11, all samples showed viscoelastic gel behavior since storage modulus (G') was higher than loss modulus (G'') values (Figure S6).

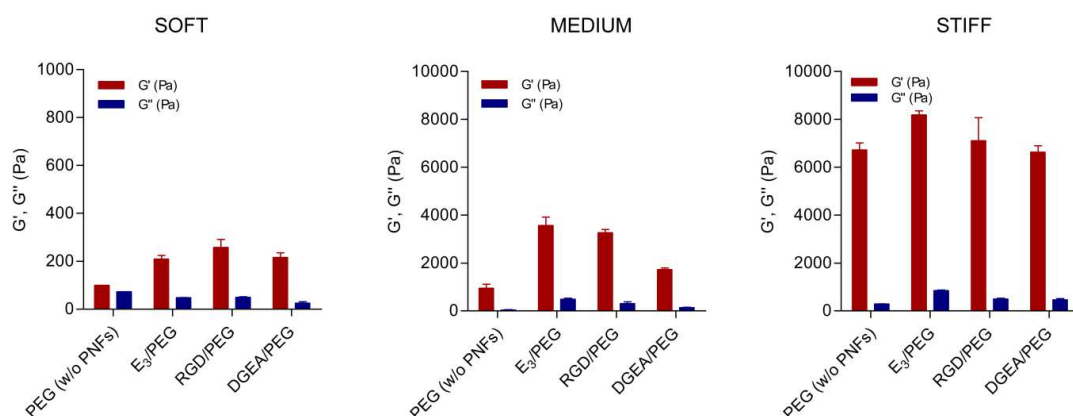


Figure 4.11 Equilibrium storage and loss moduli of the hydrogels

The gels were determined as soft, medium and stiff depending on the mechanical properties ranging from 0.1-0.3 to 1-4 and 6-8 kPa (Figure 4.12a). The increase of PEG concentration within the hydrogels led to the regular increase of the mechanical properties of the both systems showing the changeability of the composite network to control material properties.

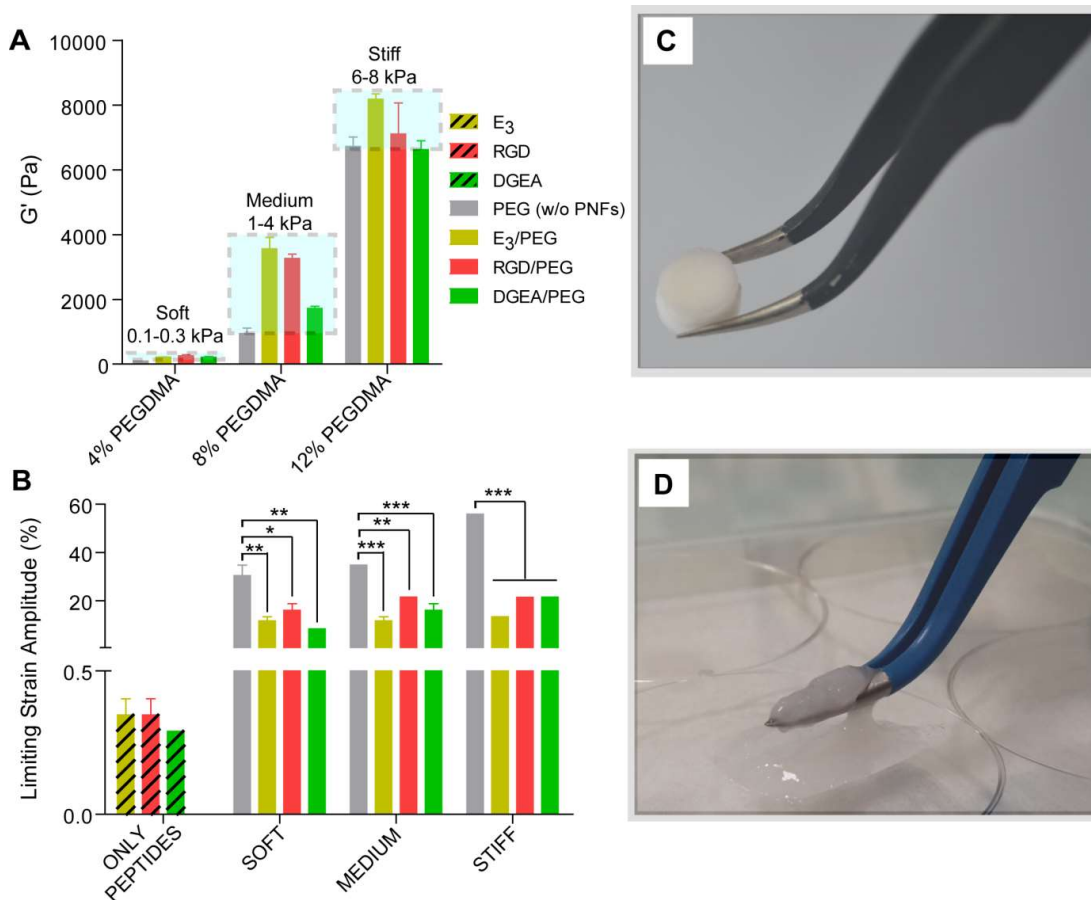


Figure 4.12 Equilibrium storage moduli (a) and limiting strain amplitude values (b) of the hydrogels prepared at different concentrations. Photographs of PA/PEG composite (c) and only PA hydrogel (d) with the same storage moduli.

Furthermore, the amplitude sweep analysis was applied to study viscoelastic behavior of the hydrogels under gradually increased strain values. Linear viscoelastic range (LVR) is defined as the region where the materials preserved their elasticity by keeping the storage modulus constant under elastic deformation. When the gel modulus starts to decrease depending on the increase of strain values, plastic deformation of the material takes place and that boundary is called as limiting strain amplitude (LSA). The stability and durability of a material can be determined based on the length of the

LVR which is directly related with the elastic properties of the materials. It was seen that LVR of PA/PEG composite hydrogels was comparable with only PEG controls, while self-assembled PA nanofiber hydrogels showed was quite narrow LVR properties (Figure 4.13). In addition, the LSA values of these supramolecular PA gels without reinforcement with crosslinked polymer networks were under 0.5% (Figure 4.12b). On the other hand, PA/PEG composite systems showed similar LSA values compare to the control PEG gels.

As it was seen in Figure 4.12, while the PA/PEG composite hydrogel was hold using a tweezer, it was not possible to handle supramolecular PA nanofiber gel without disrupting the gel integrity. Although both system had the same storage moduli, the increased elasticity of the composite hydrogels highlighted via LVR measurements resulted the enhanced hydrogel stability. That is a promising material quality for clinical applications, especially on the tissue engineering applications of load bearing bone and cartilage tissues.

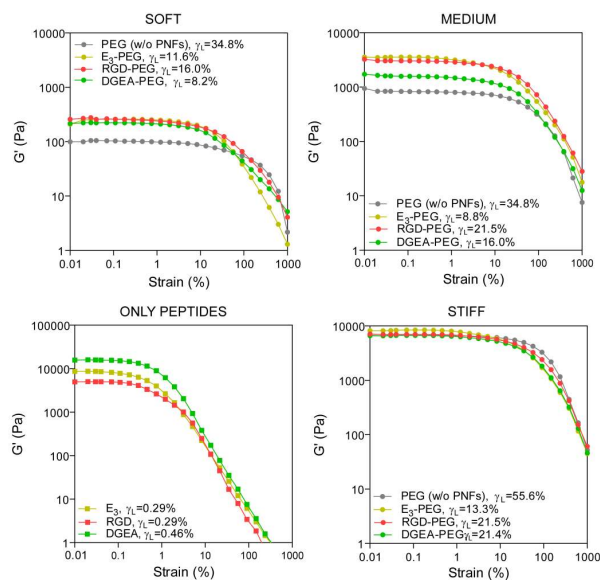


Figure 4.13 Rheological characterizations of the hydrogels based on amplitude sweep analysis

4.3.3 *In Vitro* Studies

The complex cellular responses towards the mechanical and biochemical properties of the hydrogels were examined to understand the potential of the biomaterials as an ECM mimetic scaffolds for tissue engineering and regenerative medicine applications. Osteoprogenitor Saos-2 cells are in the early commitment phase of osteogenic differentiation. On the other hand, they can show changeable stages of their commitment to the late osteogenic differentiation relying on the presence of variable factors.[375] To reveal the synergistic outcome of different epitopes presenting on the PA nanofibers along with the physical properties of the hydrogels including mechanical stiffness and porosity on the cellular behavior; *in vitro* studies were conducted.

The biocompatibility of PEG (w/o PA nanofibers) and PA/PEG composite hydrogels were tested performing calcein-AM/ethidium homodimer live/dead assay. Calcein-AM is normally non-fluorescent and cell membrane permeable substance. When it is uptake by the live cells and hydrolyzed due to the metabolic activity of esterases found in the cytoplasm, the product called calcein yields an intense fluorescence that enable us to visualize live cells. On the other hand, ethidium homodimer can interact with nucleic acids when cells lose their membrane integrity due to apoptosis or necrosis.[376] As it was seen in Figure 4.14, the most of the cells were stained with calcein (seen as green); and all samples sustained the cellular viability. Only a few dead cells (stained with ethidium homodimer and indicated as red) were seen in the images.

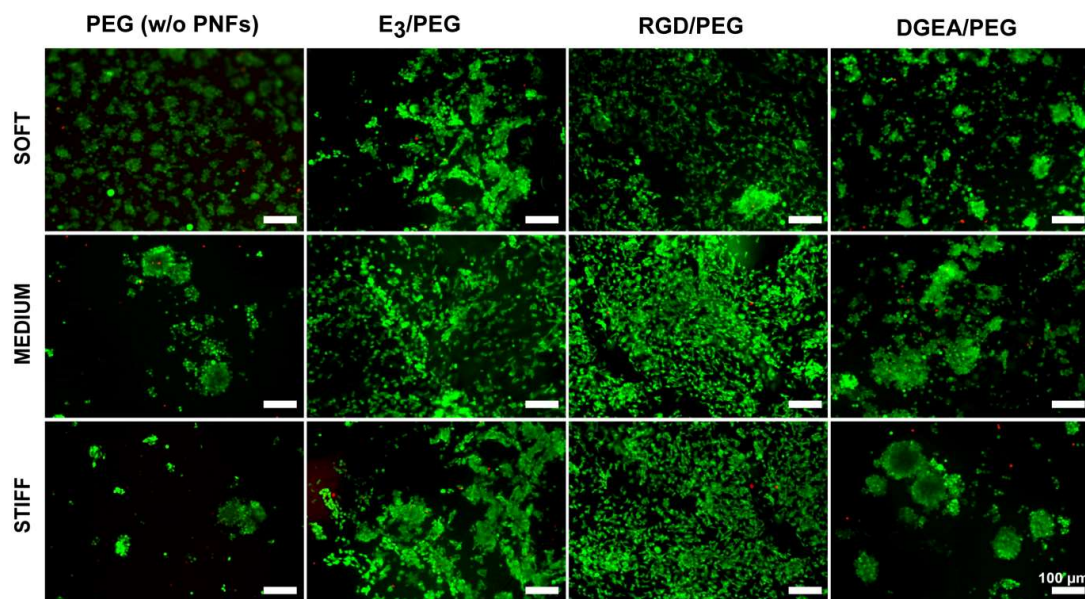


Figure 4.14 Fluorescence images of Saos-2 cells cultured on PEG and PA/PEG composite hydrogels and stained with calcein-AM (green) and ethidium homodimer (red) (scale bars are 100 μm)

For the analysis of cellular adhesion on the hydrogels, serum-free culture medium was used. The stiff PEG hydrogel did not enhance the cellular attachment due to lack of bioactivity at 24 h as seen in Figure 4.15a. It was an expected outcome of the protein-repellent property of the PEG system that hinder the cell-material interactions.[349] However, the addition of the self-assembled PA networks into the hydrogel system significantly supported the cellular adhesion on both medium and stiff PA/PEG hydrogels independent from the availability of integrin binding epitopes responsible for the cell adhesion (Figure 4.15b). E₃/PEG composite hydrogel which did not present bioactivity for integrin binding was also sufficient to enhance cellular adhesion similar to RGD/PEG and DGEA/PEG composite systems (Figure 4.15b).

When the cellular adhesion on the soft hydrogels was examined, the PEG (w/o PA nanofibers) system surprisingly sustained cellular adhesion similar to PA/PEG

composites based on the quantification of the adhered cells on the hydrogels (Figure 4.15b). It was thought that this was an outcome of the physical entrapment of the cells within the cells due to the soft nature of the hydrogels. Although the hydrogels was washed several times, these physically embedded cells on the control were not removed. On the other hand, the adhered cells on the PEG controls preserved their spherical morphology and did not show any contact on the biomaterials shown by actin staining (Figure 4.15c).

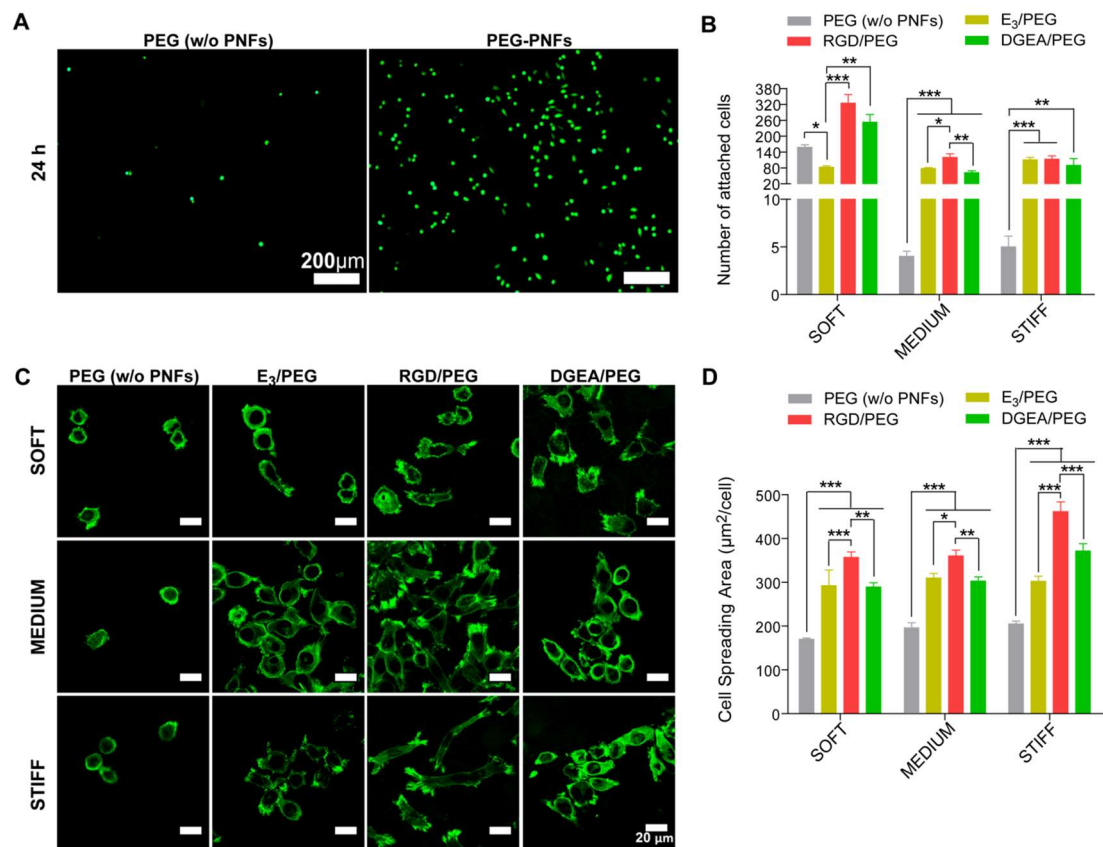


Figure 4.15 a) Fluorescence images of Saos-2 cells cultured on stiff PEG and PA/PEG (prepared with E₃-PA) composite hydrogels and stained with calcein-AM, b) the number of adhered cells on the all systems at 24 h in serum free culture conditions, c) the fluorescence images of the cells stained with phalloidin (green); and d) the spreading areas of the cells cultured on the substances at 72 h

The significant increase on the adhered cells on nanofibrous PA/PEG composite hydrogel prepared with non-integrin binding E₃PA was observed compare to the only PEG system when the cell culturing period was continued to 48 and 72 h. That also showed us the importance of the biofunctionality to sustain cell-material interactions in long term applications (Figure 4.16).

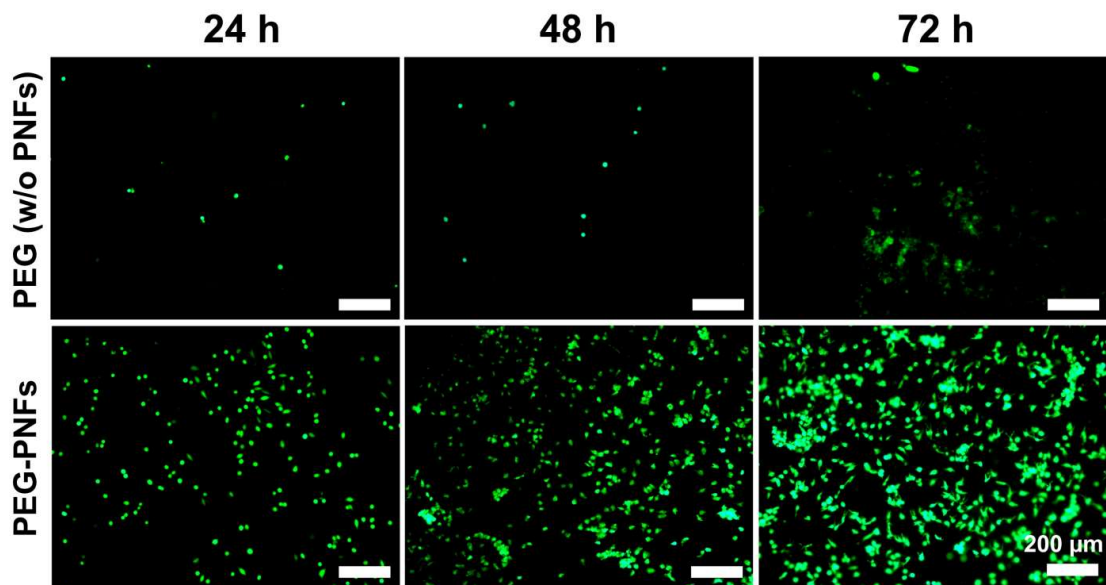


Figure 4.16 Fluorescence images of Saos-2 cells cultured on stiff PEG and PA/PEG (prepared with E₃-PA) composite hydrogels and stained with calcein-AM (scale bars are 200 μm)

F-actin staining of the cells using phalloidin was also conducted to examine the cellular morphologies and interactions with the material surfaces. As it is seen in Figure 4.15c, the cell-material interactions were sustained on all PA/PEG composite hydrogels. On the other hand, the cells culture PEG hydrogels preserved a spherical morphology independent of mechanical properties, since there was no bioactive epitopes guiding the cells to sense material stiffness. The quantitative analysis of the cell spreading area was completed using Image J program; and the results showed us the widespread

cellular spreading on all of the PA/PEG composites when compared to PEG control (Figure 4.15d). Especially, presentation of RGD epitope on PA nanofibers within the crosslinked PEG system suppressed the protein-repellent property of PEG and enhanced cell-material interactions as clearly observed in Figure 4.15c. The quantification of the spreading area of the cells on RGD/PEG composite hydrogel was significantly higher than other PA/PEG combinations for all of the soft, medium and stiff hydrogels (Figure 4.15d).

Surprisingly, a pronounced effect between the mechanical properties and integrin binding epitopes on the cellular adhesion and spreading was also observed. The calculated spreading area of the cells increased depending on the increase stiffness of the RGD/PA and DGEA hydrogels presenting integrin binding epitopes. On the other hand, the cellular spreading areas were independent on the mechanical stiffness of non-integrin binding E₃/PEG combinations and not affected by the change of the hydrogel stiffness (Figure 4.15d). It was concluded that the exact control on the mechanical properties of PA/PEG composite hydrogels independently from their biochemical properties made these systems novel ECM mimetic microenvironments for guiding of the cellular behavior. Since both biochemical and biophysical properties of a scaffold can affect cellular responses, it is quite challenging to develop a scaffold which optimally directs cellular differentiation and tissue regeneration with the use of current uni-functional strategies. The hydrogel system presented in this thesis can serve as a convenient platform to direct cell behavior according to preferred outcomes.

To examine the osteogenic commitment and further differentiation capacity of Saos-2 cells cultured on the composite hydrogels presenting complex biochemical and biophysical signals, Runt-related transcription factor 2 (RUNX2) and collagen type I

(COL1) gene expressions of the cells were investigated. The fluorescence images of the cells with ICC stainings for RUNX2 and COL1, indicated that both of RUNX2 and COL1 genes were expressed on the only PEG and all combinations of PA/PEG composite hydrogel (Figure 4.17).

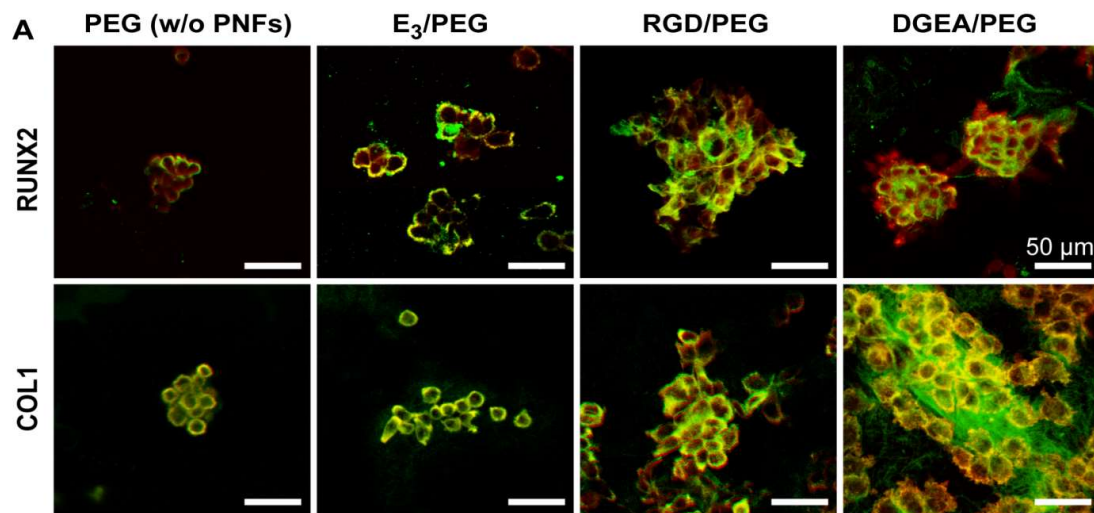


Figure 4.17 Representative fluorescence images of the cells with ICC staining at day 7 (scale bars are 50 μm). Green indicated RUNX2 and COL1 expressions at the top and bottom row images, respectively. In both rows, phalloidin staining was shown as red color

To quantify and analyze the gene expression levels of the cells, qRT-PCR technique was conducted. It was seen that both RUNX2 and COL1 gene expressions of Saos-2 cells cultured on the only PEG control hydrogels increased depending on the increase in the hydrogel stiffness (Figure 4.18). Although the cellular viability was sustained on the only PEG hydrogels regardless of their stiffness, the cellular morphology were round shape and the cell-material interactions were limited on all of the PEG concentrations (4%, 8% and 12% (w/v)) (Figure S8). Therefore, the increase level of the genes related with the osteogenic differentiation cannot be the result of the cellular

response towards the material properties. This behavior might be the consequence of the non-natural cellular state due to the low cell numbers adhered on the surfaces.

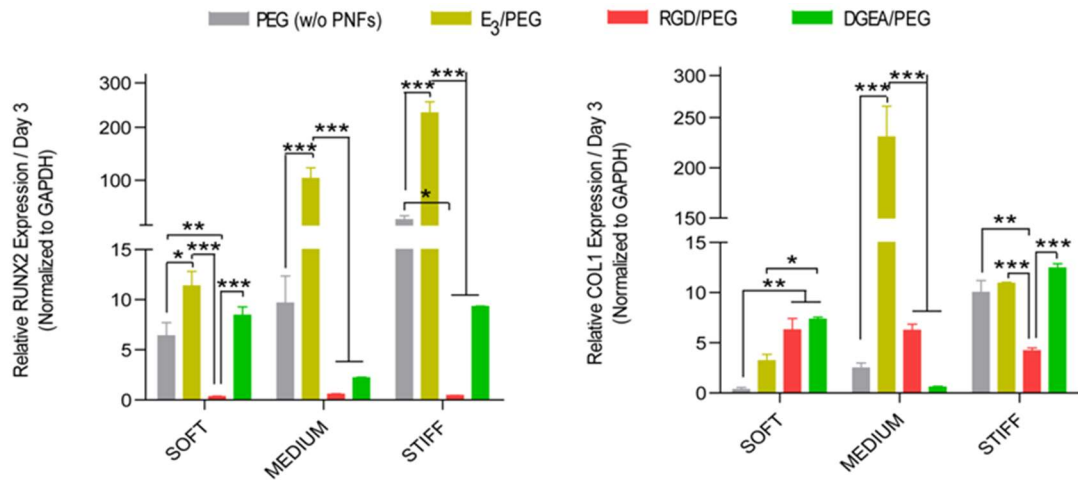


Figure 4.18 The gene expression levels of the cells cultured on PEG and PA/PEG composite hydrogels at day 3

The highest RUNX2 gene expression level was obtained from the cells cultured on E₃/PEG composite hydrogel groups both on day 3 and day 7. The expression level was also correlated with the increase in hydrogel stiffness (Figure 4.18 and 4.19). Moreover, the highest COL1 gene expression level was observed for E₃/PEG hydrogels with medium stiffness compared to integrin binding RGD/PEG and DGEA/PEG hydrogels along with non-bioactive PEG control (Figure 4.18 and 4.19). In the literature, it was shown that the integration of the non-integrin binding EEE peptide sequence (E₃) to PA molecules and their supramolecular nanofibrous assemblies presented an osteoinductive effect on the hMSCs mimicking the acidic residues of non-collagenous bone matrix proteins.[362] Hence, the culturing of the cells on the E₃/PEG composite hydrogels improved osteogenic differentiation of the cells similar to the literature.

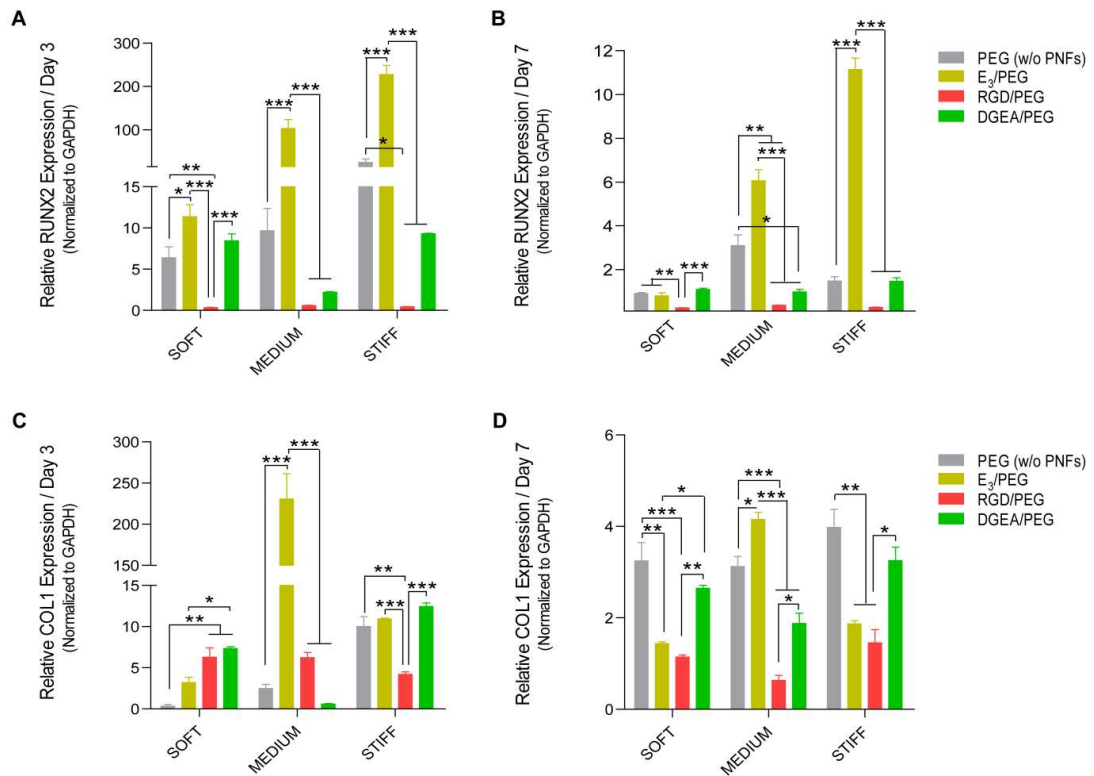


Figure 4.19 The gene expression levels of the cells cultured on PEG and PA/PEG composite hydrogels at day 3 and 7

The different differentiation patterns were obtained when the integrin-binding epitopes were presented on the hydrogels compared to non-integrin binding E₃/PEG system. These cell cultured on these combinations showed the differentiation behavior independent from the material stiffness.

The gene expression levels of the cells cultured on RGD/PEG hydrogels were not dependent on the mechanical stiffness of the hydrogels; and they were close to each other for all of the soft, medium and stiff hydrogels (Figure 4.18). The increase of RUNX2 expression was not seen whereas 6 fold upregulation of COL1 expression was obtained on RGD/PEG combinations independent from material stiffness on day 3. In addition, soft and stiff DGEA/PEG composite hydrogels showed higher expression of RUNX2 and COL1 (Figure 4.18) compared to medium DGEA/PEG. To understand

the detailed cellular mechanism behind such a cellular behavior, the further investigation is required. However, it is known that in the existence of complex signals, different material stiffness and biochemical signaling can substitute each other under different conditions.^[377]

On the other hand, the increase on osteogenic differentiation on both soft and stiff DGEA/PEG composite hydrogels can be clarified in the light of the literature studies conducted on the osteoblast differentiation. The upregulated expression of α_2 -integrin on the cell membrane depending on the increase of matrix stiffness was shown in previously.^[378] In addition, DGEA is a collagen type I derived bioactive epitope and binds to $\alpha_2\beta_1$ integrin receptor directing cell fate toward the osteogenic differentiation. Depending on the increase of hydrogel stiffness, upregulated α_2 -integrin expression of the cells may result to advance influence of DGEA signaling on the osteoblast differentiation. On the other hand, it was also shown that *in vitro* osteogenic differentiation can be enhanced on soft biomaterials consisting similar mechanical properties with developing bone.^[379, 380] Bone formation and osteogenic differentiation happens within a soft matrix in the range of 100-1000 Pa shear modulus.^[381, 382] The gene expression profiles of the cells cultured on the DGEA/PEG composite hydrogels also indicated similar consequences; and the importance of the optimum biomaterial design as ECM mimetic microenvironment considering all aspects including complex biochemical signaling factors and physical properties of the materials.^[383]

In vivo studies discussed above conducted on the surface of the materials and cell-material interactions were examined on the two-dimensional microenvironment. The applicability of the nanofibrous PA/PEG composite hydrogels as three-dimensional

microenvironment was also studied encapsulating the cells within the matrix via facile fabrication method. We compared the cellular viability within the PEG and PA/PEG hydrogels considering the effects of bioactive nanofibrous architecture of the composite scaffolds on the 3D environment. To support cellular viability in 3D microenvironment, all PA molecules, PEG monomers and the initiator were dissolved in culture medium (DMEM) instead of water; and then the cells were mixed with the polymer solution prior to the mixing with PA solutions. Hence, the cell-friendly encapsulation process was followed; and the mixtures was exposed to the UV irradiation (365 nm for 15 min) for the crosslinking of the system within the eppendorf tubes. Finally, the hydrogels encapsulated with the cells were cultured in a bioreactor with rotating apparatus (Synthecon RCCS-4H).

The cell culturing was proceed for 7 days, and then the viability within the 3D hydrogels were assessed performing Calcein-AM/Ethidium homodimer assay. As it was discussed above, the live cells were stained with calcein and seen as green on the fluorescence images; on the other hand, ethidium homodimer interacted with nucleic acids of the dead cells and shown as red on the images (Figure 4.20).

As it was seen in Figure 4.20, the 3D composite hydrogel system (RGD/PEG) was sustained the cellular viability compare to the only PEG hydrogel; and the cytotoxic effect of the composite 3D hydrogel was not observed. On the other hand, the cell viability was significantly low within the 3D PEG system although the cytotoxicity was reported for 2D conditions of the same material. It was thought that the nanofibrous architecture of the composite system might sustain the nutrient and gas transfer to the system efficiently compare to the non-porous PEG hydrogel. Furthermore, the presentation of RGD integrin binding epitope on the PA nanofibers

within the composite hydrogel could increase the cell-material interactions; and hence support the biocompatibility of the composite system as being 3D ECM mimetic microenvironment for tissue engineering and regenerative medicine applications.

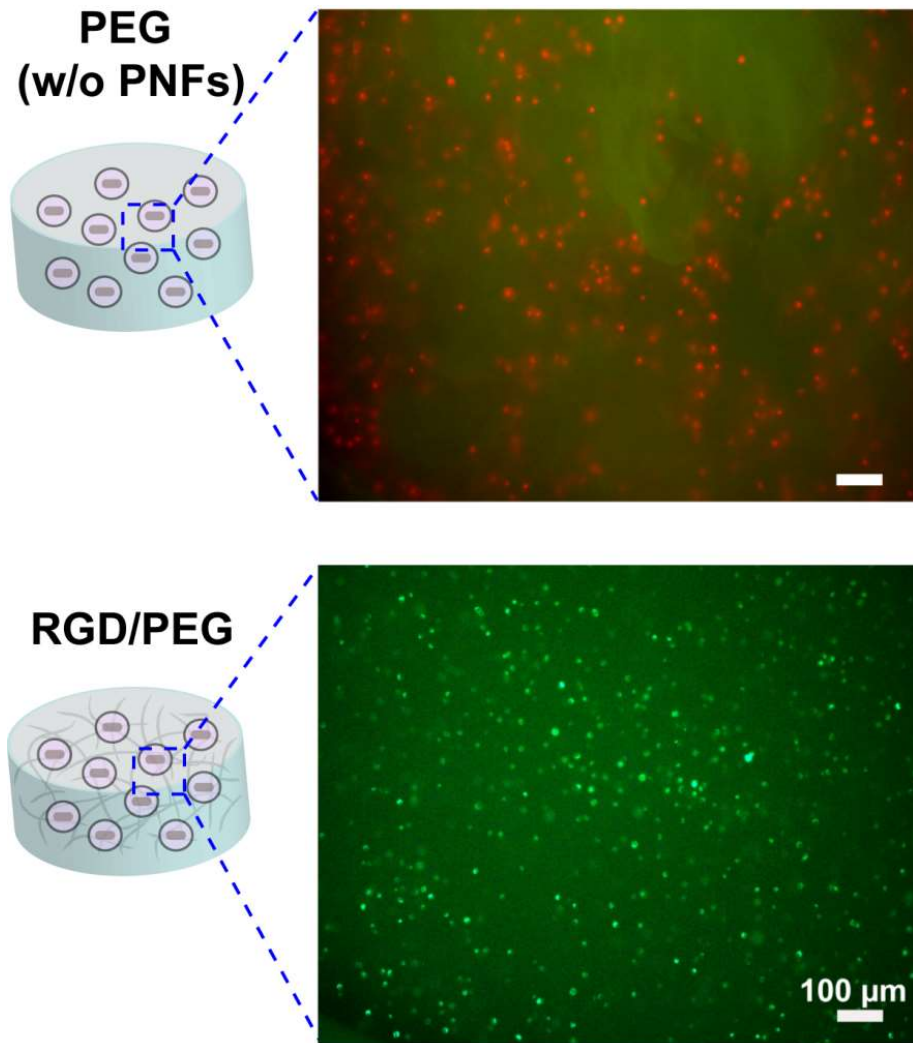


Figure 4.20 Fluorescence images of Saos-2 cells cultured within the 3D PEG and PA/PEG composite hydrogels and stained with calcein-AM (green) and ethidium homodimer (red) (scale bars are 100 μm)

4.3.4 Protein Encapsulation and Controlled Protein Release through the PA/PEG Composite Hydrogels

Hydrogels have been studied for drug delivery purposes due to their high encapsulation efficacy and controlled release of therapeutics for long term. The potential of the composite hydrogels as controlled protein delivery system was also examined for the possible therapeutic applications. It was thought that the affinity of the bioactive PA molecules to the therapeutic proteins such as growth factors and cytokines and highly nanofibrous native architectures of the composite hydrogel system can provide both protection environment and sustain the activity of the molecules presenting them within a tunable ECM mimetic microenvironment for tissue regeneration.

As it was discussed above, PEG concentration within the composite hydrogels controlled the mechanical stability and rigidity of the networks. In addition, porosity of the PEG hydrogels was very low compare to the PA/PEG composite hydrogels as seen in both SEM and BET analysis results. Considering both porosity and mechanical rigidity, PEG concentration within the networks has to be optimized for controlled release of therapeutics. For PEG concentration optimization experiments, BSA was chosen as a model small protein molecule. In the literature, controlled BSA release through the self-assembled peptide hydrogels were studied in details.[229] It was also shown that the self-assembled networks can be used as delivery system protecting the activity of the proteins at physiological conditions.[224]

Prior to the controlled release experiments, the standard calibration curve for the determination of the released amount of BSA molecules through the hydrogels was obtained using the Bradford assay was conducted. The standard curve of the BSA concentration was given as Figure 4.21 below.

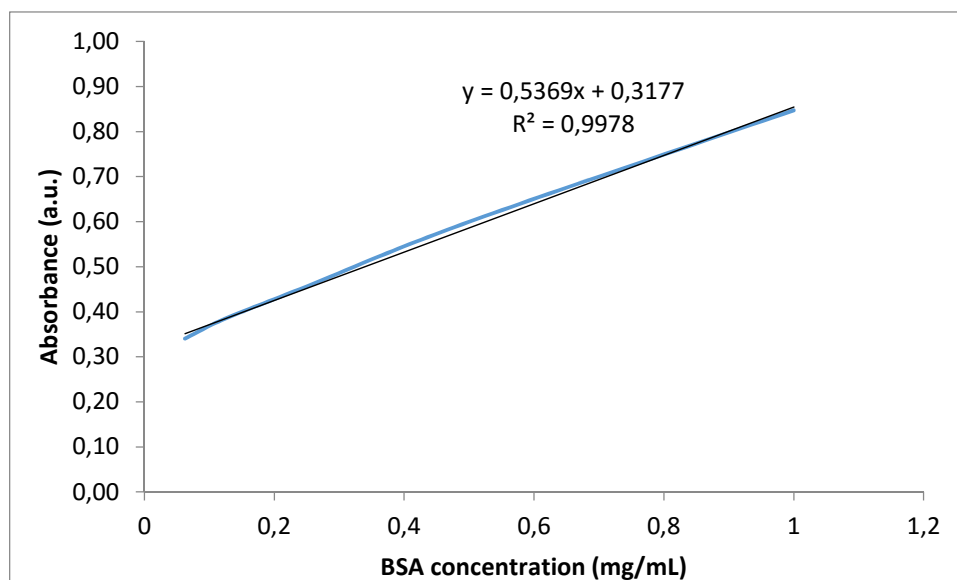


Figure 4.21 The standard calibration curve for the determination of BSA concentration based on absorbance measurements

The amount of encapsulated BSA within the hydrogels were determined as 2 mg/mL. The release experiments were performed using 4%, 8% and 12% (v/v) PA/PEG composite hydrogels and only PEG hydrogels prepared at the same concentrations as controls. Within the time intervals, the samples from the buffer placed to the top of the hydrogels were taken and freezeed for the determination of concentration using Bradford assay at the same time. The controlled release of BSA molecules through the hydrogels was monitored and given in Figure 4.22.

As it was seen in Figure 4.22, the sustained BSA release was obtained for both only PEG and PA/PEG composite hydrogels for all concentrations. On the other hand, the initial burst release of the proteins were eliminated on the PA/PEG composite system. The affinity of the PA network to the protein molecules due to the possible non-covalent interactions may prevent the initial burst release and provided a significant advantage to the composite systems compare to the only PEG hydrogels. The protein-

repellent nature of the PEG network may also trigger the burst release of the molecules at time zero.

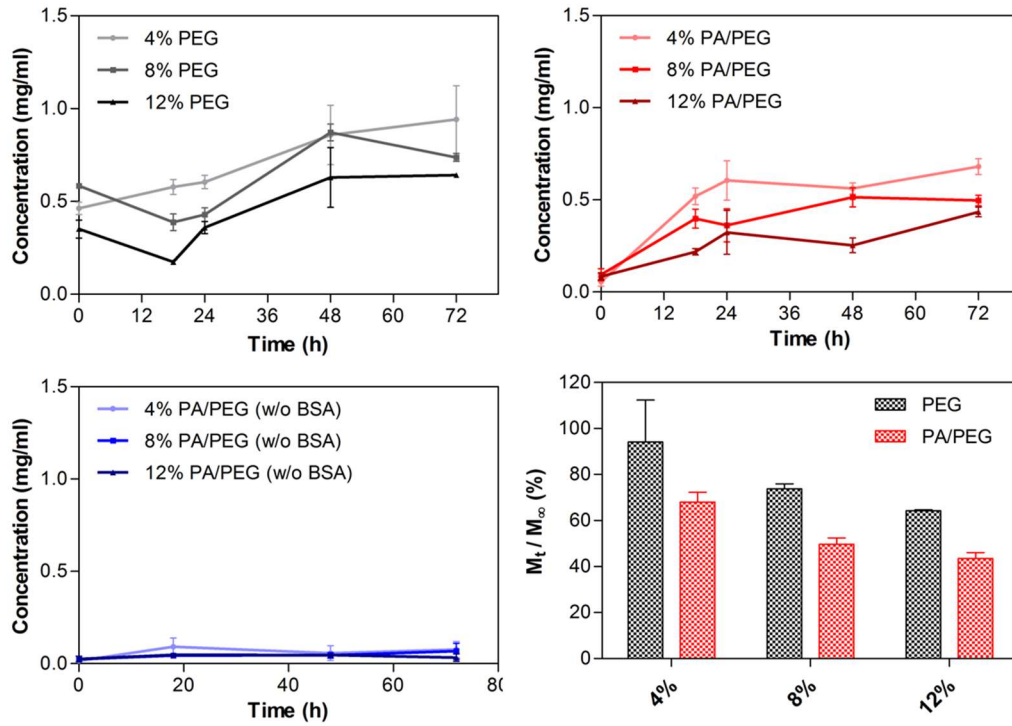
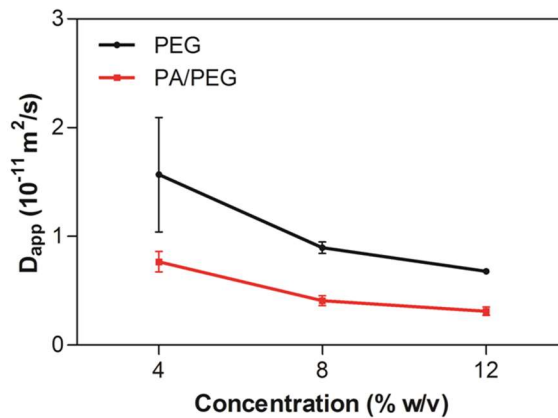


Figure 4.22 The controlled release profiles of the BSA molecules through the only PEG and PA/PEG composite hydrogels

To estimate apparent diffusivity coefficients the BSA molecules released through the PEG and PA/PEG composite hydrogels for the quantitative comparison of the mass transport properties of the hydrogels, Fick's second law of diffusion for 1D unsteady-state systems given in Eqn. 1 was used. In the equation, D_{app} , M_t , M_∞ , H and t was defined as the apparent diffusivity, the cumulative mass of the diffused molecules at time t and infinite and the thickness of the hydrogel, respectively.

$$\frac{M_t}{M_\infty} = \left(\frac{16 D_{app} t}{\pi H^2} \right)^{0.5} \quad (\text{Eqn. 1})$$

The estimated apparent diffusion coefficients were given in Figure 4.23. Although the composite PA/PEG hydrogels consist of the nanofibrous PA architecture and higher internal porosity compare to the only PEG gels, the slower release of the BSA molecules was obtained for the composite system. As discussed above, the possible non-covalent interactions between the BSA molecules and PA network may decrease the transport rate of the molecules. In addition, the difference between transport properties of only PEG and PA/PEG composite hydrogels showed that controlled release of proteins can be modulated self-assembled PA network in composite hydrogels and sustain long term affinity controlled protein release system for therapeutic applications such as growth factor and cytokine delivery to the regenerating tissues.



		4%	8%	12%
D_{app} ($10^{-11}m^2/s$)	PEG	1.57±0.91	0.90±0.09	0.68±0.02
	PA/PEG	0.77±0.16	0.41±0.08	0.31±0.07

Figure 4.23 The estimated apparent diffusion coefficients

4.4 Conclusion

In conclusion, design, synthesis and *in vitro* applicability of nanofibrous PA/PEG composite hydrogels as ECM mimetic scaffold for tissue engineering and regenerative medicine were presented in this chapter of the thesis. The fabrication method developed for the composite hydrogel gave us the exact control on the physical properties including porosity and mechanical stiffness independent from the biochemical properties of the hydrogels. The cooperation of the self-assembled bioactive nanofibers with the chemically crosslinked PEG network was the first example of the straightforward development process of the composite hydrogels which can be employed in different fields including materials biology, materials science and engineering. Furthermore, the design principles of the composite system provide a flexibility for fine-tuning biomaterial properties using different class of self-assembling molecules and chemically crosslinkable natural or synthetic polymers. The biocompatibility of the composite hydrogels examined at both 2D and 3D *in vivo* conditions made these nanofibrous architectures suitable ECM mimetic scaffold candidates for tissue regeneration applications.

Chapter 5

5. Conclusion and Future Prospects

The advances on the nanotechnology, material science and engineering; and the integration of them with the fundamental scientific disciplines has pioneered molecular self-assembly approach for the fabrication of highly adaptable and tunable architectures inspired from the perfection of the nature. The non-covalent interactions between the building blocks which are the sources of their responsive nature to the environmental changes provide a tool-box set to control shape, size and also function of the self-assembled materials developed for different applications.

Peptide self-assembly enable us to design and develop hierarchically assembled novel biomaterials mimicking the structure and functionality of the components found living cells, ECM microenvironment, tissues and also organs. Furthermore, these supramolecular architectures are further functionalized to orchestrate biological processes and direct cellular responses due to the small molecule delivery capacities such as drugs, soluble factors, proteins, nucleic acids, growth factors or cytokines at both nano and bulk scales. This thesis describes how to design and build peptide based functional biomaterials such as biocompatible coassembled nanofibers, supramolecular nanofiber gels or self-assembled PA and crosslinked polymer composite scaffolds. In addition to the development of these hierarchical peptide based architectures as functional biomaterials for biomedical applications, the biocompatibility and applicability of them were also examined for drug delivery and tissue engineering purposes.

In the first study, the design of short amyloid inspired synthetic peptides in view of the noncovalent interactions found in native amyloid aggregations resulted the formation of coassembled supramolecular nanostructures at physiological conditions. Especially, the facile coassembly of the building blocks without any need of external factors; biocompatibility and the mechanical stability of the supramolecular coassemblies at both nano and bulk scales provide an advantage particularly for biomedical applications. These amyloid inspired peptide molecules can be functionalized via bioactive epitopes, soluble factors or therapeutic molecules for specific purposes. In addition, the mechanistic experiments conducted to reveal the coassembly mechanism and kinetics shown in this study can aid the progress of therapeutic strategies for amyloid-aggregation related neurodegenerative diseases; and the design of mechanically improved hierarchical architectures derived from self-assembled amyloid inspired peptides.

The motivation of the second study was to develop biocompatible and injectable drug delivery system for local chemotherapeutic applications to treat soft-tissue cancer types such as breast cancer. Supramolecular PA nanofiber gels presented in the third chapter of this thesis prolonged the local delivery of the chemotherapeutics at physiological conditions; and improved the bioavailability of the drug molecules at the specific area. The significant decrease in tumor growth rate via injection of the drug encapsulated PA gels under *in vivo* conditions also showed us their high potential for the clinical applications. In addition, this approach reduced the side effects of the chemotherapeutic molecule for the healthy tissues by introducing the drug encapsulated nanofiber gels to the tumor site. Biodegradability of these biomaterials by the proteases found in body were also the additional advantages of these

architectures. Moreover, the degradation properties of the self-assembled PA nanofiber gels can be further modulated via the decoration of the PA molecules with enzyme cleavable specific amino acid sequences as future research perspective.

The last study discussed in this thesis was the first example of development of the composite hydrogel network consisting both self-assembled bioactive PA nanofibers and chemically crosslinked non-bioactive PEG network in the literature. This approach gave us the exact control on the physical properties including porosity and mechanical stiffness independent from the biochemical properties of the composite hydrogels. Furthermore, the design strategy of the composite system provide a flexibility to use different class of self-assembling peptide based building blocks and chemically crosslinkable natural or synthetic polymers depending on the application purpose. In the study, the osteogenic differentiation capacity of these nanofibrous ECM mimetic scaffolds decorating them with the bioactive epitopes which cascade the signaling pathway related with the bone regeneration and remodeling was shown. In addition to the bioactivity, these composite hydrogels can be also incorporated with the inorganic biomineral content to mimic biophysical and biochemical properties of the native bone tissue for further studies.

Although different self-assembled peptide based strategies and biomaterials have been examined in the literature and also in this thesis for drug delivery and regenerative medicine purposes in the pre-clinical studies, the widespread use of these supramolecular peptide based architectures in clinical applications is still limited. There are different aspects that prevent the progress in clinical applicability of these materials such as cost effectiveness, technical limitations for the industrial scale production and also safety concerns related with the nanosized materials. However,

the developments in fabrication techniques, the advances on fundamental biological studies related with the safety of peptide based architectures and supramolecular assemblies will contribute to the progress of this field. Moreover, industrial collaboration with scientific community synergize the commercialization of the developed systems for drug delivery and tissue engineering applications. Overall, I believe that the advances on this field cooperating with other scientific disciplines and industry will boost the clinical use of smart self-assembled peptide based biomaterials for drug delivery, biomedicine and tissue engineering.

Bibliography

- [1] A. C. Mendes, E. T. Baran, R. L. Reis, and H. S. Azevedo, "Self-assembly in nature: using the principles of nature to create complex nanobiomaterials," *Wiley Interdisciplinary Reviews: Nanomedicine and Nanobiotechnology*, vol. 5, pp. 582-612, 2013.
- [2] J.-M. Lehn, "Toward complex matter: Supramolecular chemistry and self-organization," *Proceedings of the National Academy of Sciences*, vol. 99, pp. 4763-4768, 2002.
- [3] P. A. Monnard and D. W. Deamer, "Membrane self-assembly processes: Steps toward the first cellular life," *The Anatomical Record*, vol. 268, pp. 196-207, 2002.
- [4] J. A. Elemans, A. E. Rowan, and R. J. Nolte, "Mastering molecular matter. Supramolecular architectures by hierarchical self-assembly," *Journal of Materials Chemistry*, vol. 13, pp. 2661-2670, 2003.
- [5] G. M. Whitesides and B. Grzybowski, "Self-assembly at all scales," *Science*, vol. 295, pp. 2418-2421, 2002.
- [6] S. Zhang, "Fabrication of novel biomaterials through molecular self-assembly," *Nat Biotech*, vol. 21, pp. 1171-1178, 2003.
- [7] L. Cademartiri and K. J. Bishop, "Programmable self-assembly," *Nature materials*, vol. 14, pp. 2-9, 2015.
- [8] S. T. Nguyen, D. L. Gin, J. T. Hupp, and X. Zhang, "Supramolecular chemistry: Functional structures on the mesoscale," *Proceedings of the National Academy of Sciences*, vol. 98, pp. 11849-11850, 2001.
- [9] Y. Yin and D. Talapin, "The chemistry of functional nanomaterials," *Chemical Society Reviews*, vol. 42, pp. 2484-2487, 2013.
- [10] H. Hosseinkhani, P.-D. Hong, and D.-S. Yu, "Self-Assembled Proteins and Peptides for Regenerative Medicine," *Chemical Reviews*, vol. 113, pp. 4837-4861, 2013.
- [11] D. Moreira Leite, E. Barbu, G. J. Pilkington, and A. Lalatsa, "Peptide self-assemblies in drug delivery," *Current topics in medicinal chemistry*, 2015.

- [12] D. W. Löwik, E. Leunissen, M. Van den Heuvel, M. Hansen, and J. C. van Hest, "Stimulus responsive peptide based materials," *Chemical Society Reviews*, vol. 39, pp. 3394-3412, 2010.
- [13] M. O. Guler, R. C. Claussen, and S. I. Stupp, "Encapsulation of pyrene within self-assembled peptide amphiphile nanofibers," *Journal of Materials Chemistry*, vol. 15, pp. 4507-4512, 2005.
- [14] S. Vauthey, S. Santoso, H. Gong, N. Watson, and S. Zhang, "Molecular self-assembly of surfactant-like peptides to form nanotubes and nanovesicles," *Proceedings of the National Academy of Sciences*, vol. 99, pp. 5355-5360, 2002.
- [15] H. Xu, J. Wang, S. Han, J. Wang, D. Yu, H. Zhang, *et al.*, "Hydrophobic-Region-Induced Transitions in Self-Assembled Peptide Nanostructures†," *Langmuir*, vol. 25, pp. 4115-4123, 2008.
- [16] V. Castelletto, I. Hamley, M. Segarra-Maset, C. B. Gumbau, J. Miravet, B. Escuder, *et al.*, "Tuning chelation by the surfactant-like peptide A6H using predetermined pH values," *Biomacromolecules*, vol. 15, pp. 591-598, 2014.
- [17] F. Qiu, Y. Chen, C. Tang, Q. Zhou, C. Wang, Y. K. Shi, *et al.*, "De novo design of a bolaamphiphilic peptide with only natural amino acids," *Macromolecular bioscience*, vol. 8, pp. 1053-1059, 2008.
- [18] E. R. da Silva, M. N. M. Walter, M. Reza, V. Castelletto, J. Ruokolainen, C. J. Connon, *et al.*, "Self-Assembled Arginine-Capped Peptide Bolaamphiphile Nanosheets for Cell Culture and Controlled Wettability Surfaces," *Biomacromolecules*, vol. 16, pp. 3180-3190, 2015.
- [19] Y. Chen, F. Qiu, Y. Lu, Y.-K. Shi, and X. Zhao, "Geometrical shape of hydrophobic section determines the self-assembling structure of peptide detergents and bolaamphiphilic peptides," *Current Nanoscience*, vol. 5, pp. 69-74, 2009.
- [20] E. R. da Silva, W. A. Alves, V. Castelletto, M. Reza, J. Ruokolainen, R. Hussain, *et al.*, "Self-assembly pathway of peptide nanotubes formed by a glutamatic acid-based bolaamphiphile," *Chemical Communications*, 2015.

- [21] Y. Hu, R. Lin, P. Zhang, J. Fern, A. G. Cheetham, K. Patel, *et al.*, "Electrostatic-Driven Lamination and Untwisting of β -Sheet Assemblies," *ACS nano*, 2015.
- [22] M. Cao, C. Cao, P. Zhou, N. Wang, D. Wang, J. Wang, *et al.*, "Self-assembly of amphiphilic peptides: Effects of the single-chain-to-gemini structural transition and the side chain groups," *Colloids and Surfaces A: Physicochemical and Engineering Aspects*, vol. 469, pp. 263-270, 2015.
- [23] S. Zhang, T. Holmes, C. Lockshin, and A. Rich, "Spontaneous assembly of a self-complementary oligopeptide to form a stable macroscopic membrane," *Proceedings of the National Academy of Sciences*, vol. 90, pp. 3334-3338, 1993.
- [24] S. Zhang, T. C. Holmes, C. M. DiPersio, R. O. Hynes, X. Su, and A. Rich, "Self-complementary oligopeptide matrices support mammalian cell attachment," *Biomaterials*, vol. 16, pp. 1385-1393, 1995.
- [25] T. C. Holmes, S. de Lacalle, X. Su, G. Liu, A. Rich, and S. Zhang, "Extensive neurite outgrowth and active synapse formation on self-assembling peptide scaffolds," *Proceedings of the National Academy of Sciences*, vol. 97, pp. 6728-6733, 2000.
- [26] N. R. Lee, C. J. Bowerman, and B. L. Nilsson, "Effects of varied sequence pattern on the self-assembly of amphipathic peptides," *Biomacromolecules*, vol. 14, pp. 3267-3277, 2013.
- [27] H. Dong, S. E. Paramonov, L. Aulisa, E. L. Bakota, and J. D. Hartgerink, "Self-assembly of multidomain peptides: balancing molecular frustration controls conformation and nanostructure," *Journal of the American Chemical Society*, vol. 129, pp. 12468-12472, 2007.
- [28] L. Aulisa, H. Dong, and J. D. Hartgerink, "Self-assembly of multidomain peptides: sequence variation allows control over cross-linking and viscoelasticity," *Biomacromolecules*, vol. 10, pp. 2694-2698, 2009.
- [29] E. L. Bakota, O. Sensoy, B. Ozgur, M. Sayar, and J. D. Hartgerink, "Self-assembling multidomain peptide fibers with aromatic cores," *Biomacromolecules*, vol. 14, pp. 1370-1378, 2013.

- [30] K. Hinterding, D. Alonso-Díaz, and H. Waldmann, "Organic synthesis and biological signal transduction," *Angewandte Chemie International Edition*, vol. 37, pp. 688-749, 1998.
- [31] D. W. Löwik and J. C. van Hest, "Peptide based amphiphiles," *Chemical Society Reviews*, vol. 33, pp. 234-245, 2004.
- [32] Y. Chen, H. X. Gan, and Y. W. Tong, "pH-Controlled Hierarchical Self-Assembly of Peptide Amphiphile," *Macromolecules*, vol. 48, pp. 2647-2653, 2015.
- [33] K. L. Niece, J. D. Hartgerink, J. J. J. M. Donners, and S. I. Stupp, "Self-Assembly Combining Two Bioactive Peptide-Amphiphile Molecules into Nanofibers by Electrostatic Attraction," *Journal of the American Chemical Society*, vol. 125, pp. 7146-7147, 2003.
- [34] M. Goktas, G. Cinar, I. Orujalipoor, S. Ide, A. B. Tekinay, and M. O. Guler, "Self-Assembled Peptide Amphiphile Nanofibers and PEG Composite Hydrogels as Tunable ECM Mimetic Microenvironment," *Biomacromolecules*, vol. 16, pp. 1247-1258, 2015.
- [35] R. Zou, Q. Wang, J. Wu, J. Wu, C. Schmuck, and H. Tian, "Peptide self-assembly triggered by metal ions," *Chemical Society Reviews*, vol. 44, pp. 5200-5219, 2015.
- [36] A. Tanaka, Y. Fukuoka, Y. Morimoto, T. Honjo, D. Koda, M. Goto, *et al.*, "Cancer cell death induced by the intracellular self-assembly of an enzyme-responsive supramolecular gelator," *Journal of the American Chemical Society*, vol. 137, pp. 770-775, 2015.
- [37] J. N. Israelachvili, *Intermolecular and surface forces: revised third edition*: Academic press, 2011.
- [38] A. Lalatsa, A. G. Schätzlein, M. Mazza, T. B. H. Le, and I. F. Uchegbu, "Amphiphilic poly (l-amino acids)—new materials for drug delivery," *Journal of Controlled Release*, vol. 161, pp. 523-536, 2012.
- [39] L. K. Shrestha, K. M. Strzelczyk, R. G. Shrestha, K. Ichikawa, K. Aramaki, J. P. Hill, *et al.*, "Nonionic amphiphile nanoarchitectonics: self-assembly into micelles and lyotropic liquid crystals," *Nanotechnology*, vol. 26, p. 204002, 2015.

- [40] D. M. Leite, E. Barbu, G. J. Pilkington, and A. Lalatsa, "Peptide Self-Assemblies for Drug Delivery," *Current topics in medicinal chemistry*, vol. 15, pp. 2277-2289, 2015.
- [41] M. A. Greenfield, J. R. Hoffman, M. Olvera de la Cruz, and S. I. Stupp, "Tunable mechanics of peptide nanofiber gels," *Langmuir*, vol. 26, pp. 3641-3647, 2009.
- [42] Y. S. Dagdas, A. Tombuloglu, A. B. Tekinay, A. Dana, and M. O. Guler, "Interfiber interactions alter the stiffness of gels formed by supramolecular self-assembled nanofibers," *Soft Matter*, vol. 7, pp. 3524-3532, 2011.
- [43] J. H. Ortony, C. J. Newcomb, J. B. Matson, L. C. Palmer, P. E. Doan, B. M. Hoffman, *et al.*, "Internal dynamics of a supramolecular nanofibre," *Nature materials*, vol. 13, pp. 812-816, 2014.
- [44] C. J. Newcomb, S. Sur, J. H. Ortony, O.-S. Lee, J. B. Matson, J. Boekhoven, *et al.*, "Cell death versus cell survival instructed by supramolecular cohesion of nanostructures," *Nature communications*, vol. 5, 2014.
- [45] T. Shimada, S. Lee, F. S. Bates, A. Hotta, and M. Tirrell, "Wormlike Micelle Formation in Peptide-Lipid Conjugates Driven by Secondary Structure Transformation of the Headgroups[†]," *The Journal of Physical Chemistry B*, vol. 113, pp. 13711-13714, 2009.
- [46] D. Missirlis, A. Chworos, C. J. Fu, H. A. Khant, D. V. Krogstad, and M. Tirrell, "Effect of the peptide secondary structure on the peptide amphiphile supramolecular structure and interactions," *Langmuir*, vol. 27, pp. 6163-6170, 2011.
- [47] K. L. Niece, J. D. Hartgerink, J. J. Donners, and S. I. Stupp, "Self-assembly combining two bioactive peptide-amphiphile molecules into nanofibers by electrostatic attraction," *Journal of the American Chemical Society*, vol. 125, pp. 7146-7147, 2003.
- [48] H. A. Behanna, J. J. Donners, A. C. Gordon, and S. I. Stupp, "Coassembly of amphiphiles with opposite peptide polarities into nanofibers," *Journal of the American Chemical Society*, vol. 127, pp. 1193-1200, 2005.

- [49] S. Toksoz, R. Mammadov, A. B. Tekinay, and M. O. Guler, "Electrostatic effects on nanofiber formation of self-assembling peptide amphiphiles," *Journal of colloid and interface science*, vol. 356, pp. 131-137, 2011.
- [50] M. Sever, B. Mammadov, M. O. Guler, and A. B. Tekinay, "Tenascin-C mimetic peptide nanofibers direct stem cell differentiation to osteogenic lineage," *Biomacromolecules*, vol. 15, pp. 4480-4487, 2014.
- [51] B. Mammadov, R. Mammadov, M. O. Guler, and A. B. Tekinay, "Cooperative effect of heparan sulfate and laminin mimetic peptide nanofibers on the promotion of neurite outgrowth," *Acta biomaterialia*, vol. 8, pp. 2077-2086, 2012.
- [52] H. Ceylan, S. Kocabey, A. B. Tekinay, and M. O. Guler, "Surface-adhesive and osteogenic self-assembled peptide nanofibers for bioinspired functionalization of titanium surfaces," *Soft matter*, vol. 8, pp. 3929-3937, 2012.
- [53] I. Hamley, A. Dehsorkhi, and V. Castelletto, "Coassembly in binary mixtures of peptide amphiphiles containing oppositely charged residues," *Langmuir*, vol. 29, pp. 5050-5059, 2013.
- [54] D. Mumcuoglu, M. Sardan, T. Tekinay, M. O. Guler, and A. B. Tekinay, "Oligonucleotide Delivery with Cell Surface Binding and Cell Penetrating Peptide Amphiphile Nanospheres," *Molecular pharmaceuticals*, vol. 12, pp. 1584-1591, 2015.
- [55] R. Mammadov, G. Cinar, N. Gunduz, M. Goktas, H. Kayhan, S. Tohumeken, *et al.*, "Virus-like nanostructures for tuning immune response," *Scientific Reports*, vol. 5, p. 16728, 2015.
- [56] L. Adler-Abramovich and E. Gazit, "The physical properties of supramolecular peptide assemblies: from building block association to technological applications," *Chemical Society Reviews*, vol. 43, pp. 6881-6893, 2014.
- [57] G. Fichman and E. Gazit, "Self-assembly of short peptides to form hydrogels: Design of building blocks, physical properties and technological applications," *Acta biomaterialia*, vol. 10, pp. 1671-1682, 2014.

- [58] S. Fleming and R. V. Ulijn, "Design of nanostructures based on aromatic peptide amphiphiles," *Chemical Society Reviews*, vol. 43, pp. 8150-8177, 2014.
- [59] C. Tang, R. V. Ulijn, and A. Saiani, "Effect of glycine substitution on fmoc–diphenylalanine self-assembly and gelation properties," *Langmuir*, vol. 27, pp. 14438-14449, 2011.
- [60] D. M. Ryan, S. B. Anderson, and B. L. Nilsson, "The influence of side-chain halogenation on the self-assembly and hydrogelation of Fmoc-phenylalanine derivatives," *Soft matter*, vol. 6, pp. 3220-3231, 2010.
- [61] D. M. Ryan, T. M. Doran, S. B. Anderson, and B. L. Nilsson, "Effect of C-terminal modification on the self-assembly and hydrogelation of fluorinated Fmoc-Phe derivatives," *Langmuir*, vol. 27, pp. 4029-4039, 2011.
- [62] Y. Kuang, Y. Gao, J. Shi, J. Li, and B. Xu, "The first supramolecular peptidic hydrogelator containing taurine," *Chemical Communications*, vol. 50, pp. 2772-2774, 2014.
- [63] C. Ou, J. Zhang, X. Zhang, Z. Yang, and M. Chen, "Phenothiazine as an aromatic capping group to construct a short peptide-based ‘super gelator’," *Chemical Communications*, vol. 49, pp. 1853-1855, 2013.
- [64] R. Garifullin and M. O. Guler, "Supramolecular chirality in self-assembled peptide amphiphile nanostructures," *Chemical Communications*, vol. 51, pp. 12470-12473, 2015.
- [65] L. Adler-Abramovich, N. Kol, I. Yanai, D. Barlam, R. Z. Shneck, E. Gazit, *et al.*, "Self-Assembled Organic Nanostructures with Metallic-Like Stiffness," *Angewandte Chemie International Edition*, vol. 49, pp. 9939-9942, 2010.
- [66] G. L. Eakins, J. K. Gallaher, R. A. Keyzers, A. Falber, J. E. Webb, A. Laos, *et al.*, "Thermodynamic Factors Impacting the Peptide-Driven Self-Assembly of Perylene Diimide Nanofibers," *The Journal of Physical Chemistry B*, vol. 118, pp. 8642-8651, 2014.
- [67] J. A. Lehrman, H. Cui, W.-W. Tsai, T. J. Moyer, and S. I. Stupp, "Supramolecular control of self-assembling terthiophene–peptide conjugates through the amino acid side chain," *Chemical Communications*, vol. 48, pp. 9711-9713, 2012.

- [68] H. A. M. Ardoña, K. Besar, M. Togninalli, H. E. Katz, and J. D. Tovar, "Sequence-dependent mechanical, photophysical and electrical properties of pi-conjugated peptide hydrogelators," *Journal of Materials Chemistry C*, 2015.
- [69] K. Matsuura, H. Hayashi, K. Murasato, and N. Kimizuka, "Trigonal tryptophane zipper as a novel building block for pH-responsive peptide nano-assemblies," *Chemical Communications*, vol. 47, pp. 265-267, 2011.
- [70] N. Tzokova, C. M. Fernyhough, P. D. Topham, N. Sandon, D. J. Adams, M. F. Butler, *et al.*, "Soft Hydrogels from Nanotubes of Poly (ethylene oxide)–Tetraphenylalanine Conjugates Prepared by Click Chemistry," *Langmuir*, vol. 25, pp. 2479-2485, 2009.
- [71] T. K. Paira, A. Saha, S. Banerjee, T. Das, P. Das, N. R. Jana, *et al.*, "Fluorescent Amphiphilic PEG-Peptide-PEG Triblock Conjugate Micelles for Cell Imaging," *Macromolecular bioscience*, vol. 14, pp. 929-935, 2014.
- [72] D. Peters, M. Kastantin, V. R. Kotamraju, P. P. Karmali, K. Gujraty, M. Tirrell, *et al.*, "Targeting atherosclerosis by using modular, multifunctional micelles," *Proceedings of the National Academy of Sciences*, vol. 106, pp. 9815-9819, 2009.
- [73] M. O. Guler, J. K. Pokorski, D. H. Appella, and S. I. Stupp, "Enhanced oligonucleotide binding to self-assembled nanofibers," *Bioconjugate chemistry*, vol. 16, pp. 501-503, 2005.
- [74] L.-H. Liu, Z.-Y. Li, L. Rong, S.-Y. Qin, Q. Lei, H. Cheng, *et al.*, "Self-Assembly of Hybridized Peptide Nucleic Acid Amphiphiles," *ACS Macro Letters*, vol. 3, pp. 467-471, 2014.
- [75] X. Li, Y. Kuang, J. Shi, Y. Gao, H.-C. Lin, and B. Xu, "Multifunctional, biocompatible supramolecular hydrogelators consist only of nucleobase, amino acid, and glycoside," *Journal of the American Chemical Society*, vol. 133, pp. 17513-17518, 2011.
- [76] C. R. Martinez and B. L. Iverson, "Rethinking the term “pi-stacking”," *Chemical Science*, vol. 3, pp. 2191-2201, 2012.
- [77] V. Jayawarna, M. Ali, T. A. Jowitt, A. F. Miller, A. Saiani, J. E. Gough, *et al.*, "Nanostructured Hydrogels for Three-Dimensional Cell Culture Through Self-

- Assembly of Fluorenylmethoxycarbonyl–Dipeptides," *Advanced Materials*, vol. 18, pp. 611-614, 2006.
- [78] M. Reches and E. Gazit, "Self-assembly of peptide nanotubes and amyloid-like structures by charged-termini-capped diphenylalanine peptide analogues," *Israel journal of chemistry*, vol. 45, pp. 363-371, 2005.
- [79] C. Tang, R. V. Ulijn, and A. Saiani, "Self-assembly and gelation properties of glycine/leucine Fmoc-dipeptides," *The European Physical Journal E*, vol. 36, pp. 1-11, 2013.
- [80] X. Du, J. Zhou, and B. Xu, "Supramolecular hydrogels made of basic biological building blocks," *Chemistry–An Asian Journal*, vol. 9, pp. 1446-1472, 2014.
- [81] M. Hughes, L. S. Birchall, K. Zuberi, L. A. Aitken, S. Debnath, N. Javid, *et al.*, "Differential supramolecular organisation of Fmoc-dipeptides with hydrophilic terminal amino acid residues by biocatalytic self-assembly," *Soft matter*, vol. 8, pp. 11565-11574, 2012.
- [82] G. Cheng, V. Castelletto, C. Moulton, G. Newby, and I. Hamley, "Hydrogelation and self-assembly of Fmoc-tripeptides: unexpected influence of sequence on self-assembled fibril structure, and hydrogel modulus and anisotropy," *Langmuir*, vol. 26, pp. 4990-4998, 2010.
- [83] G. Cheng, V. Castelletto, R. Jones, C. J. Connon, and I. W. Hamley, "Hydrogelation of self-assembling RGD-based peptides," *Soft matter*, vol. 7, pp. 1326-1333, 2011.
- [84] R. Orbach, L. Adler-Abramovich, S. Zigerson, I. Mironi-Harpaz, D. Seliktar, and E. Gazit, "Self-assembled Fmoc-peptides as a platform for the formation of nanostructures and hydrogels," *Biomacromolecules*, vol. 10, pp. 2646-2651, 2009.
- [85] T. Nakayama, T. Sakuraba, S. Tomita, A. Kaneko, E. Takai, K. Shiraki, *et al.*, "Charge-Separated Fmoc-Peptide β -Sheets: Sequence-Secondary Structure Relationship for Arranging Charged Side Chains on Both Sides," *Asian Journal of Organic Chemistry*, vol. 3, pp. 1182-1188, 2014.

- [86] H. Wang, C. Yang, M. Tan, L. Wang, D. Kong, and Z. Yang, "A structure–gelation ability study in a short peptide-based ‘Super Hydrogelator’ system," *Soft matter*, vol. 7, pp. 3897-3905, 2011.
- [87] M. Tena-Solsona, J. F. Miravet, and B. Escuder, "Tetrapeptidic Molecular Hydrogels: Self-assembly and Co-aggregation with Amyloid Fragment A β 1-40," *Chemistry–A European Journal*, vol. 20, pp. 1023-1031, 2014.
- [88] Y. Matsuzawa and N. Tamaoki, "Photoisomerization of azobenzene units controls the reversible dispersion and reorganization of fibrous self-assembled systems," *The Journal of Physical Chemistry B*, vol. 114, pp. 1586-1590, 2010.
- [89] G. Zeng, L. Liu, D. Xia, Q. Li, Z. Xin, J. Wang, *et al.*, "Transition of chemically modified diphenylalanine peptide assemblies revealed by atomic force microscopy," *RSC Adv.*, vol. 4, pp. 7516-7520, 2014.
- [90] S.-Y. Qin, H.-F. Jiang, M.-Y. Peng, Q. Lei, R.-X. Zhuo, and X.-Z. Zhang, "Adjustable nanofibers self-assembled from an irregular conformational peptide amphiphile," *Polymer Chemistry*, vol. 6, pp. 519-524, 2015.
- [91] A. D. Martin, J. Wojciechowski, M. Bhadbhade, and P. Thordarson, "A capped dipeptide which simultaneously exhibits gelation and crystallization behavior," *Langmuir*, 2016.
- [92] M. Amit, S. Appel, R. Cohen, G. Cheng, I. W. Hamley, and N. Ashkenasy, "Hybrid Proton and Electron Transport in Peptide Fibrils," *Advanced Functional Materials*, vol. 24, pp. 5873-5880, 2014.
- [93] D. A. Stone, L. Hsu, and S. I. Stupp, "Self-assembling quinquethiophene–oligopeptide hydrogelators," *Soft matter*, vol. 5, pp. 1990-1993, 2009.
- [94] R. Matmour, I. De Cat, S. J. George, W. Adriaens, P. Leclère, P. H. Bomans, *et al.*, "Oligo (p-phenylenevinylene)– Peptide Conjugates: Synthesis and Self-Assembly in Solution and at the Solid– Liquid Interface," *Journal of the American Chemical Society*, vol. 130, pp. 14576-14583, 2008.
- [95] D. González-Rodríguez and A. P. Schenning, "Hydrogen-bonded Supramolecular π -Functional Materials†," *Chemistry of Materials*, vol. 23, pp. 310-325, 2010.

- [96] H. A. M. Ardoña and J. D. Tovar, "Peptide π -Electron Conjugates: Organic Electronics for Biology?," *Bioconjugate chemistry*, vol. 26, pp. 2290-2302, 2015.
- [97] P. Wilson, J. Nicolas, and D. M. Haddleton, "Polymer–Protein/Peptide Bioconjugates," *Chemistry of Organo-Hybrids: Synthesis and Characterization of Functional Nano-Objects*, pp. 466-502, 2015.
- [98] J. Y. Shu, B. Panganiban, and T. Xu, "Peptide-polymer conjugates: from fundamental science to application," *Annual review of physical chemistry*, vol. 64, pp. 631-657, 2013.
- [99] D. J. Adams and P. D. Topham, "Peptide conjugate hydrogelators," *Soft matter*, vol. 6, pp. 3707-3721, 2010.
- [100] S. Ustun Yaylaci, M. Sardan Ekiz, E. Arslan, N. Can, E. Kilic, H. Ozkan, *et al.*, "Supramolecular GAG-like Self-Assembled Glycopeptide Nanofibers Induce Chondrogenesis and Cartilage Regeneration," *Biomacromolecules*, 2015.
- [101] S. H. Kim, J. A. Kaplan, Y. Sun, A. Shieh, H. L. Sun, C. M. Croce, *et al.*, "The Self-Assembly of Anticancer Camptothecin–Dipeptide Nanotubes: A Minimalistic and High Drug Loading Approach to Increased Efficacy," *Chemistry—A European Journal*, vol. 21, pp. 101-105, 2015.
- [102] F. Zhao, B. A. Heesters, I. Chiu, Y. Gao, J. Shi, N. Zhou, *et al.*, "l-Rhamnose-containing supramolecular nanofibrils as potential immunosuppressive materials," *Organic & biomolecular chemistry*, vol. 12, pp. 6816-6819, 2014.
- [103] Y.-b. Lim, S. Park, E. Lee, H. Jeong, J.-H. Ryu, M. S. Lee, *et al.*, "Glycoconjugate nanoribbons from the self-assembly of carbohydrate-peptide block molecules for controllable bacterial cell cluster formation," *Biomacromolecules*, vol. 8, pp. 1404-1408, 2007.
- [104] M. P. Williamson and J. P. Waltho, "Peptide structure from NMR," *Chemical Society Reviews*, vol. 21, pp. 227-236, 1992.
- [105] V. Singh, K. Snigdha, C. Singh, N. Sinha, and A. K. Thakur, "Understanding the self-assembly of Fmoc-phenylalanine to hydrogel formation," *Soft Matter*, 2015.

- [106] C. M. Rienstra, L. Tucker-Kellogg, C. P. Jaroniec, M. Hohwy, B. Reif, M. T. McMahon, *et al.*, "De novo determination of peptide structure with solid-state magic-angle spinning NMR spectroscopy," *Proceedings of the National Academy of Sciences*, vol. 99, pp. 10260-10265, 2002.
- [107] C. P. Jaroniec, C. E. MacPhee, V. S. Bajaj, M. T. McMahon, C. M. Dobson, and R. G. Griffin, "High-resolution molecular structure of a peptide in an amyloid fibril determined by magic angle spinning NMR spectroscopy," *Proceedings of the National Academy of Sciences of the United States of America*, vol. 101, pp. 711-716, 2004.
- [108] D. A. Middleton, J. Madine, V. Castelletto, and I. W. Hamley, "Insights into the Molecular Architecture of a Peptide Nanotube Using FTIR and Solid-State NMR Spectroscopic Measurements on an Aligned Sample," *Angewandte Chemie*, vol. 125, pp. 10731-10734, 2013.
- [109] M. Rad-Malekshahi, K. M. Visscher, J. P. Rodrigues, R. De Vries, W. E. Hennink, M. Baldus, *et al.*, "The supramolecular organization of a peptide-based nanocarrier at high molecular detail," *Journal of the American Chemical Society*, 2015.
- [110] K. Nagy-Smith, E. Moore, J. Schneider, and R. Tycko, "Molecular structure of monomorphic peptide fibrils within a kinetically trapped hydrogel network," *Proceedings of the National Academy of Sciences*, vol. 112, pp. 9816-9821, 2015.
- [111] W. H. Moore and S. Krimm, "Vibrational analysis of peptides, polypeptides, and proteins. II. β -Poly (L-alanine) and β -poly (L-alanylglycine)," *Biopolymers*, vol. 15, pp. 2465-2483, 1976.
- [112] K. Bakshi, M. Liyanage, D. Volkin, and C. R. Middaugh, "Fourier Transform Infrared Spectroscopy of Peptides," in *Therapeutic Peptides*. vol. 1088, A. E. Nixon, Ed., ed: Humana Press, 2014, pp. 255-269.
- [113] J. Kong and S. Yu, "Fourier Transform Infrared Spectroscopic Analysis of Protein Secondary Structures," *Acta Biochimica et Biophysica Sinica*, vol. 39, pp. 549-559, 2007.

- [114] R. Wei, C. C. Jin, J. Quan, H. I. Nie, and L. M. Zhu, "A novel self-assembling peptide with UV-responsive properties," *Biopolymers*, vol. 101, pp. 272-278, 2014.
- [115] C. G. Pappas, P. W. Frederix, T. Mutasa, S. Fleming, Y. M. Abul-Haija, S. M. Kelly, *et al.*, "Alignment of nanostructured tripeptide gels by directional ultrasonication," *Chemical Communications*, vol. 51, pp. 8465-8468, 2015.
- [116] C. G. Pappas, T. Mutasa, P. W. J. M. Frederix, S. Fleming, S. Bai, S. Debnath, *et al.*, "Transient supramolecular reconfiguration of peptide nanostructures using ultrasound," *Materials Horizons*, vol. 2, pp. 198-202, 2015.
- [117] M. Zhou, A. M. Smith, A. K. Das, N. W. Hodson, R. F. Collins, R. V. Ulijn, *et al.*, "Self-assembled peptide-based hydrogels as scaffolds for anchorage-dependent cells," *Biomaterials*, vol. 30, pp. 2523-2530, 2009.
- [118] M. Amorín, A. Pérez, J. Barberá, H. L. Ozores, J. L. Serrano, J. R. Granja, *et al.*, "Liquid crystal organization of self-assembling cyclic peptides," *Chemical Communications*, vol. 50, pp. 688-690, 2014.
- [119] F. Boulmedais, V. Ball, P. Schwinte, B. Frisch, P. Schaaf, and J.-C. Voegel, "Buildup of exponentially growing multilayer polypeptide films with internal secondary structure," *Langmuir*, vol. 19, pp. 440-445, 2003.
- [120] A. K. Nowinski, F. Sun, A. D. White, A. J. Keefe, and S. Jiang, "Sequence, structure, and function of peptide self-assembled monolayers," *Journal of the American Chemical Society*, vol. 134, pp. 6000-6005, 2012.
- [121] K. Ramaswamy, P. Kumaraswamy, S. Sethuraman, and U. M. Krishnan, "Self-assembly characteristics of a structural analogue of Tjernberg peptide," *RSC Advances*, vol. 4, pp. 16517-16523, 2014.
- [122] R. Tuma, "Raman spectroscopy of proteins: from peptides to large assemblies," *Journal of Raman Spectroscopy*, vol. 36, pp. 307-319, 2005.
- [123] S. Ayas, G. Cinar, A. D. Ozkan, Z. Soran, O. Ekiz, D. Kocaay, *et al.*, "Label-free nanometer-resolution imaging of biological architectures through surface enhanced raman scattering," *Scientific reports*, vol. 3, 2013.
- [124] S. Stewart and P. M. Fredericks, "Surface-enhanced Raman spectroscopy of peptides and proteins adsorbed on an electrochemically prepared silver

- surface," *Spectrochimica Acta Part A: Molecular and Biomolecular Spectroscopy*, vol. 55, pp. 1615-1640, 1999.
- [125] M. Paulite, C. Blum, T. Schmid, L. Opilik, K. Eyer, G. C. Walker, *et al.*, "Full Spectroscopic Tip-Enhanced Raman Imaging of Single Nanotapes Formed from β -Amyloid(1–40) Peptide Fragments," *ACS Nano*, vol. 7, pp. 911-920, 2013.
- [126] M. D. Sonntag, E. A. Pozzi, N. Jiang, M. C. Hersam, and R. P. Van Duyne, "Recent advances in tip-enhanced Raman spectroscopy," *The Journal of Physical Chemistry Letters*, vol. 5, pp. 3125-3130, 2014.
- [127] Z. Fan and A. O. Govorov, "Plasmonic circular dichroism of chiral metal nanoparticle assemblies," *Nano letters*, vol. 10, pp. 2580-2587, 2010.
- [128] K. Bakshi, M. R. Liyanage, D. B. Volkin, and C. R. Middaugh, "Circular Dichroism of Peptides," in *Therapeutic Peptides*, ed: Springer, 2014, pp. 247-253.
- [129] N. Singh, M. P. Conte, R. Ulijn, J. F. Miravet, and B. Escuder, "Insight into the esterase like activity demonstrated by an imidazole appended self-assembling hydrogelator," *Chemical Communications*, vol. 51, pp. 13213-13216, 2015.
- [130] Y. Tidhar, H. Weissman, S. G. Wolf, A. Gulino, and B. Rybtchinski, "Pathway-Dependent Self-Assembly of Perylene Diimide/Peptide Conjugates in Aqueous Medium," *Chemistry-A European Journal*, vol. 17, pp. 6068-6075, 2011.
- [131] Y. Liebes-Peer, H. Rapaport, and N. Ashkenasy, "Amplification of single molecule translocation signal using β -strand peptide functionalized nanopores," *ACS nano*, vol. 8, pp. 6822-6832, 2014.
- [132] P. Punzi, C. Giordano, F. Marino, S. Morosetti, P. De Santis, and A. Scipioni, "Metal chelates anchored to poly-l-peptides and linear d, l- α -peptides with promising nanotechnological applications," *Nanotechnology*, vol. 23, p. 395703, 2012.
- [133] D. Van Gough, J. S. Wheeler, S. Cheng, M. J. Stevens, and E. D. Spörke, "Supramolecular assembly of asymmetric self-neutralizing amphiphilic peptide wedges," *Langmuir*, vol. 30, pp. 9201-9209, 2014.

- [134] S. Mondal, L. Adler-Abramovich, A. Lampel, Y. Bram, S. Lipstman, and E. Gazit, "Formation of functional super-helical assemblies by constrained single heptad repeat," *Nature communications*, vol. 6, 2015.
- [135] E. T. Pashuck, H. Cui, and S. I. Stupp, "Tuning Supramolecular Rigidity of Peptide Fibers through Molecular Structure," *Journal of the American Chemical Society*, vol. 132, pp. 6041-6046, 2010.
- [136] C. W. Fishwick, A. J. Beevers, L. M. Carrick, C. D. Whitehouse, A. Aggeli, and N. Boden, "Structures of helical β -tapes and twisted ribbons: The role of side-chain interactions on twist and bend behavior," *Nano letters*, vol. 3, pp. 1475-1479, 2003.
- [137] S. Emamyari and H. Fazli, "pH-dependent self-assembly of EAK16 peptides in the presence of a hydrophobic surface: Coarse-grained molecular dynamics simulation," *Soft matter*, vol. 10, pp. 4248-4257, 2014.
- [138] T. Yu, O.-S. Lee, and G. C. Schatz, "Molecular dynamics simulations and electronic excited state properties of a self-assembled peptide amphiphile nanofiber with metalloporphyrin arrays," *The Journal of Physical Chemistry A*, vol. 118, pp. 8553-8562, 2014.
- [139] I. W. Fu, C. B. Markegard, B. K. Chu, and H. D. Nguyen, "Role of Hydrophobicity on Self-Assembly by Peptide Amphiphiles via Molecular Dynamics Simulations," *Langmuir*, vol. 30, pp. 7745-7754, 2014.
- [140] I. W. Fu and H. D. Nguyen, "Sequence-Dependent Structural Stability of Self-Assembled Cylindrical Nanofibers by Peptide Amphiphiles," *Biomacromolecules*, vol. 16, pp. 2209-2219, 2015.
- [141] G. Lanza, U. Chiacchio, S. Motta, S. Pellegrino, and G. Brogini, "On the Stability of Polyalanine Secondary Structures: The Role of the Polyproline II Helix," *ChemPhysChem*, vol. 12, pp. 2724-2727, 2011.
- [142] J. R. Perilla, B. C. Goh, C. K. Cassidy, B. Liu, R. C. Bernardi, T. Rudack, *et al.*, "Molecular dynamics simulations of large macromolecular complexes," *Current opinion in structural biology*, vol. 31, pp. 64-74, 2015.
- [143] P. Tamamis, K. Terzaki, M. Kassinopoulos, L. Mastrogiannis, E. Mossou, V. T. Forsyth, *et al.*, "Self-assembly of an aspartate-rich sequence from the adenovirus fiber shaft: insights from molecular dynamics simulations and

- experiments," *The Journal of Physical Chemistry B*, vol. 118, pp. 1765-1774, 2014.
- [144] D. J. Rubin, S. Amini, F. Zhou, H. Su, A. Miserez, and N. S. Joshi, "Structural, Nanomechanical, and Computational Characterization of d, l-Cyclic Peptide Assemblies," *ACS nano*, vol. 9, pp. 3360-3368, 2015.
- [145] S. C. Lange, J. Unsleber, P. Drücker, H.-J. Galla, M. P. Waller, and B. J. Ravoo, "pH response and molecular recognition in a low molecular weight peptide hydrogel," *Organic & biomolecular chemistry*, vol. 13, pp. 561-569, 2015.
- [146] P. W. Frederix, G. G. Scott, Y. M. Abul-Haija, D. Kalafatovic, C. G. Pappas, N. Javid, *et al.*, "Exploring the sequence space for (tri-) peptide self-assembly to design and discover new hydrogels," *Nature chemistry*, 2014.
- [147] I. W. Hamley, D. R. Nutt, G. D. Brown, J. F. Miravet, B. Escuder, and F. Rodríguez-Llansola, "Influence of the Solvent on the Self-Assembly of a Modified Amyloid Beta Peptide Fragment. II. NMR and Computer Simulation Investigation," *The Journal of Physical Chemistry B*, vol. 114, pp. 940-951, 2010.
- [148] R. Schweitzer-Stenner, "Simulated IR, isotropic and anisotropic Raman, and vibrational circular dichroism amide I band profiles of stacked β -sheets," *The Journal of Physical Chemistry B*, vol. 116, pp. 4141-4153, 2012.
- [149] W. R. Welch, J. Kubelka, and T. A. Keiderling, "Infrared, vibrational circular dichroism, and Raman spectral simulations for β -sheet structures with various isotopic labels, interstrand, and stacking arrangements using density functional theory," *The Journal of Physical Chemistry B*, vol. 117, pp. 10343-10358, 2013.
- [150] M. Hughes, P. W. Frederix, J. Raeburn, L. S. Birchall, J. Sadownik, F. C. Coomer, *et al.*, "Sequence/structure relationships in aromatic dipeptide hydrogels formed under thermodynamic control by enzyme-assisted self-assembly," *Soft Matter*, vol. 8, pp. 5595-5602, 2012.
- [151] A. Baral, S. Roy, A. Dehsorkhi, I. W. Hamley, S. Mohapatra, S. Ghosh, *et al.*, "Assembly of an injectable noncytotoxic peptide-based hydrogelator for sustained release of drugs," *Langmuir*, vol. 30, pp. 929-936, 2014.

- [152] Q. Li, Y. Jia, L. Dai, Y. Yang, and J. Li, "Controlled Rod Nanostructured Assembly of Diphenylalanine and Their Optical Waveguide Properties," *ACS Nano*, vol. 9, pp. 2689-2695, 2015.
- [153] V. Castelletto, I. W. Hamley, R. A. Hule, and D. Pochan, "Helical-Ribbon Formation by a β -Amino Acid Modified Amyloid β -Peptide Fragment," *Angewandte Chemie International Edition*, vol. 48, pp. 2317-2320, 2009.
- [154] E. T. Pashuck and S. I. Stupp, "Direct observation of morphological transformation from twisted ribbons into helical ribbons," *Journal of the American Chemical Society*, vol. 132, pp. 8819-8821, 2010.
- [155] H. Cui, A. G. Cheetham, E. T. Pashuck, and S. I. Stupp, "Amino acid sequence in constitutionally isomeric tetrapeptide amphiphiles dictates architecture of one-dimensional nanostructures," *Journal of the American Chemical Society*, vol. 136, pp. 12461-12468, 2014.
- [156] K. A. Houton, K. L. Morris, L. Chen, M. Schmidtman, J. T. Jones, L. C. Serpell, *et al.*, "On crystal versus fiber formation in dipeptide hydrogelator systems," *Langmuir*, vol. 28, pp. 9797-9806, 2012.
- [157] P. Bernadó, E. Mylonas, M. V. Petoukhov, M. Blackledge, and D. I. Svergun, "Structural characterization of flexible proteins using small-angle X-ray scattering," *Journal of the American Chemical Society*, vol. 129, pp. 5656-5664, 2007.
- [158] J.-B. Guilbaud and A. Saiani, "Using small angle scattering (SAS) to structurally characterise peptide and protein self-assembled materials," *Chemical Society Reviews*, vol. 40, pp. 1200-1210, 2011.
- [159] I. W. Hamley, A. Dehsorkhi, and V. Castelletto, "Coassembly in Binary Mixtures of Peptide Amphiphiles Containing Oppositely Charged Residues," *Langmuir*, vol. 29, pp. 5050-5059, 2013.
- [160] R. H. Zha, S. Sur, J. Boekhoven, H. Y. Shi, M. Zhang, and S. I. Stupp, "Supramolecular assembly of multifunctional maspin-mimetic nanostructures as a potent peptide-based angiogenesis inhibitor," *Acta Biomaterialia*, vol. 12, pp. 1-10, 2015.
- [161] R. Mammadov, A. B. Tekinay, A. Dana, and M. O. Guler, "Microscopic characterization of peptide nanostructures," *Micron*, vol. 43, pp. 69-84, 2012.

- [162] F. Thomas, N. C. Burgess, A. R. Thomson, and D. N. Woolfson, "Controlling the Assembly of Coiled-Coil Peptide Nanotubes," *Angewandte Chemie International Edition*, 2015.
- [163] Y. Wang, W. Qi, R. Huang, X. Yang, M. Wang, R. Su, *et al.*, "Rational Design of Chiral Nanostructures from Self-Assembly of a Ferrocene-Modified Dipeptide," *Journal of the American Chemical Society*, vol. 137, pp. 7869-7880, 2015.
- [164] C. J. Newcomb, T. J. Moyer, S. S. Lee, and S. I. Stupp, "Advances in cryogenic transmission electron microscopy for the characterization of dynamic self-assembling nanostructures," *Current Opinion in Colloid & Interface Science*, vol. 17, pp. 350-359, 2012.
- [165] D. Danino, "Cryo-TEM of soft molecular assemblies," *Current Opinion in Colloid & Interface Science*, vol. 17, pp. 316-329, 2012.
- [166] T. H. Sharp, M. Bruning, J. Mantell, R. B. Sessions, A. R. Thomson, N. R. Zaccai, *et al.*, "Cryo-transmission electron microscopy structure of a gigadalton peptide fiber of de novo design," *Proceedings of the National Academy of Sciences*, vol. 109, pp. 13266-13271, 2012.
- [167] V. Castelletto, I. W. Hamley, C. e. Cenker, U. Olsson, J. Adamcik, R. Mezzenga, *et al.*, "Influence of end-capping on the self-assembly of model amyloid peptide fragments," *The Journal of Physical Chemistry B*, vol. 115, pp. 2107-2116, 2011.
- [168] C. Goldsbury, J. Kistler, U. Aebi, T. Arvinte, and G. J. Cooper, "Watching amyloid fibrils grow by time-lapse atomic force microscopy," *Journal of molecular biology*, vol. 285, pp. 33-39, 1999.
- [169] A. Bracalello, V. Santopietro, M. Vassalli, G. Marletta, R. Del Gaudio, B. Bochicchio, *et al.*, "Design and Production of a Chimeric Resilin-, Elastin-, and Collagen-Like Engineered Polypeptide," *Biomacromolecules*, vol. 12, pp. 2957-2965, 2011.
- [170] C. Lara, N. P. Reynolds, J. T. Berryman, A. Xu, A. Zhang, and R. Mezzenga, "ILQINS hexapeptide, identified in lysozyme left-handed helical ribbons and nanotubes, forms right-handed helical ribbons and crystals," *Journal of the American Chemical Society*, vol. 136, pp. 4732-4739, 2014.

- [171] D. Pinotsi, A. K. Buell, C. Galvagnion, C. M. Dobson, G. S. Kaminski Schierle, and C. F. Kaminski, "Direct observation of heterogeneous amyloid fibril growth kinetics via two-color super-resolution microscopy," *Nano letters*, vol. 14, pp. 339-345, 2013.
- [172] L. L. del Mercato, P. P. Pompa, G. Maruccio, A. Della Torre, S. Sabella, A. M. Tamburro, *et al.*, "Charge transport and intrinsic fluorescence in amyloid-like fibrils," *Proceedings of the National Academy of Sciences*, vol. 104, pp. 18019-18024, 2007.
- [173] D. Pinotsi, A. K. Buell, C. M. Dobson, G. S. Kaminski Schierle, and C. F. Kaminski, "A Label-Free, Quantitative Assay of Amyloid Fibril Growth Based on Intrinsic Fluorescence," *ChemBioChem*, vol. 14, pp. 846-850, 2013.
- [174] R. Petry, M. Schmitt, and J. Popp, "Raman spectroscopy—a prospective tool in the life sciences," *ChemPhysChem*, vol. 4, pp. 14-30, 2003.
- [175] K. A. Antonio and Z. D. Schultz, "Advances in biomedical Raman microscopy," *Analytical chemistry*, vol. 86, pp. 30-46, 2013.
- [176] E. A. Pozzi, M. D. Sonntag, N. Jiang, J. M. Klingsporn, M. C. Hersam, and R. P. Van Duyne, "Tip-enhanced Raman imaging: An emergent tool for probing biology at the nanoscale," *ACS nano*, vol. 7, pp. 885-888, 2013.
- [177] N. E. Kurland, Z. Drira, and V. K. Yadavalli, "Measurement of nanomechanical properties of biomolecules using atomic force microscopy," *Micron*, vol. 43, pp. 116-128, 2012.
- [178] S. Zhang, H. Aslan, F. Besenbacher, and M. Dong, "Quantitative biomolecular imaging by dynamic nanomechanical mapping," *Chemical Society Reviews*, vol. 43, pp. 7412-7429, 2014.
- [179] D. Tranchida, S. Piccarolo, and R. A. C. Deblieck, "Some experimental issues of AFM tip blind estimation: the effect of noise and resolution," *Measurement Science and Technology*, vol. 17, p. 2630, 2006.
- [180] L. Calabri, N. Pugno, C. Menozzi, and S. Valeri, "AFM nanoindentation: tip shape and tip radius of curvature effect on the hardness measurement," *Journal of Physics: Condensed Matter*, vol. 20, p. 474208, 2008.

- [181] X. Li and B. Bhushan, "A review of nanoindentation continuous stiffness measurement technique and its applications," *Materials characterization*, vol. 48, pp. 11-36, 2002.
- [182] S. Yuran, Y. Razvag, P. Das, and M. Reches, "Self-assembly of azide containing dipeptides," *Journal of Peptide Science*, vol. 20, pp. 479-486, 2014.
- [183] Y. S. Dagdas, M. N. Aslan, A. B. Tekinay, M. O. Guler, and A. Dâna, "Nanomechanical characterization by double-pass force–distance mapping," *Nanotechnology*, vol. 22, p. 295704, 2011.
- [184] G. Cinar, H. Ceylan, M. Urel, T. S. Erkal, E. Deniz Tekin, A. B. Tekinay, *et al.*, "Amyloid inspired self-assembled Peptide nanofibers," *Biomacromolecules*, vol. 13, pp. 3377-3387, 2012.
- [185] S. Bolisetty, J. Adamcik, J. Heier, and R. Mezzenga, "Amyloid directed synthesis of titanium dioxide nanowires and their applications in hybrid photovoltaic devices," *Advanced Functional Materials*, vol. 22, pp. 3424-3428, 2012.
- [186] H. Sakai, K. Watanabe, Y. Asanomi, Y. Kobayashi, Y. Chuman, L. Shi, *et al.*, "Formation of Functionalized Nanowires by Control of Self-Assembly Using Multiple Modified Amyloid Peptides," *Advanced Functional Materials*, vol. 23, pp. 4881-4887, 2013.
- [187] D. Li, H. Furukawa, H. Deng, C. Liu, O. M. Yaghi, and D. S. Eisenberg, "Designed amyloid fibers as materials for selective carbon dioxide capture," *Proceedings of the National Academy of Sciences*, vol. 111, pp. 191-196, 2014.
- [188] U. Shimanovich, I. Efimov, T. O. Mason, P. Flagmeier, A. K. Buell, A. Gedanken, *et al.*, "Protein Microgels from Amyloid Fibril Networks," *ACS nano*, vol. 9, pp. 43-51, 2015.
- [189] N. P. Reynolds, M. Charnley, M. N. Bongiovanni, P. G. Hartley, and S. L. Gras, "Biomimetic topography and chemistry control cell attachment to amyloid fibrils," *Biomacromolecules*, vol. 16, pp. 1556-1565, 2015.
- [190] T. P. Knowles and M. J. Buehler, "Nanomechanics of functional and pathological amyloid materials," *Nature nanotechnology*, vol. 6, pp. 469-479, 2011.

- [191] C. Bortolini, N. C. Jones, S. V. Hoffmann, C. Wang, F. Besenbacher, and M. Dong, "Mechanical properties of amyloid-like fibrils defined by secondary structures," *Nanoscale*, vol. 7, pp. 7745-7752, 2015.
- [192] D. J. Rubin, H. T. Nia, T. Desire, P. Q. Nguyen, M. Gevelber, C. Ortiz, *et al.*, "Mechanical Reinforcement of Polymeric Fibers through Peptide Nanotube Incorporation," *Biomacromolecules*, vol. 14, pp. 3370-3375, 2013.
- [193] S. Sathaye, A. Mbi, C. Sonmez, Y. Chen, D. L. Blair, J. P. Schneider, *et al.*, "Rheology of peptide- and protein-based physical hydrogels: Are everyday measurements just scratching the surface?," *Wiley Interdisciplinary Reviews: Nanomedicine and Nanobiotechnology*, vol. 7, pp. 34-68, 2015.
- [194] R. Chapman, M. Danial, M. L. Koh, K. A. Jolliffe, and S. Perrier, "Design and properties of functional nanotubes from the self-assembly of cyclic peptide templates," *Chemical Society Reviews*, vol. 41, pp. 6023-6041, 2012.
- [195] B. H. Jones, A. M. Martinez, J. S. Wheeler, and E. D. Spörke, "Surfactant-induced assembly of enzymatically-stable peptide hydrogels," *Soft matter*, vol. 11, pp. 3572-3580, 2015.
- [196] P. J. King, M. G. Lizio, A. Booth, R. F. Collins, J. E. Gough, A. F. Miller, *et al.*, "A modular self-assembly approach to functionalised β -sheet peptide hydrogel biomaterials," *Soft matter*, 2016.
- [197] C. Veerman, K. Rajagopal, C. S. Palla, D. J. Pochan, J. P. Schneider, and E. M. Furst, "Gelation kinetics of β -hairpin peptide hydrogel networks," *Macromolecules*, vol. 39, pp. 6608-6614, 2006.
- [198] M. Owczarz, S. Bolisetty, R. Mezzenga, and P. Arosio, "Sol–gel transition of charged fibrils composed of a model amphiphilic peptide," *Journal of colloid and interface science*, vol. 437, pp. 244-251, 2015.
- [199] T.-W. Chu, J. Feng, J. Yang, and J. Kopeček, "Hybrid polymeric hydrogels via peptide nucleic acid (PNA)/DNA complexation," *Journal of Controlled Release*, vol. 220, pp. 608-616, 2015.
- [200] T. W. Herling, G. A. Garcia, T. C. Michaels, W. Grentz, J. Dean, U. Shimanovich, *et al.*, "Force generation by the growth of amyloid aggregates," *Proceedings of the National Academy of Sciences*, vol. 112, pp. 9524-9529, 2015.

- [201] C. Alvarez-Lorenzo and A. Concheiro, "From drug dosage forms to intelligent drug delivery systems: a change of paradigm," *Smart materials for drug delivery*, vol. 1, pp. 1-32, 2013.
- [202] J. Shi, A. R. Votruba, O. C. Farokhzad, and R. Langer, "Nanotechnology in drug delivery and tissue engineering: from discovery to applications," *Nano letters*, vol. 10, pp. 3223-3230, 2010.
- [203] Y. Zhang, H. F. Chan, and K. W. Leong, "Advanced materials and processing for drug delivery: the past and the future," *Advanced drug delivery reviews*, vol. 65, pp. 104-120, 2013.
- [204] D. Patra, S. Sengupta, W. Duan, H. Zhang, R. Pavlick, and A. Sen, "Intelligent, self-powered, drug delivery systems," *Nanoscale*, vol. 5, pp. 1273-1283, 2013.
- [205] G. Cinar, D. Mumcuoglu, A. B. Tekinay, and M. O. Guler, "NANOSIZED DELIVERY SYSTEMS FOR TISSUE REGENERATION," *Therapeutic Nanomaterials*, p. 7, 2016.
- [206] G. Verma and P. Hassan, "Self assembled materials: design strategies and drug delivery perspectives," *Physical Chemistry Chemical Physics*, vol. 15, pp. 17016-17028, 2013.
- [207] M. C. Branco and J. P. Schneider, "Self-assembling materials for therapeutic delivery," *Acta biomaterialia*, vol. 5, pp. 817-831, 2009.
- [208] E. Busseron, Y. Ruff, E. Moulin, and N. Giuseppone, "Supramolecular self-assemblies as functional nanomaterials," *Nanoscale*, vol. 5, pp. 7098-7140, 2013.
- [209] J. J. Panda and V. S. Chauhan, "Short peptide based self-assembled nanostructures: implications in drug delivery and tissue engineering," *Polymer Chemistry*, vol. 5, pp. 4418-4436, 2014.
- [210] J. C. Rodríguez-Cabello, F. J. Arias, M. A. Rodrigo, and A. Girotti, "Elastin-like polypeptides in drug delivery," *Advanced Drug Delivery Reviews*, vol. 97, pp. 85-100, 2016.
- [211] S. Sundar, Y. Chen, and Y. Tong, "Delivery of therapeutics and molecules using self-assembled peptides," *Current medicinal chemistry*, vol. 21, pp. 2469-2479, 2014.

- [212] R. Mammadov, G. Cinar, N. Gunduz, M. Goktas, H. Kayhan, S. Tohumeken, *et al.*, "Virus-like nanostructures for tuning immune response," *Scientific reports*, vol. 5, 2015.
- [213] H. W. Jun, V. Yuwono, S. E. Paramonov, and J. D. Hartgerink, "Enzyme-Mediated Degradation of Peptide-Amphiphile Nanofiber Networks," *Advanced Materials*, vol. 17, pp. 2612-2617, 2005.
- [214] R. H. Zha, S. Sur, and S. I. Stupp, "Self-assembly of Cytotoxic Peptide Amphiphiles into Supramolecular Membranes for Cancer Therapy," *Advanced healthcare materials*, vol. 2, pp. 126-133, 2013.
- [215] A. Dehsorkhi, I. W. Hamley, J. Seitsonen, and J. Ruokolainen, "Tuning self-assembled nanostructures through enzymatic degradation of a peptide amphiphile," *Langmuir*, vol. 29, pp. 6665-6672, 2013.
- [216] J.-K. Kim, J. Anderson, H.-W. Jun, M. A. Repka, and S. Jo, "Self-assembling peptide amphiphile-based nanofiber gel for bioresponsive cisplatin delivery," *Molecular pharmaceutics*, vol. 6, pp. 978-985, 2009.
- [217] S. Soukasene, D. J. Toft, T. J. Moyer, H. Lu, H.-K. Lee, S. M. Standley, *et al.*, "Antitumor activity of peptide amphiphile nanofiber-encapsulated camptothecin," *ACS nano*, vol. 5, pp. 9113-9121, 2011.
- [218] T. Ji, Y. Ding, Y. Zhao, J. Wang, H. Qin, X. Liu, *et al.*, "Peptide Assembly Integration of Fibroblast-Targeting and Cell-Penetration Features for Enhanced Antitumor Drug Delivery," *Advanced Materials*, vol. 27, pp. 1865-1873, 2015.
- [219] R. Tian, H. Wang, R. Niu, and D. Ding, "Drug delivery with nanospherical supramolecular cell penetrating peptide-taxol conjugates containing a high drug loading," *Journal of colloid and interface science*, vol. 453, pp. 15-20, 2015.
- [220] A. G. Cheetham, P. Zhang, Y.-a. Lin, L. L. Lock, and H. Cui, "Supramolecular nanostructures formed by anticancer drug assembly," *Journal of the American Chemical Society*, vol. 135, pp. 2907-2910, 2013.
- [221] Z. Chen, P. Zhang, A. G. Cheetham, J. H. Moon, J. W. Moxley, Y.-a. Lin, *et al.*, "Controlled release of free doxorubicin from peptide-drug conjugates by drug loading," *Journal of Controlled Release*, vol. 191, pp. 123-130, 2014.

- [222] M. C. Branco, D. J. Pochan, N. J. Wagner, and J. P. Schneider, "Macromolecular diffusion and release from self-assembled β -hairpin peptide hydrogels," *Biomaterials*, vol. 30, pp. 1339-1347, 2009.
- [223] J. B. Matson, C. J. Newcomb, R. Bitton, and S. I. Stupp, "Nanostructure-templated control of drug release from peptide amphiphile nanofiber gels," *Soft Matter*, vol. 8, pp. 3586-3595, 2012.
- [224] S. Koutsopoulos and S. Zhang, "Two-layered injectable self-assembling peptide scaffold hydrogels for long-term sustained release of human antibodies," *Journal of controlled release*, vol. 160, pp. 451-458, 2012.
- [225] H. W. Seo, D. Y. Kwon, J. S. Kwon, L. M. Jin, B. Lee, J. H. Kim, *et al.*, "Injectable intratumoral hydrogel as 5-fluorouracil drug depot," *Biomaterials*, vol. 34, pp. 2748-2757, 2013.
- [226] W. Wang, L. Deng, S. Xu, X. Zhao, N. Lv, G. Zhang, *et al.*, "A reconstituted "two into one" thermosensitive hydrogel system assembled by drug-loaded amphiphilic copolymer nanoparticles for the local delivery of paclitaxel," *Journal of Materials Chemistry B*, vol. 1, pp. 552-563, 2013.
- [227] G. Chang, T. Ci, L. Yu, and J. Ding, "Enhancement of the fraction of the active form of an antitumor drug topotecan via an injectable hydrogel," *Journal of Controlled Release*, vol. 156, pp. 21-27, 2011.
- [228] J. Y. Lee, K. S. Kim, Y. M. Kang, E. S. Kim, S.-J. Hwang, H. B. Lee, *et al.*, "In vivo efficacy of paclitaxel-loaded injectable in situ-forming gel against subcutaneous tumor growth," *International journal of pharmaceutics*, vol. 392, pp. 51-56, 2010.
- [229] S. Koutsopoulos, L. D. Unsworth, Y. Nagai, and S. Zhang, "Controlled release of functional proteins through designer self-assembling peptide nanofiber hydrogel scaffold," *Proceedings of the National Academy of Sciences*, vol. 106, pp. 4623-4628, 2009.
- [230] V. A. Kumar, S. Shi, B. K. Wang, I.-C. Li, A. A. Jalan, B. Sarkar, *et al.*, "Drug-triggered and cross-linked self-assembling nanofibrous hydrogels," *Journal of the American Chemical Society*, vol. 137, pp. 4823-4830, 2015.

- [231] V. A. Kumar, N. L. Taylor, S. Shi, N. C. Wickremasinghe, R. N. D'Souza, and J. D. Hartgerink, "Self-assembling multidomain peptides tailor biological responses through biphasic release," *Biomaterials*, vol. 52, pp. 71-78, 2015.
- [232] M. Guvendiren, H. D. Lu, and J. A. Burdick, "Shear-thinning hydrogels for biomedical applications," *Soft Matter*, vol. 8, pp. 260-272, 2012.
- [233] X.-D. Xu, L. Liang, C.-S. Chen, B. Lu, N.-l. Wang, F.-G. Jiang, *et al.*, "Peptide Hydrogel as an Intraocular Drug Delivery System for Inhibition of Postoperative Scarring Formation," *ACS Applied Materials & Interfaces*, vol. 2, pp. 2663-2671, 2010.
- [234] A. Altunbas, S. J. Lee, S. A. Rajasekaran, J. P. Schneider, and D. J. Pochan, "Encapsulation of curcumin in self-assembling peptide hydrogels as injectable drug delivery vehicles," *Biomaterials*, vol. 32, pp. 5906-5914, 2011.
- [235] J. E. Sun, B. Stewart, A. Litan, S. J. Lee, J. P. Schneider, S. A. Langhans, *et al.*, "Sustained release of active chemotherapeutics from injectable-solid β -hairpin peptide hydrogel," *Biomaterials science*, 2016.
- [236] Y. Loo, S. Zhang, and C. A. Hauser, "From short peptides to nanofibers to macromolecular assemblies in biomedicine," *Biotechnology advances*, vol. 30, pp. 593-603, 2012.
- [237] L. E. O'Leary, J. A. Fallas, E. L. Bakota, M. K. Kang, and J. D. Hartgerink, "Multi-hierarchical self-assembly of a collagen mimetic peptide from triple helix to nanofibre and hydrogel," *Nature chemistry*, vol. 3, pp. 821-828, 2011.
- [238] J. A. Fallas, L. E. O'Leary, and J. D. Hartgerink, "Synthetic collagen mimics: self-assembly of homotrimers, heterotrimers and higher order structures," *Chemical Society Reviews*, vol. 39, pp. 3510-3527, 2010.
- [239] V. M. Tysseling-Mattiace, V. Sahni, K. L. Niece, D. Birch, C. Czeisler, M. G. Fehlings, *et al.*, "Self-assembling nanofibers inhibit glial scar formation and promote axon elongation after spinal cord injury," *The Journal of Neuroscience*, vol. 28, pp. 3814-3823, 2008.
- [240] E. J. Berns, S. Sur, L. Pan, J. E. Goldberger, S. Suresh, S. Zhang, *et al.*, "Aligned neurite outgrowth and directed cell migration in self-assembled monodomain gels," *Biomaterials*, vol. 35, pp. 185-195, 2014.

- [241] S. S. Lee, E. L. Hsu, M. Mendoza, J. Ghodasra, M. S. Nickoli, A. Ashtekar, *et al.*, "Gel Scaffolds of BMP-2-Binding Peptide Amphiphile Nanofibers for Spinal Arthrodesis," *Advanced Healthcare Materials*, vol. 4, pp. 131-141, 2015.
- [242] R. Mammadov, B. Mammadov, M. O. Guler, and A. B. Tekinay, "Growth Factor Binding on Heparin Mimetic Peptide Nanofibers," *Biomacromolecules*, vol. 13, pp. 3311-3319, 2012.
- [243] S. Ustun, A. Tombuloglu, M. Kilinc, M. O. Guler, and A. B. Tekinay, "Growth and Differentiation of Prechondrogenic Cells on Bioactive Self-Assembled Peptide Nanofibers," *Biomacromolecules*, vol. 14, pp. 17-26, 2013.
- [244] S. U. Yaylaci, M. Sen, O. Bulut, E. Arslan, M. O. Guler, and A. B. Tekinay, "Chondrogenic Differentiation of Mesenchymal Stem Cells on Glycosaminoglycan-Mimetic Peptide Nanofibers," *ACS Biomaterials Science & Engineering*, vol. 2, pp. 871-878, 2016.
- [245] G. Cinar, I. Orujalipoor, C.-J. Su, U. S. Jeng, S. Ide, and M. O. Guler, "Supramolecular Nanostructure Formation of Coassembled Amyloid Inspired Peptides," *Langmuir*, vol. 32, pp. 6506-6514, 2016.
- [246] C. C. VandenAkker, M. F. Engel, K. P. Velikov, M. Bonn, and G. H. Koenderink, "Morphology and persistence length of amyloid fibrils are correlated to peptide molecular structure," *J. Am. Chem. Soc.*, vol. 133, pp. 18030-18033, 2011.
- [247] T. P. Knowles and M. J. Buehler, "Nanomechanics of functional and pathological amyloid materials," *Nat. Nanotechnol.*, vol. 6, pp. 469-479, 2011.
- [248] J. F. Smith, T. P. Knowles, C. M. Dobson, C. E. MacPhee, and M. E. Welland, "Characterization of the nanoscale properties of individual amyloid fibrils," *Proc. Natl. Acad. Sci.*, vol. 103, pp. 15806-15811, 2006.
- [249] M. R. Sawaya, S. Sambashivan, R. Nelson, M. I. Ivanova, S. A. Sievers, M. I. Apostol, *et al.*, "Atomic structures of amyloid cross- β spines reveal varied steric zippers," *Nature*, vol. 447, pp. 453-457, 2007.
- [250] R. Nelson, M. R. Sawaya, M. Balbirnie, A. Ø. Madsen, C. Riek, R. Grothe, *et al.*, "Structure of the cross- β spine of amyloid-like fibrils," *Nature*, vol. 435, pp. 773-778, 2005.

- [251] K. L. Morris, A. Rodger, M. R. Hicks, M. Debulpaep, J. Schymkowitz, F. Rousseau, *et al.*, "Exploring the sequence–structure relationship for amyloid peptides," *Biochem. J.*, vol. 450, pp. 275-283, 2013.
- [252] O. S. Makin, E. Atkins, P. Sikorski, J. Johansson, and L. C. Serpell, "Molecular basis for amyloid fibril formation and stability," *Proc. Natl. Acad. Sci. U. S. A.*, vol. 102, pp. 315-320, 2005.
- [253] K. Sweers, K. van der Werf, M. Bennink, and V. Subramaniam, "Nanomechanical properties of α -synuclein amyloid fibrils: a comparative study by nanoindentation, harmonic force microscopy, and Peakforce QNM," *Nanoscale Res. Lett.*, vol. 6, pp. 1-10, 2011.
- [254] R. Paparcone, S. Keten, and M. J. Buehler, "Atomistic simulation of nanomechanical properties of Alzheimer's A β (1–40) amyloid fibrils under compressive and tensile loading," *J. Biomech.*, vol. 43, pp. 1196-1201, 2010.
- [255] S. Guo and B. B. Akhremitchev, "Packing density and structural heterogeneity of insulin amyloid fibrils measured by AFM nanoindentation," *Biomacromolecules*, vol. 7, pp. 1630-1636, 2006.
- [256] N. E. Kurland, Z. Drira, and V. K. Yadavalli, "Measurement of nanomechanical properties of biomolecules using atomic force microscopy," *Micron*, vol. 43, pp. 116-128, 2011.
- [257] T. P. J. Knowles and M. J. Buehler, "Nanomechanics of functional and pathological amyloid materials," *Nat. Nanotechnol.*, vol. 6, pp. 469-479, 2011.
- [258] N. R. Anthony, A. K. Mehta, D. G. Lynn, and K. M. Berland, "Mapping amyloid- β (16-22) nucleation pathways using fluorescence lifetime imaging microscopy," *Soft Matter*, vol. 10, pp. 4162-4172, 2014.
- [259] T. P. Knowles, C. A. Waudby, G. L. Devlin, S. I. Cohen, A. Aguzzi, M. Vendruscolo, *et al.*, "An analytical solution to the kinetics of breakable filament assembly," *Science*, vol. 326, pp. 1533-1537, 2009.
- [260] A. K. Buell, C. Galvagnion, R. Gaspar, E. Sparr, M. Vendruscolo, T. P. Knowles, *et al.*, "Solution conditions determine the relative importance of nucleation and growth processes in α -synuclein aggregation," *Proc. Natl. Acad. Sci.*, vol. 111, pp. 7671-7676, 2014.

- [261] T. Scheibel, J. Bloom, and S. L. Lindquist, "The elongation of yeast prion fibers involves separable steps of association and conversion," *Proc. Natl. Acad. Sci.*, vol. 101, pp. 2287-2292, 2004.
- [262] R. Paparcone, S. W. Cranford, and M. J. Buehler, "Self-folding and aggregation of amyloid nanofibrils," *Nanoscale*, vol. 3, pp. 1748-1755, 2011.
- [263] D. Li, H. Furukawa, H. Deng, C. Liu, O. M. Yaghi, and D. S. Eisenberg, "Designed amyloid fibers as materials for selective carbon dioxide capture," *Proc. Natl. Acad. Sci.*, vol. 111, pp. 191-196, 2014.
- [264] R. S. Jacob, D. Ghosh, P. K. Singh, S. K. Basu, N. N. Jha, S. Das, *et al.*, "Self healing hydrogels composed of amyloid nano fibrils for cell culture and stem cell differentiation," *Biomaterials*, vol. 54, pp. 97-105, 2015.
- [265] C. E. Brubaker and P. B. Messersmith, "The present and future of biologically inspired adhesive interfaces and materials," *Langmuir*, vol. 28, pp. 2200-2205, 2012.
- [266] M. R. Krebs, E. H. Bromley, and A. M. Donald, "The binding of thioflavin-T to amyloid fibrils: localisation and implications," *J. Struct. Biol.*, vol. 149, pp. 30-37, 2005.
- [267] T. Miti, M. Mulaj, J. D. Schmit, and M. Muschol, "Stable, metastable, and kinetically trapped amyloid aggregate phases," *Biomacromolecules*, vol. 16, pp. 326-335, 2014.
- [268] A. M. Streets, Y. Sourigues, R. R. Kopito, R. Melki, and S. R. Quake, "Simultaneous measurement of amyloid fibril formation by dynamic light scattering and fluorescence reveals complex aggregation kinetics," *PloS ONE*, vol. 8, p. e54541, 2013.
- [269] M. M. Wördehoff, O. Bannach, H. Shaykhalishahi, A. Kulawik, S. Schiefer, D. Willbold, *et al.*, "Single Fibril Growth Kinetics of α -Synuclein," *J. Mol. Biol.*, vol. 427, pp. 1428-1435, 2015.
- [270] H.-M. Chan, L. Xiao, K.-M. Yeung, S.-L. Ho, D. Zhao, W.-H. Chan, *et al.*, "Effect of surface-functionalized nanoparticles on the elongation phase of beta-amyloid (1–40) fibrillogenesis," *Biomaterials*, vol. 33, pp. 4443-4450, 2012.

- [271] J.-B. Guilbaud and A. Saiani, "Using small angle scattering (SAS) to structurally characterise peptide and protein self-assembled materials," *Chem. Soc. Rev.*, vol. 40, pp. 1200-1210, 2011.
- [272] A. E. Langkilde and B. Vestergaard, "Methods for structural characterization of prefibrillar intermediates and amyloid fibrils," *FEBS Lett.*, vol. 583, pp. 2600-2609, 2009.
- [273] F. Bemporad and F. Chiti, "Protein misfolded oligomers: experimental approaches, mechanism of formation, and structure-toxicity relationships," *Chemistry & biology*, vol. 19, pp. 315-327, 2012.
- [274] A. Altunbas, N. Sharma, M. S. Lamm, C. Yan, R. P. Nagarkar, J. P. Schneider, *et al.*, "Peptide– Silica Hybrid Networks: Biomimetic Control of Network Mechanical Behavior," *ACS Nano*, vol. 4, pp. 181-188, 2009.
- [275] M. A. Thompson and M. C. Zerner, "A theoretical examination of the electronic structure and spectroscopy of the photosynthetic reaction center from *Rhodospseudomonas viridis*," *J. Am. Chem. Soc.*, vol. 113, pp. 8210-8215, 1991.
- [276] C. Oostenbrink, A. Villa, A. E. Mark, and W. F. Van Gunsteren, "A biomolecular force field based on the free enthalpy of hydration and solvation: The GROMOS force-field parameter sets 53A5 and 53A6," *J. Comput. Chem.*, vol. 25, pp. 1656-1676, 2004.
- [277] D. Van Der Spoel, E. Lindahl, B. Hess, G. Groenhof, A. E. Mark, and H. J. C. Berendsen, "GROMACS: fast, flexible, and free," *J. Comput. Chem.*, vol. 26, pp. 1701-1718, 2005.
- [278] P. E. Smith and W. F. van Gunsteren, "The viscosity of SPC and SPC/E water at 277 and 300 K," *Chem. Phys. Lett.*, vol. 215, pp. 315-318, 1993.
- [279] R. Hockney, S. Goel, and J. Eastwood, "Quiet high-resolution computer models of a plasma," *J. Comput. Phys.*, vol. 14, pp. 148-158, 1974.
- [280] B. Hess, H. Bekker, H. J. C. Berendsen, and J. G. E. M. Fraaije, "LINCS: a linear constraint solver for molecular simulations," *J. Comput. Chem.*, vol. 18, pp. 1463-1472, 1997.

- [281] T. Darden, D. York, and L. Pedersen, "Particle mesh Ewald: An $N \cdot \log(N)$ method for Ewald sums in large systems," *J. Chem. Phys.*, vol. 98, pp. 10089-10092, 1993.
- [282] U. Essmann, L. Perera, M. L. Berkowitz, T. Darden, H. Lee, and L. G. Pedersen, "A smooth particle mesh Ewald method," *J. Chem. Phys.*, vol. 103, pp. 8577-8593, 1995.
- [283] M. Parrinello and A. Rahman, "Polymorphic transitions in single crystals: A new molecular dynamics method," *J. Appl. Phys.*, vol. 52, pp. 7182-7190, 1981.
- [284] G. Bussi, D. Donadio, and M. Parrinello, "Canonical sampling through velocity rescaling," *J. Chem. Phys.*, vol. 126, pp. 014101-014107, 2007.
- [285] W. Humphrey, A. Dalke, and K. Schulten, "VMD: visual molecular dynamics," *J. Mol. Graphics*, vol. 14, pp. 33-38, 1996.
- [286] P. Kumaraswamy, S. Sethuraman, and U. M. Krishnan, "Hierarchical self-assembly of Tjernberg peptide at nanoscale," *Soft Matter*, vol. 9, pp. 2684-2694, 2013.
- [287] A. Guimer and G. Fournet, "Small angle scattering of X-rays," *J. Wiley & Sons, New York*, 1955.
- [288] J. S. Pedersen and P. Schurtenberger, "Scattering functions of semiflexible polymers with and without excluded volume effects," *Macromolecules*, vol. 29, pp. 7602-7612, 1996.
- [289] W.-R. Chen, P. D. Butler, and L. J. Magid, "Incorporating intermicellar interactions in the fitting of SANS data from cationic wormlike micelles," *Langmuir*, vol. 22, pp. 6539-6548, 2006.
- [290] S. R. Kline, "Reduction and analysis of SANS and USANS data using IGOR Pro," *J. Appl. Crystallogr.*, vol. 39, pp. 895-900, 2006.
- [291] O. Glatter and O. Kratky, *Small angle X-ray scattering*: Academic press, 1982.
- [292] G. Schulz, "The kinetics of chain polymerization, V," *The effect of various reaction species on the multimolecularity. Z. Phys. Chem.*, vol. 43, pp. 25-46, 1939.
- [293] O. Kratky and G. Porod, "X-ray investigation of dissolved chain molecules," *Recl. Trav. Chim. Pays-Bas*, vol. 68, pp. 1106-1122, 1949.

- [294] D. Pötschke, P. Hickl, M. Ballauff, P. O. Åstrand, and J. S. Pedersen, "Analysis of the conformation of worm-like chains by small-angle scattering: Monte-Carlo simulations in comparison to analytical theory," *Macromol. Theory Simul.*, vol. 9, pp. 345-353, 2000.
- [295] Y. S. Dagdas, M. Necip Aslan, A. B. Tekinay, M. O. Guler, and A. Dâna, "Nanomechanical characterization by double-pass force–distance mapping," *Nanotechnology*, vol. 22, p. 295704, 2011.
- [296] B. Baudin, A. Bruneel, N. Bosselut, and M. Vaubourdolle, "A protocol for isolation and culture of human umbilical vein endothelial cells," *Nat. Protoc.*, vol. 2, pp. 481-485, 2007.
- [297] H. Ceylan, A. B. Tekinay, and M. O. Guler, "Selective adhesion and growth of vascular endothelial cells on bioactive peptide nanofiber functionalized stainless steel surface," *Biomaterials*, vol. 32, pp. 8797-8805 2011.
- [298] T. R. Jahn, O. S. Makin, K. L. Morris, K. E. Marshall, P. Tian, P. Sikorski, *et al.*, "The Common Architecture of Cross-[beta] Amyloid," *J. Mol. Biol.*, vol. 395, pp. 717-727, 2010.
- [299] D. M. Ryan and B. L. Nilsson, "Self-assembled amino acids and dipeptides as noncovalent hydrogels for tissue engineering," *Polym. Chem.*, vol. 3, pp. 18-33, 2012.
- [300] A. Thomas, R. Meurisse, B. Charlotiaux, and R. Brasseur, "Aromatic side-chain interactions in proteins. I. Main structural features," *Proteins: Struct., Funct., Bioinf.*, vol. 48, pp. 628-634, 2002.
- [301] E. Gazit, "A possible role for π -stacking in the self-assembly of amyloid fibrils," *FASEB J.*, vol. 16, pp. 77-83, 2002.
- [302] K. L. Niece, J. D. Hartgerink, J. J. Donners, and S. I. Stupp, "Self-assembly combining two bioactive peptide-amphiphile molecules into nanofibers by electrostatic attraction," *J. Am. Chem. Soc.*, vol. 125, pp. 7146-7147, 2003.
- [303] X.-D. Xu, C.-S. Chen, B. Lu, S.-X. Cheng, X.-Z. Zhang, and R.-X. Zhuo, "Coassembly of oppositely charged short peptides into well-defined supramolecular hydrogels," *J. Phys. Chem. B*, vol. 114, pp. 2365-2372, 2010.

- [304] Y. Takahashi, A. Ueno, and H. Mihara, "Amyloid architecture: complementary assembly of heterogeneous combinations of three or four peptides into amyloid fibrils," *ChemBioChem*, vol. 3, pp. 637-642, 2002.
- [305] S. Ramachandran, J. Trewella, Y. Tseng, and Y. B. Yu, "Coassembling peptide-based biomaterials: effects of pairing equal and unequal chain length oligopeptides," *Chem. Mater.*, vol. 18, pp. 6157-6162, 2006.
- [306] R. J. Swanekamp, J. T. DiMaio, C. J. Bowerman, and B. L. Nilsson, "Coassembly of enantiomeric amphipathic peptides into amyloid-inspired rippled β -sheet fibrils," *J. Am. Chem. Soc.*, vol. 134, pp. 5556-5559, 2012.
- [307] O. S. Makin, E. Atkins, P. Sikorski, J. Johansson, and L. C. Serpell, "Molecular basis for amyloid fibril formation and stability," *Proc. Natl. Acad. Sci.*, vol. 102, pp. 315-320, 2005.
- [308] T. R. Jahn, O. S. Makin, K. L. Morris, K. E. Marshall, P. Tian, P. Sikorski, *et al.*, "The common architecture of cross- β amyloid," *J. Mol. Biol.*, vol. 395, pp. 717-727, 2010.
- [309] W. Kabsch and C. Sander, "Dictionary of protein secondary structure: pattern recognition of hydrogen-bonded and geometrical features," *Biopolymers*, vol. 22, pp. 2577-2637, 1983.
- [310] M. Sunde, L. C. Serpell, M. Bartlam, P. E. Fraser, M. B. Pepys, and C. C. F. Blake, "Common core structure of amyloid fibrils by synchrotron X-ray diffraction1," *J. Mol. Biol.*, vol. 273, pp. 729-739, 1997.
- [311] H. Hiramatsu and T. Kitagawa, "FT-IR approaches on amyloid fibril structure," *Biochim. Biophys. Acta, Proteins Proteomics*, vol. 1753, pp. 100-107, 2005.
- [312] G. Zandomenighi, M. R. H. Krebs, M. G. McCammon, and M. Fändrich, "FTIR reveals structural differences between native β -sheet proteins and amyloid fibrils," *Protein Sci.*, vol. 13, pp. 3314-3321, 2004.
- [313] H. Hiramatsu, Y. Goto, H. Naiki, and T. Kitagawa, "Core structure of amyloid fibril proposed from IR-microscope linear dichroism," *J. Am. Chem. Soc.*, vol. 126, pp. 3008-3009, 2004.
- [314] J. Kubelka and T. A. Keiderling, "Differentiation of β -Sheet-Forming Structures: Ab Initio-Based Simulations of IR Absorption and Vibrational CD

- for Model Peptide and Protein β -Sheets," *J. Am. Chem. Soc.*, vol. 123, pp. 12048-12058, 2001.
- [315] E. T. Pashuck, H. Cui, and S. I. Stupp, "Tuning supramolecular rigidity of peptide fibers through molecular structure," *J. Am. Chem. Soc.*, vol. 132, pp. 6041-6046, 2010.
- [316] H. Acar, R. Garifullin, and M. O. Guler, "Self-Assembled Template-Directed Synthesis of One-Dimensional Silica and Titania Nanostructures," *Langmuir*, vol. 27, pp. 1079-1084, 2011.
- [317] D. Carter and K. C. Chou, "A model for structure-dependent binding of Congo red to Alzheimer β -amyloid fibrils," *Neurobiol. Aging*, vol. 19, pp. 37-40, 1998.
- [318] G. Liang, K. Xu, L. Li, L. Wang, Y. Kuang, Z. Yang, *et al.*, "Using Congo red to report intracellular hydrogelation resulted from self-assembly of small molecules," *Chem. Commun.*, pp. 4096-4098, 2007.
- [319] M. Biancalana and S. Koide, "Molecular mechanism of Thioflavin-T binding to amyloid fibrils," *Biochim. Biophys. Acta, Proteins Proteomics*, vol. 1804, pp. 1405-1412, 2010.
- [320] M. R. Nilsson, "Techniques to study amyloid fibril formation in vitro," *Methods*, vol. 34, pp. 151-160, 2004.
- [321] E. Hellstrand, B. Boland, D. M. Walsh, and S. Linse, "Amyloid β -protein aggregation produces highly reproducible kinetic data and occurs by a two-phase process," *ACS Chem. Neurosci.*, vol. 1, pp. 13-18, 2009.
- [322] G. Meisl, X. Yang, E. Hellstrand, B. Frohm, J. B. Kirkegaard, S. I. Cohen, *et al.*, "Differences in nucleation behavior underlie the contrasting aggregation kinetics of the A β 40 and A β 42 peptides," *Proc. Natl. Acad. Sci.*, vol. 111, pp. 9384-9389, 2014.
- [323] P. Arosio, T. P. Knowles, and S. Linse, "On the lag phase in amyloid fibril formation," *Phys. Chem. Chem. Phys.*, vol. 17, pp. 7606-7618, 2015.
- [324] T. C. Michaels and T. P. Knowles, "Kinetic theory of protein filament growth: Self-consistent methods and perturbative techniques," *Int. J. Mod. Phys. A*, vol. 29, p. 1530002, 2015.

- [325] R. Orbach, I. Mironi-Harpaz, L. Adler-Abramovich, E. Mossou, E. P. Mitchell, V. T. Forsyth, *et al.*, "The rheological and structural properties of Fmoc-peptide-based hydrogels: the effect of aromatic molecular architecture on self-assembly and physical characteristics," *Langmuir*, vol. 28, pp. 2015-2022, 2012.
- [326] F. Xu, J. Li, V. Jain, R. S. Tu, Q. Huang, and V. Nanda, "Compositional control of higher order assembly using synthetic collagen peptides," *J. Am. Chem. Soc.*, vol. 134, pp. 47-50, 2011.
- [327] E. Chatani, Y.-H. Lee, H. Yagi, Y. Yoshimura, H. Naiki, and Y. Goto, "Ultrasonication-dependent production and breakdown lead to minimum-sized amyloid fibrils," *Proc. Natl. Acad. Sci.*, vol. 106, pp. 11119-11124, 2009.
- [328] M. B. Enright and D. M. Leitner, "Mass fractal dimension and the compactness of proteins," *Phys. Rev. E*, vol. 71, p. 011912, 2005.
- [329] S. Koizumi, M. Annaka, S. Borbely, and D. Schwahn, "Fractal structures of a poly (N-isopropylacrylamide) gel studied by small-angle neutron scattering over a Q -range from 10^{-5} to 0.1 \AA^{-1} ," *Physica B: Condensed Matter*, vol. 276, pp. 367-368, 2000.
- [330] F. Chiti and C. M. Dobson, "Protein misfolding, functional amyloid, and human disease," *Annu. Rev. Biochem.*, vol. 75, pp. 333-366, 2006.
- [331] R. B. Weiss, "The anthracyclines: will we ever find a better doxorubicin?," in *Seminars in oncology*, 1992, pp. 670-686.
- [332] G. Minotti, P. Menna, E. Salvatorelli, G. Cairo, and L. Gianni, "Anthracyclines: molecular advances and pharmacologic developments in antitumor activity and cardiotoxicity," *Pharmacological reviews*, vol. 56, pp. 185-229, 2004.
- [333] P. K. Singal and N. Iliskovic, "Doxorubicin-induced cardiomyopathy," *New England Journal of Medicine*, vol. 339, pp. 900-905, 1998.
- [334] J. L. Quiles, J. R. Huertas, M. Battino, J. Mataix, and M. C. Ramírez-Tortosa, "Antioxidant nutrients and adriamycin toxicity," *Toxicology*, vol. 180, pp. 79-95, 2002.
- [335] J. J. Perona and C. S. Craik, "Structural basis of substrate specificity in the serine proteases," *Protein Science*, vol. 4, pp. 337-360, 1995.

- [336] W. K. Baumann, S. A. Bizzozero, and H. Dutler, "Specificity of α -chymotrypsin. Dipeptide substrates," *FEBS Letters*, vol. 8, pp. 257-260, 1970.
- [337] W. Ebeling, N. Hennrich, M. Klockow, H. Metz, H. D. Orth, and H. Lang, "Proteinase K from *Tritirachium album limber*," *European Journal of Biochemistry*, vol. 47, pp. 91-97, 1974.
- [338] P. Jönsson, M. P. Jonsson, J. O. Tegenfeldt, and F. Höök, "A method improving the accuracy of fluorescence recovery after photobleaching analysis," *Biophysical journal*, vol. 95, pp. 5334-5348, 2008.
- [339] S. Wang, E. A. Konorev, S. Kotamraju, J. Joseph, S. Kalivendi, and B. Kalyanaraman, "Doxorubicin induces apoptosis in normal and tumor cells via distinctly different mechanisms intermediacy of H₂O₂-and p53-dependent pathways," *Journal of Biological Chemistry*, vol. 279, pp. 25535-25543, 2004.
- [340] S. F. Badylak, "The extracellular matrix as a biologic scaffold material," *Biomaterials*, vol. 28, pp. 3587-3593, 2007.
- [341] S. F. Badylak, D. O. Freytes, and T. W. Gilbert, "Extracellular matrix as a biological scaffold material: Structure and function," *Acta Biomaterialia*, vol. 5, pp. 1-13, 2009.
- [342] M. Lutolf and J. Hubbell, "Synthetic biomaterials as instructive extracellular microenvironments for morphogenesis in tissue engineering," *Nat. Biotechnol.*, vol. 23, pp. 47-55, 2005.
- [343] K. Y. Lee and D. J. Mooney, "Hydrogels for tissue engineering," *Chem. Rev.*, vol. 101, pp. 1869-1880, 2001.
- [344] A. S. Hoffman, "Hydrogels for biomedical applications," *Adv. Drug Delivery Rev.*, vol. 54, pp. 3-12, 2002.
- [345] R. Langer and N. A. Peppas, "Advances in biomaterials, drug delivery, and bionanotechnology," *AIChE J.*, vol. 49, pp. 2990-3006, 2003.
- [346] J. Thiele, Y. Ma, S. Bruekers, S. Ma, and W. T. Huck, "25th Anniversary Article: Designer Hydrogels for Cell Cultures: A Materials Selection Guide," *Adv. Mater.*, vol. 26, pp. 125-148, 2014.
- [347] J. L. Drury and D. J. Mooney, "Hydrogels for tissue engineering: scaffold design variables and applications," *Biomaterials*, vol. 24, pp. 4337-4351, 2003.

- [348] D. L. Hern and J. A. Hubbell, "Incorporation of adhesion peptides into nonadhesive hydrogels useful for tissue resurfacing," *J. Biomed. Mater. Res.* , vol. 39, pp. 266-276, 1998.
- [349] J. Zhu, "Bioactive modification of poly (ethylene glycol) hydrogels for tissue engineering," *Biomaterials*, vol. 31, pp. 4639-4656, 2010.
- [350] E. A. Phelps, N. O. Enemchukwu, V. F. Fiore, J. C. Sy, N. Murthy, T. A. Sulchek, *et al.*, "Maleimide cross-linked bioactive peg hydrogel exhibits improved reaction kinetics and cross-linking for cell encapsulation and in situ delivery," *Adv. Mater.* , vol. 24, pp. 64-70, 2012.
- [351] H. J. Lee, J.-S. Lee, T. Chansakul, C. Yu, J. H. Elisseeff, and M. Y. Seungju, "Collagen mimetic peptide-conjugated photopolymerizable PEG hydrogel," *Biomaterials*, vol. 27, pp. 5268-5276, 2006.
- [352] H. K. Lau and K. L. Kiick, "Opportunities for Multicomponent Hybrid Hydrogels in Biomedical Applications," *Biomacromolecules*, vol. 16, pp. 28-42, 2015.
- [353] F. Yang, C. G. Williams, D.-a. Wang, H. Lee, P. N. Manson, and J. Elisseeff, "The effect of incorporating RGD adhesive peptide in polyethylene glycol diacrylate hydrogel on osteogenesis of bone marrow stromal cells," *Biomaterials*, vol. 26, pp. 5991-5998, 2005.
- [354] Q. Hou, D. W. Grijpma, and J. Feijen, "Preparation of interconnected highly porous polymeric structures by a replication and freeze-drying process," *Journal of Biomedical Materials Research Part B: Applied Biomaterials*, vol. 67, pp. 732-740, 2003.
- [355] Y.-C. Chiu, J. C. Larson, A. Isom Jr, and E. M. Brey, "Generation of porous poly (ethylene glycol) hydrogels by salt leaching," *Tissue Eng., Part C Methods* vol. 16, pp. 905-912, 2010.
- [356] R. M. Namba, A. A. Cole, K. B. Bjugstad, and M. J. Mahoney, "Development of porous PEG hydrogels that enable efficient, uniform cell-seeding and permit early neural process extension," *Acta Biomaterialia*, vol. 5, pp. 1884-1897, 2009.
- [357] J. B. Matson and S. I. Stupp, "Self-assembling peptide scaffolds for regenerative medicine," *Chem. Commun.* , vol. 48, pp. 26-33, 2012.

- [358] S. Sur, F. Tantakitti, J. B. Matson, and S. I. Stupp, "Epitope topography controls bioactivity in supramolecular nanofibers," *Biomater. Sci.*, vol. 3, pp. 520-532, 2015.
- [359] M. O. Guler, L. Hsu, S. Soukasene, D. A. Harrington, J. F. Hulvat, and S. I. Stupp, "Presentation of RGDS epitopes on self-assembled nanofibers of branched peptide amphiphiles," *Biomacromolecules*, vol. 7, pp. 1855-1863, 2006.
- [360] K. M. Galler, L. Aulisa, K. R. Regan, R. N. D'Souza, and J. D. Hartgerink, "Self-assembling multidomain peptide hydrogels: designed susceptibility to enzymatic cleavage allows enhanced cell migration and spreading," *J. Am. Chem. Soc.*, vol. 132, pp. 3217-3223, 2010.
- [361] J. M. Anderson, M. Kushwaha, A. Tambralli, S. L. Bellis, R. P. Camata, and H.-W. Jun, "Osteogenic differentiation of human mesenchymal stem cells directed by extracellular matrix-mimicking ligands in a biomimetic self-assembled peptide amphiphile nanomatrix," *Biomacromolecules*, vol. 10, pp. 2935-2944, 2009.
- [362] H. Ceylan, S. Kocabey, H. Unal Gulsuner, O. S. Balcik, M. O. Guler, and A. B. Tekinay, "Bone-Like Mineral Nucleating Peptide Nanofibers Induce Differentiation of Human Mesenchymal Stem Cells into Mature Osteoblasts," *Biomacromolecules*, vol. 15, pp. 2407-2418, 2014.
- [363] G. M. Harbers and K. E. Healy, "The effect of ligand type and density on osteoblast adhesion, proliferation, and matrix mineralization," *Journal of Biomedical Materials Research Part A*, vol. 75A, pp. 855-869, 2005.
- [364] J.-Y. Sun, X. Zhao, W. R. Illeperuma, O. Chaudhuri, K. H. Oh, D. J. Mooney, *et al.*, "Highly stretchable and tough hydrogels," *Nature*, vol. 489, pp. 133-136, 2012.
- [365] D. J. Munoz-Pinto, A. C. Jimenez-Vergara, T. P. Gharat, and M. S. Hahn, "Characterization of sequential collagen-poly (ethylene glycol) diacrylate interpenetrating networks and initial assessment of their potential for vascular tissue engineering," *Biomaterials*, vol. 40, pp. 32-42, 2015.

- [366] J.-T. Zhang, S. Petersen, M. Thunga, E. Leipold, R. Weidisch, X. Liu, *et al.*, "Micro-structured smart hydrogels with enhanced protein loading and release efficiency," *Acta Biomater.*, vol. 6, pp. 1297-1306, 2010.
- [367] S. Yang, J. Wang, H. Tan, F. Zeng, and C. Liu, "Mechanically robust PEGDA–MSNs-OH nanocomposite hydrogel with hierarchical meso-macroporous structure for tissue engineering," *Soft Matter*, vol. 8, pp. 8981-8989, 2012.
- [368] K. Y. Suh, J. Seong, A. Khademhosseini, P. E. Laibinis, and R. Langer, "A simple soft lithographic route to fabrication of poly (ethylene glycol) microstructures for protein and cell patterning," *Biomaterials*, vol. 25, pp. 557-563, 2004.
- [369] K. L. Niece, J. D. Hartgerink, J. J. Donners, and S. I. Stupp, "Self-assembly combining two bioactive peptide-amphiphile molecules into nanofibers by electrostatic attraction," *J. Am. Chem. Soc.*, vol. 125, pp. 7146-7147, 2003.
- [370] V. Karageorgiou and D. Kaplan, "Porosity of 3D biomaterial scaffolds and osteogenesis," *Biomaterials*, vol. 26, pp. 5474-5491, 2005.
- [371] M. Mastrogiacomo, S. Scaglione, R. Martinetti, L. Dolcini, F. Beltrame, R. Cancedda, *et al.*, "Role of scaffold internal structure on in vivo bone formation in macroporous calcium phosphate bioceramics," *Biomaterials*, vol. 27, pp. 3230-3237, 2006.
- [372] S. Hansen, "Bayesian estimation of hyperparameters for indirect Fourier transformation in small-angle scattering," *J. Appl. Crystallogr.*, vol. 33, pp. 1415-1421, 2000.
- [373] S. R. Kline, "Reduction and analysis of SANS and USANS data using IGOR Pro," *J. Appl. Crystallogr.*, vol. 39, pp. 895-900, 2006.
- [374] A. Bacioğlu, U. Kazan, and S. İde, "Single and multilayered a-SiO_x:H (x < 1) thin film samples analyzed by optical absorption and small-angle X-ray scattering," *Mater. Chem. Phys.*, vol. 146, pp. 425-430, 2014.
- [375] S. Kocabey, H. Ceylan, A. B. Tekinay, and M. O. Guler, "Glycosaminoglycan mimetic peptide nanofibers promote mineralization by osteogenic cells," *Acta Biomater.*, vol. 9, pp. 9075-9085, 2013.

- [376] R. P. Haugland, I. C. MacCoubrey, and P. L. Moore, "Dual-fluorescence cell viability assay using ethidium homodimer and calcein AM," ed: Google Patents, 1994.
- [377] A. J. Engler, S. Sen, H. L. Sweeney, and D. E. Discher, "Matrix elasticity directs stem cell lineage specification," *Cell*, vol. 126, pp. 677-689, 2006.
- [378] Y. R. V. Shih, K. F. Tseng, H. Y. Lai, C. H. Lin, and O. K. Lee, "Matrix stiffness regulation of integrin-mediated mechanotransduction during osteogenic differentiation of human mesenchymal stem cells," *J. Bone Miner. Res.*, vol. 26, pp. 730-738, 2011.
- [379] N. Marí-Buyé, T. Luque, D. Navajas, and C. E. Semino, "Development of a three-dimensional bone-like construct in a soft self-assembling peptide matrix," *Tissue Eng., Part A* vol. 19, pp. 870-881, 2013.
- [380] L. C. Wu, J. Yang, and J. Kopeček, "Hybrid hydrogels self-assembled from graft copolymers containing complementary β -sheets as hydroxyapatite nucleation scaffolds," *Biomaterials*, vol. 32, pp. 5341-5353, 2011.
- [381] F. Shapiro, "Bone development and its relation to fracture repair. The role of mesenchymal osteoblasts and surface osteoblasts," *Eur. Cells Mater.*, vol. 15, pp. 53-76, 2008.
- [382] G. Forgacs, R. A. Foty, Y. Shafir, and M. S. Steinberg, "Viscoelastic properties of living embryonic tissues: a quantitative study," *Biophys. J.*, vol. 74, pp. 2227-2234, 1998.
- [383] M. P. Lutolf, P. M. Gilbert, and H. M. Blau, "Designing materials to direct stem-cell fate," *Nature*, vol. 462, pp. 433-441, 2009.